Universitat Autònoma de Barcelona

Processing and Structuring of Molecular Materials for Environmental and Biomedical Applications

César Díez Gil

Tesi Doctoral

Programa de Doctorat de Ciència de Materials

Directors

Jaume Veciana i Imma Ratera

Departament de Química

Facultat de Ciències

2010

Memòria presentada per aspirar al Grau de Doctor per:

César Díez Gil

Vist i plau:

Prof. Jaume Veciana

Dr. Imma Ratera

a Bellaterra, 14 de Septiembre de 2010

JAUME VECIANA MIRÓ, Research Professor and **IMMA RATERA BASTARDAS** Titular Scientist, of the Spanish Council of Research at the Materials Science Institute of Barcelona (ICMAB-CSIC)

CERTIFY

That **César Díez Gil**, "licenciado" in Chemistry, has performed, under their management, the research work entitled **"Processing and Structuring of Molecular Materials for Environmental and Biomedical Applications".** This work has been performed under the mark of the Materials Science Ph. D. program of the Chemistry Department of the Autonomous University of Barcelona.

An in witness whereof this is signed by

Directors

Imma Ratera Bastardas

Jaume Veciana Miró

FECHA

Parto sudau, parto curau

Refrán popular aragonés

Agradecimientos

Pese a que una única persona aparece como autor final de esta Tesis Doctoral, la culminación de este proyecto es fruto del trabajo y esfuerzo de mucha más gente. Así pues no querría desaprovechar esta oportunidad para demostrar mi gratitud hacia todas las personas que me han ayudado tanto laboral como personalmente durante estos casi cinco años.

En primer lugar me gustaría agradecer al Prof. Jaume Veciana no solo por haberme dado la oportunidad de realizar la Tésis Doctoral en su grupo, permitiendome de esta manera descubrir el mundo de la investigación, sino también por su completa involucración y apoyo durante la realización de este, a veces no tan agradecido, trabajo.

Tampoco puedo ni quiero olvidar a la Dra. Imma Ratera cuya presencia y consejo han sido cruciales para la consecución de este proyecto.

Por supuesto, agradecer también el soporte tanto del Ministerio de Educación como de la Unión Europea que han hecho economicamente factible el desarrollo de este trabajo de investigación y me han permitido completar mi formación a través de congresos, escuelas y seminarios.

A su vez, esta Tésis no hubiese sido posible sin las multiples y fructiferas colaboraciones de las que he disfrutado durante este periodo de tiempo. Primero, me gustaría agradecer especialmente al grupo del Prof. Pedro Molina la Universidad de Murcia y más especificamente a Antonio y Charo por su eficacia a la hora de proporcionarme los receptores de mercurio sin protestar pese a lo, probablemente, desproporcionado de mis demandas. De la misma forma, dar las gracias a todo el grupo del Prof. Antonio Villaverde del IBB, Elena, Escar, Quim, Olivia, Esther, y el resto de colaboradores por recordarme lo bonitas que son la biologia y la bioquímica. Al Prof. Otto S. Wolfbeis y al Dr. Thomas Hirsch por acojerme en su laboratorio en Regensburg y permitirme el uso de su SPR. Por último, pero no menos importante, dar las gracias a Sven sin cuyo trabajo y dedicación mucho de lo estudiado con los cuerpos de inclusión no hubiese sido posible. A todos ellos gracias, parte de esta Tésis también es vuestra.

Dejando a un lado la parte más científica me gustaría dar las gracias a todas las personas que han pasado por el grupo durante estos años que me han hecho sentir bien tanto en los buenos momentos, como en los no tan buenos. A todos ellos mil gracias.

Para terminar dar muy especialmente las gracias a mi familia, ya no solo por estos últimos cinco años sino por toda una vida de esfuerzos y trabajo que me ha permitido llegar hasta donde estoy y ser quien soy. Gracias a los que están y a los que no. Especialmente a mi abuelo Antonio, gracias de corazón.
Y en último lugar dar las gracias a las personas más importantes de mi vida: Papá, Mamá, Ana y Eli porque siempre habeis estado, estais y se que estareís, os quiero mucho.

Summary

During the last decades the construction of devices based on molecular functional materials with specific properties has become one of the major objectives of materials scientists, since they can offer new and exciting functionalities to the present human activities. Although their basic properties will be guided by the fundamental -electronic, magnetic, optical, mechanical, etc- properties of their molecular constituent units, the final functionality of a device will depend, in a major way, on the processing and structuring techniques used during its construction.

In this context, the main objective of this Thesis has been the use of different processing and structuring techniques for the development of new functional materials based on already tested environmentally and biologically active compounds.

Among all the environmentally hazardous substances present in our environment, heavy metal ions, and specially mercury, are highly toxic elements which contamination, due to both natural and anthropogenic reasons, has become severe in some parts of the world, resulting in health damage to their inhabitants. Therefore, the developing of new sensors able to detect selectively and sensitively Hg^{2+} on aqueous media is still an actual challenge.

In this work we present two 1,4-disubstituted-2,3-diaza-1,3-butadiene derivatives (**1** and **2**) able to selectively perform optical detection of Hg^{2+} in aqueous media, that combined with different nanostructuring and anchoring techniques allowed us to obtain highly sensitive solid-supported mercury detection systems. The first of them is based on the physisorption of the diaza butadiene indicators on porous cellulose membranes obtaining indicator coated probes that could be used as new cheap and reliable Hg^{2+} sensing systems. In order to do that, two different structuring techniques have been used. The most intuitive one, which we have named *"developing technique"*, is founded on the use of the optically active Hg^{2+} organic receptor **1** as a Hg^{2+} developing agent of a cellulose substrate, previously impregnated with the contaminated solution. Although Hg^{2+} detection tests performed using this colorimetric chemosensing probes, based on receptor **1**, showed good selectivity and reproducibility, they presented a limited sensitivity *vs.* Hg^{2+}. The detection limit of the probes was set on tens of ppm (10^{-2}g/l), far away from the 1 ppb (μg/l) fixed by the European Union (EU) and the North American Environmental Protection Agency (EPA) as the maximum amount of Hg^{2+} allowed in drinkable water. Nevertheless, this procedure served as a prove of concept for the developing of probes based on the use of cheap and renewable materials to be

applied on the *in situ* detection of contaminants. The other structuring technique used is based on a new physisorption procedure, involving the production and deposition of nanoparticles of the organic sensing molecules on nanoporous cellulose membranes for the fabrication of hybrid membranes. In this case, excellent Hg^{2+} detection results showing a high Hg^{2+} sensitivity and selectivity were obtained for the receptor **2** based cellulose probes. In contrast to the previous case, the detection limit obtained matched the EU and EPA requirements for drinkable water, reaching the level of ppb (μg/l).

On a second approach the covalent bonding was used as a driving force for the receptor anchoring onto a solid substrate. In this case we developed a surface plasmon resonance (SPR) sensor able to perform picomolar detection of Hg^{2+} on aqueous systems. The rational design of the Hg^{2+} receptors (**3** and **4**) optimizes the sensitivity and reliability of the sensor allowing us to selectively detect, in presence of other divalent cations, Hg^{2+} concentrations on aqueous systems on the picomolar range, meliorating on three orders of magnitude the EU and EPA Hg^{2+} detection limit on drinkable water.

As contamination control and pollutant removal, regenerative medicine in general and particularly in tissue engineering (TE) has the enormous potential of improving the quality of life for many thousands of people throughout the world.

Although most of the more commonly used biomaterials match all the structural and mechanical resistance requirements to be applied in regenerative medicine, the interaction of such materials with the surrounding biological media is still not well controlled, leading to undesired immunological responses such as infections or uncontrolled inflammation in some cases.

The work developed on the second part of this thesis has been focused on the study, characterization and processing of a new kind of proteinaceous nanoparticulate biomaterial, known as inclusion bodies (IBs), as a promising additive for cell proliferation enhancement.

The first part of the research regarding the processing and structuring of biologically active materials is centered on the characterization of the nanoscale, physicochemical and structural properties of a novel family of proteinaceous aggregates known as "inclusion bodies" (IBs). Thus, IBs coming from different genetic backgrounds have been characterized by means of light dispersion and surface analysis techniques, such as dynamic light scattering (DLS), atomic force microscopy (AFM) or contact angle (CA). Results obtained indicated that IBs produced in absence of different elements of the cellular heat shock machinery (DnaK, ClpA,

and ClpP genes) exhibit a range of sizes, wettability and stiffness values, that let us conclude the existence of a direct relationship between the conformation status of the recombinant proteins inside the IBs and their physicochemical and structural properties.

Randomly distributed IBs, from different genetic backgrounds, were used to decorate amine terminated silicon surfaces. It was possible to observe how cultured mammalian cells respond differentially to IB variants when used as particulate materials to engineer the physicochemical surface properties, proving that the actual range of referred mechanical as well as other physicochemical properties is sensed and discriminated by biological systems. To further prove the validity of IBs as stimulator of cell proliferation, microstructuring of the IBs onto the same substrate was performed using the Microcontact Printing (μCP) technique. The obtained results confirmed again the ability of IBs to stimulate cell proliferation on surfaces initially not suitable for cell growth.

Therefore, it is possible to conclude that the tuning opportunities offered through adjusting the genetic background of the cell where the IBs are produced, definitively expands the spectrum of biomedical applications of this novel bacterial nanomaterial.

Contents

List of Abbreviations

ACN	Acetonitrile
AFM	Atomic Force Microscopy
BODIPY	Boron Dipyrromethene
ClpA$^-$	IBs produced in ClpA deficient *E. Coli*
ClpP$^-$	IBs produced in ClpP deficient *E. Coli*
CVD	Chemical Vapor Deposition
CFs	Compressed Fluids
CPs	Conjugated Polymers
CA	Contact Angle
DFT	Density Functional Theory
DNA	Deoxyribonucleic acid
DnaK$^-$	IBs produced in DnaK deficient *E. Coli*
DEPH	Diethylphosphoroushydrazidate
DMSO	Dimethylsulphoxide
DLS	Dynamic Light Scattering
dsDAN	Double Strand DNA
EDTA	Ethylenediaminetetraacetic acid
EDX	Energy Dispersive X-ray
EET	Energetic Electron Transfer
ELISA	Enzyme-Linked Immunosorbent Assay
EW	Evanescent Wave
EPA	Environmental Protection Agency
EU	European Union

FSAFM	Force Spectroscopy Atomic Force Microscopy
FT-IR	Fourier Transform Infrared
GFP	Green Fluorescent Protein
Au-NPs	Gold nanoparticles
IB(s)	Inclusion Body(ies)
ITO	Indium Tin Oxide
ICP-MS	Inductive Coupled Plasm Mass Spectrometry
IR	Infrared
ICMAB	Instituto de Ciencia de Materiales de Barcelona
LSER	Linear Solvation Energy Relationship
LES	Locally Excited State
MST	Materials Science Tetrahedron
μCP	Micro Contact Printing
MolFM	Molecular Functional Materials
NMP	N-methylpirrolidine
NMR	Nuclear Magnetic Resonance
PET	Photo-induced Electron Transfer
ppm	Parts per Million (mg/L)
ppb	Parts per Billion (μg/L)
ppt	Parts per Trillion (ng/L)
PBS	Phosphate Buffer Solution
PDMS	Polydimethylsiloxane
PVC	Poly(Vinil Chloride)
RIU	Refractive Index Units
RI	Refractive Index
RNA	Ribonucleic acid
SAMDI-ToF	Surface-Assisted Laser Desorption/Ionization Time of Flight
SAM(s)	Self Assembled Monolayer(s)
SEM	Scanning Electron Microscopy

SRB	Sulpho-Reductive bacteria
SPR	Surface Plasmon Resonance
ssDNA	Single Strand DNA
THF	Tetrahydrofurane
TPB^-	tetrakis(4-chlorophenyl)borate anion
TE	Tissue Engineering
UV-Vis	Ultraviolet-Visible
UHV	Ultra High Vacuum
UNEP	United Nations Environment Program
wt	IBs produced in non modified *E. Coli*

Para los que siempre están ahí
Papá, Mamá, Ana y Eli...

Part I

Introduction

"Coal and diamonds, sand and computer chips, cancer and healthy tissue: throughout history, variations in the arrangement of atoms have distinguished the cheap from the cherished, the diseased from the healthy. Arranged one way, atoms make up soil, air, and water arranged another, they make up ripe strawberries. Arranged one way, they make up homes and fresh air; arranged another, they make up ash and smoke"

Eric Drexler: *Engines of Creation* p.3 1983

Chapter 1

Functional Materials: Past, Present and Future

Since the beginning of the times, the development and use of new materials has been linked to human beings and to the evolution of our society. It is hard to imagine how human civilization would have developed without the use of stone, wood, clay, bronze, iron, copper, or steel among other kinds of materials from which our tools and instruments are made of. Hence, it is not surprising that they have served to demarcate large historical periods in human civilization, such as the Stone Age, Bronze Age, or Iron Age. Thus, it is possible to say that the study and development of new materials is essential for our lives.

The extension and diversification of materials, extracted from natural objects and produced in workshops, factories, and laboratories, are among the most impressive manifestations of technological and scientific productivity of the human history. Therefore, as a consequence of the knowledge acquired during hundreds of generations, the databases of chemists and material scientists list more than ten millions of different materials and chemical substances.[1]

At this moment, it is extremely difficult for anybody not to recognize the importance of the so called *technological era*, which completely domains our actual existence. The appearance of global communication networks, massive data storage devices, new energy sources or safer and faster transport media has been the result of the sustained research and development of materials, namely *functional materials*. Although by definition *functional materials* are substances showing a certain function different from the merely structural ones. Such a broad definition

includes a wide set of materials bearing a large range of properties and applications. Therefore, the classification of *functional materials* is usually limited to materials whose "function" is associated with the present human activities, like information technology, energy production, biologic applications, space technology, or environmental control, among many others. A more detailed classification of *functional materials* according to their final application is depicted in Figure 1.1.

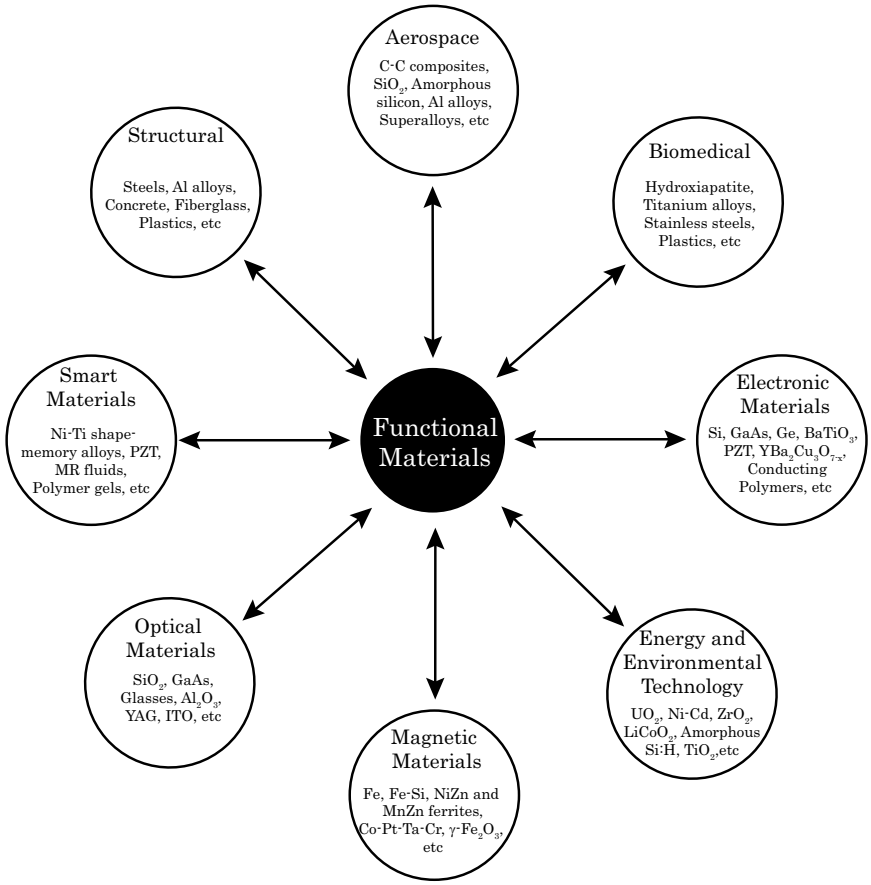

Figure 1.1: Functional classification of materials.

The increasing importance of *functional materials* is a reflect of their unique properties, which are directly dependent on their chemical composition, structure or manufacture process, factors that, at the same time, are closely linked between them. Therefore, the complete knowledge and understanding of the relationships between these has become the actual *Philosopher's Stone* of Material Science, as

its control will allow the production of improved materials for known applications as well as for new uses and in a sustainable and cost efficient way.

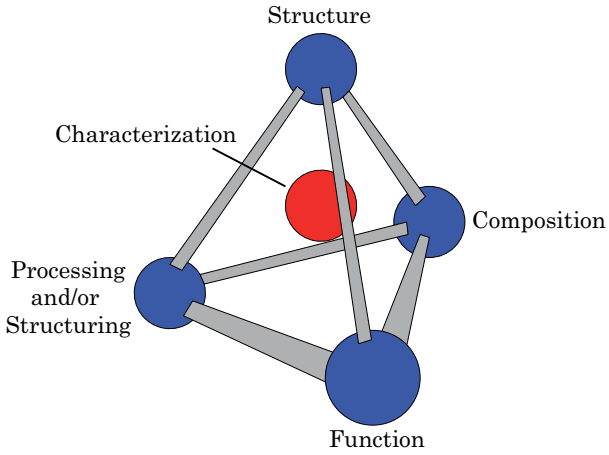

Figure 1.2: Materials Science Tetrahedron.

A fair representation of the above described relationship is depicted in Figure 1.2, more known as the *Materials Science Tetrahedron* (MST).[2] As shown, the four elements present in the MST are closely connected, by means of interrelated bonds. Thus, while the *function* of a determined material represents the reason for its developing, the only path to achieve it will be the obtaining of a determined substance with the appropriate *composition* and *micro- nano-structure*, which at the same time are closely related to each other. In addition, the correct understanding of the *structure-property* relationship is basic for the development of any material, and this process should be carried out trough the appropriate *characterization* of its *structure*, *composition* and *function*. For this reason, the *characterization* activity is placed in the center of the MST. Once this relationship is clear, material properties can be modified by changing structure of the matter through engineering approaches, that is, its *processing or structuring*, and thereby delivering the desired functional *performance*.

Chapter 2

Processing of Molecular Functional Materials

Apart form the traditional disciplines, such as metallurgy, ceramics or polymer science, recent advances in other disciplinary fields, such as molecular materials, surface chemistry, genetic engineering or microelectronics, have made of materials science one of the main pillars of the actual applied research. More recently, the enormous stimulus that the developing of the nanoworld and the advances obtained on new ways of micro- and nano-structuring the materials, have made even more attractive the field of materials science and technology.

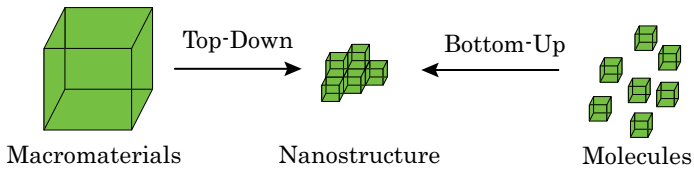

Figure 2.1: Scheme of the two existent approximations for the nanofabrication of devices; Top-Down and Botom-Up.

Two main strategies can be followed for the fabrication and/or structuring of micro- or nanometric systems, the *Top-Down* and the *Bottom-Up* approaches, represented in Figure 2.1.

For the *Top-Down* approach the processing of the material is carried out starting from a macroscopic element whose shape and structure are modified until the desired product is achieved. Numerous methods can be included in this category, from which it is worthy to remark those devoted to the particle milling and

grinding, such as ball- or vibro- milling techniques of extensive use on the pharmaceutical enterprise.

Nevertheless, the most classical example of a *Top-Down* processing technique is the manufacturing of integrated circuits in microelectronics. Here the *Top-Down* approach makes use of improved photolithographic methods to pattern structures onto the surface of a nearly perfect monocrystaline silicon wafer (Figure 2.2).

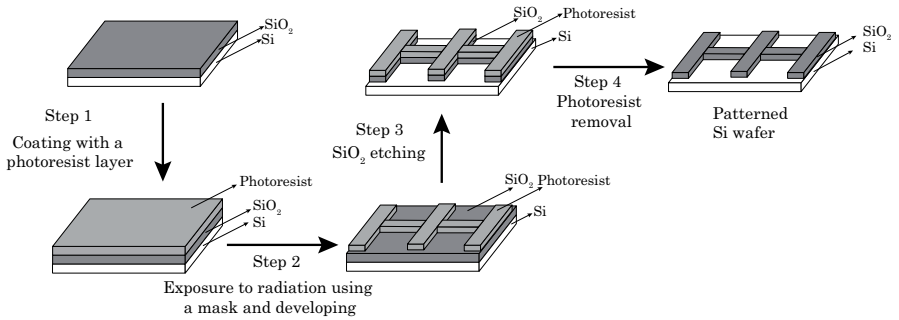

Figure 2.2: Basic photolithography and pattern transfer. The example uses an oxidized Si wafer and a negative photoresist system. Processing steps include photoresist coating, exposure to radiation with a mask and developing, oxide etching and photoresist removal.

The main advantages of the photolithographic methods for the obtaining of structured materials are their easy scale-up and the possibility of achieving complex and well controlled large area structures with lateral resolutions down to the tens of nanometer. However, the continuous improvement of the processing capabilities of the chips by means of the reduction of the sizes of the patterned features, has become a big problem as it starts to reach the physical limits of the traditional photolithographic methods. Therefore, the employment of new lithographic techniques with better lateral resolutions, using e-beam lithography or x-ray photolithography, is needed for fulfilling the technological demand existing nowadays. Nonetheless, due to their complexity those new techniques require the use of much intense radiation sources and cleaner working environments; facts that exponentially increment the production costs, making the fabrication procedures less and less profitable.[3,4]

The appearance of *Bottom-Up* approaches came as the logical alternative to solve some of the *Top-Down* processes related problems. Firstly conceptually proposed by *E. Drexler* back in 1986, it points out towards the complete opposite direction than the *Top-Down* concept. Instead of sculpting a bulk material until obtaining the desired micro- or nano-structure, it makes use of the atomic and molecular

components of matter as building blocks for the construction of more complex structures and organizations until the achievement of the desired product. This novel concept has not only entailed the appearance of new and promising fabrication and structuring technologies, but also the emergence of a new kind of functional materials, the so called *Molecular Functional Materials* (MolFM).
Contrary to materials processed following the *Top-Down* approach, where standard substances with well defined properties are employed as starting materials, the design of a new MolMF starts with the synthesis of its molecular building blocks. The synthesis of molecules, although tedious, allows the scientists to specifically modify the properties of a molecule towards a determined objective, which dramatically increases their control over the final properties of the MolFM. Nevertheless, this is not the only factor affecting the final functionality of a MolFM, being the material processing and structuring as important as the molecular synthesis itself.

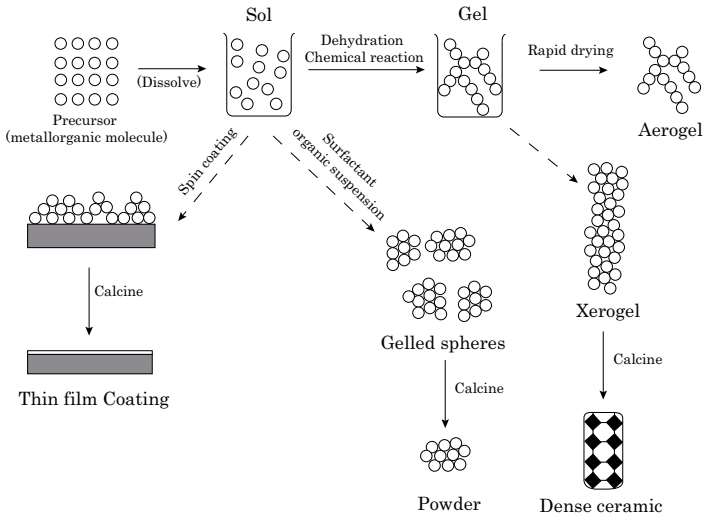

Figure 2.3: Example of the different final materials that are achievable following a *Bottom-Up* strategy as the *sol-gel* method.

Although the building blocks of a MolFM are held together internally by the action of strong bonds, mainly covalent or ionic, the interaction between the different molecules forming the final structure of the MolFM is mainly driven by interaction of their constituent molecular units by means of weak forces, such as hydrogen bonds or van der Waals interactions, among others.

In contrast with the *Top-Down* processing techniques, where the materials' final structure emerges as a consequence of the manufacturing treatment, the appearance, strength and number of these weak intermolecular bonds is highly dependent of the surrounding medium, enabling the achievement of different molecular self-organizations (also known as self-assembling[5]) with the same constituent units just by changing the environmental processing conditions. This versatility bestows scientists with a very powerful tool for the obtaining of different materials, bearing different properties and functionalities, just by changing the preparation procedure.

One clear example of this paradox is the "*sol-gel*" materials processing (Figure 2.3). The "*sol-gel*" process is a versatile technique for making ceramic and glass materials from solutions or colloids. In general it involves the transition of a system from a liquid, the "*sol*" state, into a solid, the "*gel*" phase. The starting materials used in the preparation of the "*sol*" are usually inorganic metal salts or metal organic compounds such as metal alkoxides. In a typical "*sol-gel*" process, the precursor is subjected to a series of hydrolysis and polymerization reactions to form a colloidal suspension, or a "*sol*". Further processing of the "*sol*" enables to fabricate ceramic, glass materials or even hybrid organic/inorganic materials in a wide variety of forms, from ultrafine or spherical powders to thin film coatings or extremely porous areogels.[6]

Nevertheless, the "*sol-gel*" is not the only *Bottom-Up* MolFM preparation technique, since there are a large variety of different techniques that yielded a whole family of different functional materials. During the last years several other procedures have been employed for the processing of different kinds of MolFM. Among them it is worthy to remark those based on the reaction between a substrate surface and a gaseous precursor like Chemical Vapor Deposition methods (CVD), widely used to produce carbon nanotubes, those based on the use of electricity, such as electrospinning, mainly used for the obtaining of polymeric fibers, or those based on the use of pressurized liquid or gases for the obtaining of organic nanoparticles. One clear example or this are the recent works developed in our group at the Materials Research Institute of Barcelona (ICMAB) where the use of supercritical fluids*, and more particularly CO_2, appears as an extremely interesting

*A fluid at a temperature and pressure above its critical point. Supercritical fluids are suitable as a substitute for organic solvents in a range of industrial and laboratory processes. Carbon dioxide and water are the most commonly used supercritical fluids, being used in several industrial processes.

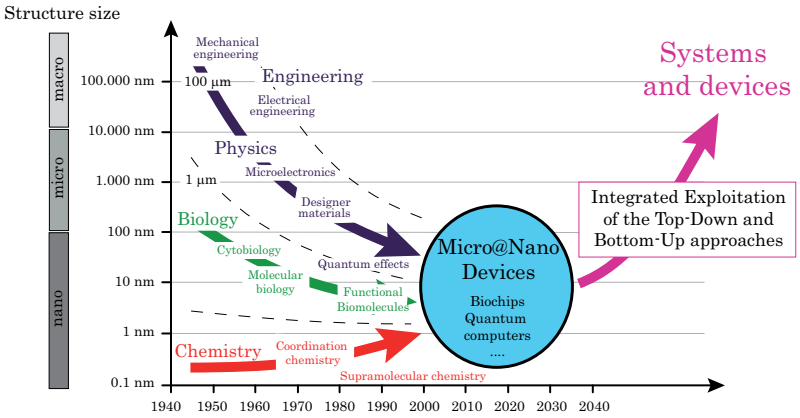

Figure 2.4: Scheme of the multidisciplinary evolution and the future trends of the *Top-Down* and the *Bottom-Up* nanomaterials processing approaches.

processing technique substitute of the classical *Top-Down* milling nanoparticularization processes due to the excellent quality and homogeneity of the particles obtained together with their cost effectiveness and easy scale-up. Furthermore, the versatility of this *Bottom-Up* approach exceeds largely the achieved for the classical *Top-Down* methods being possible, just by performing small variations of the preparation scheme, the obtaining of novel materials, such as 0D vesicular systems, with interesting biomedical properties for drug delivery applications.

During the first decades of the micro-nanotechnological revolution researchers from the different scientific fields involved, considered the micro- nanostructuring of materials (via *Top-Down* or *Bottom-Up*) as something proper of their research area and independent from any other. However, with the pass of time it has been demonstrated that the developing of complex systems and devices such as medical biosensors, can not be accomplished if only the *Top-Down* or *Bottom-Up* approaches are employed but a combined use of both approaches is required (Figure 2.4).

As previously stated, probably the most clear example of this is the fabrication of biochips for the selective detection of biological molecules. Figure 2.5 represent one of these devices designed to electrochemically detect and quantify the interaction of complementary deoxyribonucleic acid (DNA) strands to double-stranded hybrids or protein-protein interactions with an Enzyme-Linked Immunosorbent Assay (ELISA)† like test.[7]

†A biochemical technique used mainly in immunology to detect the presence of an antibody or an antigen in a sample.

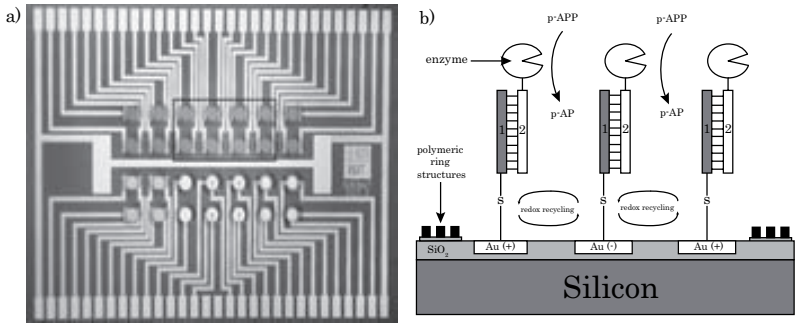

Figure 2.5: a) Details of the electrical array-chip. The chip is equipped with 28 positions of 200 μm in diameter. Of these, 14 positions have test structures, and 14 have interdigitated gold ultramicroelectrode-arrays (IDAs) with 0.8 μm gap and 0.8 μm width b) Scheme of the DNA-ELISA. Target molecules bound specifically to the thiol-linked capture molecules and were then enzyme labeled. The enzyme converted its substrate p-aminophenyl phosphate (p-APP) to the electroactive p-aminophenole (p-AP) which was measured at the electrodes. Image obtained from *Albers et al Analytical and Bioanalytical chemistry*, 2003, 377, 521.

The development of such electrical multiposition chips requires both, the use of interdigitated gold ultramicroelectrode arrays of 0.8 μm width and 0.8 μm gap manufactured in Si technology by means of traditional *Top-Down* Si photolithography and a *Bottom-Up* approach for the incorporation of the molecular detection system. The molecular detection system is, in this case, based on redox signals of a set of products generated by the entrapment of the target molecules by a Self Assembled Monolayer (SAM) of thiol-linked molecules over the gold electrodes (Figure 2.5). Furthermore, this detection systems can be further implemented in much more complicated devices such as the one depicted in Figure 2.6.[8] There, a fully integrated biochip device consisting on a set of microfluidic mixers, valves, pumps, channels, chambers, heaters, and DNA microarray sensors completely developed by the combined use of simple *Top-Down* and *Bottom-Up* approaches is shown.

Therefore, it is possible to conclude that although the development of new compounds with improved properties is extremely important for the evolution of science and technology, the correct processing and structuring of those already existent, might lead us to the obtaining of new, better and cheaper materials with improved properties that otherwise would never have been displayed.

Thus, the main objective of this thesis work will be the use of material processing techniques for the development of new functional materials with unique and

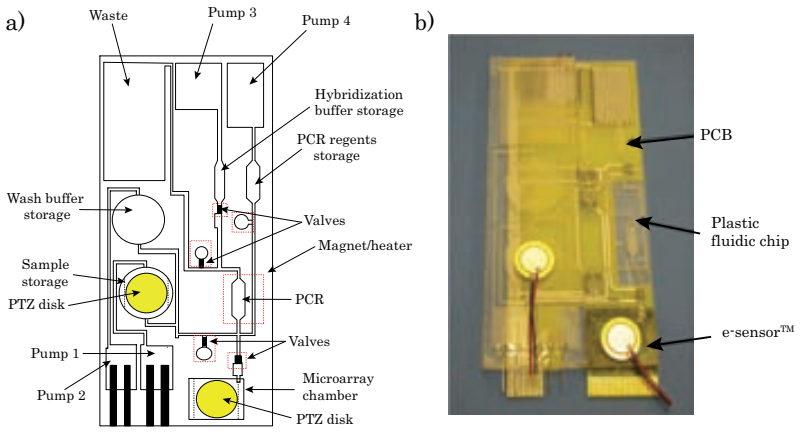

Figure 2.6: a) Schematic of the plastic fluidic chip, b) Photograph of the integrated device that consists of a plastic fluidic chip, a printed circuit board (PCB), and a Motorola eSensor microarray chip. Imagen obtained from *Liu et al Analytical Chemistry*, 2004, 76, 1824.

improved environmental and biomedical properties. In order to do that we will focus our work on the micro- and nanostructuring of already tested environmentally and biologically active compounds, with the aim of enhancing and discovering new properties for their applicability on the environmental and biomedical fields.

Bibliography

[1] Schummer, J. *Sientometrics* **1997**, *29*, 107–123.

[2] Changquan-Calvin, S. *Journal of Pharmaceutical Sciences* **2009**, *98*, 1671–1687.

[3] Wallraff, G. M.; Hinsberg, W. D. *Chemical Reviews* **1999**, *99*, 1801–1822.

[4] Ito, T.; Okazaki, S. *Nature* **2000**, *406*, 1027–1031.

[5] Whitesides, G. M.; Grzybowski, B. *Science* **2002**, *295*, 2418–2421.

[6] Wen, J.; Wilkes, G. L. *Chemistry of Materials* **1996**, *8*, 1667–1681.

[7] Albers, J.; Grunwald, T.; Nebling, E.; Piechotta, G.; Hintsche, R. *Analytical and Bioanalytical Chemistry* **2003**, *377*, 521–527.

[8] Hui Liu, R.; Yang, J.; Lenigk, R.; Bonanno, J.; Grodzinski, P. *Analytical Chemistry* **2004**, *76*, 1824–1831.

Part II

General Objectives

Chapter 3

General Objectives

The main research objectives of this Thesis will be centered on the structuring and characterization of a set of functional organic molecules and biomaterials with the objective of obtaining a variety of devices, which properties and functions can be included into the fields of the applied environmental and biomedical research. In order to do that we will make use of a large variety of nanostructuring and characterization techniques to process such molecular material as particles and on surfaces.

In the first part of the thesis we will focus on the developing of new and highly sensitive and selective Hg^{2+} sensing molecular devices. This will be made by means of the study, characterization and structuring of a new family of organic compounds which have been previously probed their ability as Hg^{2+} sensing ligands in solution. Such Hg^{2+} sensing molecules demonstrate that with their appropriate structuring it is possible to completely change its original properties improving not only their applicability but also the intrinsic properties of the molecule.

In the second part of the research work, our efforts will be directed to the nanoscale characterization of the structural and physicochemical properties of novel proteinaceous biomaterial and their further use after their structuring onto solid substrates, as promising cell proliferation vectors.

Part III

Processing of Molecular Materials for Hg^{2+} Detection

Chapter 4

Objectives

The research work developed and presented in the first part of this Thesis has been focused on the study and preparation of solid devices for Hg^{2+} detection, based on different organic receptors and processing methods. The molecules chosen for the accomplishment of this objective belong to a family of disubstituted 2,3-diazabutadiene derivatives, which receptor core was previously proved for their highly selective colorimetric and/or fluorescent Hg^{2+} recognition properties in solution (Figure 4.1).

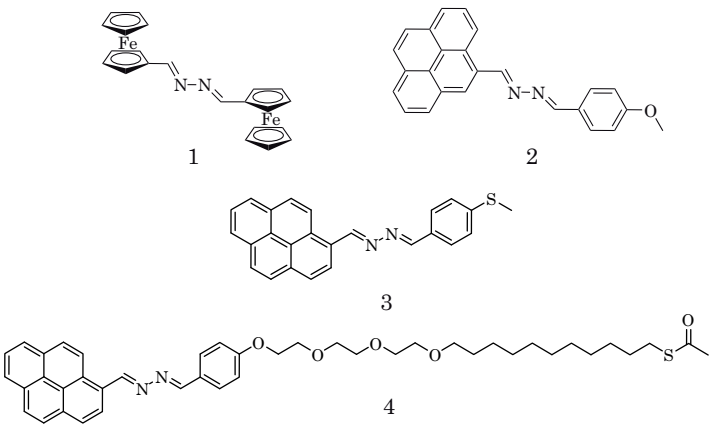

Figure 4.1: Mercury ion chemosensor molecules 1,4-diferrocenyl-2,3-diaza-1,3-butadiene (**1**); 1-(4'-metoxyphenyl)-4(2'-pyrenyl)-2,3-diaza-1,3-butadiene (**2**); 1-(p-methylthiophenyl)-4-(1-pyrenyl)-2,3-diaza-1,3-butadiene (**3**); 1-(4-alkoxyphenyl)-4-(1-pyrenyl)-2,3-diaza-1,3-butadiene derivative (**4**).

The experimental work could be divided into three main parts: 1) Study of the

Hg^{2+} recognition mechanism in solution of 2,3-diazabutadiene receptors, 2) the obtaining of heterogeneous Hg^{2+} sensors using various substrates and different deposition and/or anchoring techniques and 3) development of a Hg^{2+} remediation material. In more detail the posed objectives are:

1. **Study of the Hg^{2+} recognition mechanism of the 1-(4'-metoxyphenyl)-4(2'-pyrenyl)-2,3-diaza-1,3-butadiene (2) in solution, clarifying their origin and nature**. More specifically, we want to distinguish if the recognition process with **2** occurs via the formation of an exciplex or an excimer identifying the species involved in the fluorescent emission.

2. **Development of heterogeneous Hg^{2+} sensing systems for cheap, reliable and fast *"in-field"* detection of Hg^{2+} in aqueous media.** More precisely, we divided the task in two sections, the first one will be focused on the development of a one-shoot Hg^{2+} sensing probe, based on the use of cellulose as solid substrate, as a fast and economic device to perform the control and analysis of Hg^{2+} contamination. The organic molecules chosen to perform these probes were the 1,4-diferrocenyl-2,3-diaza-1,3-butadiene (**1**) and the 1-(4'-metoxyphenyl)-4(2'-pyrenyl)-2,3-diaza-1,3-butadiene (**2**). The second section will be centered on the developing of a extremely sensitive and selective optical sensor based on the use of a gold chip as solid substrate and the surface plasmon resonance as analytical tool. In this case two chemically modified variants, **3** and **4**, of the receptor **2**, provided with a sulphur anchoring moiety to graft them on the gold surface, will be used.

3. **Production of a cost effective Hg^{2+} remediation material**, based on the use of receptor **2** as Hg^{2+} recognition moiety and cellulose as supporting material, with the purpose of removing the Hg^{2+} present on contaminated water sources without the need of any special sampling of the contaminated water.

Chapter 5

Introduction

5.1 Chemical Sensors. Concepts and Definitions

In the last 30 years, there has been a great advance in the chemical sensors field, concerning not only its research, but also the industrial development of real devices. This enormous expansion is related to the increasing social need of knowing and controlling everything that surround us. Furthermore, the recent advances in optoelectronic devices, microfluidics and microfabrication techniques, together with the increasing needs of new clinical and environmental sensing systems, have reinforced the scientific research at the field. For this reason, it is feasible to foretell the beginning of a new era in which reefers to the sensor field, being possible to talk about a *"sensing revolution"* as it happened in the past within the microelectronics and the computer science.
Despite its importance, the term sensor is usually inadequately used to refer to a probe or an indicator. Hence, the establishment of a clear definition is useful to overcome this ambiguity. If we pay attention to the definition of sensor referred by *Janata*[1] a chemical sensor might be considered as:

> *"a transducer which provides direct information about the chemical composition of its surrounding"*

Thus, a chemical sensor would be composed by a *physical transducer* and a chemically selective *active layer* responsible of the recognition of the analyte. The composition and layout of this active layer will be crucial on the final performance and effectiveness of the chemical sensor, since it will be the main responsible of the selectivity, sensitivity, life time and the analytical response of the device. There

are also wider definitions, as the one given by *Wolfbeis*,[2] who defined the *chemical sensor* as a:

> *"device of small size consistent of a recognition element, a transducer and a signal processor, capable of reversibly supply continuous information about the chemical composition of a particular specie"*

This author remarks the importance of the size and the reversibility of a chemical sensor, thus, differentiating them from the *chemical probes*,[2] a term which can be perfectly defined as:

> *"one shot, small size devices consistent on a recognition element, a transducer and a signal processor able to supply punctual information about the chemical composition of a particular species"*

The most relevant characteristics of a *chemical sensor* or a *chemical probe*, are given by a series of ideal parameters, such as sensitivity, selectivity or response time. The definition of the most important ones are depicted in Table 5.1.
From a theoretical point of view, every *chemical sensor* is formed by a receptor and a transducer that might be separated by a spacer (Figure 5.1).

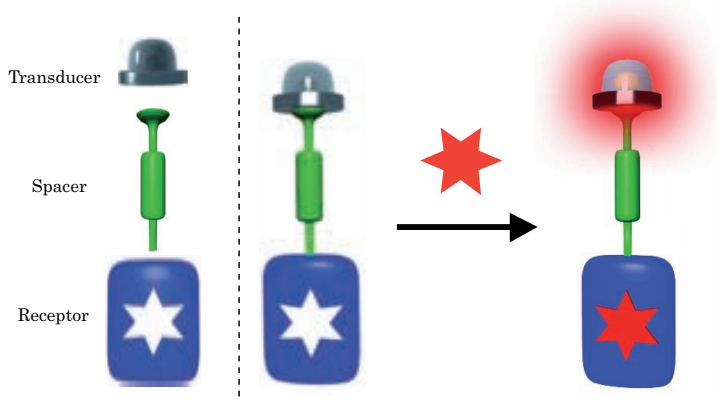

Figure 5.1: Scheme of the basic components of a chemical sensor.

- *The receptor* is in charge of the analyte recognition and it is the major responsible of the final selectivity and sensitivity of the sensor. According to their basis, sensors can be classified in *physical* (the recognition process is

Table 5.1: Chemical sensor or probe characteristics.

Required parameters	***Definition***
Sensitivity	It corresponds to the analytical signal observed by the system per unit of analyte concentration. It is a measurement of the ability of a sensor or probe to discriminate between small analyte concentration differences.
Selectivity	It is a crucial parameter to any sensor or probe as it relates the analytical signal to the target analyte and not other.
Signal/Noise ratio	Determines the detection limit of a sensor or probe, the bigger the value the smaller the concentrations of analyte that can be measured.
Response time	It is determined by the kinetic response of the sensor or probe towards a change of the analyte concentration. The smaller the time, the faster the system will response to the change. The response time represents a crucial parameter for the on-line detection systems, such as clinical or radioactivity sensors.

not linked with any chemical reaction), *chemical* (the analytical signal is generated by a chemical reaction between the analyte and the receptor) and *biochemical* (sometimes considered as a subgroup of the chemical sensors making use of biochemical processes as origin of the analytical signal).

- *The transducer*, also known as indicator or chemosensor (in the case of chemical sensors), is a device able to convert the signal coming from the receptor into a useful analytical signal. A transducer is not involved on the recognition process as it lacks of affinity towards the analyte.

5.2 Optical Sensors

Due to the number and variety of sensors that can be found nowadays, it is extraordinarily difficult to classify them according to the nature of the receptor. However this task becomes much easier if one takes into account the mechanism of signal transduction employed. Thus, chemical sensors can be generally divided into the following categories: *electrochemical, mass-sensitive* and *optical*. In the same way that a change in mass give us information about a phenomenon occurred on a determined system, variations suffered by electromagnetic waves while interacting with matter provide us data about its nature and characteristics.
Even though all of them present useful properties and a broad number of applications,[1,3] we will focus our attention only in a set of *optical sensors* in which this thesis is centered, the *absorption* and *emission chemosensors* and the *evanescent wave chemosensors*.

5.2.1 Absorption and emission techniques

Any process working on energy absorption (or emission) is linked to the transition of an electron of the system from an (or to) internal energy level (A) to (or from) an excited one (A*). Nevertheless, in order such a process to occur, the wavelength or energy ($h\nu$) of the absorbed or emitted radiation must match the values corresponding to transitions between well-defined internal energy levels of the system, corresponding to the quantized states of three different types of transitions: *rotational*, *vibrational* and *electronic*. Depending on the wavelength of the radiation involved, the detection techniques can be classified according to the following spectral regions in: a) X-Ray (λ = 0.01-10 nm), b) UV-Vis (λ = 10-780 nm), c) IR and Raman (λ = 0.78-100 μm) and d) Microwave (λ = 0.1-30 cm). However, the detection techniques using wavelengths between (10 nm $\leq \lambda \leq$ 100 μm) are the most used from an analytical point of view.
It is worth to mention here some of the basic concepts associated with these detection techniques.

Absorption techniques. The absorbance of radiation from the UV-Vis region (λ = 10-780 nm) is a process associated with the excitation of the external electrons of the great majority of organic molecules, although not so usual when talking

about inorganic analytes. Thus, the use of analytically active organic molecules to perform a proper analytical detection of inorganic analytes is often required. The study of the absorption bands of a spectrum after the analyte detection give us information not only about the chromophores present in our sample, but also it can be used to quantify the amount of analyte in the problem sample. Working inside the lineal range (low analyte concentration), the radiation intensity changes, due to light absorption, can be related with the concentration of absorbing species via the Beer-Lambert law, which is expressed as

$$A = logT = logI_0/I = \epsilon lc \tag{5.1}$$

where A is the absorbance, T is the transmittance, I_0 is the incident light, I is the transmitted light, ϵ ($M^{-1}cm^{-1}$) is the molar absorptivity, l (cm) is the path length traversed by the light, and c (M) corresponds to the concentration of the absorbing species. Absorption processes are accumulative and non selective, thus, if in one sample there are different UV-Vis active species absorbing on the same λ range, the total measured intensity is the sum of all the individual ones.

$$A_t = \sum_n (\epsilon_n l c_n) \tag{5.2}$$

Despite the simplicity of the detection method, the potential shown by sensors based on UV-Vis radiation is extremely high. One clear example of this, is the work developed by *Rakow et al.*[4] where an array of metalloporphyin complexes was immobilized onto a solid support (a reverse phase silica gel) and used to detect the presence of different toxic organic vapors even in presence of water vapour. The different colorimetric response of the metalloprophyrins used allows not only to detect and quantify the different analytes but also to visually identify the presence of a wide rate of molecules such as alcohols, amines or phosphines, among others. Figure 5.2 depicts an example of the colorimetric response of the metalloporphyrines to the presence of the organic vapors. Unique fingerprints at vapors concentrations below 2 ppm were obtained, while responses below 100 ppb were observed for some analytes.

Emission techniques. In such techniques, the luminescence is related with the electron promotion by absorption of UV-Vis or IR radiation of the atoms or molecules involved and the subsequent emission of radiation. The main difference

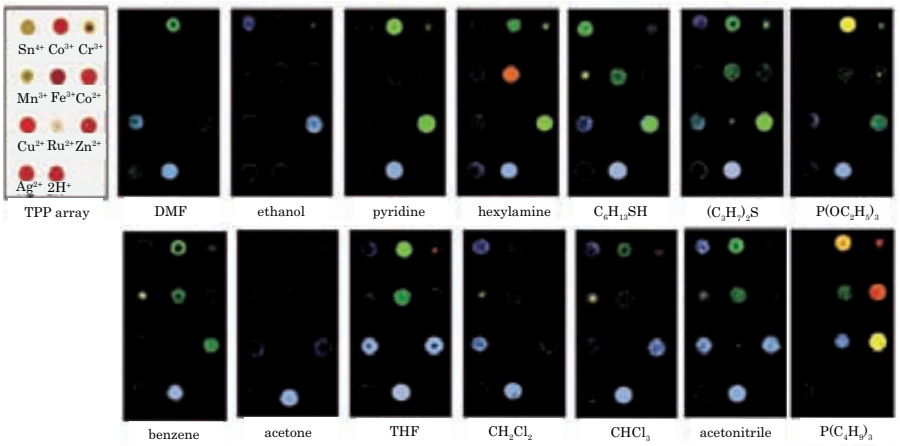

Figure 5.2: Color change profiles of a metalloporphyrin (TTP) sensor array treated with a series of organic vapors. Each analyte was delivered to the array as a nitrogen stream saturated with the analyte vapor at 20°C (to ensure complete saturation, vapor exposures of 15 min or greater were used). DMF, dimethylformamide; THF, tetrahydrofuran. Image obtained from: *Rakow, N. A. et al. Nature*, **2000**, *406*, 710-713.

with the previous case, where the relaxation of the promoted electron happened exclusively trough non radiative processes, is that in the luminescent phenomena there is also the possibility of relaxation via light emission.

The term luminescence was defined for the first time by *Wiedmann* in 1888 as the ultraviolet, visible or infrared light emitted by electronically excited atoms or molecules during their relaxation. In order to produce an electronic excitation a source of energy is needed and depending on this source it is possible to distinguish different kinds of luminescence: electroluminescence, chemoluminescence, thermoluminescence and photoluminescence. Generally, every luminescent process can be divided into three main phases: the first one is related to the absorption of light, thus an electron is promoted from its fundamental state to a more energetic one. Then, on a second step the excited species suffer a set of very fast and non radiative relaxations until reaching a less energetic excited state. Finally, transitions from this intermediate state to the fundamental one is responsible of the luminescent emission. According to this transition mechanism it is possible to talk about:

- Fluorescence (F): On this process the deactivation of the excited state to the fundamental one is produced trough a photon emission. As this radiative

phenomenon happens between singlet states, the probability for the transition to occur is high and the photon emission will happens in the picoseconds range. There is a big number of fluorescent substances, being specially interesting the aromatic derivatives such as pyrene, anthracene and other conjugated rings.

- Phosphorescence (P): This second path, also radiative, entails the existence of a conversion process from one excited singlet state to a triplet one, previous to the photon emission. This transformation takes place generally through a non radiative path. As in fluorescence, the new excited state can suffer a radiative relaxation process from the excited triplet state to the fundamental singlet state. Since such a relaxation process is forbidden by selection rules, the probability of the transition to happen, as well as its rate (milisenconds), is much smaller than for the fluorescent phenomena. This radiative relaxation is known as phosphorescence.

- Quenching (Q): The quenching phenomenon brings together not only all the non radiative processes that inactivate or avoid the formation of the excited state (collisions, chemical reactions, dimers formation...) but also all those that, once the emission is produced, reduce its intensity such as the autoabsorption phenomena.

Although usually associated to single molecules, certain compounds are able to form dimers which present fluorescent activity under determined conditions. According to the definition of *Briks*[5], these dimers can be classified as *excimers* or *exciplexes*:

> *"An excimer is a dimer between equal entities, associated in an excited electronic state and which are dissociative in its ground electronic state"*

while an *exciplex* is:

> *"an electronically excited atomic or molecular hetero complex of definite stoichiometry, which is dissociative or dissociated in its electronic ground state"*

The fluorescence emission bands corresponding to excimer or exciplex dimers are localized into less energetic regions of the electromagnetic spectra and tend to be

broad and structureless, lacking of any vibrionic structure (Figure 5.3). Depending on their origin, "excimers" can be divided into *inter* and *intramolecular* when the moieties taking part on the dimer formation belong to different or the same molecular entity, respectively.

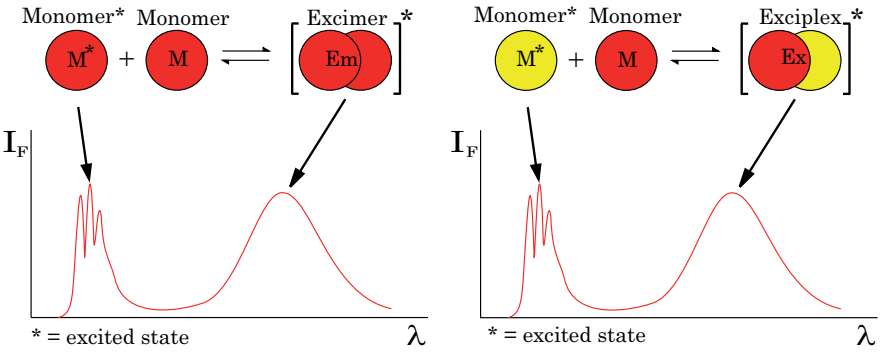

Figure 5.3: Representation of the fluorescence spectra of a monomer (M*) and an excimer (Em*) and exciplex (Ex*) systems.

Among all the substances capable to form this kind of dimers under appropriate conditions, it is worthy to remark the novel gas halide exciplexes, such as the xenon chloride, which form part of the *excimer lasers*. Furthermore, several fluorescent sensors base the generation of their analytical signal on the formation or dissociation of excimers or exciplexes.

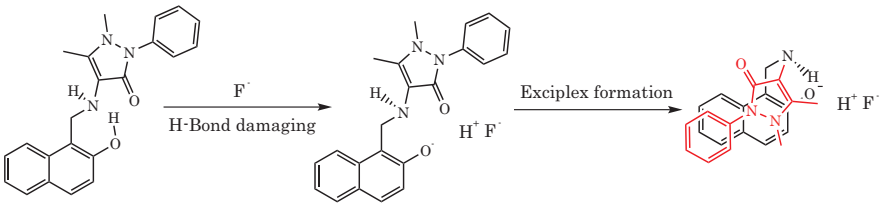

Figure 5.4: Schematic illustration of the breaking of intramolecular hydrogen bonding upon addition of fluoride ion. The molecular structure changes from rigid to flexible permitting, therefore, the exciplex formation by the proper folding. Scheme obtained from: *Wu et al.*, *Organic Letters*, **2005**, *7*, 2133.

One example of this is the work developed by *Wu et al.*[6] where an aminonaphthol unit is able to form an exciplex with an antipyrine moiety of the same molecule by the complexation of F^- anions (Figure 5.4). The formation of this F^- mediated exciplex is selective versus other anions such as, Cl^-, Br^-, I^- or NO_3^- and allows the detection of concentrations of this anion down to the μM range.

5.2.2 Evanescent wave techniques

Evanescent wave (EW) techniques emerge as analytical techniques derivatized from the special properties of light when it is propagated through a waveguide. In a light guiding mode the electromagnetic waves are internally reflected at the boundary of two media with different refractive index (η_1, η_2). According to *Snellius* law (Equation 5.3) the total internal reflection occurs when the incident angle (θ)

$$\eta_1 sin(\theta) = \eta_2 sin(\alpha) \qquad \theta_c = arcsin(\frac{\eta_2}{\eta_1}) \tag{5.3}$$

is bigger than the critical angle (θ_c). In this condition a small fraction of the total incident light is capable to penetrate in the media of lower η, where interacts with the surroundings. During this phenomenon, named evanescent field, the intensity of the electromagnetic wave decays exponentially with the distance from the interface.

Despite the classical optical sensors, based on the direct interaction of light with the matter, EW techniques base their detection on the interaction of the analyte with the evanescent field generated during the internal reflexion of the wave. The use of this kind of sensors entails an increase on the sensitivity of the detection process due to the reduction of light dispersion and the large optical path. Furthermore, the evanescent wave techniques can be combined with other optical techniques in order to obtain gained measurements of absorbance, fluorescence, or refractive index. Surface Plasmon Resonance (SPR) is one of these techniques based on EW, which is more explained in Annex A.2.

One example of the properties and scope of this family of sensing techniques is the work developed by *Masson et al.*[7] They make use of the excellent anchoring characteristics of the antibodies to, through the functionalization of a Self Assembled Monolayer (SAM) modified SPR gold sensor, perform the detection of two myocardial infarction biomarkers; the myoglobin and the cardiac troponin I in undiluted serum. The enormous specificity of the antibodies together with the sensitivity of the SPR permitted to reach detection limits for both markers below 1μg/L, which is well below the threshold needed to detect myocardial infarction.

5.3 Receptors for Optical Sensors

Despite the large amount of available optical techniques, the number of substances susceptible of being detected without the use of indicators is reduced. Therefore, to detect this kind of substances the use of some intermediary compounds, known as receptors, that will act as chemical linkers for the analyte, is needed.
The design and synthesis of coordinative ligands has always been a challenge and a motivation for organic chemists. However, the development of new sensing molecules is usually not an easy task and most of the available molecular probes present different disadvantages such as lack of selectivity, stability problems, and often reduced compatibility with the target media. Thus, the synthesis of new selective and sensitive receptors is still one of the biggest challenges on the development of this kind of chemosensors.
The optical receptors can be classified in two main groups according to the response presented when they react with the analyte.

- *Chromophoric receptors*: This kind of chemosensors constitute the most classic of all the optical sensor families. They are based on the monitoring of the appearance or the disappearance of color of the receptor, being indicative of a specific analyte detection. They present large advantages in the detection process of ionic species such as anions and metallic cations. One of the principal advantages of this kind of receptors is that they do not require expensive instrumentation, being sometimes possible to perform a *"naked eye"* detection of the analyte.

- *Fluorophoric receptors*: As previously stated, fluorescence is an extremely powerful and versatile analytical tool. This is the reason why the synthesis of new compounds, able to generate a fluorescent analytical signal when interacting with the analyte, has been and is one of the main chemical challenges of the organic chemists. According to the nature of the fluorophoric receptors we can separate them into two types:

  - *Intrinsic receptors*[8]: The recognition process and the fluorescent emission take place in the same part of the molecule.
  - *Conjugate receptors*[9]: The recognition process and the fluorescent emission take place in different parts of the molecule, although the two subunits are kept in close proximity by means of covalent bonds.

The photo-physical mechanism which take place in this kind of receptors after the analyte anchoring is highly dependent of the nature of the molecule used. Among all of them, signaling phenomena based on the activation or deactivation of quenching by means of *Photo-induced Electron Transfer (PET)* or *Energetic Electron Transfer (EET)* are two of the most common ones.[10] Other mechanisms are based on the existence of *excimers* or *exciplexes*, by the formation of homo and heterodimers respectively, which entail the appearance of new luminescence bands.[11] This signal generation is very common in molecules with π delocalized systems such as pyrene or anthracene.

The principal advantage of the fluorescent receptors lays on its high sensitivity, reaching detection limits which can be a million times smaller than the ones obtained with other kind of optical sensors such as the chromophores. The selectivity of this kind of systems is mainly dependent of the receptor design, however it can be increased by the bigger specificity intrinsic to the fluorescence phenomena. Due to this high analytic potential, it is possible to find on the literature several examples of fluorescent sensors for a large amount of substances of different nature such as heavy metals, explosives, nerve agents or biological molecules.

5.4 Processing Receptor Units

In order to develop a solid supported chemosensor device, it is not only need to count with a highly sensitive and selective receptor but also it is crucial to use an appropriate immobilization matrix, which can determine not only the final use of the device but also other very important parameters, such as the response time or the permeability.

Although the number of substances that have been used for the anchoring of chemical receptors is really high, polymeric matrices[12,13] (organic and inorganic) stand out for their profusion. However, in the last decades a number of new supporting materials such as silica particles,[14] glass and gold surfaces,[15] quantum dots,[16] Langmuir-Blodgett films,[17,18] micelles[19] and liposomes,[20] among others have also been used to create sensitive materials.

One of the main difficulties found in this area is the firm fixation of the molecular

probes on the solid substrates. In order to solve this problem different anchoring approaches have been used.

Physisorption. The use of physisoprtion processes as an anchoring strategy for the entrapment of the sensitive chemoreceptor into a solid matrix has been widely used either for scientific and/or industrial applications. Nevertheless the use of this strategy entails the need of highly adsorbent and versatile solid substrates. Among all the available anchoring matrices polymeric materials have proved to be the most suitable ones.[21] The success of this kind of substrates is based on its enormous processability. Thus, the use of organic and inorganic polymers, has made possible the easy obtaining of films, particles or even porous materials with high sensitivity and selectivity to a wide range of analytes, such as gases, organic vapors or ions.[22–24]

A clear example of this kind of sensors is the work developed by the group of *Meyerhoff*.[22] They prepared a polymer film-based optical sensor, by means of an In^{3+} octaethylporphyrin hydroxide ion-bridged dimer species embebed into the polymer matrix, that responded reversibly to the presence of gas-phase amine species at sub-ppm levels. Thus, the ligation of the amine with the In^{3+} center of the porphyrin structure causes the dimers to dissociate yielding a significant change in the visible absorption spectrum of the film. Detection limits down to 0.1 ppm of some amine compounds were obtained.

However, despite its simplicity and cost effectiveness, physical entrapment of the receptor dyes often produces inhomogeneity in the resulting materials and causes stability problems due to the leaching of the molecular receptor, thus reducing the life time and reproducibility of the sensor.

Chemisorption. Recent advances in surface chemistry and the appearance of new characterization and processing techniques such as the Atomic Force Microscopy (AFM),[25] SAMs and the Microcontact Printing (μCP)[26] technique have made of the covalently modified substrates one of the most interesting subjects for the development of sensors. In the last decades, a large variety of sensors containing covalently linked receptors have been developed. In contrast to the use of physisorption as an anchoring strategy, the specificity and intrinsic strength of the covalent bond proportionates to the heterogeneous sensor not only the stability and reliability required but also a higher density of active sites. Thus an increase

of the potential recognition properties of the sensor is obtained. Conjugated polymers[27] and SAMs based[28] sensors are a clear examples of that.

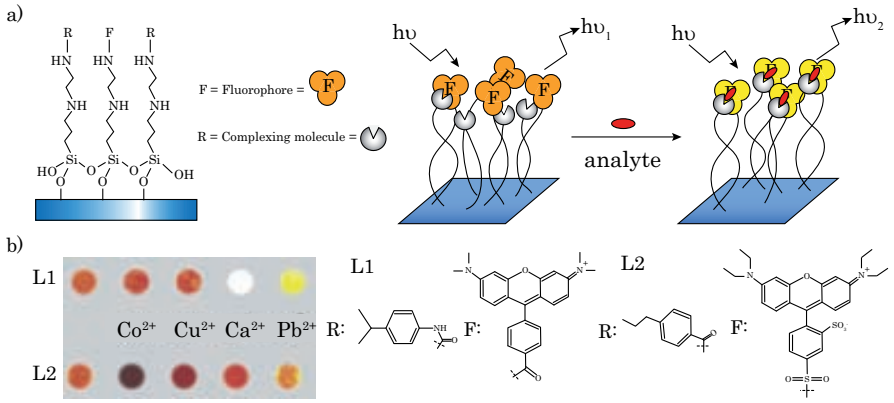

Figure 5.5: a) Schematic representation of a SAM on glass with fluorophores and recognition sites independently attached. b) Array of fluorescence confocal microscopy images of two different fluorescent SAMs (Layer 1 and Layer 2) in contact with acetonitrile (first spot) and 10^{-4} M acetonitrile solutions of Co^{2+}, Cu^{2+}, Ca^{2+} and Pb^{2+} perchlorates. Image reproduced from *Basabe-Desmonts L. et al.*, *Chemical Society Reviews*, **2007**, *37*, 993

Figure 5.5 depicts an example of the use of SAMs and μCP for the preparation of chemically modified surfaces with sensing purposes. In this work, developed by *Basabe-Desmonts et al.*[29], functionalized SAMs on glass were used as a platform to sequentially deposit fluorophores and small molecules for ion sensing, allowing to obtain sensing systems based on small molecules. The resulting libraries are easily measured and show different responses to a series of both cations and anions. Furthermore, the use of Bottom-Up patterning techniques such as the μCP, where the fluorophore is printed onto a glass surface, permits the easy transfer of this technology from the macro to the microscale allowing the generation of a wide variety of simple yet efficient sensing microarrays.

5.5 Environmental Mercury Contamination

If we analyze the substances and chemical elements that surround us, it is possible to observe how a relatively high percentage of them present certain toxicity. One of these substances are the heavy metals. There are many ways of defining what

a heavy metal is,[30] some of them are based on their chemical and physical properties, such as density, reactivity, atomic weight or even their toxicity. However, regardless of the definition used, mercury will always be considered as one of them. Mercury is a naturally occurring element and even though its average earth crustal abundance reaches only 0.08 parts per million (ppm, by mass),[31] its presence is spread all over the world. The most common mineral source of this toxic element is its sulphur salt, more known as cinnabar (HgS), although mercury is also present, as a trace element, in many other common materials such as coal.
The exceptional properties of this liquid metal have made of it an essential element in several cultures over time. Thus, ancient Chinese and Hindus used the cinnabar as skin pigment, while for Romans and Greeks it was believed to be the panacea of any illness. But it was in 1557, when *Bartolomé Medina* developed a process for the cold amalgamation of silver minerals using mercury, when the consumption and application of this metal reached a new level. Nowadays mercury and its derivatives are used on a huge variety of processes, from lamp production to wiring devices or even as additive on certain pharmaceutical products.[32] This fact has supposed an increase on the natural background environmental level of mercury that have been present since long before humans appeared, becoming a mayor problem all over the world.[33,34]
Mercury in the earth crust can be released in several ways, and understanding the emission sources is critical for the development of relevant and cost-efficient strategies towards reducing the negative impacts of this global pollutant. In Figure 5.6 a schematic description of the main sources of mercury is presented.

5.5.1 Main sources of mercury

In order to be able to control mercury pollution, it is of extreme importance to distinguish between the various categories of emission sources. According to the nature of its origin it is possible to divide mercury contamination sources in two main families; those derived from *natural processes* and those with an *anthropogenic origin*.

Natural Sources. The action of atmospheric and natural phenomena over the earth crust generate a continuous and ubiquitous weathering of mercury-containing rocks, producing therefore, its emission or re-emission to the media. Furthermore,

Figure 5.6: Schematic representation of the natural and anthropogenic sources of mercury contamination. Image obtained from *United Nations Environment Program (UNEP) Chemicals Branch*, **2008**. The Global Atmospheric Mercury Assessment: Sources, Emissions and Transport. UNEP-Chemicals, Geneva.

punctual events such as volcanoes eruptions or geothermal activity, release enormous amounts of matter from the earth crust to the atmosphere, being mercury one of those substances. Some recent models of the flow of mercury through the environment suggest that primary natural sources account for only about one third to one half of mercury emissions to the atmosphere, being the rest of it directly or indirectly related to human activity (Figure 5.6).

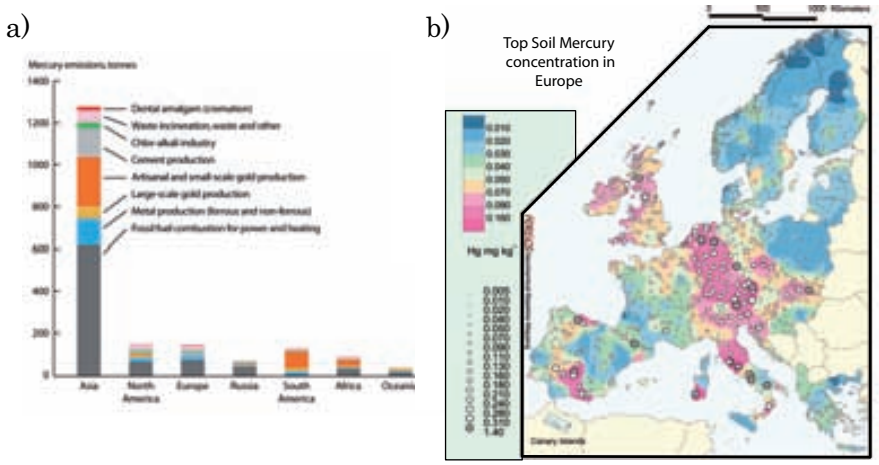

Figure 5.7: a) Proportion of global anthropogenic mercury emissions to air in 2005. Image obtained from *UNEP Chemicals Branch*, **2008**. The Global Atmospheric Mercury Assessment: Sources, Emissions and Transport. UNEP-Chemicals, Geneva. b) Mercury concentration at the top soil level in the European continent. Map available from *http://eusoils.jrc.ec.europa.eu/foregshmc/*.

Anthropogenic Sources. Due to the enormous increase of human activity that has taken place during the last decade, the mobilization of mercury into the environment has suffered an important rise, elevating, therefore, the amounts of it in the atmosphere, soils, fresh waters and oceans. Anthropogenic sources of mercury contamination can be divided into two: primary (related with direct emissions) and secondary (due to residual wastes of mercury containing products) sources. The main *primary anthropogenic* sources of mercury are (Figure 5.7):

- *Coal burning* is the largest anthropogenic source of mercury emissions to the atmosphere.
- *Metal mining* of mercury itself or of precious metals such as gold, releases considerable amounts of mercury.
- *Industrial activities*, such as cement production. However, and due to the localized nature of these emissions, the presence of pollution control measures can greatly reduce emissions from individual plants.

Once mercury has been produced for human use, it becomes a potential *secondary source* of contamination. Even though, national and international environmental legislations are becoming more and more restrictive *versus* the mercury containing goods. A lot of products, such as batteries, paints, electrical and electronic

devices, fluorescent and energy-saving lamps, pesticides, medicines, cosmetics, etc still count with it in their composition. Furthermore, and due to the lack of appropriate waste disposal facilities, once used this kind of products are typically disposed or incinerated, increasing the environmental mercury contamination by releasing the held mercury to the environment.

5.5.2 Chemistry of mercury and its derivatives

Mercury can exist in nature in three oxidation states which present distinct properties in the different compounds:

- *Hg^0 (metallic).* Elemental mercury (Hg^0), is a heavy, silvery-white liquid metal at typical ambient temperatures and atmospheric pressures. Its vapor pressure is strongly dependent on temperature, and it vaporizes readily under ambient conditions. It is also extremely dense, being 13.5 times more dense than liquid water under ambient conditions. In terms of toxicity is the less hazardous of all the oxidation states, being only dangerous when directly inhaled.

- *Hg_2^{2+} (mercurous) compounds.* Mercury (I) oxidation state of mercury is the less common of the three states. Even though in aquatic media the Hg_2^{2+} can be obtained from the reduction of Hg^{2+}, the existence of relatively few stable mercurous compounds together with the low solubility of the Hg^{2+} inorganic derivatives displaces the disproportionation equilibrium to the formation of the mercuric and elemental species, according to the following equilibrium (Equation 5.4).[35]

$$Hg_2^{2+} \rightleftharpoons Hg^{2+} + Hg^0 \tag{5.4}$$

- *Hg^{2+} (mercuric) compounds.* Mercury (II) ion is the most reactive and toxic of the three oxidation states and due to the great affinity to form complexes with a large number of inorganic and organic ligands, is also the most abundant specie in aqueous media, reaching the 70% of the total disolved mercury.

As any other natural element, mercury concentration is regulated by a series of complex chemical processes more know as the *Mercury Cycle* (Figure 5.8).
Mercury cycle is a global process, which takes place in either gaseous, liquid or

solid state. However, it is on aqueous media were most of the transformations occur. Although the solubility of elemental mercury in water is low, 60-80 μg/L,

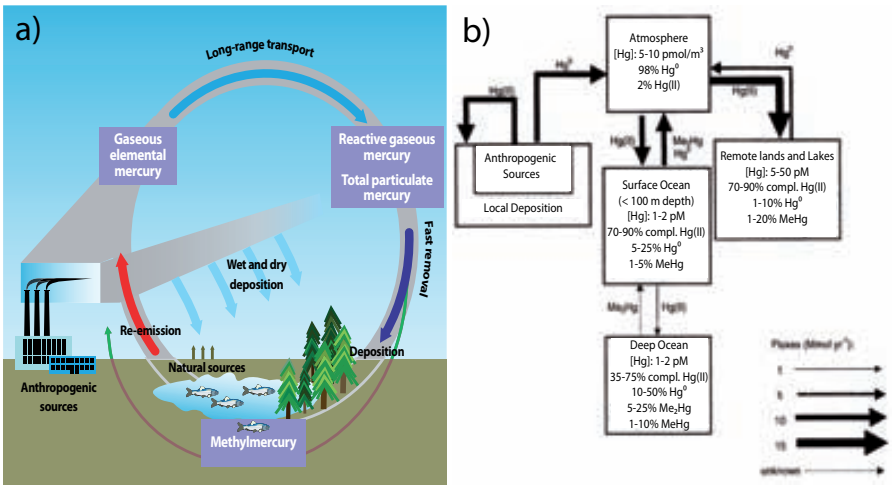

Figure 5.8: Environmental global flux of mercury a) Global scheme and b) Environmental migration of the different mercury species. The width of the arrows corresponds to the importance of the different mercury rates (Image obtained from *UNEP Chemicals Branch*, **2008**. The Global Atmospheric Mercury Assessment: Sources, Emissions and Transport. UNEP-Chemicals, Geneva).

between a 10-30% of the mercury found in aquatic systems is in the form of elemental mercury. The presence of this Hg^0 in aqueous media stays from the reduction processes sufered by certains amounts of Hg^{2+}, which through biotic[36] (microorganisim mediated) or abiotic[37,38] (reactions with humic substances, photoreduction, antropogenic wastes ...) pathways, are transformed to Hg^0. Due to such processes, most of the superficial waters are supersaturated on elemental mercury with respect to the surrounding atmosphere. This fact together with its low vapour presure involves the existence of a net flux of Hg^0 from the water to the atmosphere (Figure 5.8). Once there, Hg^0 is able to slowly react with environmental oxidants, such as O_3,[39] to be reconverted again to Hg^{2+}.

$$Hg^0(g) + O_3(g) \rightleftharpoons Hg^{2+}(aq) \tag{5.5}$$

These reactions take usually place on the gas-liquid interphase, present in clouds, thus the recently formed Hg^{2+} is rapidly redeposited with the rain. As a consequence, while the mean lifetime of elemental mercury in the atmosphere might reach a year, time enough to travel all over the world,[40] mercuric derivatives do

not usually exceed a residence time of one month.

Although the land represents only a 30% of the total surface of the earth, aproximately a 60% of the movilized mercury is deposited on the ground, where the Hg^{2+} derivatives are exposed to a big number of chemical and biological reactions, which in most of the cases lead to insoluble compounds, limiting their movility. Despite this natural tendency to the accumulation of Hg^{2+} in solid ground, oceans an lakes still suppose the bigger mercury reserve of the world with an estimated remaining amount of 10^{17}g, mainly as sedimented HgS. Nevertheless, not all the Hg^{2+} present on aqueous media is unactive and its speciation is highly influenced by a big number of factors, such as pH, redox potentials (E_h), and the presence of certain bacteria. Figure 5.9 shows a detailed picture of the aquatic mercury cycle taking into account the diferent mercury speciation with the surrounding environment.

5.5.2.1 Inorganic species of mercury

The chemistry of mercuric ions is mainly driven by its large polarizability, reflected in their soft acid properties. As a consequence, Hg^{2+} ions tend to strongly associate with soft bases such as S^{2-}.

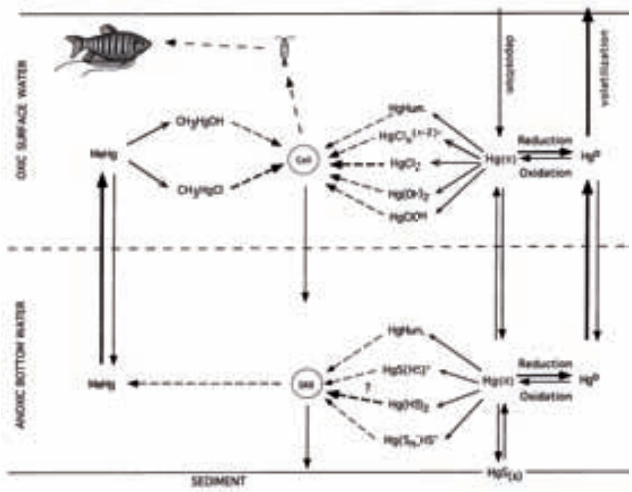

Figure 5.9: Aquatic mercury cycle, taking into account the different speciation of mercury derivatives according to the surrounding environment. The width of the arrows corresponds to the importance of the different mercury rates (Image obtained from *Moreland et al.*, *Annual Review of Ecology and Systematics*, **1998**, *29*, 543-566).

Nevertheless, when in contact with oxic waters (rich in oxigen), where the concentration of sulphide derivatives is relatively low, mercuric chemistry will be regulated by the formation of inorganic halides and hydroxide complexes. Being the chloride complexes and compounds, such as $HgCl^+$, $HgCl(OH)$, $HgCl_2$, $HgCl_3^-$ and $HgCl_4^{2-}$, dominant in acidic environments, while hydroxides such as, $Hg(OH)^+$, $Hg(OH)_2$, $Hg(OH)_3^-$ will prevail in alkaline ones. On the other hand, Hg^{2+} speciation in anoxic waters (poor in oxygen) is mainly controlled by the formation of sulfide and bisulphide complexes, being HgS the most common of all of them. Even tough the solubility of HgS in water is extremely low (10^{-53} M), it has been proved that in the presence of high concentrations of S^{2-}, part of it might be redissolved trough the formation of bi and polysulfide derivatives, increasing the amount of Hg^{2+} compounds available on the media (Figure 5.9).

5.5.2.2 Organic species of mercury

In addition to the inorganic derivatives, Hg^{2+} can also be bound to dissolved organic matter, independently of the oxic nature of the media. In oxidant environments mercuric ion will appear as metal center of organometallic complexes with ligands of a poorly defined family constituted by organic compounds generally named humic acids. This fraction has been quantified by some authors and depending of the water source can represent up to a 95% of the total disolved Hg^{2+}.

When mercury is located on an oxygen deficient media it can also be found as linked to organic ligands. However, despite for superficial waters, the number of available ligands is limited being the methyl derivatives, monomethyl and dimethylmercury, the most common ones. Although methylation of mercury can occur through several ways, it is believed that approximately 95% of it comes from the biomethylation carried out by Sulpho-Reductive Bacteria (SRB),[41] mainly present in anoxic waters and sediments (Figure 5.9). This process is strongly dependent of several factors, such as the mercury and sulphide concentration in the reaction media,[42,43] temperature, redox conditions, among others.[44] Furthermore it seems that not all the SRB are able to methylate mercury, but only those provided with certain enzymes that recognize mercury as an apropiate substrate.[41]

5.5.3 Toxicity of mercury

Toxicity of mercury has been known since Antiquity. Already described by *Hippocrates* (370 a.C.), father of the modern medicine, Greeks and Romans where aware of the toxic effects of the cinnabar mining and left the tedious task of extracting this precious element to slaves, whose life expectancy oddly exceed more than 6 months of work.[45] Industrial revolution and technological advances introduced a big number of uses and applications for mercury and its compounds, increasing therefore its global pollution and occupational exposure. The worst mercury related environmental and social event of the recent era occurred on Minamata Bay (Japan) in the mid-fifties. There, an acetaldehyde plant dumped huge amounts of mercury directly to the sea causing thousands of affected and more than 1500 dead.[46] However, this has not been the only mercury pollution episode, since in 1971-72 in Irak a methylmercury treated wheat and barley cargo caused more than 6530 intoxications and over 459 dead.[47]

All this poisonings made the international community to act, and since then, several books, normatives and laws have tried to limit, reduce and finally avoid as much as possible the use of any mercury derivative in industrial processes.[34,48]

All reported works agree that the danger associated to mercury is determined not only by the kind of exposure but also by the chemical form in which mercury is found. Although all mercury species have reported both physiological and neurological toxic effects, it has been prove that the pernicious effects that methyl and dimethylmercury have on the human body are the most destructive. This is due at the fact that methylmercury derivatives are not only extremely powerful neurotoxines,[49] but they are also liposoluble and bioaccumulable substances, able to interact with the adipose tissues of fish and mammals, where they concentrate.[49] As a consequence, they enter in the food chain biomagnifying their presence in higher organisms, especially in the muscles of large predatory fish which are subsequently ingested by mammals and humans. Thus, and considering all this characteristics, it is possible to say that both mercury and its methyl derivatives, specially their mono and dimethylmercury, are extremely toxic and that the excessive exposure to them represents a serious danger not only for the environment but also for human beings.

5.6 Mercury Chemosensors

As stated on the previous section, mercury and specially its organic derivatives CH_3Hg^+ and $(CH_3)_2Hg$, are highly toxic substances. Therefore, the developing of systems able to detect, prevent or remediate mercury pollution has been a great challenge for scientists from several disciplines such as, organic and organometallic chemistry, analytical chemistry, material science, etc...

In the last decades, the number of available mercury detection methods has increased considerately, being possible to use systems of diverse nature as those based on atomic absorption or emission spectroscopies,[50–52] and mass spectrometries,[52] among others. Although in several cases a high sensitivity and selectivity is obtained, the use of complex instrumentation and/or expensive materials, as well the need of trained personnel has entailed an increase on the difficulty, accessibility and immediacy of the measurement. Thus, the developing of new, cheap, fast and reliable systems able to selectively perform mercury detection at low levels is still a great challenge.

The use of optical sensors (fluorescent or colorimetric), based on small organic ligands as molecular probes has supposed, not only, the overcoming of most of the previously established limitations, but also an increase on the sensing possibilities due to the enormous versatility that organic chemistry has. Such discipline allows scientists to tune the molecular properties of the probes until the obtaining of robust, versatile and highly processable compounds with an enormous sensitivity and selective behavior towards mercury detection.[53] In addition, these organic ligands are cheap compounds, which use do not suppose the employment of any sophisticated instrumentation.

Although the main toxicity of mercury lies on its organometallic species, its presence is intimately linked to the concentration of Hg^{2+}, as they are a direct product from the Hg^{2+} methylation process. Therefore, and in order to reduce the dangerousness of the mercury sensor development, Hg^{2+} has been chosen as the global reference for Hg^{2+} contamination. In this regard, the understanding of the chemical nature and the coordination chemistry of Hg^{2+} is basic in order to be able to design suitable Hg^{2+} responsive receptor moieties to be incorporated into the probes. Because of its $5d^{10}6s^2$ electronic configuration and lack of ligand field stabilization energy, Hg^{2+} can accommodate a range of coordination numbers and geometries, being the linear (bicoordinate) and tetrahedral (tetracoordinate) species the most

common ones. Furthermore, and due to the same reason, Hg^{2+} has no optical spectroscopic signature, a fact that entails the need of introducing external signaling units for the probe design.

From the chemical point of view, and according to the hard and soft acid base theory, Hg^{2+} can be included inside the family of the soft acids. Therefore ligands rich in soft donor atoms, such as *Sulphur* (S), *Nitrogen* (N) or *Phosphorus* (P) atoms, will generally increase its affinity and selectivity for Hg^{2+}. While both the affinity and selectivity of a sensor can be tuned through modifications of the binding unit, there are other characteristics, specially for fluorescent chemosensors that are less predictable.

In the case of fluorescent indicators, the excitation and emission wavelengths are dictated by the choice of the fluorophore, and the brightness is defined as the product of the quantum yield and extinction coefficient ($\Phi \cdot \epsilon$). However, anticipating the Hg^{2+} response (*turn-off vs turn-on*) of an intensity-based fluorogenic probe is often not straightforward. This process is simplified for colorimetric based probes were only the choice of the chromophore will determine the absorption profile of a colorimetric sensor.

5.6.1 Fluorescent Hg^{2+} detection

During the last decades, a huge number of fluorescent Hg^{2+} molecular probes, based on different families of fluorophores and receptors, have appeared on the literature. However, only few of them are able to perform this detection in pure aqueous media, being a great majority, those which need pure organic or mixed aqueous/organic solutions.

Compound **9**[54] represent a clear example of this last kind of Hg^{2+} molecular probes (Figure 5.10). Based on the use of a pyrene moiety as signaling element, the recognition element is composed by a *p*-tert-butylcalix[4]arene appended with a diaza-crown ether and the detection of Hg^{2+} has been described when operating in MeOH or mixtures MeOH/H_2O. In this case, the signaling process occur by the disappearance of the pyrene excimer emission upon complexation of Hg^{2+} , and even though the final sensitivity is not very high it presents a high Hg^{2+} selectivity. The same chelating structure was used for compound **10**[55] replacing the two pyrene fluorophore units by two anthracenes. Now, the anchoring of Hg^{2+} increases the fluorescence of the system by the decreasing of the PET[9] quenching of the anthracene units by the deprotonated amine groups.

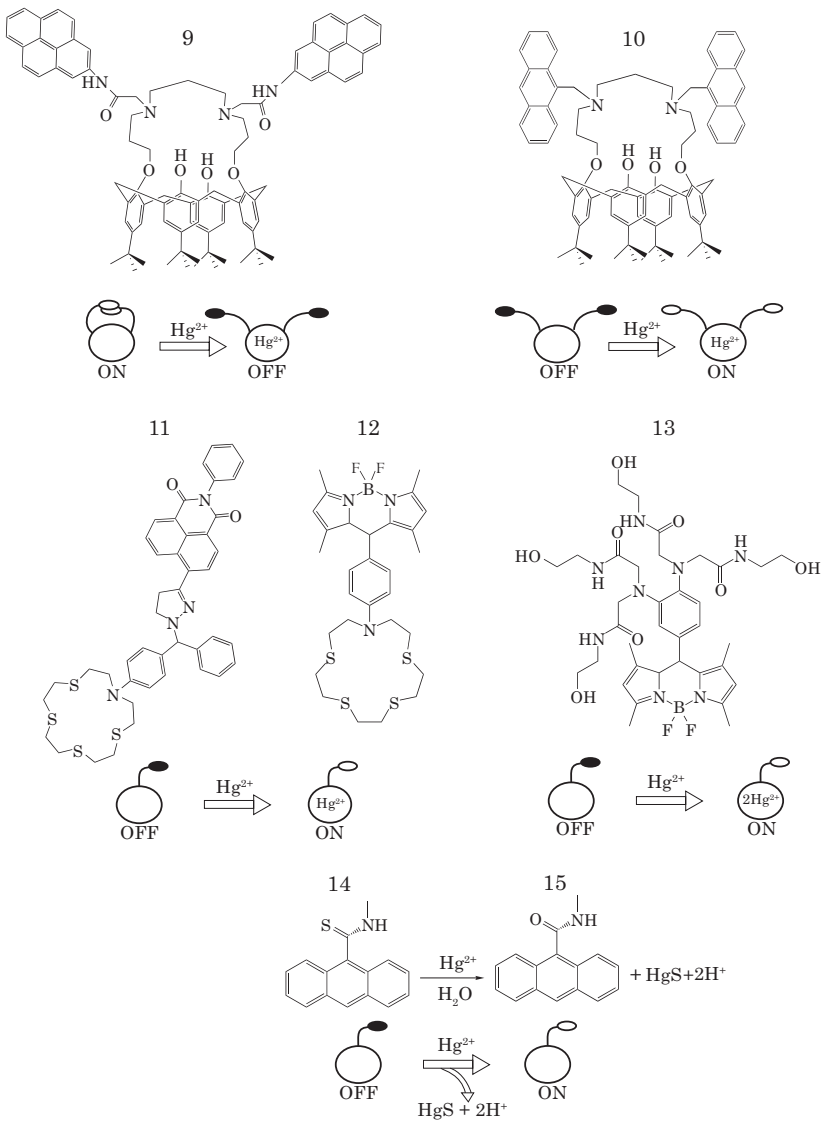

Figure 5.10: Examples of some fluorescent Hg^{2+} chemodosimeters based on different chelating and signaling strategies.

Polyheteroatomic (S-N) macrocycles have also been widely used as Hg^{2+}recognition elements, in order to increase the selectivity and affinity for soft metal ions such as Hg^{2+} or Pb^{2+}. An example of this is the work developed by *Rurack et al.* (**11** and **12**)[56,57] where a NS_4 crown donor is linked to a naphthalimide acceptor

through a 1,3,5-trisubstituted Δ^2-pyrazoline ring for compound **11** and to a boron dipyrromethene (BODIPY) for compound **12**. In both cases the anchoring of the Hg^{2+} produces an increase on the fluorescence intensity by enhancing the quantum yield (15 fold for compound **11** and up to 5900 fold for compound **12**). Even though for both chemosensors a good sensitivity and selectivity was obtained, none of them was suitable to perform the Hg^{2+} detection in either aqueous or mixed aqueous/organic solutions.

There are relatively few examples of Hg^{2+} responsive probes working in pure aqueous solutions. To the best of our knowledge, the very first example of *turn-on* Hg^{2+} chemosensor was reported back in the 1992.[58] However, in this work a different approach was used, since the Hg^{2+} was not used as a complexing cation but as a chemical reactive. Initially, compound **14** has a thioamide group that acts as fluorescence inhibitor. Thus, the addition of Hg^{2+} promotes the desulfurization reaction and formation of the subsequent anthrylamide **15** entailing a 55-fold emission enhancement. Although interesting, this kind of approach is very limited by the physicochemical parameters (kinetics, yield, stecheometry...) of the reaction chosen.

In oder to avoid this kind of problems, other authors have made use of the solubility and the coordinative properties of some amide derivatives. *Wang et al.*[59] presented the polyamide chemosensor **13** were four amide units were linked to a BODIPY receptor. This hexadentated ligand was able to form a 1:2 ligand:Hg^{2+} complex where each Hg^{2+} was bonded to 3 nitrogens and to the other metallic atom through a water bridge entailing a significant increase of the fluorescence of the signaling unit, and reaching Hg^{2+} detection limits of 2ppb.

Even tough all the Hg^{2+} probes described are based on intensity measurements, this is not the only approach which has been used on fluorescent Hg^{2+} detection processes. Ratiometric chemosensors (based on the comparison of fluorescence intensities at different wavelengths upon metal complexation) is also gaining the attention in the mercury sensing community, and although the number of examples found in the literature is still smaller than the ones based on intensity measurements, some of them show very interesting properties. This is the case of compound **16** (Figure 5.11).[53] Based on a seminaphthofluorescein platform attached to an aniline derivate pyridylaminethioether chelating unit. This water soluble Hg^{2+} probe bears two emission wavelengths (524 and 624 nm), which, upon complexation of Hg^{2+} , will suffer an asymmetric response (pH$\geq$8) providing a ratiometric detection through comparison of I_{624nm}/I_{524nm} before and after

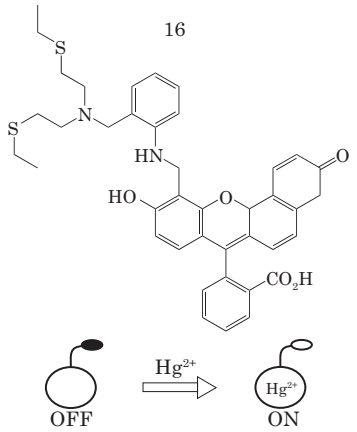

Figure 5.11: Water soluble ratiometric Hg^{2+} chemosensor.

Hg^{2+}addition. The detection limit observed for Hg^{2+}ions in aqueous media reaches the 50 nM.

5.6.2 Colorimetric Hg^{2+} detection

Although, the intrinsic properties of fluorescence phenomena make it one of the most sensible optical techniques, colorimetric detection has been always a hot issue for research laboratories. This is due to the fact that there is a clearer approximation to the market by the use of these products as they can be evaluated visually without any external equipment. Hg^{2+} sensing has not been an exception. As fluorescent detectors, colorimetric probes can be designed using a big variety of chromophores and receptors, from which some of their structures are depicted in Figure 5.12. Even though they use different signaling element, the design approaches used for this kind of chemosensors is essentially the same. Compound **17** shows a similar Hg^{2+} receptor based on polyheteroatomic macrocycles as for compounds **11** and **12**. However in this case, the signaling process is carried out by a squaraine moiety. This reporter moiety provides an intense absorption on the visible and near-IR regions of the electromagnetic spectra that is bleached upon addition of Hg^{2+}. This process has been successfully tested in organic solvent/water mixtures obtaining a detection limit of 10 nM. A different sensing approach is the one represented by compound **18**, where Hg^{2+} recognition is indicated by an absorption shift followed by the precipitation of a 2:1 ligand:metal complex.

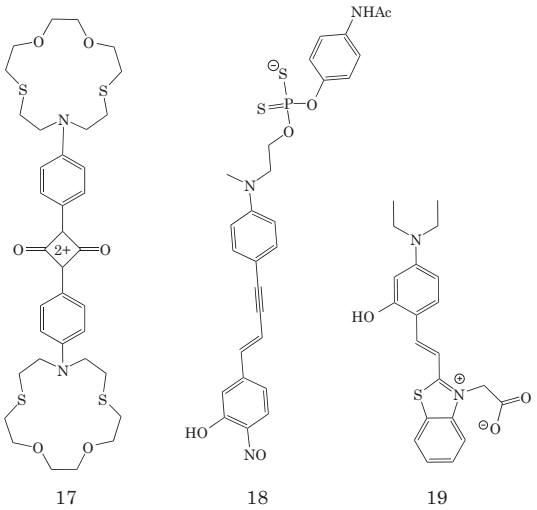

Figure 5.12: Colorimetric Hg^{2+} molecular probes.

Although a number of other metals are able to produce changes of color, selectivity studies depict that Hg^{2+} detection is the only one involving the complex precipitation.

However, the classification of chemosensor is not always clear, as some of them behave as fluoro and chromophoric species at the same time. This is the case of compound **19**. This probe, synthesized by *Tatay et al.*,[60] presents either an absorbance blue-shift of 100 nm and a fluorescence quenching of about an 85%, upon complexation of Hg^{2+}.

5.6.3 Solid supported Hg^{2+} sensors

As it has been shown in the previous section, there is a big number of Hg^{2+}molecular detectors able to sense this extremely toxic metal in an homogeneous system.[53] Nevertheless, the next step towards the fabrication of a sensor device of practical use is the production of a solid sensing material by the incorporation and structuring of the indicator into a solid support. However, the number of indicators able to perform the Hg^{2+} detection in water attached to a solid substrate is very limited.

Until today the most common approach for the immobilization step has been the physical entrapment of the sensitive probe in a polymer matrix. Back in the late 90's, *Murkovic et al.*[61] developed a turn-off Hg^{2+} detection system based on

the use of a modified cation sensitive poly(vinyl chloride) (PVC) membrane. The membrane, consisting of a solid solution of the Hg^{2+} sensing layer, was formed by a tetrakis(4-chlorophenyl)borate anion (TPB^-, **20**) and a 3,3(E-dihexadecyldicarbocyanine) cation (D^+, **21**) which froms a fluorescent ion pair in PVC. This material was prepared by drop casting and evaporation of a tetrahydrofurane (THF) solution of all the components over a $Mylar^{TM}$ film. Once prepared and introduced into a mercury containing aqueous solution, the TPB^- is decomposed by the Hg^{2+}, disrupting the borate-dye ion pair and entailing the formation of non fluorescent $(D^+)_n$ aggregates and the quenching of the membrane fluorescent emission. This system presents a linear response to Hg^{2+} concentration in the range of 0.1 to 0.5 μM, which is still one order of magnitude higher than the 10 nM Hg^{2+} concentration limit stated for drinkable water by the European Union[62] and the North American Environmental Protection Agency (EPA).[34]

Nevertheless, this kind of ligand entrapment generally produces inhomogeneity in the materials reducing its life time and reproducibility due to the leaching of the molecular probe.

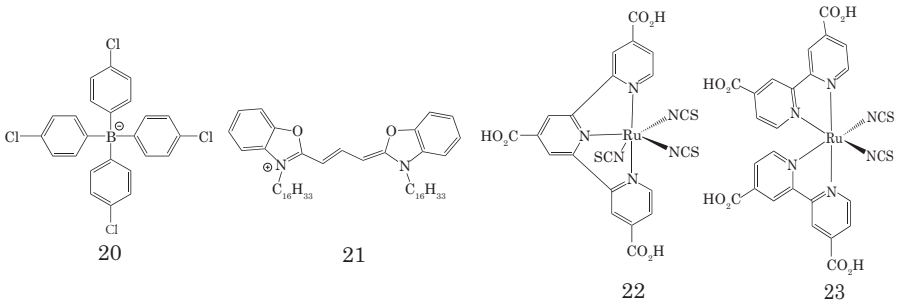

Figure 5.13: Hg^{2+} molecular sensing probes used in heterogeneous systems.

To solve the instability of these materials, the alternative has been the covalent attachment of the probes into the supporting substrate. *Coronado et al.*[63] made use of mesoporous nanocristaline TiO_2 film as heterogeneous substrate of a colorimetric Hg^{2+} probe based on a ruthenium complex (**22**). Substrate preparation was done by simply immersing a freshly prepared TiO_2 film in an organic solution of compound **22**. Once prepared, the heterogeneous probe provided a specific colorimetric signal when dipped in a Hg^{2+} containing aqueous solution. The main advantage of this sensor, in respect to the previous one, is the possibility to performed naked eye mercury detection, as the active layer is based on a colorimetric signaling unit. However, the detection limit achieved is limited to low μM range,

typical of colorimetric sensors, which does not fulfill the EU or EPA requirements for drinkable water.

The same approach was used by *Palomares et al.*,[64] who using a very similar ruthenium complex (**23**), developed a TiO_2 film based colorimetric Hg^{2+} test stripe which once developed allow to perform the naked eye and spectrometric detection of Hg^{2+} with detection limits of 20 μM and 0.3 μM respectively. Although it represents an improvement of two orders on magnitude, the detection limit achieved with this kind of sensors is still far away form the legal limit of 10 nM.

Several other processing methods have also been tried for the obtaining of efficient Hg^{2+} sensing materials. In analogy to microelectronic devices, where signal amplification systems are commonly used, the developing of sensing systems with the ability of enhancing the initial optical signal obtained during the recognition process have been commonly used. This is the case of conjugated polymers (CPs).[27] The main advantage of these family of molecular functional materials lies on the combination of their excellent processability, typical of polymer materials, together with the exceptional properties derived from their conjugated backbone, which is capable to serve as a highly efficient transport medium for electronic exited states enhancing the optical response of its monomers up to 10^6 times.[65,66] CPs have been employed for the optical sensing of several analytes including metal ions such as Hg^{2+}.[67]

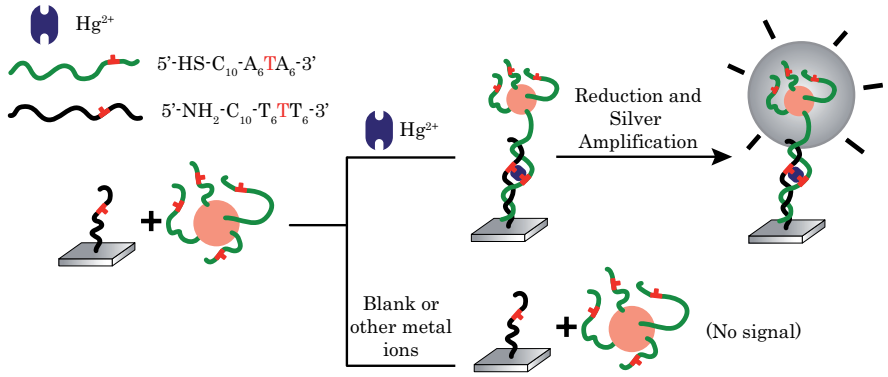

Figure 5.14: Depiction of the chip-based scanometric detection of Hg^{2+} Using DNA-Au nanoparticles (Au-NPs) (Image obtained from *Lee et al.*, *Analitical Chemistry*, **2008**, *80*, 6805-6808).

CP's are not the only colorimetric amplifying systems that have been used for the heterogeneous sensing of Hg^{2+} . Thus, in 2008 *Lee et al.*[68] developed a new

highly sensitive scanometric Hg^{2+} sensing probe based on the use of DNA functionalized gold nanoparticles (Au-NPs) as active sensing layer for the Hg^{2+} detection* (Figure 5.14). Complementary DNA strains bearing thymine-thymine (T-T) mismatches were used to functionalize both, the Au-NPs and the surface of a gold sensor chip by means of the formation of self assembled monolayers (SAMs), so that, once in contact, the subsequent DNA duplexes will not be from unless in the presence of Hg^{2+} , which will act as a bridge between both thymine residues due to the affinity that Hg^{2+} have this amino acid.[70] The Hg^{2+} mediated stabilization of the duplex avoids also the attached Au-NPs to be washed away from the surface. Therefore, a stringency wash followed by the hybridization signal amplification through Ag^{+} reduction catalyzed by the Au-NP's leads to a highly sensitive Hg^{2+} detection. The analytical Hg^{2+} concentration was determined by means of measuring the scattering of light produced by the silver nanoparticles generated on top of the Au-NPs during the reduction process. Hg^{2+} detection limits reached were below 10 nM. Selectivity studies were also performed showing no significant signal for any of the fifteen tested cations.

Although as stated before, several different materials, such as films,[61,71] modified polymers,[27,67] mesoporous materials[63,72] or metal surfaces[68,73] have been assayed in the developing of heterogeneous Hg^{2+} chemosensors. Most of them have important short-comings for their real application, such as a lack of selectivity, complexity, water stability and high-cost. Thus, the development of cheap, practical and reliable mercury heterogeneous sensors is still a challenge.

5.6.4 Mercury remediation

As previously stated, once in the environment, mercury is a persistent contaminant, and although anthropogenic emissions have been lessened in the recent years, historically emitted mercury is still a dangerous threat to all the living beings. Even though with the use of new technologies the control of contaminated wastewater is achievable, it may still take a very long time, perhaps centuries, for the nature to reach relatively safe mercury levels in both deep and superficial waters of aquatic contaminated areas. In addition, the possibility of mercury remobilization towards unpolluted areas, is one of the major concerns about mercury

*This work evolved from a previous one developed in the group of *Prof. Letsinger*,[69] where it was demonstrated the possibility of using the Ag^{+} reduction catalytic properties of Au-NPs for the amplification of DNA hybridization signaling.

contamination. Thus, the improvement and development of new and reliable mercury remediation procedures, able to completely remove Hg^{2+} contamination, is needed. According to their nature, mercury remediation processes can be classified into two main categories (Figure 5.15):

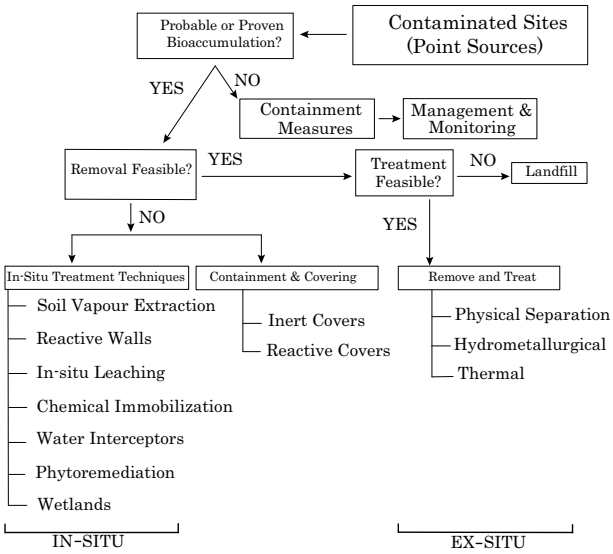

Figure 5.15: Response diagram to source mercury contamination (Image obtained from *Harada et al.*, *National Institute for Minamata Disease*, **2001**, 19-20)

- ***Ex-situ* treatments.** Are the most effective and established processes, but as they involve the mobilization of the contaminated area prior to treatment, they are mainly used for superficial and very localized contaminated areas. Physical separation and thermal or hydrometallurgical treatments are the most common ones.[74]

- ***In-situ* treatments.** Although they are not as effective as the *ex-situ* treatments, the main advantage of the *in-situ* treatments lies on its low cost and versatility, as they are possible to be applied in larger and more dispersed areas. Electro-kinetic separation, chemical immobilization and phytoremediation[75] are three of the most representatives procedures.

Nevertheless, during the last decades, a big effort has been made in the developing of new and alternative systems capable of effectively remove Hg^{2+} reducing the cost of the remediation processes.[76,77] Among the various materials tested it is

possible to include mesoporous substances,[78] chitosan[79], modified polymers[80] or even microorganisms.[81] One clear example of Hg^{2+} remediation functional material is the work developed by *Manos et al.*[82] They make use of a layered sulfide material, more particularly $K_{2x}Mn_xSn_{3-x}S_6$ (x = 0.5 - 0.95), as a heavy metal decontamination compound. The layered structure of the previously described inorganic compound allows rapid ion-exchange kinetics of the intercalated K^+ ions, present on its structure, with soft Lewis acids, such as heavy metal ions like Hg^{2+}, Pb^{2+} and Cd^{2+}. Hg^{2+} remediation experiments performed indicate the selective reduction of this kind of toxic ions to levels below the government allowed safe drinking levels (Figure 5.16).

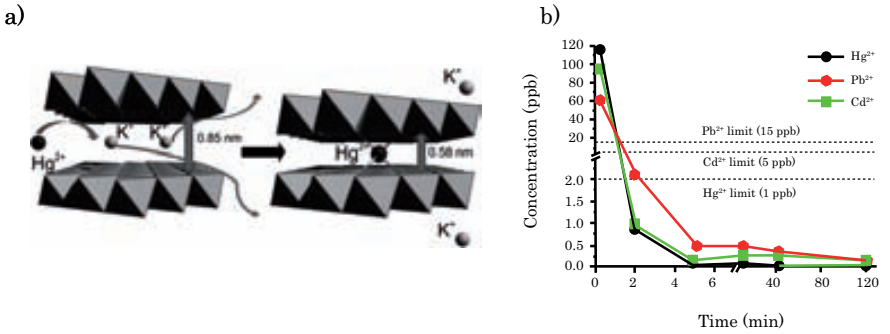

Figure 5.16: a) Scheme of the intercalative mechanism of capture of heavy metal ions (specifically of Hg^{2+}) by means of a mixed manganese tin sulfide derivative through exchange of its interlayer potassium cation; b) Kinetics for the decontamination of a potable water sample containing Hg^{2+} (116 ppb), Pb^{2+} (61 ppb), and Cd^{2+} (98 ppb) with a pre-treated (sonicated for approx. 30 min) $K_{2x}Mn_xSn_{3-x}S_6$ (x = 0.5 - 0.95) sample.

Since the implementation of genetic manipulation techniques, biologist, and more specifically genetic engineers have become a very active part on the materials science research field, being the environmental and pollutants control one of their most active research fields. Back in year 2000 *Wagner-Dobler et al.*[81] presented a work were they made use of the enzymatic reduction of Hg^{2+} to water insoluble Hg^0 by mercury resistant bacteria for the removal of mercury from wastewater in technical scale. A mercury retention efficiency of 97% was obtained within 10 h of inoculation of the bioreactor. At optimum performance, the bioreactor Hg^{2+} outflow concentrations were below 50 μg Hg/L, which fulfill the discharge limit for industrial wastewater. Specially remarkable is also the work of *Ros-Lis et al*[83] with the development of the first dual (remediation/signaling) Hg^{2+} removal

material. They used a thiol modified mesoporous silica substrate to anchor a squarine chemodosimeter. Thus, the coordination of mercury to the surface thiol releases the dye producing the analytical signal. Adsorbed Hg^{2+} (ranging from 0.7 to 1.7 mmol·g^{-1}) will remain attached to the sorbent material until substrate regeneration. However the multigram production and purification of this kind of mesoporous silica materials is still a problem.

Despite genetically modified microorganisms and complex mesoporous materials, natural polymers are low cost environmentally friendly substances which have already shown exceptional absorption properties that can be applied to Hg^{2+} remediation. Several works have been developed with this kind of materials, being cellulose one of the most promising.

5.7 Summary and Future Trends

In this introduction we have gone through some of the basis of chemical sensing, focusing our attention on the optical sensors, and more particularly on those able to detect Hg^{2+} ions in aqueous media. Mercury, as explained previously, is an ubiquitous and highly toxic element, which presence in the environment does not only denote a big risk for animals but also for human beings. Recent advances on the organic chemistry and material science fields have allowed the developing of highly selective and sensitive Hg^{2+} sensing probes capable to detect its presence, even at low concentrations, in homogeneous systems. However, the number of them able to perform the detection process anchored to a solid substrate is very limited. Thus, the developing of new functional Hg^{2+} chemosensors able to work once supported on a solid material and to continuously and reversibly report recognition events, still represent a great challenge.

Chapter 6

Results and Discussion

6.1 Homogeneous Hg^{2+} Chemosensors based on Diazabutadiene Derivatives

6.1.1 Introduction

As previously stated on the Introduction, the sensitivity and selectivity of a chemical sensor relies on the sensing unit. Thus, on the development of a new sensor it is essential to count with an appropriate analyte indicator. There is a countless number of chemical groups with linking and metal chelating properties. However, among all the possible families of organic ligands only some of them present the appropriate characteristics to act as heavy metal ions receptors,[53] being more reduced the number of those that can be incorporated to a solid substrate and even less, those showing high selectivity for Hg^{2+}. Our group in collaboration with the group of Prof. Pedro Molina from the *University of Murcia*, has carried out the design and synthesis of a new family of mercury ions chemosensors, based on disubstituted 2,3 diazabutadiene derivatives (Figure 6.1). The presence of this azine bridge, which is responsible of the analyte anchoring, provides the organic ligand with a versatile receptor core whose analytical response (electrochemical, optical or both) can be easily tuned by strategically choosing its substituents acting as signaling units.[84] Previous studies on metal ions complexation using azines with ferrocene substituents have shown that not only the characteristic UV-Vis band between 400 and 500 nm, ascribed to the lowest energy metal-to-ligand transition, is perturbed by the recognition process but also a positive shift of the Fe^{II}/Fe^{III} redox couple can be observed.[85] Other substituents, such as the pyrene, have

also often been used as an effective fluorescence signaling units because of its high detection sensitivity.[86]

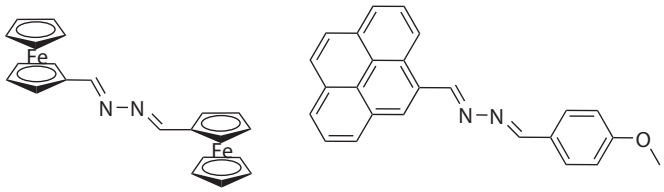

Figure 6.1: Mercury ion chemosensors 1,4-diferrocenyl-2,3-diaza-1,3-butadiene (**1**); 1-(4'-metoxyphenyl)-4(2'-pyrenyl)-2,3-diaza-1,3-butadiene (**2**).

On the basis of such precedents, suitable designed diazabutadiene cores with ferrocene and pyrene substituents (**1** and **2**, respectively) were synthesized, and their metal ion recognition properties in aqueous solutions were evaluated by both electrochemical and optical analysis.[87] Whereas no perturbation was observed upon addition of several divalent ion like Mg^{2+}, Ca^{2+}, Ni^{2+}, Zn^{2+}, and Cd^{2+} to organic solutions of the ligands **1** and **2**, a significant modification either on its electrochemical and/or optical behavior was observed upon addition of Hg^{2+} ions (Figure 6.2). Such behavior indicates the existence of a highly selective recognition process between the ligands and such a heavy metal ion. According to the absorption spectra data obtained from a Hg^{2+} titration experiment of a CH_3CN/H_2O (7:3) solution of **1** (Figure 6.2 a, c), these changes can be attributed to the formation of a 1:1 (ligand:Hg^{2+}) coordination complex. However, for compound **2** the situation is less straightforward and the fluorescence increase, resulting after Hg^{2+} addition, can be assigned to different phenomena, such as the deactivation of the existing pyrene fluorescence quenching. Such a quenching might be based on a PET effect involving the free electrons of the N atoms or to the formation of emitting dimers either between ligands from the same or from two different complex entities (Figure 6.2 b, d). Depending on the nature of the interacting units present in the emitting dimer, they can be excimers or exciplexes. Thus, in the excimers the interaction inside the dimer occurs between equal entities, like pyrene-pyrene or phenyl-phenyl, which are associated in an excited electronic state and dissociated in its ground electronic state. By contrast in the exciplexes the emission is based on the formation of an electronically excited molecular hetero complex of definite stoichiometry; in this case a pyrene-phenyl, which are dissociated in its electronic

ground state.[5]

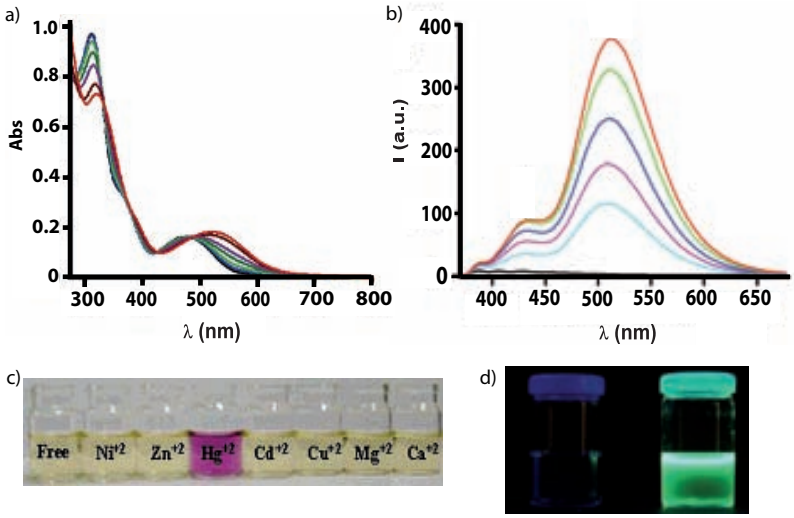

Figure 6.2: a) Absorption spectra of **1** ($c = 1{\cdot}10^{-4}$ M) in CH_3CN/H_2O (7:3) upon addition of increasing amounts of $Hg(ClO_4)_2$; b) Fluorescence emission spectra of a $2.5{\cdot}10^{-5}$ M solution of **2** in CH_3CN upon addition of increasing amounts of $Hg(ClO_4)_2$ in water (excitation wavelength, λ_{exc} 305 nm); c) Color change due to binding of **1**(10^{-4}M) in CH_3CN/H_2O (7:3) with Hg^{2+} in comparison with other metal cations; d) Photograph of a $2.5{\cdot}10^{-5}$ M solution of **2** in CH_3CN before (left) and after (right) the addition of 1 equivalent of $Hg(ClO_4)_2$ in water.

The formation and disgregation of pyrene excimers and exciplexes have been extensively used as analytical signaling units.[88–91] Two informative parameters associated with the pyrene dimers are the intensity ratio of the dimer to the monomer emission (I_D/I_M) and the wavelength corresponding to the maximum of the dimer emission (λ_D). While the I_D/I_M parameter is sensitive to the ratio of excimer and monomer, the emission parameter λ_D proportionates information about whether the system is constituted by excimers or exciplexes. Thus, the exciplex emission (λ_{ex}) is known to be quenched and shifted to higher values as the solvent becomes more polar, in contrast to the excimer emission (λ_{em}) which is independent of solvent polarity.[92–94]

6.1.2 Fluorescence of the Complex between 2 and Hg^{2+}. Mechanism of Detection and Signaling

As stated before, the addition of increasing amounts of aqueous Hg^{2+} to an organic solution of chemosensor **2** entails a significant increase on the fluorescence of the sample. Although the detection of Hg^{2+} ions by compound **2** had been widely studied in our group, the exact mechanism of the Hg^{2+} complexation and the luminescence emission was still unclear when this thesis started. For this reason, we decided to study in more detail such an emission phenomena in order to unravel its origin and to get insights about the structure of the involved complex.

Fluorescence studies performed on a $2.5{\cdot}10^{-5}$ M solution of compound **2** in toluene (Figure 6.3, a (red)) ($\lambda_{exc} = 340$ nm) depict the existence of two weak bands ($\lambda = 388$ nm and $\lambda = 406$ nm) characteristics of the Locally Excited State (LES) emission of the pyrene. The exceptional weakness and low quantum yield ($\phi = 0.0006$) of these bands, if compared with those of an unmodified pyrene ($\phi = 0.3$) (Figure 6.3, a (black)), can be attributed to the existence of an intramolecular PET process involving the free electrons of the N atoms, present on the azine bridge, that inhibits almost completely, the pyrene monomer fluorescence. Nevertheless, the addition of Hg^{2+} ions to a solution of **2** triggers a set of unidentified effects that involve a significant change on its emission spectra, involving the appearance of an intense broad band at higher wavelengths.

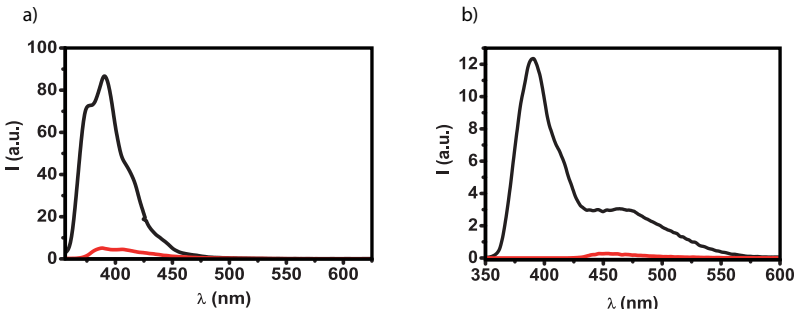

Figure 6.3: Fluorescence spectra of a) $2.5{\cdot}10^{-5}$ M and b) 10^{-3} M solutions of pyrene (black) and chemosensor **2** (red) respectively, in toluene. The influence of concentration can be observed on the disappearance of the LES bands (attributed to the monomer) and the appearance of a less energetic emission at higher wavelengths assigned to the formation of pyrene excimers.

In order to clarify the origin and mechanism of these photochemical changes, Hg^{2+} titration experiments of a $2.5{\cdot}10^{-5}$ M solution of compound **2** in acetonitrile

were carried out, showing the appearance of a broad and structureless emission band on the blue-green region of the electromagnetic spectra (450 nm $\leq \lambda \leq$ 650 nm, λ_{max} = 490 nm), while those corresponding to the LES emission of the pyrene monomer remained unchanged. This new band resembles in shape and wavelength to those characteristic of the fluorescent emission of excimers or exciplexes (Section 5.2.1). Moreover, this emission cannot be attributed to the presence of intermolecular excimer or exciplex formation of compound **2**, as no similar emission signals were detected either for pyrene or compound **2** at the same concentration and under identical conditions (Figure 6.4).

By other hand, a 40 fold increase on the concentration of the solution of **2** (10^{-3} M) allowed us to observe the presence of an incipient trifling band with a λ_{max} of around 450 nm, pretty similar to the one observed for the pyrene in similar conditions that permit, therefore, to be assigned to the formation of intermolecular excimers between the pyrene moieties of compound **2** (Figure 6.3, b). However, a comparison between the λ_{max} of this band (450 nm) and the one of the Hg^{2+} complex (490 nm) depicts the existence of a 40 nm red shift. Such a big change in energy can be hardly explained if the emission is due to the formation of the same kind of pyrene excited dimers, being thereby more likely the hypothesis of an intramolecular exciplex or excimer mediated signaling process.

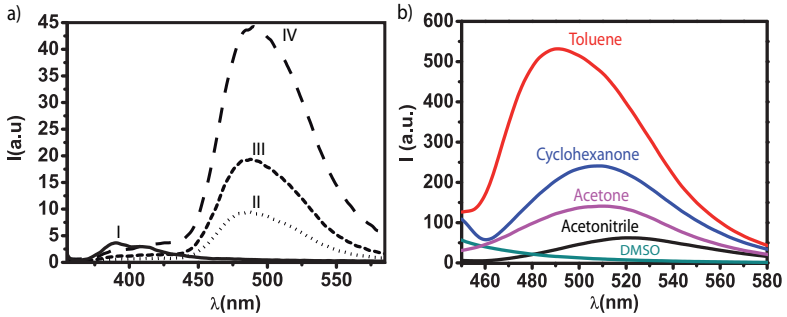

Figure 6.4: a) Emission spectra of the **2**:Hg^{2+} complex with different ligand concentrations (IV = 10^{-5} M; III = 10^{-6} M; II = 10^{-7} M; I = free ligand) in toluene; b) Representative emission spectra of the **2**:Hg^{2+} complex ($2.5 \cdot 10^{-5}$ M) in various organic solvents.

In order to clarify the photochemical features of the **2**:Hg^{2+} complex, further solvent and concentration dependence studies were performed. If the emission phenomena were due to intermolecular interactions between different **2**:Hg^{2+} complex

molecules, a sudden disappearance of the fluorescence would be expected at concentrations lower than 10^{-4} M where single molecule emission are expected. However, the results obtained (Figure 6.4 a) exhibit the presence of emission even at much lower concentrations (10^{-7} M), in agreement with an emission phenomenon due to an intramolecular process.

Fluorescence solvatochromism of **2**:Hg^{2+} was also analyzed in a broad range of organic solvents with different polarities and dielectric constants ranging from 2.38 to 47.2. The resulting emission values, λ_{max}, along with the dielectric constant (ϵ), the Onsager polarity function $\Delta f(\epsilon)$ [95] and the Π^* parameter of different solvents are summarized in Table 6.1.

Table 6.1: Solvent polarity parameters (ϵ, $\Delta f(\epsilon)$ and Π^*) and fluorescence emission maximum of the **2**:Hg^{2+} complex in different organic solvents. An Excitation wavelength of 340 nm was used which corresponded to the λ^M_{max} of excitation of the pyrene monomer.

Solvent	ϵ	$\Delta f(\epsilon)$[i]	Π^*	λ_{max} *(nm)*
Toluene	2.38	0.65	0.54	490.5
Ethyl Acetate	6.02	0.84	0.55	496.5
Ciclohexanone	18.30	0.94	0.76	508.5
Acetone	20.70	0.95	0.71	510.0
Methanol	32.70	0.97	0.60	516.5
Dimethylformamide	36.71	0.97	0.88	513.5
Acetonitrile	37.50	0.97	0.75	520.5
Dimethylsulphoxide	47.20	0.98	1.00	N/A

[i] $\Delta f(\epsilon) = \frac{(2\epsilon-1)}{(2\epsilon+1)}$

The results obtained indicate the existence of a clear solvatochromic effect on the emission λ_{max} varying over a range of 30 nm, from toluene (490.5 nm) to acetonitrile (520.5 nm)(Figure 6.4 b). This experimental observation is consistent with those found in the literature showing that solvent polarity is crucial to the properties of exciplexes,[92–94] whilst the wavelength of excimer emission is relatively solvent independent. Furthermore it is possible to observe (Figure 6.4 b) that this solvent-induced red shift of λ_{max} is accompanied by a decrease on emission intensity that became total for dimethylsulphoxide (DMSO).

Thus, two effects due to the increase of the solvent polarity over the complex fluorescence could be noticed: an intensity quenching and a λ_{max} red shift, being both characteristics of an exciplex emission. Detailed correlation studies of the λ_{max} values (Figure 6.5 a) indicate a linear dependence with the dielectric constant of the solvent polarity. Experimental data of λ_{max} also shows a linear dependence with the Onsager polarity function although the value for toluene show a large

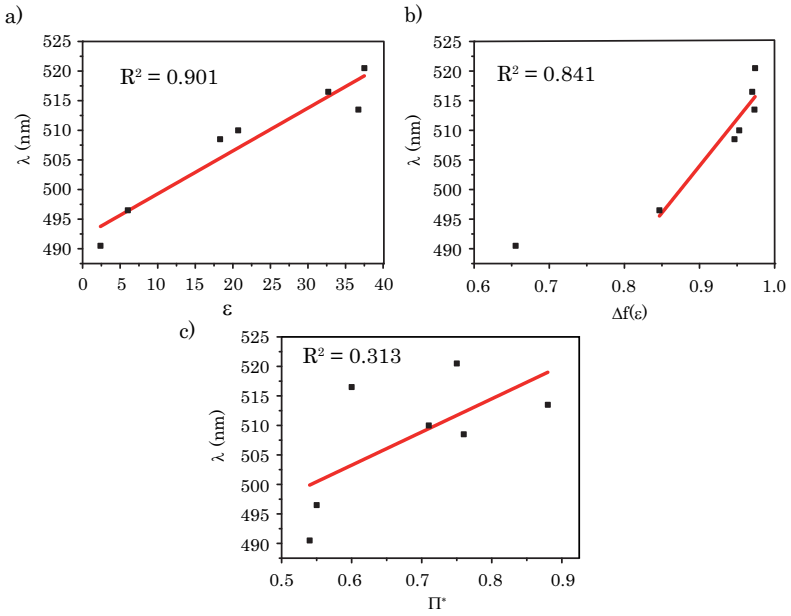

Figure 6.5: Representation of the dependence of the **2**:Hg^{2+} complex emission λ_{max} with different solvent parameters; a) dielectric constant (ϵ); b) Onsager polarity function ($\Delta f(\epsilon)$) and c) Π^* parameter.

deviation from linearity (Figure 6.5 b). This can be explained by the existence of important specific interactions between the aromatic moieties of **2** and the solvent. Nevertheless, when only the solvent parameter Π^*, which measures their polarizability is considered no special trend on the the λ_{max} values can be observed (Figure 6.5 c), indicating that the **2**:Hg^{2+} complex emission phenomena is mainly influenced by the dielectric constant of the media although other interactions play a role in this phenomena.

Therefore, from the experimental data previously described, it is possible to determine that for compound **2**, the Hg^{2+} detection and signaling mechanism occurs via the formation of an intramolecular excited heterodimer, also known as exciplex, probably between the pyrenyl and the phenyl moieties present in the chemical structure of **2**.

More detailed studies over the influence of the solvent on the final **2**:Hg^{2+} complex λ_{max} were performed by means of a Linear Solvation Energy Relationship (LSER) analysis.[96] The LSER treatment is a powerful tool for the study of the principal intermolecular interactions that control a specific physicochemical process in

solution. It assumes that the changes in the free energy associated with a physicochemical process are the sum of different independent contributions generated from the different solvent/solute interactions, which can be categorized in two groups: the exoergic and endoergic interactions.[96] The exoergic interactions have their origins in attractive solute/solvent interactions and can be quantified by the solvatochromic parameters Π^*,[97] α,[98] and β,[99] which at the same time can be classified as nonspecific (Π^*) and specific (α and β) ones. The Π^* parameter measures the exoergic effects of dipole/dipole and dipole/induced dipole interactions between the solute and the solvent molecules; e.g., it is a measure for the dipolarity/polarizability. The solvatochromic parameter β is a quantitative empirical measure of the ability of a solvent to act as hydrogen-bond acceptor (or electron donor) toward a standard solute; i.e., it is a measure for the basicity of the solvent. By contrast, the empirical parameter α measures quantitatively the ability of a solvent to act as a hydrogen-bond donor (or electron-pair acceptor for acidity of the solvent) toward a standard solute. Finally, we have to consider the endoergic term Ω, named the cohesiveness term.[100] This term measures the work required for separating the solvent molecules to provide a suitably sized and shaped enclosure in which the solute molecule can be accommodated. The Ω term represents the physical quantity of cohesive pressure, or cohesive energy density, of the solvent. The LSER approach finds an equation, $P = \Sigma c_i \cdot p_i$, relating the studied physical properties, P, to a set of solvent empirical parameters, p_i, and coefficient c_i that depend on the molecular structural characteristics of the studied molecule. Statistics, often multilinear regression, are used to find the coefficients, c_i. In general terms, the LSER model can be written as (Equation 6.1):

$$Property = constant + bulk/cavity + dipolarity/polarizability + hydrogen\ bonding \tag{6.1}$$

then the final LSER equation can be expressed as (Equation 6.2):

$$\lambda_{max} = K + a \cdot \alpha + b \cdot \beta + c \cdot \Pi^* + d \cdot \Omega \tag{6.2}$$

where K is a constant that provides an estimation of the λ_{max} in absence of any significant interaction with the solvent; i.e. in the vacuum, α and β are the solvent hydrogen-bond donor acidity and the hydrogen-bond acceptor basicity, respectively, Π^* the solvent dipolarity/polarizability, Ω the cohesiveness term and

a,b,c,d the coefficients of the studied molecule associated with each of the previously described parameters.

Equation coefficients and statistical parameters corresponding to the seven solvents tested (Table 6.1) were obtained by multilinear correlation analysis using SYSTAT* software.

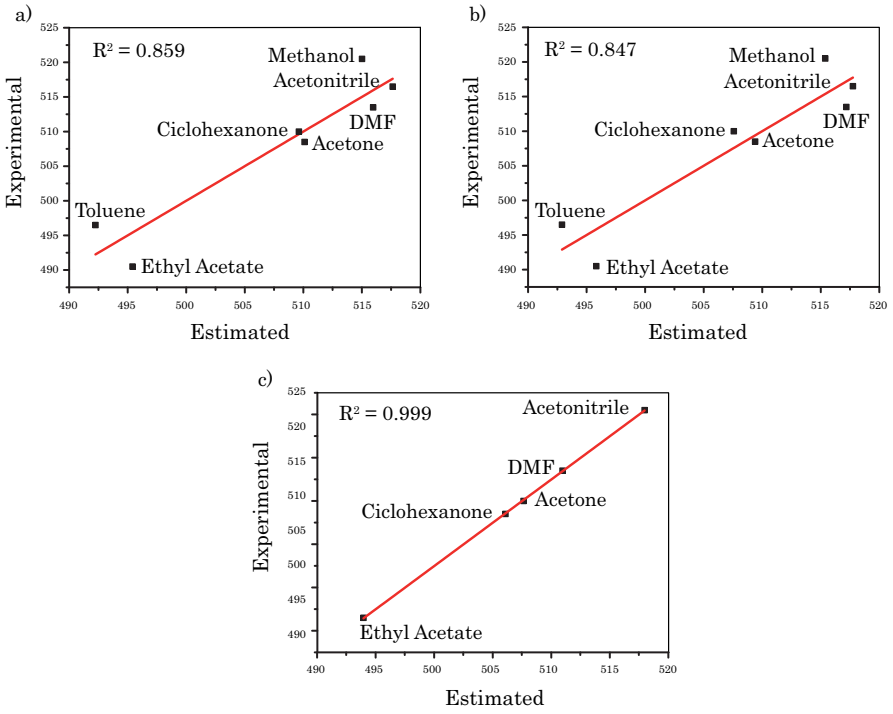

Figure 6.6: Representation of the experimental *vs.* the estimated fluorescence emission (λ_{max}) of the **2**:Hg^{2+} complex after multilinear LSER fitting considering a) α, β, Π^* and Ω parameters; b) α, β and Π^* as fitting parameters and c) considering α, β and Π^* as fitting parameters and removing toluene and methanol from the solvent data list.

Primary results obtained depicted a correlation coefficient of 0.859 between the experimental and the calculated values using the LSER approach (Figure 6.6 a). Therefore, in order to optimize the fitting those parameters with coefficients with a low significance level were removed from the calculated models (Table 6.2). This is the case of Ω (d < 0.1). A second multilinear regresion study was performed taking into account only the exoergic parameters α, β and Π. Nevertheless, the correlation coefficient obtained, in this case, was in the same range as the previous

*SYSTAT 5.01, SYSTAT Inc., Evanston, IL, USA

one, $R^2 = 0.847$ (Figure 6.6 b).

Table 6.2: LSER regression coefficients and statistical data of the multivariable linear regressions obtained for the λ_{max} emission of the **2**Hg^{2+} complex considering a) K, α, β, Π^* and Ω parameters; b) K, α, β and Π^* as fitting parameters and c) considering K, α, β and Π^* as fitting parameters and removing toluene and methanol from the solvent data list (n, indicates the number of studied solvents and the numbers in parenthesis correspond to the coefficient standard errors of the estimates).

LSER	n	K	α	β	Π^*	Ω	R^2
a	7	451.845	35.926	-12.084	95.772	-0.089	0.883
		(16.482)	(29.783)	(19.282)	(45.095)	(0.217)	
b	7	452.977	24.341	-11.006	81.589		0.873
		(13.815)	(8.081)	(16.241)	(24.634)		
c	5	468.621	56.882	-10.168	58.899		1.000
		(0.537)	(3.733)	(2.629)	(1.910)		

A closer look to the statistical studentized residuals[†] data obtained in this last LSER fitting indicated the existence of two outlier solvents, toluene and methanol, which could be, then, eliminated form the fitting. This, result was somehow expected, as toluene and methanol are two solvents that might strongly interact with the π and the non-bonded electrons, respectively, of the **2**:Hg^{2+} complex causing a more intense shift of the emission λ_{max} than expected. Nonetheless, it is worthy to remark that the elimination of these two solvents reduces the number of experimental data available for the multilinear fitting to 5, thus the information obtained from its statistical analysis should be taken carefully due to the reduced set of points.

Table 6.2 c depicts the coefficients obtained for the LSER analysis performed using the experimental data of the 5 remaining solvents and α, β and Π^* as fitting parameters.

Finally, from the analysis of the LSER models, the following information can be extracted. According to the values obtained α (hydrogen bond donor/electron acceptor) and Π^* (dipolarity/polarizability) solvent parameters would be the most

[†]The quotient resulting from division of a residual by an estimate of its standard deviation. It is a form of a Student's t-statistic, with the estimate of error varying between points.

influencing on the final emission λ_{max} while the value of β ((hydrogen bond acceptor/electron donor) has less importance. Thus, a positive value of the coefficient of the α and Π^* terms results in a decrease in the energy (a red shift of the band) of the fluorescence emission band with increasing solvent H-bond donor ability and polarizability. This fact may be explained in terms of a relative stabilization of the **2**:Hg^{2+} complex exciplex with respect the ground state in the presence of this kind of solvents.

In order to corroborate the formation of an intramolecular exciplex as the correct detection and signaling mechanism and also to clarify the stoichiometry of the **2**:Hg^{2+} complex, DFT quantum chemical calculations were performed by *Dr. A. Espinosa* from *Universidad de Murcia*, using the Truhlar hybrid metafunctional mPW1B95[101](see Part V: Experimental part Chapter 12.3).

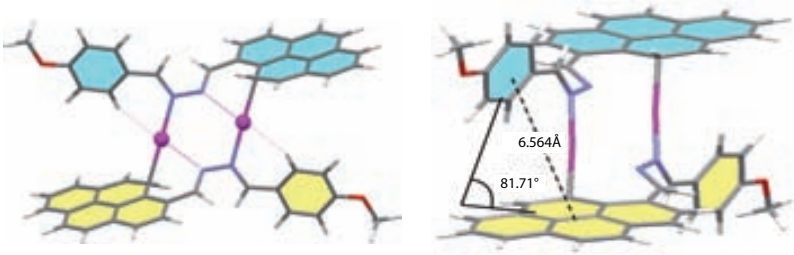

Figure 6.7: Calculated (mPW1B95/6-31G**/StRSC-ecp) structures for the 2:2 **2**:Hg^{2+} complex.

As it has been previously shown, spectrophotometrical titration studies performed with solutions of receptors belonging to the same family of compounds, indicated the preferential formation of ligand:metal complexes with a minimum stoichiometry of 1:1; where at least one Hg^{2+} for each ligand molecule is present in the complex. However, and taking into account the coordinative properties of mercury ions, with a high tendency to form linear coordinations,[102] and the chemical structure of compound **2**, observed by x-ray crystal diffraction, which has a completely conjugated and a planar and rigid structure (see Part V: Chapter 12.2) combinations involving the formation of a 2:2 or a 2:1 ligand:Hg^{2+} complexes were thought to be the most suitable ones. In such complexes the Hg^{2+} (one or two depending of the case) should be bonded to two N atoms (each one of a different ligand molecule) and the ligands should lie parallel one to the other.

Detailed DFT calculations were performed for both stoichiometries. In the case

of the 2:2 complex such calculations depicted the existence of a single energy minimum corresponding to a C_i-symmetric 2:2 Hg^{2+}:**2** complex (Figure 6.7). This structure presents two equivalent Hg atoms that are essentially linearly di-coordinated (N-Hg bonds, d_{N-Hg} = 2.182 Å; C10-Hg bonds, d_{C10-Hg} = 2.263 Å; N-Hg-C10, angle 176.5°) by the action of the pyrene C-10 atom of one ligand and a N atom belonging to the other ligand bridge. As a consequence of the bonding of the pyrene to the metal, the C-10 atom is pyramidalized as evidenced by the high value (34.0°) of the dihedral angle formed by the C10-H bond with the pyrene mean plane.

Electrostatic interactions between the two positively charged mercury atoms seem not to be important since the intermetallic distance between them is large enough ($d_{Hg\cdots Hg}$ = 4.166 Å) to significantly contribute to the formation of the complex. Even though, the pyrenyl and phenyl mean planes lie almost orthogonal (81.7°) to each other, being the distance between their centroids (the geometric centers of each of the aromatic moieties) relatively short, (R_{cent} = 6.564 Å) making the photophysical interactions between them feasible.

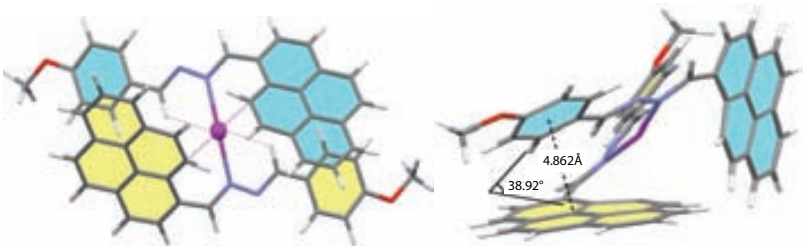

Figure 6.8: Calculated (mPW1B95/6-31G**/StRSC-ecp) structures for the 2:1 Hg^{2+} :**2** complex.

For the 2:1 complex DFT calculations show in the potential energy surface two minima close in energy (ΔE = 5.34 kcal· mol^{-1}). The absolute minimum has a C_2-symmetric structure with both ligand molecules showing an extended conformation ($dihedral_{CH=N-N=CH}$ = 168.6°) with the Hg^{2+} ion linearly bonded to two N atoms (one from each ligand molecule, N-Hg bonds, d_{N-Hg} = 2.278 Å; N-Hg-N' angle 166.32°, Figure 6.8) almost aligned with the C_2 axis. Furthermore, both a smaller torsion angle between the aromatic pyrene and phenyl rings of θ = 38.92°

and a closer centroids intermolecular distance R_{cent}=4.862 Å are found[‡].
Thus, all the experimental and theoretical evidences suggest that the mechanism of the Hg^{2+} detection and fluorescent of compound **2** is based on a exciplex formation originated from interactions between two molecules of **2** complexed by the Hg^{2+}. Furthermore, theoretical calculations also suggest that both possible stoichiometries for the ligand:Hg^{2+}, 2:2 and 2:1, correspond to energy minima. Moreover, in both cases the geometrical distribution of the ligand molecules around the Hg^{2+} ions allows the electronic interaction between the pyrene and phenyl moieties making possible the exciplex formation and emission plausible.

6.1.3 NMR Studies of the Complex between 2 and Hg^{2+}

^{1}H-Nuclear Magnetic Resonance (NMR) titration experiments have been extensively used as an alternative technique for the determination of the reaction stoichiometries during complexation processes. Therefore, in order to have a direct evidence of the structure of the complex **2**:Hg^{2+} in solution, further experiments employing NMR were performed in the group of *Prof. P. Molina* from the *Universidad de Murcia*.
The experiments were carried out using a 600 MHz NMR spectrophotometer. A 10^{-2} M solution of compound **2** in deuterated chloroform ($CDCl_3$) was titrated with increasing amounts of a 0.1 M solution of $Hg(OTf)_2$ also in $CDCl_3$. Figure 6.9 represents a selection of the ^{1}H-NMR obtained during the Hg^{2+} titration process. Taking as reference the initial spectra obtained for compound **2** (Figure 6.9 a) it is possible to observe how during titration the signal corresponding to one of the iminic protons (CH=N, red) is shifted from δ = 8.48 ppm to δ = 10.72 ppm ($\Delta\delta$ = 2.24 ppm) indicating its participation on the Hg^{2+} recognition process. By contrast, the second iminic proton (singlet at δ = 9.73 ppm) remains unshifted, and although it suffers some changes in the signal shape during titration, its position after the addition of 1 equivalent of Hg^{2+} (Figure 6.9 f) is the same than the one observed for the free ligand (Figure 6.9 a). On the other hand one of the doublets corresponding to the C-H bond of the pyrene substituent (green) is shifted from δ = 8.94 ppm to δ = 9.36 ppm ($\Delta\delta$ = 0.42 ppm) while titration, entailing its participation in the complexation phenomena. No significative changes were detected

[‡]For the parallel staggered configuration, $\pi - \pi$ interactions are optimized if the center to center distance R_{cent} is in the range 3.5-7.5 Å along the off normal angle θ, maximized for θ = 81.7°.[103] In our model θ is about 81.7° and R_{cent} = 6.564 Å for the 2:2 complex and θ = 38.92° R_{cent} = 4.862 Å for the 2:1 structure

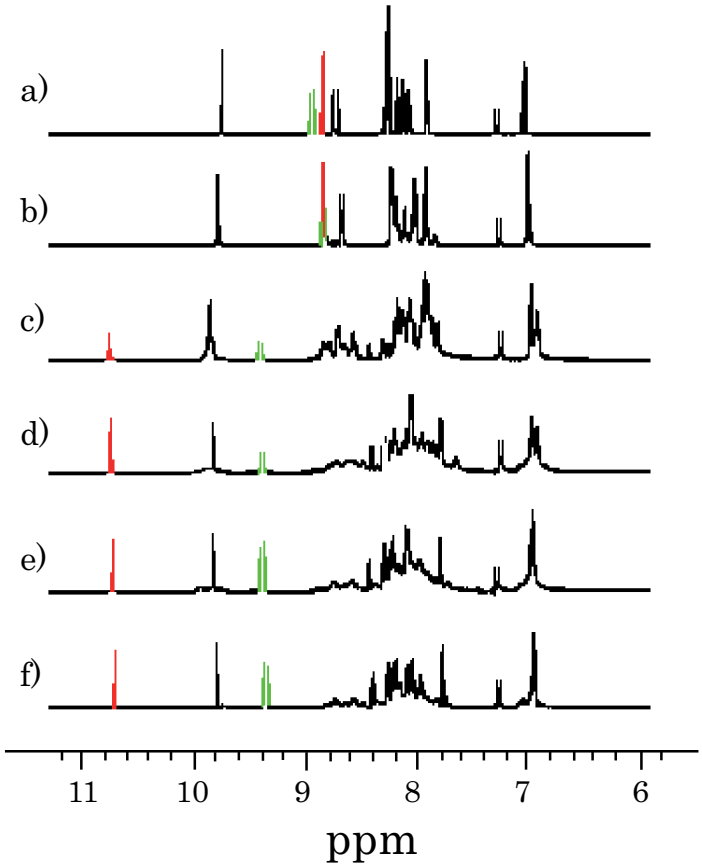

Figure 6.9: ^{1}H-NMR titration of a 10^{-2} M solution of **2** in $CDCl_3$ by the addition of a) 0 equivalents b) 0.2 equivalents c) 0.4 equivalents d) 0.6 equivalents e) 0.8 equivalents f) 1 equivalent of Hg^{2+} from a 0.1 M $Hg(OTf)_2$ solution in $CDCl_3$

on the rest for the ^{1}H-NMR signals.

Therefore, from the analysis of the ^{1}H-NMR data obtained, it is possible to conclude that both, one of the iminic carbons (CH=N) of the diaza bridge and one of the C-H groups belonging to the pyrene substituent, have a large participation on the Hg^{2+} coordination process, in agreement with the theoretical calculations previously described. Moreover, stoichiometric and kinetic studies of the complexation process[§] indicated the formation of a 1:1 (ligand:Hg^{2+}) with an association constant (K_{as}) of $1.07{\cdot}10^5$ M^{-1}.

[§]These analysis were performed with the WINEQNMR software.

6.1.4 Conclusions

During this first part of the thesis work, we have focused our attention towards the study of the compound **2** Hg^{2+} detection and signaling mechanism. Fluorescence spectroscopy studies performed to different solutions of **2**:Hg^{2+} complex indicated that the Hg^{2+} complexation occurs via the formation of an intramolecular excited heterodimer, also known as exciplex, between the pyrenyl and the phenyl moieties present on the chemical structure of **2**. This result was confirmed by DFT quantum chemical calculations and by ^{1}H-NMR titration experiments.¶

¶The study of Hg^{2+} detection and signaling mechanism by compound **2** has been submitted for publication.

*"Academics like **complexity** and **emergence**. The real world puts up with it reluctantly but really wants **simplicity**.....whatever **simplicity** is"*

George Whitesides: Toward a Science of Simplicity

6.2 Heterogeneous Hg^{2+} Chemosensors based on Diazabutadiene Derivatives

6.2.1 Introduction

As previously stated, the number of available mercury detection methods has suffer a considerable increase during the last decades, being several the techniques that allow to measure selectively the concentration of this toxic metal in aqueous systems.[50–52] However, despite their high sensitivity and selectivity, most of them require the use of tedious sample pretreatments and present a high intrinsic complexity and elevated operational costs; facts which finally reduce their general use. In addition, as far as we know, none of them can be set up to operate *"in-field"* conditions, providing an immediate response where the analytical information is needed. For this reason, the development of simple, cheap, fast, efficient, highly sensitive and selective mercury sensing devices able to measure *"in-field"* trace amounts of this heavy metal ions directly in water sources, is still a big challenge. Compounds **1** and **2** have already proved to be effective Hg^{2+} molecular probes working in homogeneous mixed organic/aqueous systems.[87] Thus, the next step toward a real sensor device would be their anchoring on a supporting substrate. Although it seems to be trivial, the choice of an appropriate immobilization support is crucial for the final properties of the device, as it can determine not only its final use but also other very important parameters such as the response time, the analyte permeability, the sensitivity and the re-using capability, among others.

Taking into account all these requirements, two different strategies have been used in this Thesis for the obtaining of different systems for Hg^{2+} detection. The first one, was inspired on the one shoot test stripes for water pH determination, and it was directed to the development of cheap, portable, fast and reliable colorimetric and/or fluorimetric probes. For this strategy the physisorption of molecular probes was used as the immobilization method of the receptors **1** and **2**. The second strategy was focused on the elaboration of a highly sensitive, miniaturizable and integrable sensor, based on the SPR technique and the gold-sulphur chemistry for the immobilization of the molecular probes. Both strategies render devices with different performances that are able to do selective detection of Hg^{2+} directly on aqueous systems.

With respect to the first strategy and due to their ephemeral nature, cost effectiveness should be specially taken into account on the developing of sensing stripes.

Among all the possible supporting substrates (Section 5.4), cellulose arose as a promising candidate. Formed by a concatenation of pyranose units linked by β(1-4) glycosidic bonds, cellulose is an abundant, inexpensive, biodegradable and renewable biopolymer exhibiting very good adsorption and mechanical properties, water compatibility and procesability, among others. Furthermore, the presence of free hydroxyl groups increments, even more, its already substantial possibilities, as it allows the chemical tailoring of its molecular structure broadening its range of application.[104,105] Hence, the use of cellulose-based materials could easily be extended to the development of new products, such as sensing materials, just by the incorporation of functional detecting molecules onto its fibrilar surface, either physisorbed or chemisorbed. In this context, there are some recent works published on the literature which make use of paper strips, for instance in biomedical assays,[106,107] or metal ions detection,[108–110] although sensitivity and selectivity results are still far from being ideal.

Herein we present two different approaches towards the obtaining of Hg^{2+} cellulose test stripes. The first, and more intuitive one, consists on a controlled coating of receptors **1** and **2** (Figure 6.1) into the cellulose matrix using a simple submersion procedure. The second one is based on the developing of a reactive sensing layer of the chemosensor over a cellulose acetate membrane substrate using nanoparticles of the sensing molecules as precursors.

6.2.2 Cellulose test stripes using receptors 1 and 2 for Hg^{2+} detection

6.2.2.1 Preparation of optical Hg^{2+} probes by the "developing technique"

Cellulose based probes using receptors **1** and **2** were prepared by a two-step protocol, depicted on Figure 6.10. Firstly the cellulose disks (θ = 40 mm, Albet) were introduced for 20 s into $Hg(ClO_4)_2$ solutions of different concentrations (ranging from 10^{-6}M to 10^{-2}M) using either an acetonitrile/water mixture (7:3 v/v) or pure acetonitrile as solvent, in order to impregnate the cellulose fibers with the analyte. Then, the wet samples were air dried for 40 s to remove the remanent solvent and the resulting stripes were subsequently developed by introducing them for 2 s into

a 10^{-3}M solution of the receptors **1** or **2** in toluene.[‖] Depending on the receptor used for the "developing process" a different spectrophotometrical response was observed, entailing the need of using different detection techniques. In the case of compound **1** probes,a characteristic color change due to the Hg^{2+} recognition was immediately observed, even by naked-eye, while the compound **2** probes were examined with a fluorescence microscope.

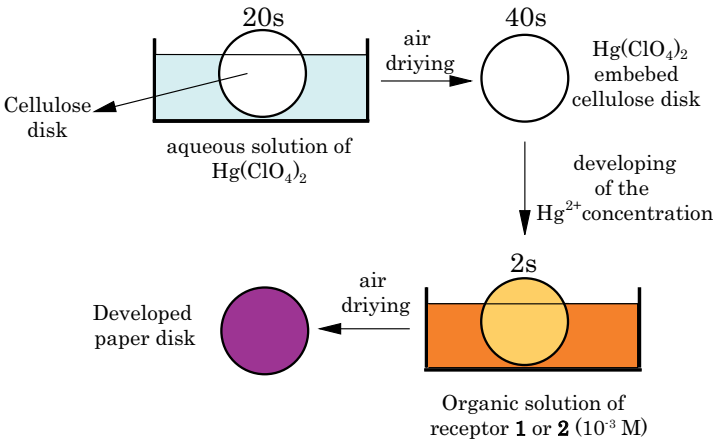

Figure 6.10: Scheme of the preparation of the colorimetric or fluorescent sensing probes via the "developing technique".

Pure aqueous solutions of $Hg(ClO_4)_2$ were also used for the initial Hg^{2+}impregnation of the paper disks, nevertheless the sensitivity suffered a considerable decrease due to the poor solubility of azines **1** and **2** in the stagnant water remaining on the inside of the cellulose matrix. Furthermore, this fact entails a poor homogeneity of the color change which might also interfere on the final Hg^{2+} quantification measurements. Thus, due to the poor solubility of **1** and **2** in aqueous media the use of both receptors is limited to pure organic or organic/aqueous mixtures, a fact that reduces its application to real samples. It is worth mentioning that the reverse procedure for the impregnation process, consisting firstly in soaking the cellulose with an organic solution of the receptor molecule and then with the mercury ion solutions, entails also a big diminution of the analytical properties of the probe. This may be attributed to a worse interaction of the mercury ions with the receptor **1** coated cellulose. In fact, it has been recently found that the cellulose is,

[‖]Cellulose stripes should be carefully introduced and removed from the ligand solution in order to minimize lixiviation of the analyte.

on average, negatively charged,[111] and thus, the interaction between the mercury cations and the cellulose surface is driven by very strong electroatractive forces that may be seriously affected once the cellulose fibers are coated with the neutral receptor molecules.

6.2.2.2 Quantification of the Hg^{2+} sensing properties of the colorimetric probes using 1 as receptor

Once the Hg^{2+} impregnated cellulose disks were developed with an organic solution of the receptor **1**, we proceed to compare the results obtained for the treatment of the probes with different $Hg(ClO_4)_2$ concentrations. Figure 6.11 depicts photographs of freshly developed sensing probes treated with different Hg^{2+} solutions. Results clearly show the existence of a color graduation that is proportional to the concentration of $Hg(ClO_4)_2$ present in the solution.

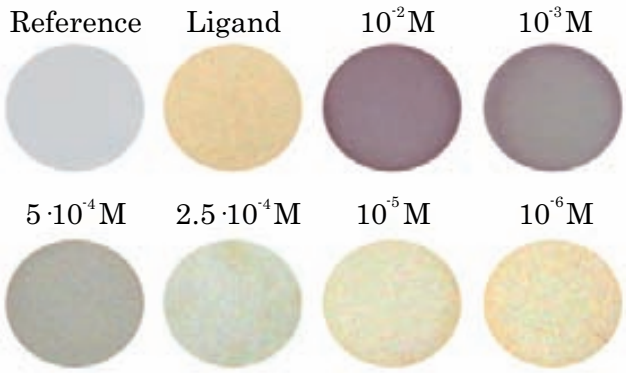

Figure 6.11: "Naked eye" detection of Hg^{2+} ions using freshly prepared colorimetric probes using **1** as receptor.

The spectacular color changes, from orange (neutral azine) to deep purple (complexed azine), suffered by the cellulose indicator paper was persistent with time, being possible to observe the difference after several days. Taking into account that the color of **1**:Hg^{2+} complex in solution is not very persistent, since it disappears after about 20 min, these results clearly demonstrate the higher stability of the complex between **1** and Hg^{2+} in solid state than in solution.
Reproducibility of the results was also measured with 3 sets of samples showing no significant color differences. All these experimental results allow us to conclude that the use of these probes permit the detection of Hg^{2+} ions without the need of any spectroscopical instrument ("naked eye") similarly to the well known pH

paper indicator.

Naked eye detection limit of the freshly prepared probes was determined by visually testing the samples. Thus, a set of 10 people were asked to classify by increasing color the developed stripes. Results were 100% positive on the range from $2.5 \cdot 10^{-4}$ M to 10^{-2} M, while 8 people were able to correctly order the samples if diminishing the lower conentration to 10^{-5} M, setting the detection limit on the hundreds of ppm range. Although the detectable Hg^{2+} concentrations do not match the legal requirements[34,62]* it represents an important probe of concept of the use of this kind of sensing molecular materials for a simple, cheap and selective detection of Hg^{2+} ions.

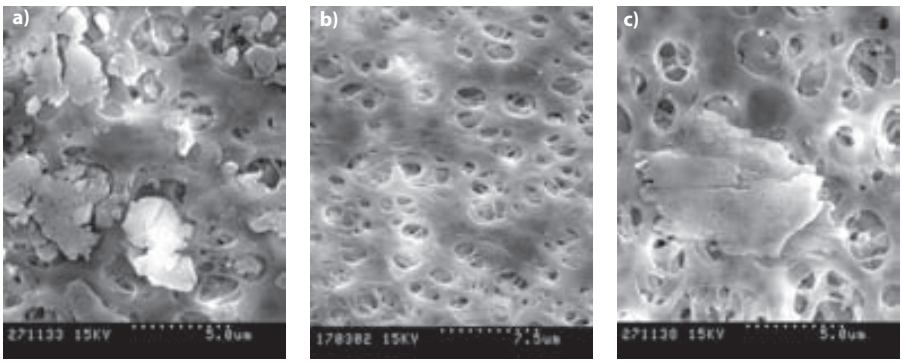

Figure 6.12: Scanning electron microscopy images of: (a) a reference Hg^{2+} free cellulose membrane after development treatment with receptor **1**. It is possible to observe the random deposition of amorphous particles of Hg^{2+} sensing material on the cellulose matrix. (b) a Hg^{2+} impregnated cellulose probe prior to development procedure and (c) a Hg^{2+} impregnated cellulose probe after developing procedure with receptor **1**.

Surface studies of the non developed and the developed chemosensing probes were also carried out (Figure 6.12) using Scanning Electron Microscopy (SEM). Figure 6.12 a shows the SEM image of a Hg^{2+} free cellulose probe after being subject to the developing treatment with receptor **1**. It is possible to observe how the azine ligand **1** is randomly deposited as an amorphous material particles over the cellulose matrix, staining the white cellulose probe with the characteristic orange color of **1**. Figures 6.12 b and c, depict SEM images of Hg^{2+} impregnated cellulose probes prior and after the development with the receptor **1**. The absence of big mercury salt crystals on Figure 6.12 b is indicative of the good dispersion and impregnation of the heavy metal onto the cellulose matrix, while after development

*Legal limits for drinkable water of 1 and 2 ppb are set by the European Union Agency and the EPA, respectively.

treatment (Figure 6.12 c) the same kind of randomly distributed organic amorphous particles, previously shown for the reference probe, were observed, denoting that the recognition procedure takes place only on the surface of the cellulose probe.

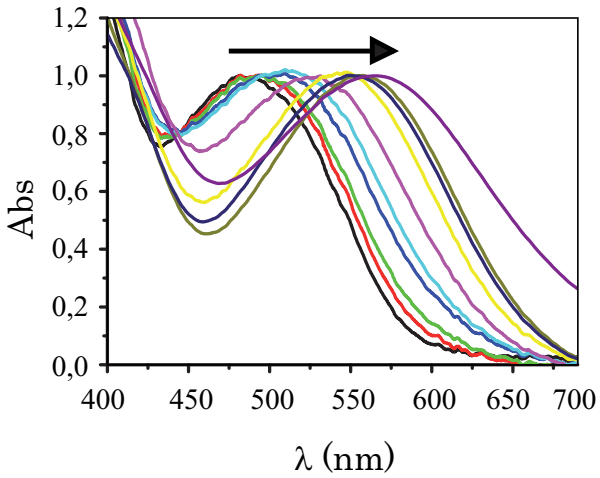

Figure 6.13: Normalized UV-Vis reflectance spectra corresponding to cellulose probes treated with acetonitrile solutions of $Hg(ClO_4)_2$ with concentrations ranging from $7.5 \cdot 10^{-5}M$ to $10^{-2}M$ and after being developed with compound **1**.

In order to perform quantitative detection measurements of the cellulose probes, a spectrophotometric calibration of the Hg^{2+} detection, was made using an UV-Vis spectrophotometer equipped with an integrating sphere expansion pack. This accessory was employed to determine the absorption spectra of the solid substrates by the reflectance of the light allowing to perform UV-Vis spectra of non transparent samples. An untreated cellulose paper was set as reference sample during the measurements.

Normalized UV-Vis spectra of the freshly developed probes (Figure 6.13) show a neat interconversion between the uncomplexed ($\lambda_{max} = 485nm$) and the Hg^{2+} complexed species ($\lambda_{max} = 565nm$) of **1**. The increase in concentration of Hg^{2+} of the tested solutions entailed an enhancement of the presence of **1**:Hg^{2+} complex, and therefore its absorption band, producing the apparent shift of the absorption λ_{max} of the system from 485 nm to higher wavelengths.

As for regular UV-Vis spectroscopy, it is possible to use the change of intensity of the measured bands in order to quantify the amount of chromophore present in

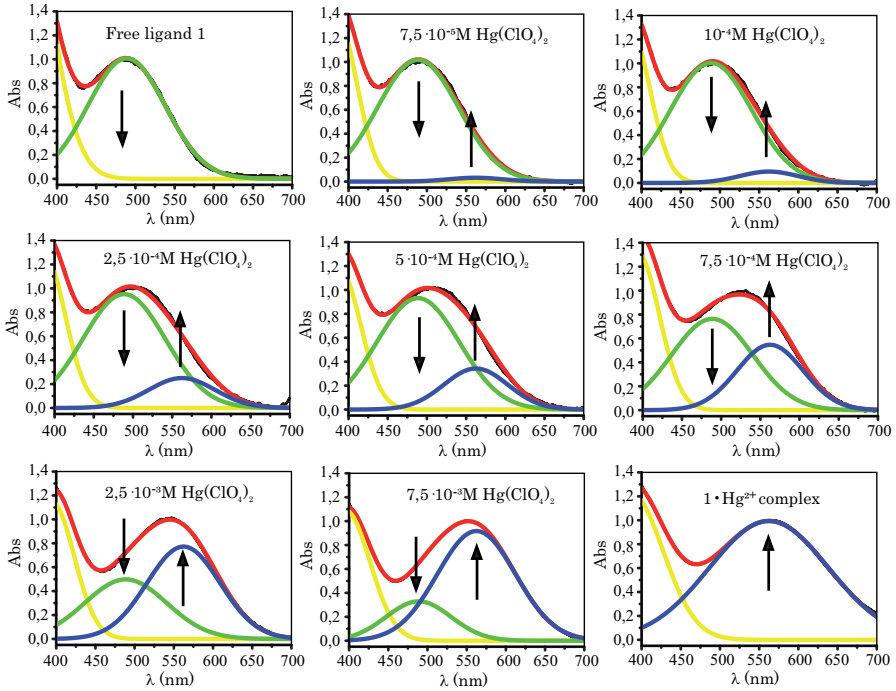

Figure 6.14: Two Gaussian deconvolution of the normalized UV-Vis spectra of freshly developed probes obtained using an integrating sphere accessory. The two component deconvolution was performed using as fix wavelengths for the λ_{max} bands corresponding to the Hg^{2+} free and the totally complexed (**1**:Hg^{2+}) probes at 485 and 565 nm, respectively.

solution. Thus, spectra obtained were mathematically deconvoluted into two different Gaussian bands; one centered at 485 nm that corresponds to the absorption maximum for the free ligand **1** and another band corresponding to the mercury complex **1**:Hg^{2+} , centered at 565 nm. Figure 6.14 depicts the mathematical treatment for all the experiments done. With this treatment the decreasing of the free ligand band and the simultaneous increasing of the **1**:Hg^{2+} complex band upon increasing amounts of mercury ions is observed.

The calibration of the probes was carried out by following the change on the ratio of absorbances at two different wavelengths (Abs_{565nm}/Abs_{485nm}) at different mercury concentrations. This protocol allows us to calibrate the cellulose-based optical indicator with a high reproducibility, as it is shown in Figure 6.15. The detection limit of the mercury indicator papers is calculated by the interpolation from the

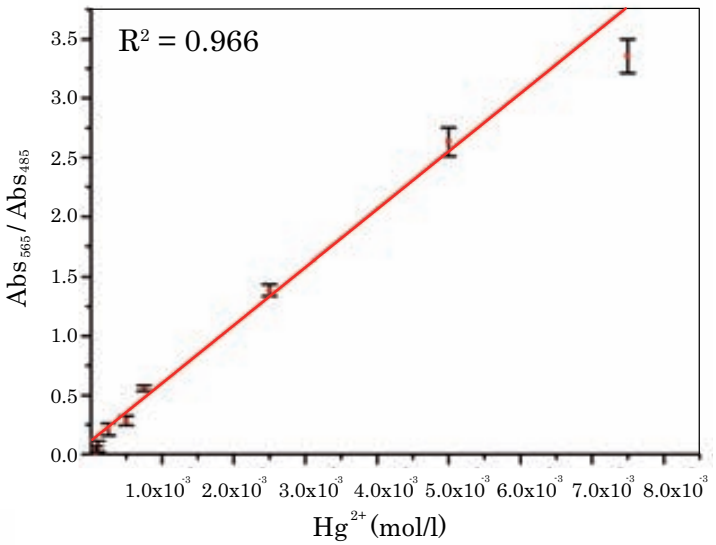

Figure 6.15: Calibration line of the response of the receptor **1** to Hg^{2+} infused cellulose probes by fitting the absorption ratio data of the two deconvoluted Gaussian bands (Figure 6.14) at the λ_{max} (abs(565nm)/abs(485nm)) vs. the Hg^{2+} concentration. The error bars obtained from the development of three replicas at each concentration are also shown.

graph reaching a concentration limit down to $7.5{\cdot}10^{-5}$, i.e. tens of ppm. Further experiments with other divalent cations, like Mg^{2+}, Ca^{2+}, Ni^{2+}, Zn^{2+}, Cd^{2+}, Pb^{2+}, and Cu^{2+}, in CH_3CN/H_2O were also performed showing a lack of any optical change of the indicator papers in all the cases. This result demonstrates a high selectivity toward mercury ions of the reported cellulose-based optical indicator. In summary, a new selective and sensitive heterogeneous indicator of mercury ions in acetonitrile-water solutions, based on the combined use of a cellulose substrate and a molecule with excellent detecting characteristics, is presented. Depending on the amount of mercury ions in contact with the cellulose indicator paper, a gradual color change is produced, being possible to determine by naked eye its concentration, with a detection limit of tens of ppm. Additionally, and no less important, this protocol takes advantage of surpassing the drawback of the low solubility in water of most of the reported Hg^{2+} chemosensors, allowing them to be used for detecting Hg^{2+} cations in water containing solutions.

6.2.2.3 Quantification of the Hg^{2+} sensing properties of the fluorescent probes using 2 as receptor

Employing the same approach as for compound **1** cellulose probes, freshly prepared Hg^{2+} impregnated cellulose disks were developed by immersion on a solution of the receptor **2** in toluene (10^{-3} M). Once dried, we proceed to compare the results obtained for different $Hg(ClO_4)_2$ concentrations. On this first approach only four $Hg(ClO_4)_2$ solutions, ranging from 10^{-6} to 10^{-3} M, were employed in order to obtain a first screening of the probe sensitivity range. Due to the fluorescent nature of the analytical response generated by receptor **2**, the use of a luminescent stereomicroscope equipped with a CCD camera was required in order to perform a quantitative determination of the presence of Hg^{2+}. Once under the microscope, the samples were irradiated at $\lambda = 360$ nm and the fluorescent emission detected at $\lambda \geq 420$ nm by the use of a cut-off filter. This method allows us to minimize the light contamination coming from the source and reflected in the sample. Several images were taken from different areas of each sample, from which an averaged intensity of fluorescence and the homogeneity index were determined by using the *Methamorph 7.5* software.

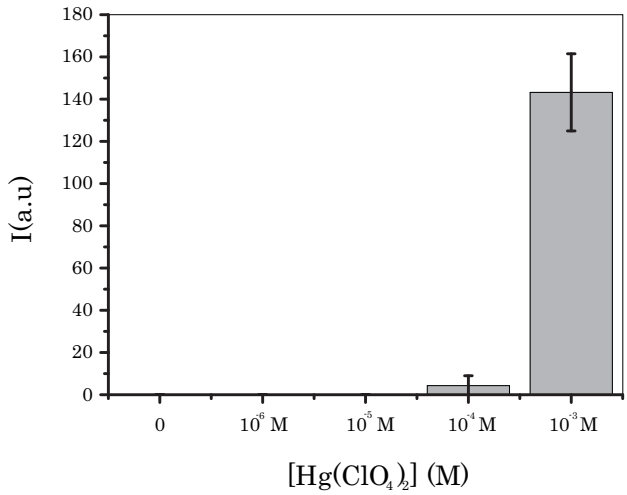

Figure 6.16: Fluorescent response of the compound **2** infused cellulose probes after being treated with increasing amounts of $Hg(ClO_4)_2$.

Results obtained show the presence of luminescence changes by augmenting the

concentration of Hg^{2+} in the solution. However, the concentration of Hg^{2+} ions required to detect this change is extremely high, between 10^{-4}-10^{-3} M (Figure 6.16), far away from the ones obtained for the colorimetric compound **1** infused cellulose probe (tens of ppm) and very much higher than the Hg^{2+} limit imposed by the European Union Agency[62] for drinkable water. Therefore, we decided not to continue with this approach for the probe based on receptor **2**.

6.2.2.4 Conclusions

The developing of Hg^{2+} infused cellulose probes based on the use of organic receptors **1** and **2** as Hg^{2+} developing agents represents a proof of concept to the use of simple molecular receptors for the obtaining of more complex systems to be applied on the detection of different analytes of interest, such as Hg^{2+}. In this case, a colorimetric probe, based on receptor **1**, has allowed us to detect the presence of tens of ppm of Hg^{2+} ions in aqueous mixtures. Being, probably, the appearance of inhomogeneity and receptor lixiviation problems during the developing stage are the main cause of its low detection limit. Despite all these problems, the use of the developing technique has proved to be an extremely simple and cheap technique for the production of cellulose based Hg^{2+} ions chemosensing probes.†

6.2.3 Cellulose nanocomposite membranes as highly efficient chemical probes for Hg^{2+} detection

The sensitivity and reproducibility of a chemosensor probe does not only depend on the intrinsic analytical properties of the receptor molecule but also, to a great extent, from a big number of parameters such as the amount of receptor anchored to the solid substrate, the homogeneity of the resulting surface and the effective contact area between the ligand and analyte, among others. Therefore, in order to improve the analytical quality of the recognition (sensitivity, time of reaction, reproducibility, etc) several other factors, like the obtaining of homogeneous indicator layers or the maximization of the surface contact ratio between the receptor and the analyte, should be taken into account. Consequently, a key issue for developing an heterogeneous mercury detector with azines **1** and **2** is to achieve a

†Some of the obtained results with the chemosensing probes of azines **1** and **2**, prepared by "developing technique", have been published in *Sensors*, *7*, 3481, **2007**.

firm and uniform coating of this signaling molecules onto an appropriate membrane with a large surface area; that is, the processing of receptors **1** and **2** on a substrate.

As reported on the previous section, the use of the developing technique process entails a set of serious intrinsic disadvantages that make it inappropriate for the developing of reliable and highly sensitive cellulose-based chemosensing probes. For this reason, the use of a substitute technique is required. Although, several processing alternatives can be found on the literature[13] most of of them depend on the use of auxiliary additives or complicated deposition procedures. Furthermore, the number of those suitable to be applied to cellulose substrates is even more reduced. For this reason, and taking into account the solubility properties of both azines **1** and **2** and the cellulose itself it was thought that a good alternative for the generation of an appropriate sensing layer on a cellulose support, could be the filtration of micro- or nanoparticles of the receptor molecules through a network of cellulose fibers, where, by the action of unspecific interactions will remain attached. This methodology presents *a priori* several advantages respect the developing technique previously employed, as it will allow to reach a higher homogeneity of the sensing layer, and a better anchoring of the receptor on the probe surface. Moreover, the reduction of the size of the particles, together with the inherent roughness of the cellulose matrices could also suppose an increase of the sensing surface area of the probe.

The obtaining of particulated organic molecules has been traditionally performed by means of mechanical techniques, such as grinding, milling, jet-milling, etc. However, these procedures are in principle unsuitable for the production of nanodisperse systems, since with the decreasing in particle size it becomes increasingly difficult to use mechanical energy for milling without procuring agglomeration or even decomposition of the sample.

Many trials have been done to obtain smaller nanoparticles without the need of such energetic procedures and several effective ways have been developed.[112–114] One of the most promising ones is the methodology developed by *Nakanishi* and co-workers, known as the *reprecipitation method*.[115] The reprecipitation method makes use of the null water solubility of most of the organic molecules in order to produce a fast nucleation and precipitation (Figure 6.17). On a first step, the organic compound has to be dissolved in a water miscible organic solvent, then a small volume of this solution is carefully dropped onto water under strong stirring. This stirring will act as dispersion promoter of the organic solvent, that

once in contact with the water will be completely mixed producing the subsequent nucleation and precipitation of all the remaining water insoluble organic matter. Nevertheless, the stirring is not the only important parameter, since other factors such as the organic solvent used or the temperature of both liquids play an important role on the nanoparticle formation. Previous works published, have already shown the feasibility of this method on the developing of nanoparticles of optical active organic compounds.[110,116,117]

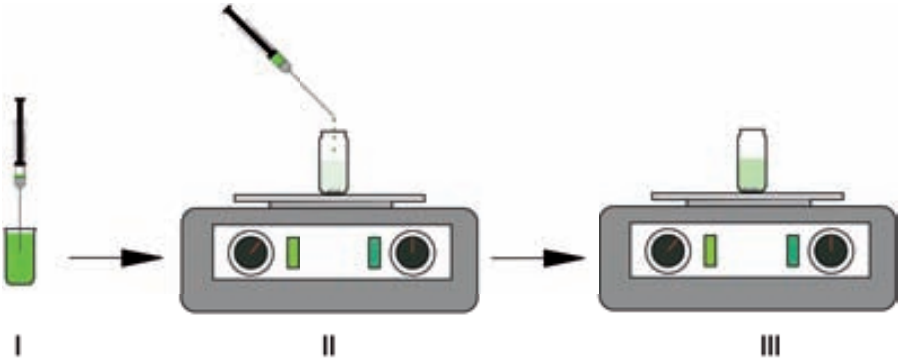

Figure 6.17: *Reprecipitation method* scheme; I) Solution of the water insoluble organic compound in a water miscible organic solvent; II) Dropwise addition of the determined volume of organic compound solution onto strongly stirred water; III) Dispersion of the miscible organic solvent in the water reservoir producing the subsequent precipitation of the nanoparticles of the water insoluble organic compound.

In order to control the uniformity and loading of the receptor on membranes like the cellulose ones, the use of nanoparticles with average diameters similar to those of the cellulose membrane pores is critical. The main reason for that is that particles with such characteristics might allow a deeper penetration of the indicator into the membrane, avoiding, at the same time, the clogging of the membrane pores. Consequently, the first goal was to find the experimental conditions to obtain particles of azines **1** and **2** with circa about 100 nm average diameters that fits with the mean pores of commercially available cellulose membranes (Advantech θ = 47 mm).

6.2.3.1 Preparation and characterization of nanoparticles of receptors 1 and 2

Nanoparticles of azines **1** and **2** were obtained following the general scheme represented on Figure 6.17. 100 μl of 10^{-3} M organic solution of the azine were dropped from a height of 10 cm to a vigorously stirred vial full (30 ml) of ultrapure water. As the average size and the size distribution of the resulting organic nanoparticles are extremely dependent of external factors such as the water stirring, temperature or the organic solvent employed, among others, precipitation experiments were developed using a set of different experimental temperatures (278 and 298 K), stirring conditions (mechanical and ultrasounds), and solvents (N-methylpyrrolidine,NMP, tetrahydrofurane,THF, or acetonitrile, ACN), in order to optimize the nanoparticle production and to be able to directly use the obtained nanosuspensions without any further treatment. Results obtained for compound **1** and **2** are depicted in Table 6.3.

a) Size and distribution of nanoparticles of receptors 1 and 2. Particle size measurements were performed using the Dynamic Light Scattering technique (DLS). It is worthy to remark that results obtained with this technique represent a statistical average of the particle sizes present in the suspension. Figure 6.18 shows an example of the size distributions obtained for receptors **1** and **2** nanoparticles obtained from THF and NMP solutions, respectively, at 298 K and under mechanical stirring. In both cases well defined narrow monomodal distributions were observed.

DLS results obtained for compound **1** nanoparticles, using NMP or THF as organic solvents and two different operating temperatures (273 and 298 K) and stirring conditions (mechanical and ultrasounds), yielded particle sizes fluctuating between 100 and 400 nm with polidispersity values typical of monodisperse size distributions (≤ 0.4). This situation was different for acetonitrile solutions where not only particle sizes, but also polidispersity values, were higher (100-720 nm and ≥ 0.4) indicating the presence of more than one particle size distribution. In the case of azine **2**, particle size values obtained in all the conditions tested (Table 6.3) range from 80 to 250 nm with narrow dispersity distributions (according to polidispersity values ≤ 0.4). Even though size differences between the different experimental settings are not substantially big, some trends can be identified. Thus, it is possible to observe how samples performed using cooled water (273

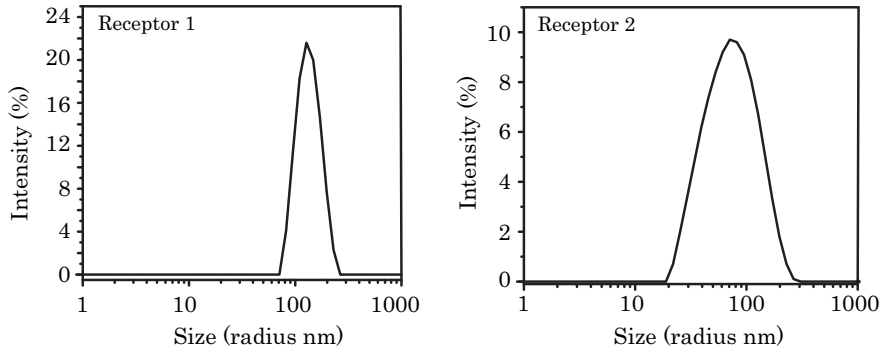

Figure 6.18: DLS size distributions nanoparticle suspensions of receptors **1** and **2** obtained from THF and NMP solutions, respectively, at 298 K and under mechanical stirring.

K) generally present a lower particle size than those obtained at room temperature. This can be easily explained as by reducing the temperature the speed of the precipitation process is increased producing a faster nucleation that reduces the particle size. This effect can also be observed by changing the organic solvent from the initial receptor solution. Therefore, for compound **1** the most appropriate particle sizes are obtained using THF solutions, while for compound **2** NMP gives better results. To check the influence of the mixing method on the final size of nanoparticles of compounds **1** and **2**, sonicated and mechanically stirred systems were tested. As it is shown in Table 6.3, the particle sizes obtained with sonication are much larger than those achieved with mechanical stirring. Accordingly, the latter procedure turns out to be much more efficient for mixing the two solutions, leading thereby to a faster nucleation and precipitation process.
Thus, it is possible to conclude that the best particle sizes and size distributions were obtain using azine solutions dissolved on THF and NMP, in the case of **1** and **2** respectively, with low temperature (273 K) and mechanical stirrings of the water.

b) Stability of the nanoparticle suspensions. Once the suspension is obtained, it is really important that the nanoparticles remain unaggregated in the dispersion media until its deposition over the selected substrate. Thus, the obtaining of sufficiently stable nanoparticle suspensions represents one of the key factors of their production protocol. In order to study the aggregation tendency of azine **1** and **2** particles, Z-potential values of the freshly prepared suspensions

Table 6.3: Experimental conditions and particle characteristics of azines **1** and **2** obtained by the reprecipitation method.

Comp.	Solvent [a]	Mixing conditions		Temp. (K)	Particle diameter (nm) [b]			Polydispersity index Pdl[d]
		Stirring	Ultrasounds		10%	50% [c]	90%	
1	NMP	Yes	No	298	220	396	712	0,376
1	THF	Yes	No	298	190	255	396	0,178
1	ACN	Yes	No	298	255	295	396	0,813
1	NMP	Yes	No	273	91	171	342	0,257
1	THF	Yes	No	273	91	249	825	0,141
1	ACN	Yes	No	273	150	248	423	0,754
1	NMP	No	Yes	298	220	342	615	0,138
1	THF	No	Yes	298	141	220	342	0,143
1	ACN	No	Yes	298	267	325	711	0,652
1	NMP	No	Yes	273	164	255	396	0,162
1	THF	No	Yes	273	105	190	458	0,110
1	ACN	No	Yes	273	234	323	532	0,545
2	NMP	Yes	No	298	91	171	342	0,376
2	THF	Yes	No	298	91	249	825	0,325
2	NMP	Yes	No	278	44	78	164	0,318
2	THF	Yes	No	273	68	111	190	0,422
2	NMP	No	Yes	298	91	222	295	0,352
2	THF	No	Yes	298	142	267	342	0,358
2	NMP	No	Yes	273	68	106	164	0,332
2	THF	No	Yes	273	68	136	255	0,213

[a] NMP, N-methylpyrrolidine; THF, Tetrahydrofurane; ACN, Acetonitrile; [b] Volumetric particle sizes measured by dynamic light scattering (DLS) and presented according to the 10, 50 and 90% of the total volume; [c] Values corresponding to the volumetric size distribution average; [d] Polydispersity index of the sample, that gives an idea about the size distribution; the smaller the value the more monodisperse the sample will be.

were measured by DLS technique.

Table 6.4: Indicative relationship of the stability of the nanoparticle suspensions with the Z-potential values.

Z-potential (mV)	**Stability behavior of the suspensions**
from 0 to ±5	Rapid coagulation or flocculation
from ±10 to ±30	Incipient instability
from ±30 to ±40	Moderate stability
from ±40 to ±60	Good stability
≥±60	Excellent stability

From a theoretical point of the view, the Z-potential is the potential difference between the dispersion medium and the stationary layer of fluid attached to the dispersed particle, and provides an indication of the degree of repulsion between adjacent particles in the dispersion. When the potential is low, attraction exceeds repulsion and the dispersion will break and flocculate. So, colloids with high zeta potential (negative or positive) are electrically stabilized, while colloids with low zeta potentials tend to coagulate or flocculate as outlined in Table 6.4.

Table 6.5: Z-Potential of the azine **1** and **2** nanoparticle suspensions obtained by the reprecipitation method.

Compound	**Solvent [a]**	**Temp (K)**	**Stirring**	**Z-potential (mV) [b]**
1	NMP	298	Yes	+31
1	THF	298	Yes	+36
1	ACN	298	Yes	+34
2	THF	298	Yes	-20
2	NMP	298	Yes	-19

[a] NMP, N-methylpyrrolidine; THF, Tetrahydrofurane; ACN, Acetonitrile; [b] Z-potential of the measured suspensions.

From a practical point of view, when the Z-potential value of a suspension is

higher, in absolute value, than 30 mV it is possible to say that this suspension is stable in time as the electrical charges present on the particle surface make them repeal each other. On the other hand, if the Z-potential does not exceed this value the particles will tend to aggregate and finally flocculate with time. Results obtained for both azine nanoparticles (Table 6.5) denote the formation of stable suspensions in the case of the **1**, while for compound **2** a certain long term instability was observed (Z-potential values lower than ±30 mV). Furthermore, no significant differences between the distinct solvents were found.

c) Morphological characterization of the azine nanoparticles. Apart from size, particle morphology might also play an important role on the total accessible surface area of the sensing layer. Therefore, scanning electron micrographs, of the azine **1** and **2** nanoparticles (obtained from 10^{-3} M solutions in THF and NMP, respectively, at 273 K and under mechanical stirring), were performed.

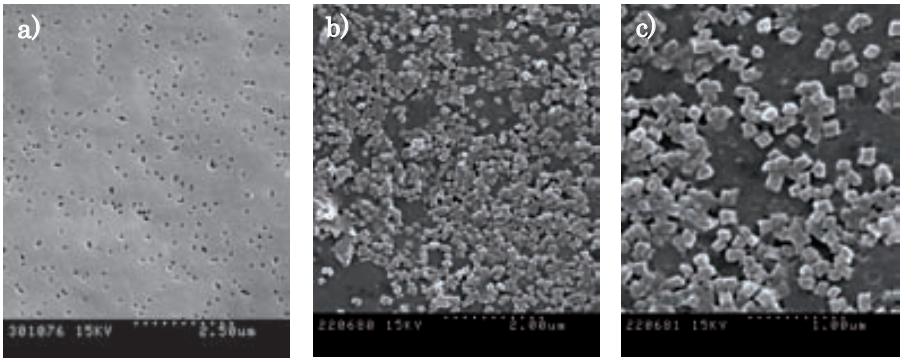

Figure 6.19: Scanning electron microscopy images of a) polycarbonate control membrane with 100 nm pore size, b) and c) nanoparticles of azine **1** deposited on the polycarbonate membrane, after filtration of 20 ml of freshly prepared nanoparticle suspension.

Figure 6.19 shows images of the resulting nanoparticles obtained after the filtration of 20 ml of freshly prepared nanoparticle suspension of **1** through a polycarbonate membrane (Advantec θ = 47 mm) with pore size of 100 nm.[‡] It is possible to observe that the nanoparticles formed present an homogeneous and very defined cube like geometrical shape with sizes of 100-300 nm, in agreement with the results obtained by DLS. Moreover, no signs of particle aggregation are shown, corroborating, as well, the data achieved from Z-potential measurements.

[‡]Once completely dried, the substrates with the deposited nanoparticles were metalized with a thin layer of gold, in order to make them conductive to avoid charge of the sample during the SEM imaging.

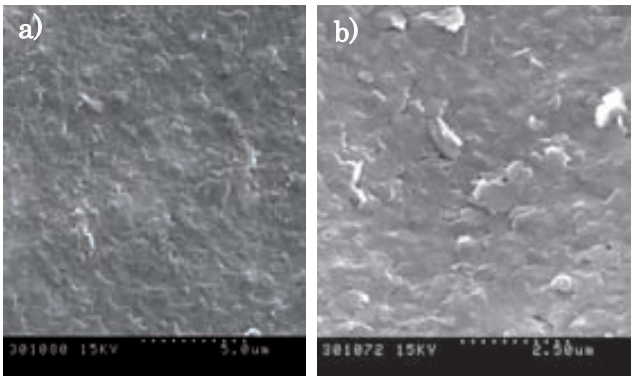

Figure 6.20: Scanning electron microscopy images of azine **2** nanoparticles deposited onto a polycarbonate membrane, after filtration of 20 ml of freshly prepared nanoparticle suspension.

Just like in the afore mentioned case, nanoparticles of azine **2** were deposited on a polycarbonate substrate by filtrating a freshly prepared nanoparticle suspension through a filtration membrane (Advantec θ = 47 mm and 0.1μm of pore size). Morphological data obtained show a different situation with respect to the one previously observed for receptor **1** nanoparticles. Despite the initial well defined characteristics of nanoparticle suspension of compound **2**, observed by DLS, Figure 6.20 discloses the appearance of an homogeneous layer of organic compound that covers the whole membrane surface and makes unfeasible to perform any particle size estimation. Nevertheless, a closer study of the obtained SEM micrographs allow us to distinguish the existence of highly aggregated small plates over the polycarbonate surface. This result is in agreement with the low Z-potential values observed for the compound **2** nanoparticle suspension that did show certain tendency of these nanoparticles to aggregate and that would explain the formation of the organic layer over the polycarbonate surface.

Although formed from the same basic azine core structure (1,4-disubstituted-1,3-butadiene), nanoparticles of receptors **1** and **2**, present completely diverse features, either in morphology, size and stability. In order to study whether these differences can be due to the presence of pyrene on the chemical structure of **2**, a 10^{-3} M solution of pyrene in THF was processed by the reprecipitation method, and the obtained nanoparticle suspension was characterized as proceed for compounds **1** and **2**. Size distribution and Z-potential values obtained by DLS showed values of 150 nm and -10 mV respectively, while SEM images (Figure 6.21) of the pyrene nanoparticles on the polycarbonate membrane presented the same aspect as the

Figure 6.21: Scanning electron microscopy images of pyrene nanoparticle on a coated polycarbonate membrane, after filtration of 10 ml of freshly prepared nanoparticle suspension.

azine **2**. Thence, it is possible to conclude that the presence of the pyrenil group plays a key role on the obtention of this kind of plaquette-like nanoparticles; possibly due to the strong π-π interactions that are characteristic of this family of compounds.

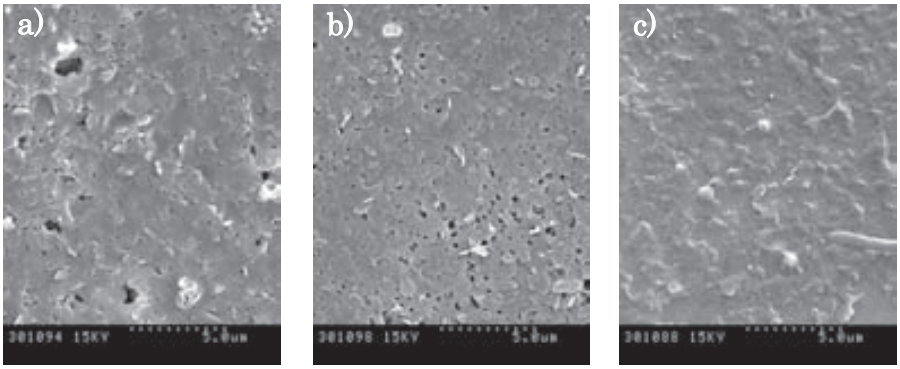

Figure 6.22: Scanning electron microscopy images of a) Nylon, b) polyethylene and c) polyethersulphone membranes after filtration of azine **2** nanoparticle suspensions.

Nevertheless, the existence of specific interactions between the pyrenil moiety and the polycarbonate of the membrane might also be another plausible factor that determine the final obtention of this type of coating. Thus, with the objective of confirming if the nature of the substrate had any influence on the nanoparticle deposition of compound **2**, these suspensions were filtered trough membranes of very

different nature such as, Nylon, polyethersulphone and polyethylene. However, no differences were observed as it is shown in Figure 6.22.

6.2.3.2 General preparation method of nanocomposite cellulose membranes based on the receptors 1 and 2

Once establish which were the best conditions for the preparation of the azine nanoparticles, the next step, towards the chemosensing probe development, was their deposition over the cellulose solid substrate. In this case, mixed cellulose ester membranes (Advantec $\theta = 47$ mm) with the same pore size (100 nm) were used. This process was done with a vacuum assisted filtration system (Figure 6.23) in order to optimize homogeneity and preparation time of the probes. Thus, a clean membrane was set between the liquid reservoir and the kitasato and tightly held with a metal clamp. Then the kitasato was connected to vacuum and the nanoparticle suspension poured on the liquid reservoir. The vacuum was regulated to obtain a filtration flux of approx. 35 ml/min. After a few seconds the totality of the suspension was filtered and the membrane was dried under the same vacuum in order to remove the remanent water for 5 minutes. Then, the nanocomposite membrane was ready for use.

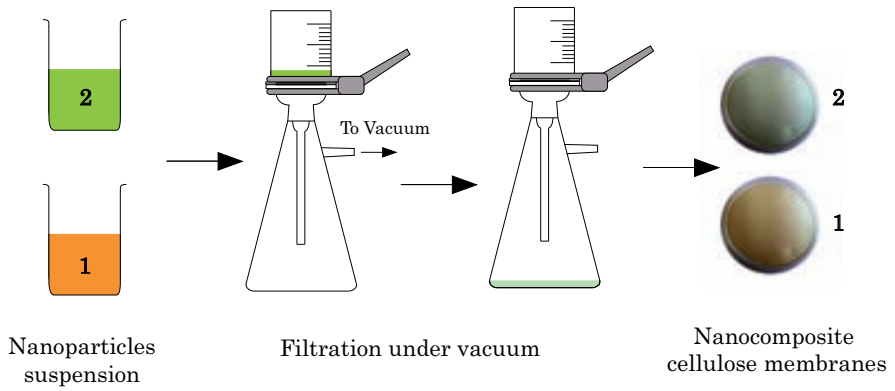

Figure 6.23: Scheme of the filtration process employed for the preparation of the nanocomposite cellulose membranes of receptors **1** and **2**.

Due to their all-terrain nature, chemosensing probes must be resistant to either ambient and operational factors. Therefore mechanical and water resistance of the azine **1** and **2** coatings were tested by 1 week of immersion in water and mechanical friction without observing any lose of material or homogeneity of the coating.

6.2.3.3 Preparation and characterization of nanocomposite cellulose membranes based Hg^{2+} probes of 1

The development of the cellulose based Hg^{2+} probe of **1** was realized using the procedure exposed on the previous section. In this first case, 20 ml of azine **1** nanoparticle suspension were filtered through the membrane. This loading quantity was chosen because of the low sensitivity observed for compound **1** ligand infused developing probes (Section 6.2.2.2). Thus, by incrementing the receptor present in the membrane it was thought that a better result could be achieved.

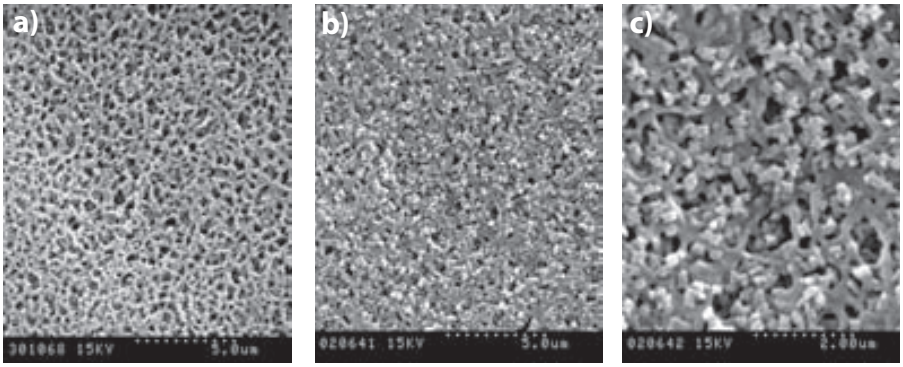

Figure 6.24: Scanning electron microscopy images of a) pristine mixed cellulose ester membrane, b) and c) azine **1** coated mixed cellulose ester membranes, after filtration of 20 ml of freshly prepared nanoparticle suspension, at two magnifications.

SEM images presented on Figure 6.24 depict no difference on the azine **1** particle morphology, with respect to those obtained over the polycarbonate membrane. A closer look into the the disposition of the nanoparticles over the cellulose surface allows us to observe that the outer cellulose fibers are not the only ones coated by particles, but also those present on the inner part of the membrane. This fact is of valuable importance on the developing of a chemosensing probe, as the receptor material must be ideally distributed over the whole cellulose matrix and not only at the surface, maximizing therefore, the contact surface area available.
In order to determine, if the resulting nanocomposite cellulose membrane was still able to detect Hg^{2+} ions, we proceed to filtrate a highly concentrated aqueous solution of $Hg(ClO_4)_2$ (10 ml of a 10^{-3} M solution), as an activity test. Disappointedly, no change of color was observed, indicating the absence of any recognition process. This negative result was assigned to the enormous insolubility of azine **1** in water media, as previously observed on the developing of the ligand infused probes

(described on Section 6.2.2.1) that probably decreases the wettability of the surface avoiding any interaction between nanoparticles and the Hg^{2+} ions. Further tests using mixtures of acetonitrile/water were also performed. However, a strong lixiviation of the indicator were observed, due to the high solubility of this compound in acetonitrile and the enormous active surface area of the nanoparticles. Then, after the evaluation of the above described results it was decided to abandon the obtaining of nanoparticles of azine **1** for the obtaining of this kind of sensing probes.

6.2.3.4 Preparation and characterization of cellulose nanocomposite membranes based Hg^{2+} probes of 2

a) Optimization of the functionalization of the cellulose membrane with azine 2. As in the previous case, mixed cellulose ester membranes (Advantec θ = 47 mm) with an average pore size of 100 nm were chosen for the development of the azine **2** based Hg^{2+} chemosensing probes.

Although the same filtering system was employed, the arrangement of the nanoparticles of **2** over the cellulose surface considerably differs from that previously observed for chemosensor **1**, as observed on Figure 6.25. This phenomena can be explained taking into account the complex network of fibers that forms the cellulose matrix and the tendency of the plaquette-like nanoparticles of **2** to coalescence. Thus, the filtered nanoparticles are retained in the membrane, not only by coalescing between them on the top of the membrane, but also around the cellulose fibers and inside the membrane, Figure 6.25. Consequently, the coating of the external cellulose fibers with the nanoparticles renders a more efficient loading of the membrane, both at the top of its surface and in its interior, without blocking the pores of the membrane.

As the amount of receptor available for recognition directly influences on the intensity of the obtained analytical response, and on the final sensitivity of the probe, a series of experiments, in order to study the maximum quantity of nanoparticles feasible to be deposited over the surface of the membrane without blocking the pores, were performed. Thus, different volumes (5, 10, 20, 25 and 50 ml) of a suspension of nanoparticles of the receptor **2**, prepared as previously described, were filtered through a mixed cellulose ester membrane and the resulting loading of the membranes was determined.

SEM images of the resulting membranes (Figure 6.26) show significant variations

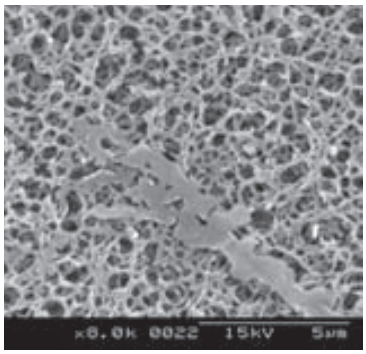

Figure 6.25: Scanning electron microscopy image of a freshly prepared nanocomposite cellulose membrane of compound **2** after filtration of 10 ml of nanoparticle suspension. It is possible to observe the formation of a coating layer by the coalescence of the receptor nanoparticles on the top and inside the cellulose fibers matrix of the membrane.

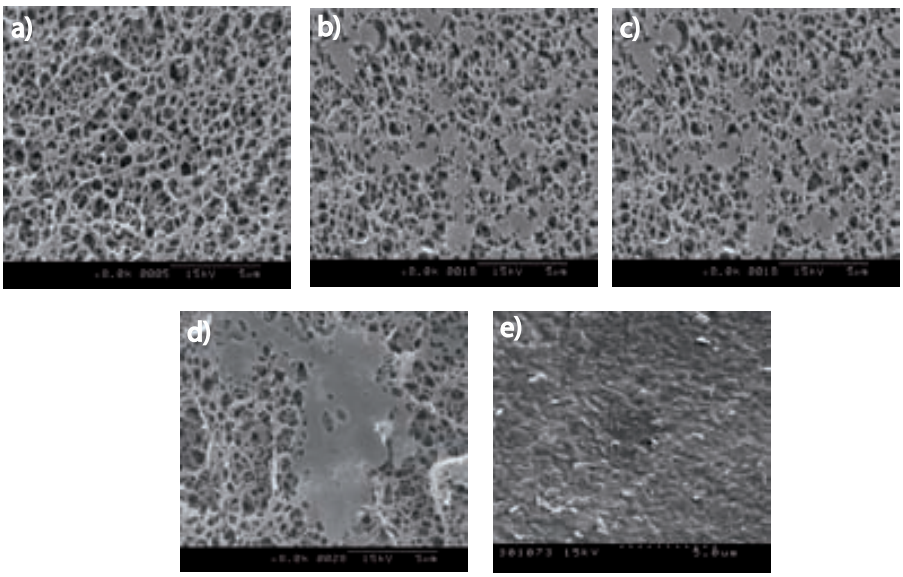

Figure 6.26: Scanning electron microscopy images of azine **2** coated mixed cellulose ester membrane after filtration of a) 5, b) 10, c) 20, d) 25 and e) 50 ml of nanoparticle suspension of **2**.

from an almost non-covered surface (Figure 6.26 a) to a completely closed membrane (Figure 6.26 e), as the quantity of filtered nanoparticles was increased. For obtaining an efficient Hg^{2+} chemosensing probes it is needed to reach a compromise between the receptor loading and the filtration capacity of the membrane, being the optimum situation reached when 25 ml of the nanoparticle suspension were

used.

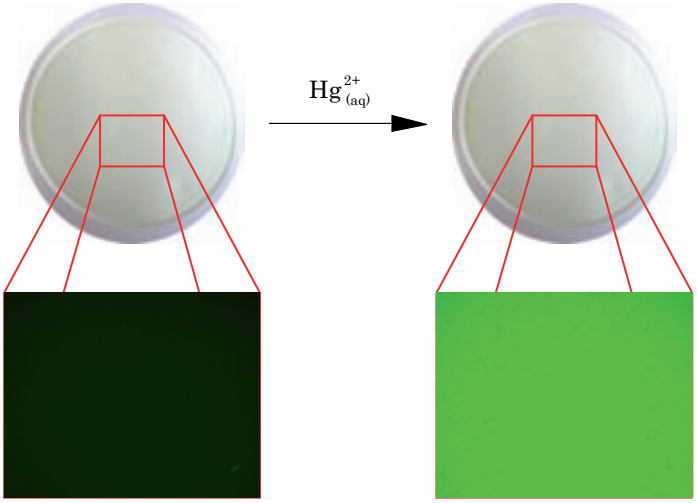

Figure 6.27: Image of a cellulose nanocomposite chemosensing probe before and after treatment with a concentrated 10^{-2} M aqueous solution of $Hg(ClO_4)_2$; Zooming areas show the fluorescent response (after treatment with Metamorph 7.5) of the membranes, revealing an increase of the intensity characteristic of the mercury recognition process.

Once the appropriate receptor loading was established, the next step was to check if the Hg^{2+} recognition activity of azine **2** was not deactivated once deposited on the surface of the membrane. Then, we proceed to filtrate through a freshly prepared coated membrane a highly concentrated aqueous solution of $Hg(ClO_4)_2$ (10 ml of a 10^{-2} M solution). In order to check the Hg^{2+} recognition activity of the functionalized membranes, the luminescence of the sample was controlled using a commercial luminescence stereomicroscope (Leica MLZIII) equipped with an incorporated CCD digital camera (Leica DC 250). Mercury treated and non treated coated membranes were irradiated with light (λ = 360 nm) and the fluorescent emission was detected at wavelengths $\lambda \geq 420$ nm by using a cut-off filter.* Results obtained show a clear increase of the fluorescence after filtration of the concentrated Hg^{2+} solution, indicating that the sensing properties of the organic molecule are unaltered when deposited on the membrane (Figure 6.27.)†

Once it has been proved that azine **2** is not only able to form homogeneous and

*This methodology allow us to minimize the light contamination coming from the source and that reflected by the sample.

†The intensity of luminiscence of the digital images was obtained after appropiate software treatment with the Methamorph 7.5 software (Universal Imaging, 2007).

stable coatings onto the cellulose membrane, but also to retain its Hg^{2+} detecting properties, we proceed to study the distribution of the receptor **2** in the inner part of the cellulose membrane.

An in-depth study of freshly prepared probes was undertaken by imaging a cross section of a freshly prepared membrane using a SEM equipped with an Energy Dispersive X-ray (EDX) detector. This accessory analyzes the x-ray emitted by the sample after being irradiated with the scanning electron beam, the energy of which is characteristic of each chemical element present in the sample, allowing the performance of space resolved elemental analysis of the sample. However, the accuracy of EDX is limited, being much more precise to the heavier elements present.

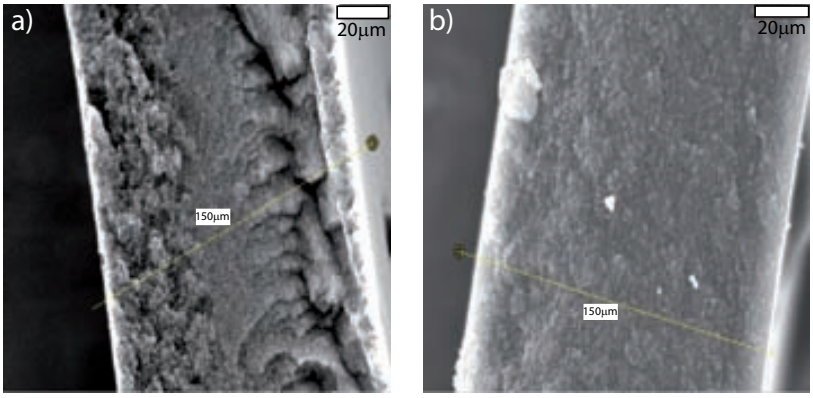

Figure 6.28: Comparison of the scanning electron micrograph of the cross section of two azine **2** Hg^{2+} chemosensing probes, a) cut performed with regular scissors, b) cut performed after previously frozen the cellulose membrane with liquid nitrogen

We performed EDX analysis of azine **2** functionalized membranes before and after filtering 10 ml of a 10^{-2} M aqueous solution of $Hg(ClO_4)_2$. On a first attempt, regular steel scissors were used to perform a transversal dissection of the membrane. However the cutting blades induced squashing on the substrate (as seen on Figure 6.28 a) making difficult the obtaining of a proper EDX analysis. Several other methods such as, cutting blades or scalpels were essayed, but the same problem was detected. Finally, in order to avoid the use of metal blade-like cutting devices, it was decided to freeze the sample using liquid nitrogen and once frozen bend it until fracture. As shown on Figure 6.28 b) a much clearer cut was obtained and EDX analysis of these membranes could be performed.

EDX linear scan performed over the cross-sectional image of the azine **2** coated

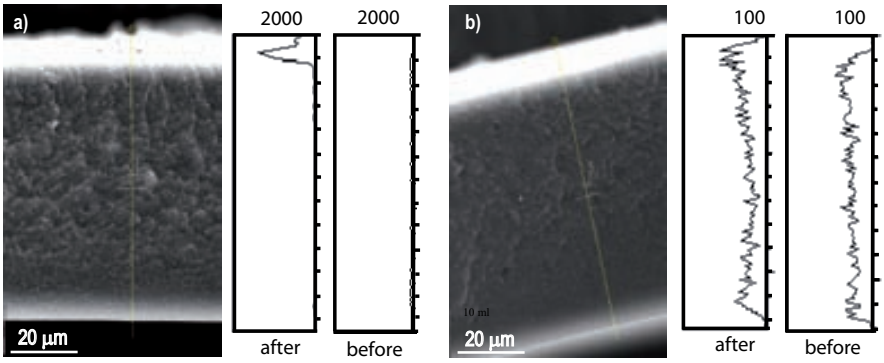

Figure 6.29: SEM images Hg^{2+} EDX analysis of a cross section of: a) coated cellulose membrane with a nanoparticle suspension of **2** after and before filtering 10 ml of 10^{-2} M Hg^{2+} aqueous solution and b) a cellulose membrane dip-coated with an 10^{-3} M organic solution of **2** after and before filtering 10 ml of a 10^{-2} M Hg^{2+} aqueous solution.

membrane after filtering 10 ml of 10^{-2} M Hg^{2+} aqueous solution (Figure 6.29 a) shows the presence of mercury atoms in the first 10 μm of the film, which might correspond to the minimum thickness of the indicator sensing layer. By contrast, the coated membrane before the Hg^{2+} filtration shows no mercury signal. Thus, it is possible to divide the probe structure into two differentiated zones; one remarkably concentrated on the receptor **2**, that corresponds to the area rich in mercury atoms, located at the first 10 μm from the surface and a second one, mainly constituted by cellulose fibers, where no significant mercury signal was observed, indicating the absence of significative quantities of receptor **2**. For comparison purposes, the same experiment was carried out using a cellulose membrane loaded with azine **2** by means of the dip-coating technique (Figure 6.29 b). From the EDX mercury signal intensity (200 times smaller), it is clear that there was a much higher mercury retention, and subsequently recognition, on the top of the membrane prepared by the nanoparticle filtration than in the dip-coated one. Furthermore, the latter membrane showed no preferential mercury accumulation across the section and only a small increase of the mercury signal all over the membrane was observed. Only a slightly more intense Hg^{2+} signal is observed on the top and the bottom of the membrane which can be assigned to dewetting effects.

b) Calibration of the fluorescent response of the Hg^{2+} chemical probes

Once the complexing ability towards Hg^{2+} ions in aqueous media of a mixed cellulose ester membrane coated with **2** was confirmed, the efficiency of these solid-state devices as potential mercury detectors was evaluated. For such a study, 100 ml of aqueous solutions with different concentrations of Hg^{2+} (ranging from $1 \cdot 10^{-8}$ M to 10^{-2} M) were filtered through the coated membranes using a flux of 35 ml/min approx. The interaction of the covering layer of the functionalized membrane with the Hg^{2+} should produce a change in the fluorogenic properties of the detector proportional to the concentration of the mercury salt in each of the aqueous solutions. The luminescence of membranes was measured with a stereomicroscope, using an excitation wavelength of 360 nm and reading the emission at $\lambda \geq 420$ nm (by the use of a cut-off filter). A digital camera was adapted for imaging the luminescence responses coming from the surfaces. Indeed, the resulting total luminescence of the membranes increased upon increasing the concentration of Hg^{2+} present in the analyzed water (Figure 6.30)

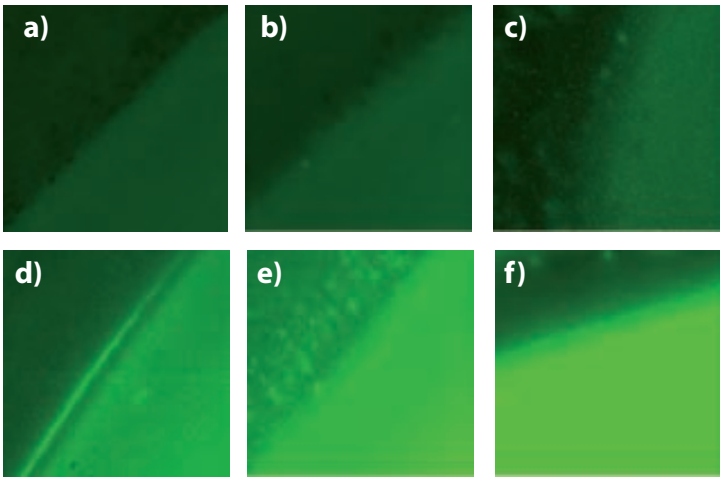

Figure 6.30: Representative optical microscope fluorescence images of the contours of the functionalized sensing membranes after filtration of 100 ml of aqueous solutions with concentrations of: a) 0 M, b) 10^{-6} M, c) 10^{-5} M, d) 10^{-4} M, e) 10^{-3} M, and f) 10^{-2} M of Hg^{2+} .

The total luminescence intensities measured for each assayed concentration were used to calibrate the response of the membranes to Hg^{2+} ions.* Due to limitations

*The intensity of luminescence of the digital images was obtained after appropriate software treatment with the Methamorph 7.5 software (Universal Imaging, 2007).

of the incorporated CCD camera settings, two calibration curves of Hg^{2+} were performed for different concentration ranges (from $2 \cdot 10^{-3}$ M to 10^{-5} M and from 10^{-5} M to 10^{-8} M Figure 6.31). Linearity of the luminescence responses with respect $\log[Hg^{2+}]$ were found for both concentration ranges, although the standard deviations were somewhat larger for the lower concentration range. Remarkable is the detection limit of 2 ppb of Hg^{2+} reached in these quantitative measurements. This amount matches the limit of mercury content of drinking water allowed by the EPA.[34] Even more outstanding is the fact that this lower limit can be decreased considerably by filtering two- or five-fold amounts of mercury solutions reaching limits well below 2 ppb of Hg^{2+} in water.

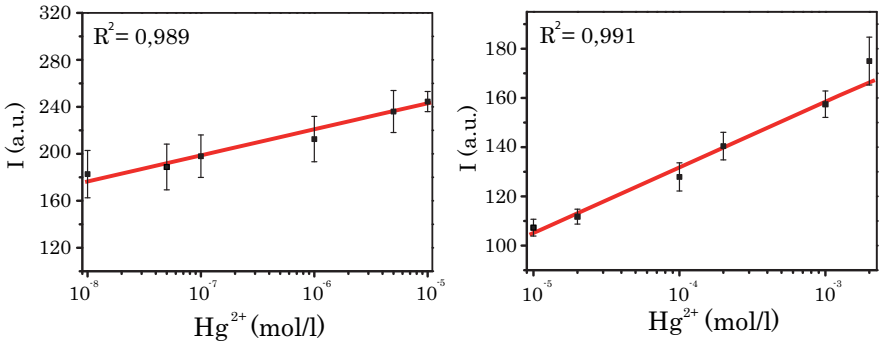

Figure 6.31: Calibration curves of the luminescence responses to Hg^{2+} of the sensing membranes after filtering 100 ml of aqueous $[Hg(ClO_4)_2]$ solutions with concentrations between (a) $1 \cdot 10^{-5}$ M and $1 \cdot 10^{-8}$ M and (b) between $2 \cdot 10^{-3}$ M and $1 \cdot 10^{5}$ M.

Although selectivity studies previously made in CH_3CN/H_2O solutions showed no interaction of the receptor **2** with other environmentally relevant metal ions in water,[87] further experiments were also carried out to confirm the absence of interference of these cations in the response of the cellulose-based detecting probes to Hg^{2+}. For this purpose 10 ml of highly concentrated (10^{-2} M) aqueous solutions of salts of Na(I), K(I), Li(I), Mg(II), Ca(II), Ni(II), Zn(II), Cu(II), Cd(II), Co(II), Pb(II), Al(III), Cr(III) and also a mixture of all of them in ultrapure water, were filtered through the composite membrane. Selectivity studies were also performed with a real tap water sample from the Barcelona's water network. The luminescence intensity measurements of each assay are shown in Figure 6.32. Moreover, the influence of the counteranions present on the Hg^{2+} salts was also tested by filtering 10^{-4} M aqueous solutions of different Hg^{2+} salts with chloride, acetate,

triflate and perchlorate as counteranions without observing any significant differences.

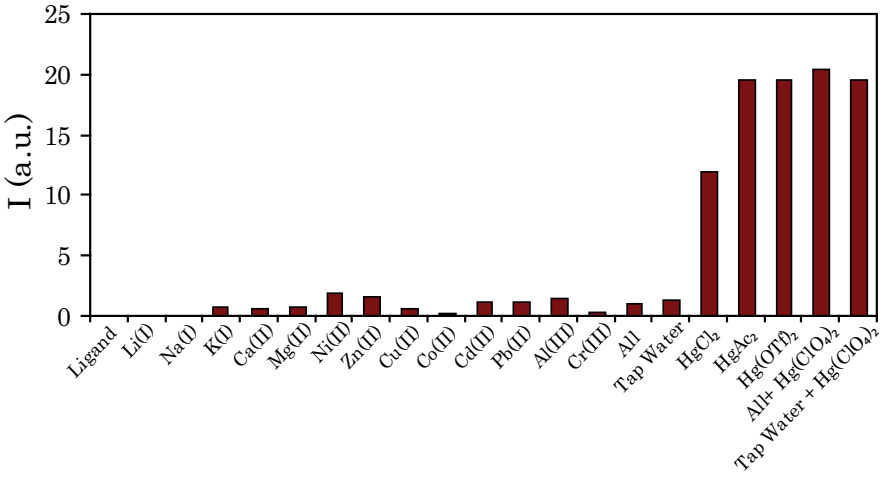

Figure 6.32: Luminescence intensity measurements of the nanocomposite cellulose sensing membranes after filtering 10 ml of 10^{-2} M solutions of Li^+, Na^+, K^+, Ca^{2+}, Mg^{2+}, Ni^{2+}, Zn^{2+}, Cu^{2+}, Pb^{2+}, Cd^{2+}, Co^{2+}, Al^{3+}, Cr^{3+} metallic salts. The influence of the counteranions on the selectivity of the probe was also tested by filtering 10^{-4} M aqueous solutions of different Hg^{2+} salts.

Although the concentrations of all tested mono-, di- and trivalent cations cations were 100 times higher than those of Hg^{2+}, no significant increase of fluorescence signals was detected, proving the high selectivity of the nanocomposite cellulose sensing probe towards Hg^{2+}. Luminescence values obtained for the different Hg^{2+} salts show no substantial changes, observing only a small decrease on the fluorescence intensity for the $HgCl_2$ which can be assigned to its lower solubility.

6.2.3.5 Conclusions

In this section it has been demonstrated that by the use of the "reprecipitation method" it is possible to achieve and modulate the structuring of organic compounds as nanoparticles without damaging its chemical structure. Using this method it has also been possible to obtain nanoparticles of **1** and **2** with sizes ranging from 80 to 400 nm. Furthermore, the possibility of using such nanoparticles for the functionalization of mixed cellulose ester membranes has also been demonstrated. In the case of azine **1**, although promising deposition over the cellulose fibers was observed, the chemical properties of azine **1** in aqueous and

organic media aborted any chance to be applied as nanocomposite material for Hg^{2+} chemosensing. On the contrary the results obtained with azine **2** were fully satisfactory, since it is possible to form an homogeneous and interconnected sensing layer over fibers of the cellulose membrane. The sensitivity and selectivity tests performed for such nanocomposite membrane showed an excellent detection limit of 2 ppb of Hg^{2+} that matches the level allowed by the EPA for drinkable water[34], without any loss of selectivity. This simple, practical, reliable, selective, and sensitive solid-state mercury detecting probe may represent a great advance for the "in-field" detection of contaminated water.*

*Sensing active layer preparation protocol has been object of protection by a patent submission, accepted with number WO2008077985, while some of the obtained results with the nanocomposite chemosensing probes of azines **1** and **2** have been published in *J. Mater. Chem.*, *18*, 1997, **2008**.

*"Everything should be made as **simple** as possible but not **simpler**"*

Albert Einstein

6.2.4 Surface confined SPR Sensor. From receptor design to ultrasensitive Hg^{2+} detection

Although the use of fluorescent methods has allow us to reach Hg^{2+} sensitivities matching the legal concentration limits for drinkable water,[34,62] the use of more elaborated but even more sensitive techniques might permit going to extremely low concentrations opening new fields of applications.

Sensors based on the formation of SAMs[118] obtained either by deposition on the surface of metallic substrates[119] (usually gold) or by covalent linking to metals (gold, silver, copper, etc) or metal oxide surfaces[120] (glass, quartz, ITO, titanium oxide), are attracting a great deal of attention. Indeed, such kind of surface confined sensor devices have recently aroused as a clear alternative to traditional anchoring systems such as by physical entrapment (Figure 6.33).

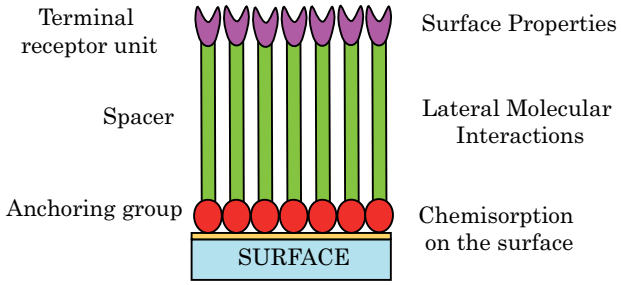

Figure 6.33: General scheme of a self assembled monolayer (SAM) used for surface confined sensor devices.

If we focus our attention to the advantages of surface confined sensor devices, they appear as fast, reliable and highly processable systems,[121] that can be easily and inexpensively manipulated to yield devices that provide independent chemical responses in the presence of target analytes. An additional benefit of the use of monolayers on the developing of sensing devices is the very small quantity of material required to prepare a monolayer increasing their cost efficiency. Furthermore, due to the covalent nature of the bonded receptor they minimize the leaching problems maximizing the durability and re-usability of the device.

However, not all the organic compounds are able to form SAMs, since they require specific chemical functions. In the case of gold substrates, the substituted alkanethiol and dialkylthiols are the two most used, because the stability of their SAMs. There are two main contributions that make the formation of SAMs of

these compounds so stable, the first one is related to the affinity between sulphur and gold[122] (S-Au bond energy is of 45 kcal/mol) and the second one is due to the larger number of lateral interactions between the alkyl chains[123] (van der Waals interactions between CH_2 groups) that pack them very tightly, stabilizing the SAM structure and protecting the arrival of chemical species to the gold surface.

Although extensively applied to chemo- and biosensing by electrochemical methods,[124,125] the number of optical gold based surface confined sensors has risen enormously during the last years.[126–128] Among all the available optical sensing techniques, SPR is one of the most sensitive.[128–130] Highly specific SPR sensors are usually based on the proper modification of a metal surface with a layer containing ligand molecules as recognizing elements.[131–134] Most of the SPR-based sensors available on the market or reported on literature are focused on the recognition and detection of biomolecules, such as proteins,[133,135,136] antigens[135,137] or DNA,[135,138] and only a few have been shown to work with analytes of low molecular weight,[134,139] let-alone those for metals or ions.[140–143]

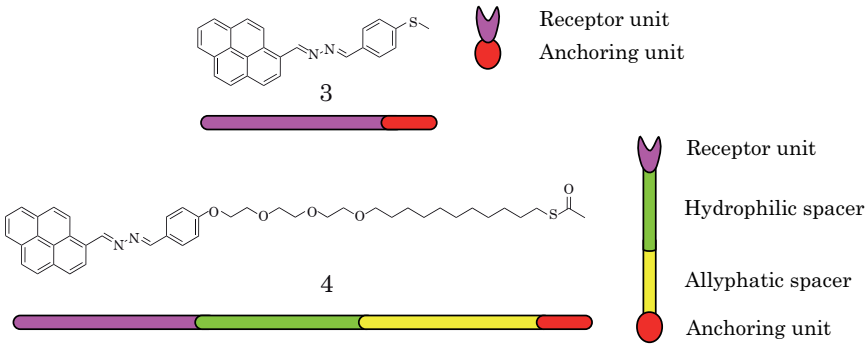

Figure 6.34: Schematic representation of receptors **3** and **4**

In this section we present the comparison of two Hg^{2+} molecular receptors, **3** and **4** (Figure 6.34), as novel ligands for gold surface confined sensing systems. While **3** consists only on a simple modification of the azine **2**, bearing a thioether group, compound **4** presents a more rational design where the 1-(4'-oxyphenyl)-4(1'-pyrenyl)-2,3-diaza-1,3-butadiene receptor unit has been extensively modified with the purpose of increasing its self assembling properties without modifying its sensing characteristics. In order to increase the final wettability and flexibility of the sensor, an additional layer of an hydrophilic spacer based on a triethyleneglycol chain followed by a hydrophobic alkyl linker (used as packing driving force for

the lateral self-assembling) have been attached to the receptor unit core. Finally, the thioacetyl unit has been used to attach the molecule to the gold surface of the sensor chip. This chemical structure was designed to prevent unspecific absorptions,[144,145] increase wetability, and optimize sensitivity and reliability of the sensor by formation of a well-packed SAM.

Monolayers of receptors based on **3** and **4** over gold substrates were obtained by the usual chemical procedures and characterized by a variety of surface characterization techniques, in order to verify either their proper formation and their physico-chemical properties, like the recognition of Hg^{2+} ions. Time resolved SPR spectroscopy was finally used to monitor the ligand-analyte interactions with the organic receptor monolayers .

6.2.4.1 Synthesis of the receptors 3 and 4

Based on the good results previously obtained with azine **2** as Hg^{2+} sensing probe, it was decided to maintain unvaried both its signaling and receptor core unit but to modify its chemical structure in order to be able to employ as receptor for surface confined sensors.

Synthesis of receptor **3** was carried out by *Dr. R. Martínez* from the (Universidad of Murcia) following the scheme represented on Figure 6.35.

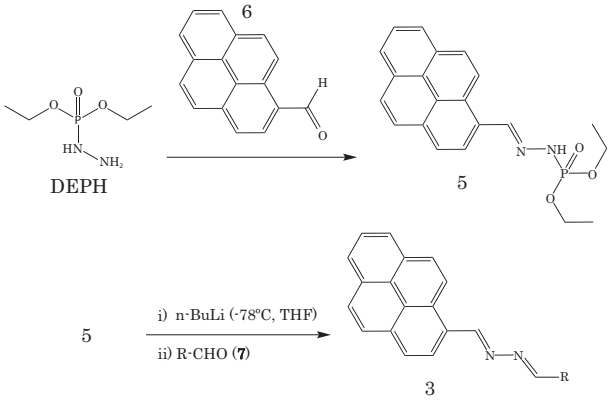

Figure 6.35: Synthetic scheme for compound **3**

This synthetic methodology is based on the Zwierzak's[146] method that uses diethylphosphoroushydrazidate (DEPH) as starting material. The process can be divided into two main stages. Firstly the intermediate **5** is formed by condensation

of the DEPH with 1-pyrenecarboxyaldehyde (**6**) and then through a Wadsworth-Emmons[147,148] reaction the second aldehyde (**7**) is coupled to form **3**. The main advantages of this synthetic approach rely on its simplicity and extreme versatility, since just by changing the chemical nature of aldehyde **7** a large number of receptors bearing different chemical and electrical properties can be obtained. Figure 6.36 represent some of the receptors synthesized by the *Dr. R. Martínez* (Universidad de Murcia) that were employed during the development of this Thesis.

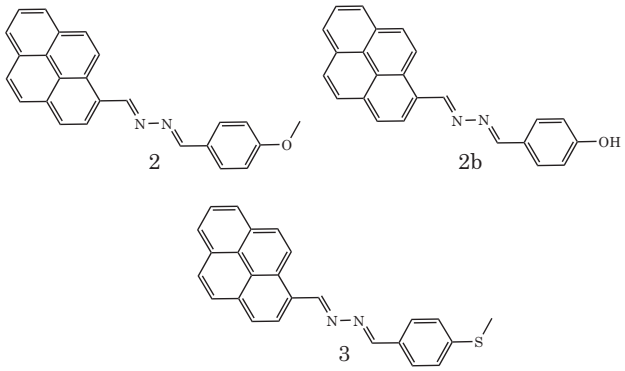

Figure 6.36: Examples of receptors synthesized following the previously described methodology.

An alternative receptor is presented in Figure 6.37. Receptor **4**, although based on the same receptor core as compounds **2** and **3**, has been extensively modified with the objective of maximizing its properties as gold surface confined sensor ligand. Thus, attached to the phenyl unit, in the *para*-position to the diaza bridge, it has a long chain composed by three repeating ethyleneglycol units, that may proportionate hydrophilicity as well as freedom of movement to the receptor core avoiding at the same time the unspecific adsorptions to the sensing layer.[145,149] Attached to the triethyleneglycol unit there is a long alkyl chain of eleven carbon atoms, that will act as lateral packing "assistant" due to formation of several van deer Waals interactions between the -CH_2 units of neighboring molecules. Finally, there is a thioacetyl anchoring unit which assures a correct bonding between the receptor and the gold surface. The synthesis of molecule **4** was carried out following the scheme shown in Figure 6.37.

The reagent 1-(thioacetyl-undec-11-yl)tri(ethylene glycol) (**8**) was prepared following the methodology described on the literature.[149,150]

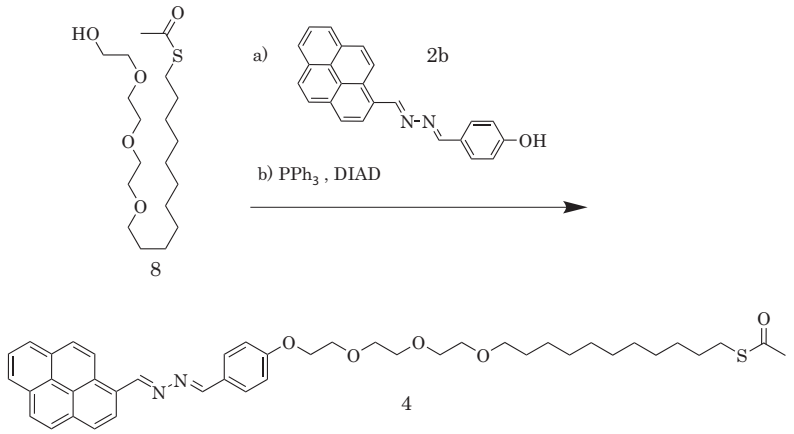

Figure 6.37: Synthetic scheme for compound **4**

6.2.4.2 Preparation and characterization of SAMs of receptors 3 and 4 over gold substrates

The preparation of SAMs **S1** and **S2** based on the receptors **3** and **4**, respectively, was carried out following the same methodology for both compounds.

Firstly, it is important to remark that SAM formation requires a preliminary cleaning process of the glass material used and the gold surfaces, involving washing with various organic solvents (apolar and polar) followed by a short treatment with piranha solution.

S1 and **S2** SAMs were prepared following the procedure depicted on Figure 6.38. On a first step, the freshly cleaned gold substrates were immersed into a 10^{-3} M ethanolic solution of the receptor **3** or **4** at 35°C. This treatment was prolonged for at least 48 hour in order to obtain a good surface coverage. Then, the substrates were removed from the solution and rinsed with copious amounts of clean ethanol, to remove the non bonded remaining molecules, and dried under a flow of N_2.

The freshly produced SAMs were characterized using contact angle (CA), cyclic voltametry (CV) and X-ray photoelectron spectroscopy (XPS), to corroborate either the correct anchoring of the molecule to the surface and the amount and quality of the coverage.

The contact angle technique is based on the determination of the angle at which a liquid/vapor interface meets a solid surface. Thus, a drop of water (aprox. 2-5 μl) is deposited over the functionalized surface, and the resultant angle between the drop and the substrate measured. Contact angle values are specific for any given

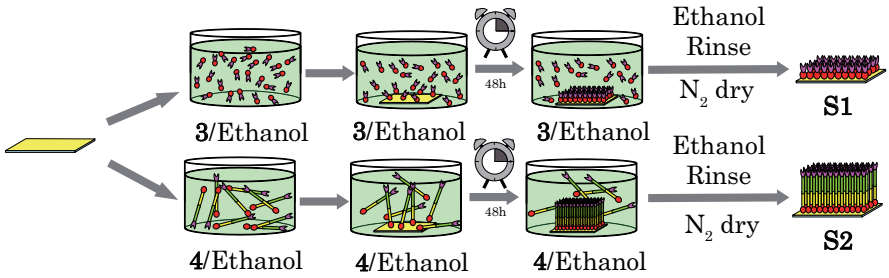

Figure 6.38: Schematic representation of the **S1** and **S2** SAMs formation procedure.

system and proportionate information about the hydrophobicity of the substrate. In both cases the obtained results for the static contact angle were similar to those previously published for pyrene terminated SAMs,[151] with values of $\theta_{st} = 96 \pm 1°$ and $\theta_{st} = 92 \pm 1°$ for **S1** and **S2**, respectively. The advancing (θ_{ad}) and receding (θ_{re}) contact angles of the same samples were also determined observing values of $\theta_{ad} = 96 \pm 3°$ and a $\theta_{re} = 64 \pm 4°$ for **S1**, and $\theta_{ad} = 94 \pm 4°$ and a $\theta_{re} = 76 \pm 2°$ for **S2**. The difference between θ_{ad} and θ_{re} is denominated hysteresis and gives an idea of the order and the packing of the monolayer.[152] For **S1** a pretty high hysteresis value of 32° was observed indicating the existence of remarkable disorder of the monolayer of compound **3**. Furthermore, if compared with the result obtained for compound **4** ($\theta_{hy} = 18°$) it is possible to conclude that the presence of the alkyl units on the organic chain attached to the receptor core of **4** does act as packing "assistant" for the formation of the monolayer, giving place to a better packed monolayer. Thence, the use of contact angle allows us to determine the order and packing degree of our monolayer, however from this measurements it is not possible to know which is the real coverage of the gold substrate.

Further characterization in order to reveal the functionalization and coverage degree of **S1** and **S2** monolayers over the gold substrates was carried out using the CV technique. In this technique the sample is subject to cyclic potential sweeps at the same time that its electrochemical activity is recorded. For the correct functioning of this method the use of an electroactive compound is essential. Taking into account that compounds **3** and **4** are non electroactive, a slight modification of this method involving the presence of a redox-active probe in the solution in contact with the SAMs was required. The use of redox-active probes to characterize the properties of non-conductive SAMs has been extensively used in surface science,[153–155] being the most common one the $Fe(CN)_6^{-3}/Fe(CN)_6^{-4}$ couple. In

our case, as shown in Figure 6.39, instead of using the traditional platinum working electrodes, the bare and SAM modified gold substrates were used as working electrodes, using crocodile clamps to connect them to the potenciostat. The other components of the electrochemical cell, remain unchanged; *i.e.* a Ag/AgCl reference electrode and a platinum counterelectrode were used. Therefore, by making use of the redox response of the active probe present in the modified electrolyte solution (0.1 M solution of KCl and 10^{-3} M in $K_3Fe(CN)_6$) it was possible to study the electron transfer between the bulk solution and the SAM modified electrodes.[155] The reference $Fe(CN)_6^{-3}/Fe(CN)_6^{-4}$ voltammogram corresponding to a fully non covered electrode was obtained using a bare gold slide as working electrode (blue CV observed in Figure 6.40).

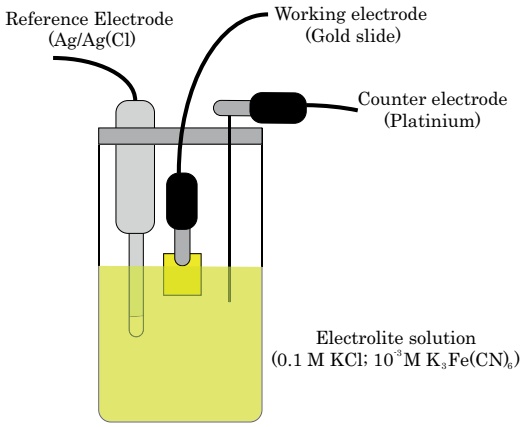

Figure 6.39: General scheme of the electrochemistry experiment designed to determine the receptor coverage percentage in **S1** and **S2** SAMs.

S1 and **S2** modified gold electrodes were measured immediately after the monolayer formation to avoid any contamination. The samples were subjected to 5 potential cycles between 0.0 V and 0.6 V at a scan rate of 100 mV/s. In this case, the reversible peak associated with the ferro/ferri cyanide redox couple is only visible for the clean electrode, being almost completely absent for both thiol functionalized electrodes (Figure 6.40). Thus, it is possible to say that the **S1** and **S2** monolayers act as an insulator, limiting the approach of the redox molecules to the electrode surface and decreasing, therefore, the rate of electron transfer.
A more detailed view of the SAM coating degree can be obtained applying equation 6.3, where B is the substrate coverage, expressed as surface percentage and $i_p^{ox}(SAM)$ and $i_p^{ox}(Au)$ are the oxidative currents of the $Fe(CN)_6^{-3}$ species obtained

for the SAM modified and the bare gold surfaces,[156] respectively.

$$(1 - i_p^{ox}(SAM)/i_p^{ox}(Au)) \cdot 100 = B \tag{6.3}$$

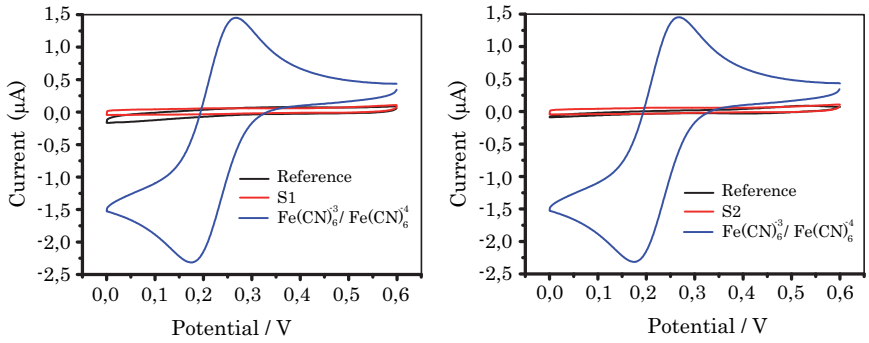

Figure 6.40: Cyclic voltammograms of 10^{-3} M $K_3Fe(CN)_6$ in 0.1 M KCl aqueous solution using functionalized gold electrodes with **S1** and **S2** SAMs, left and right, respectively, as working electrode (bare gold electrodes were used as reference in both cases).

Results obtained with a **S2** monolayer show a slightly higher coverage (97.5%) of the gold surface if compared to those of **S1** (91.5% coverage), in agreement with the contact angle data which is indicative of a better packing for **S2** than for **S1**. XPS was used in order to obtain the elemental composition of the monolayers **S1** and **S2**. Figure 6.41 depicts the high resolution XPS spectra corresponding to the C1s, N1s and S2p of both SAMs. In the C1s spectra of **S1** it is possible to observe a broad peak around 284.8 eV with small shoulders at higher energy values. After fitting the spectra, it is possible to distinguish clearly these three components, where the band situated at 284.8 eV can be assigned to the C-aromatic atoms while the peaks in the 286-289 eV range may correspond to the sum of C-aliphatic, C=N and C-S bonded atoms.[157] **S2** show an almost identical XPS peak pattern, although in this case, the intensity of the peak corresponding to the aliphatic C atoms is increased, in agreement with its chemical structure. The N1s signals appear as a single peak at 399.1 eV, assigned to the N=C bond[158], which is observed either for **S1** and **S2** monolayers. The fitting of the peaks corresponding to the S2p signals proportionates different results for both monolayers. For **S1**, a double peak corresponding to the S2p3/2 and the S2p1/2 electrons of the thioeter moitety, with bonding energies of 161.3 and 163.1 eV respectively, and a

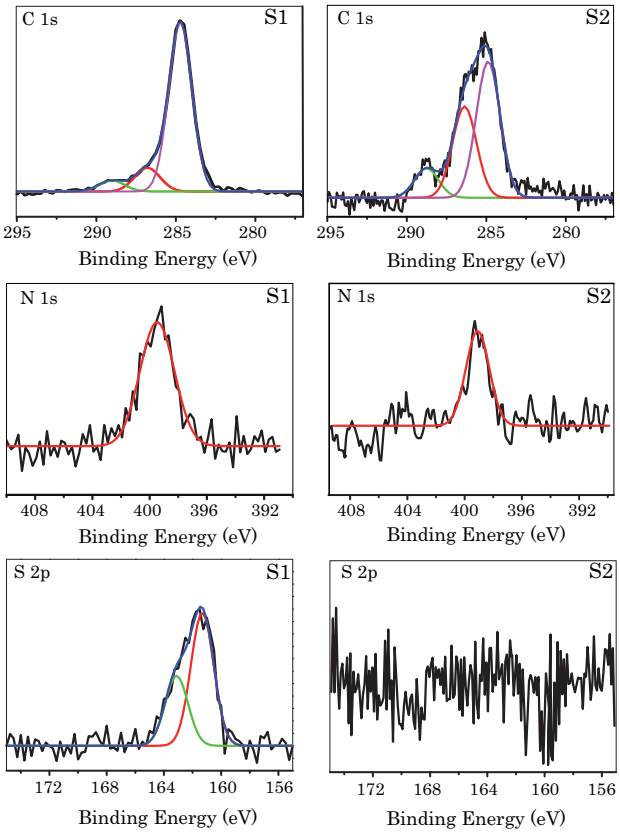

Figure 6.41: XPS spectra of freshly prepared **S1** and **S2** monolayers over a gold slide corresponding to the C1s, N1s and S2p peaks.

intensity ratio of 2:1, were observed.[157] By contrast, no signal was observed in this region for the case of **S2**. The absence of S2p signal for **S2** may be assigned to the experimental XPS settings used, since depending on the incident angle of the x-ray, the penetration of the radiation inside the monolayer is different. Therefore, due to the larger length of the molecule **4** it is possible that the S atom of the thioacetyl group remains undetected by XPS. From the XPS studies it is also possible to extract the N2s/S2p relationship for SAMs **S1**. Result obtained indicated a 1,86/1 ratio which is close to the expected 2/1 theoretical value. Thus, from the XPS spectra it is possible to assure the correct formation of both monolayers over the gold substrate.

6.2.4.3 Stability of SAMs S1 and S2 in front of Hg^{2+} ions

Until now, we have observed that in absence of Hg^{2+} good quality monolayers are obtained for both receptors, although contact angle and CV measurements indicate a worse packing in the case of **S1** substrates. Nevertheless, no information about the stability of the monolayers in presence of Hg^{2+} has been acquired.
The presence of Hg^{2+} may affect the stability of the sulfur-gold bond, and subsequently, the integrity of the **S1** and **S2** monolayers. In order to analyze the effect that these ions might have on the final properties of the **S1** and **S2** substrates, the same characterization protocol was carried out after immersion of freshly prepared monolayers **S1** and **S2** in a 10^{-7} M aqueous solution of $Hg(ClO_4)_2$ during 180 minutes.

Table 6.6: Advancing (θ_{ad}), receding (θ_{re}) and static contact angles (θ_{st}) in degrees of SAMs **S1** and **S2**, before and after being in contact with Hg^{2+}.

SAMs	Before		After	
	$\theta_{ad}(°)/\theta_{re}(°)$	$\theta_{st}(°)$	$\theta_{ad}(°)/\theta_{re}(°)$	θ_{st}
S1	96±3/64±4	96±1	73±4/64±4	75±1
S2	94±4/76±2	92±1	68±1/53±2	71±2

The resulting contact angle values after treatment with Hg^{2+} ions are lower if compared with data obtained prior the Hg^{2+} treatment, as seen in Table 6.6. More specifically, static angle (θ_{st}) measurements performed on **S1** and **S2** monolayers freshly treated with Hg^{2+}, show values of 75° and 71°, respectively, which correspond to a decrease of 21° if compared with those obtained previously for non Hg^{2+} treated. The same tendency is kept for contact angles θ_{adv} and θ_{red}. This considerable increase on the wettability of the modified substrates can be assigned to the presence of a more hydrophilic species on the treated surface related with the Hg^{2+} recognition process on the SAMs.
The integrity of the monolayers was also electrochemically determined using the same cyclic voltametry set up as previously described but in presence of Hg^{2+} ions. Voltammograms were performed for a mercury enriched (10^{-5} M $Hg(ClO_4)_2$) aqueous electrolyte solution containing, 10^{-3} M $K_3Fe(CN)_6$ and 0.1 M KCl, using **S1**

and **S2** coated gold substrates as working electrodes (Figure 6.42).

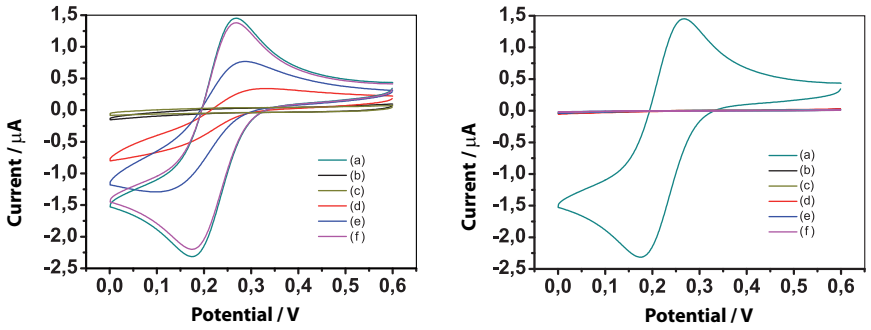

Figure 6.42: Cyclic voltammograms of 10^{-5}M $Hg(ClO_4)_2$, 10^{-3} M $K_4Fe(CN)_6$ in 0.1 M KCl aqueous solution using (a) a bare gold electrode or **S1** and **S2** SAMs coated gold electrodes (left and right, respectively) as working electrodes at (b) t = 0 min (c) t = 1 min (d) t = 10 min (e) t = 20 min and (f) t = 30 min, with a scan rate of 100 mV/s.

Results corresponding to the **S1** SAM coated gold electrode (Figure 6.42 left) show a gradual increase of the $K_3Fe(CN)_6$ peak current with time, which is due to the gradual desorption with time of compound **3** from the gold surface.

Considering a full coverage of the **S1** coated gold substrate at time 0, it is possible to estimate, using equation 6.3, the desorption rate observed for the **S1** substrate. Data obtained, shown on Figure 6.43, indicate a 3% coating loss per minute, being only stable during the first 60 seconds.

On the other hand, cyclic voltammograms performed using an **S2** modified gold electrode, showed no signs of desorption, even after 30 minutes in contact with the Hg^{2+} solution, as depicted on Figure 6.43.

This different behavior of both monolayers can be assigned to a worse monolayer packing for **S1** that allows the Hg^{2+} ion to reach and react with the sulphur atoms laying underneath the organic receptor core, removing the molecules from the gold surface. While compound **3** is anchored to the gold surface through a sulphur atom directly linked to the receptor core, limiting thereby its motility and packing capabilities, the alifatic chain present in compound **4** provides, as designed, a structural shield due to their good packing avoiding the mercury to reach the lower parts of the monolayer.

Until now, it has been proved that the monolayer based on **S2** shows better properties as Hg^{2+} sensing layer, than that based on **S1**. However, it is not still clear if the recognition of mercury does happens in any of the above mentioned cases. In order to get insights on this point, elemental XPS analysis of **S1** and **S2** treated

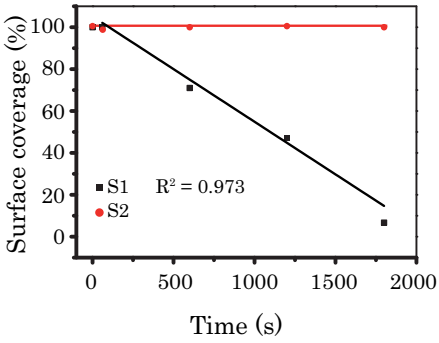

Figure 6.43: Representation of the **S1** monolayer percentage of desorption vs time when immersed on a 10^{-5} M $Hg(ClO_4)_2$ M aqueous solution and complete stability of **S2** monolayer.

with Hg^{2+} were performed. Figure 6.44 shows the high resolution XPS spectra obtained on the C1s, N1s, S2p and Hg4f (5/2f, 7/2f) energy regions for both treated monolayers. The analysis of spectra corresponding to the SAM **S1** do not show any significant change from those obtained for the untreated monolayer, which in the case of the C1s and S2p peaks was a totally expected result, as none of these atoms are involved on the Hg^{2+} complexation. However, the appearance of only one peak on the N1s region, corresponding to the N=C- signal (399,1 eV), and the lack of any Hg4f signal indicated the absence of any Hg^{2+} complexed ligand molecules over the substrate surface. This, can be assigned to the instability of the **S1** monolayer in presence of concentrated (10^{-5} M), $Hg(ClO_4)_2$ solutions, as explained on the previous section.

For **S2** monolayer after the treatment with Hg^{2+}, the XPS spectra corresponding to C1s and S2p regions showed no significant differences from those observed before the treatment. By contrast, the data obtained for the N1s showed the appearance of a small shoulder at higher energies (400.9 eV) besides the main one that remains at 399 eV. This new peak can be assigned to a N-M (M = metal ion) bonded atom.[159,160] This observation is in line with the appearance of two peaks at 100.2 and 104.4 eV, region corresponding to the Hg4f (5/2f, 7/2f) emission, that agrees with the expected signals of a complexed Hg^{2+}.[157,160]

From the forehead described experiments, it is possible to conclude that, in spite of the unstability of **S1** monolayer, the **S2** coated gold surface is capable of complexing Hg^{2+} ion maintaining its chemical structure and its 2-dimensional organization unaltered. Nevertheless, the chemical nature of the formed complex remained at

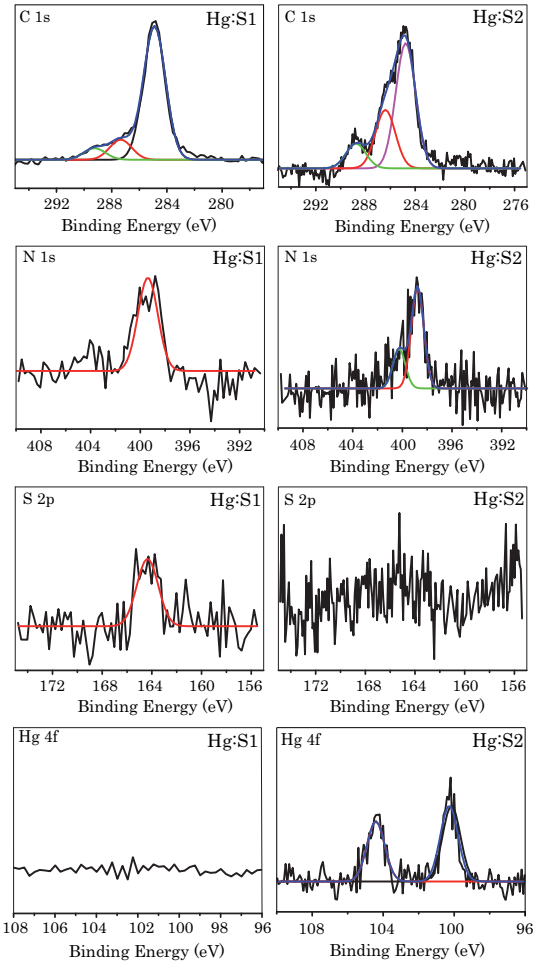

Figure 6.44: XPS spectra of **S1** and **S2** monolayers corresponding to the C 1s, N 1s, S2p and Hg4f (5/2 f 7/2 f) regions after immersion for 2 h in an aqueous solution (10^{-5}M) of $Hg(ClO_4)_2$.

this time unknown. With the objective of determining the molecular structure of the **S2**:Hg^{2+} complex, **S2** coated gold surfaces were studied by surface-assisted laser desorption/ionization time of flight (SAMDI-ToF) mass spectrometry[161,162] before and after treatment with Hg^{2+} ions (10^{-5} M $Hg(ClO_4)_2$).

The SAMDI-ToF technique (Figure 6.45) is a mass spectrometric technique based on the same principles as MALDI-ToF but applied to the analysis and study of SAMs. In this technique, a laser source is employed to ionize the molecules forming the SAM that, once released, will be directed towards the mass spectrometer.

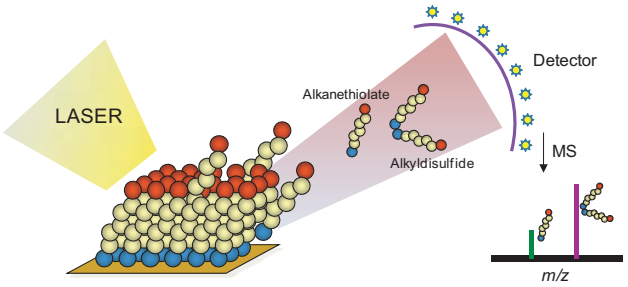

Figure 6.45: Self-assembled monolayers and matrix-assisted laser desorption/ionization mass spectrometry are combined in a technique named as SAMDI-ToF MS which permits a rapid characterization of the masses of molecules anchored to the monolayer (Figure obtained from *M. Mrksich, ACSNano,* ***2008****, 2, 7-18*).

Then, by measuring the time employed to reach the detector it is possible to determine the mass of the ionic fragments arrived.

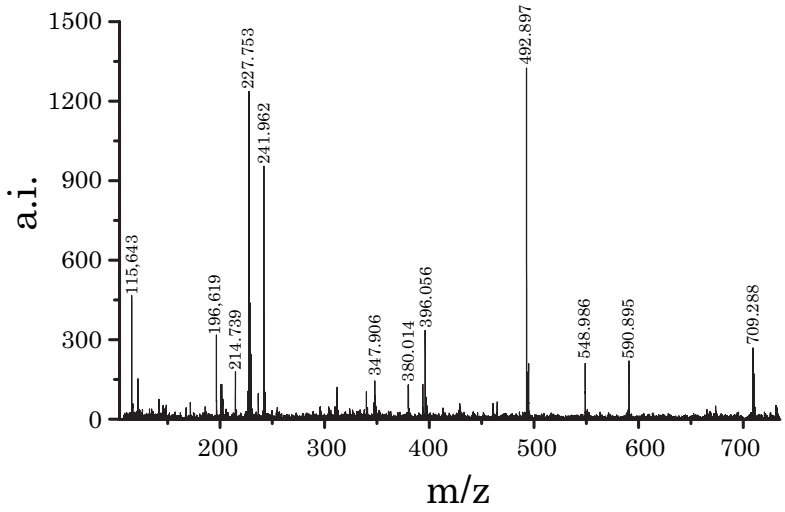

Figure 6.46: SAMDI-ToF mass spectra of a **S2** SAM on a gold slide before treatment with $Hg(ClO_4)_2$.

The SAMDI-ToF mass spectrum of the mercury-free **S2** SAM, depicted on Figure 6.46, reveals a set of peaks corresponding to different fragments and recombinations of the deattached molecule **4**. At m/z values of 709.28 a peak corresponding to the molecular mass of the complete ligand (708.95 dalton) is clearly observed. Furthermore, other peaks are observed at m/z values of 492.99, 380.01, 347.90,

241.96, and 227.76 which are assigned to different fragments of the attached chain of the receptor core.

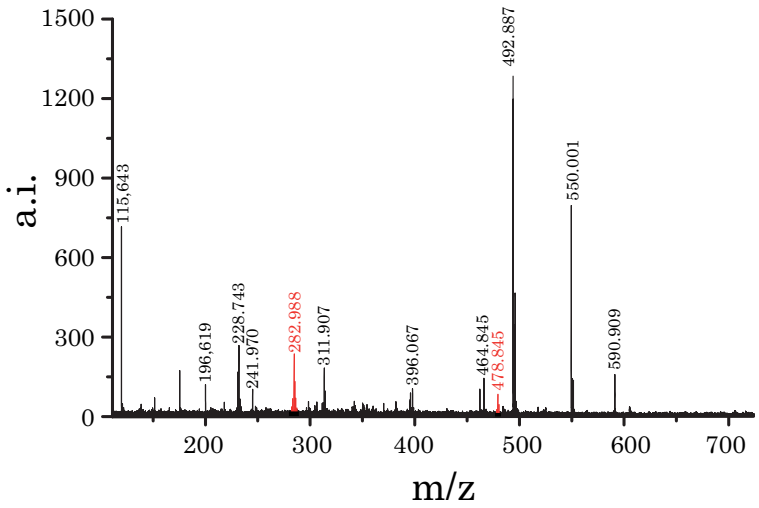

Figure 6.47: SAMDI-ToF mass spectra of a **S2** SAM on a gold slide after treatment with a 10^{-5} M aqueous solution of $Hg(ClO_4)_2$.

If we compare these results with those obtained after treating with Hg^{2+}a **S2** monolayer under the same experimental conditions (Figure 6.47), it is possible to observe the appearance of two new peaks at m/z 478.22 and 283.03. A detailed analysis of the Hg^{2+} complexing possibilities together with the plausible fractures of the molecule, allowed us to identify these peaks to ions with **4**:Hg^{2+}stoichiometries and charges like $(2:1)^{2+}$ and $(2:2)^{4+}$, where the receptor core remains unchanged but the organic chain has been cut just before the second ethylene glycol unit. These two stoichiometries found are in agreement with those obtained with the DFT quantum mechanics calculations previously described (Figure 6.7, Section 6.1.2).

6.2.4.4 Hg^{2+} detection by SPR using S1 and S2 SAMs modified gold surfaces

Having proved the recognition capacity and stability of the SAMs in the presence of Hg^{2+}, we proceed to study their analytical capabilities using a commercial Biosuplar SPR instrument (See Part VI A.2) working in continuous flow.
The general adsorption equilibrium between the Hg^{2+} ions in aqueous solution and

the solid **S2** receptor can be represented by equation 6.4:

$$Hg^{2+}_{(aq)} + L_{(s)} \underset{k_d}{\overset{k_a}{\rightleftharpoons}} HgL_{(s)} \tag{6.4}$$

where L represents the solid **S2** SAM, HgL the complex formed on the surface and k_a and k_d are the association and dissociation constants of the process, respectively.

According to the nature of the Hg^{2+} detection system, it is possible to approximate the concentration of the complex to its surface coverage, which at the same time would be proportional to the shift of refractive index suffered by the sensor surface upon ion complexation (see Part VI A.2). Thus, taking into account that SPR spectroscopy is a technique based on the measurement of small changes on the resonance angle (θ_{SPR}) between incident light and the plasmons present on the gold surface, and that this value is dependent of the refractive index (RI) at the solid-liquid interface, it is possible to assume that the observed SPR signal is proportional to the Hg^{2+} ion concentration present in the analyzed solutions.

Hence, the SPR angle shifts are dependent upon the amount of Hg^{2+} adsorbed to the **S2** surface, generating the required analytical signal. In other words, the more Hg^{2+} that are adsorbed to the **S2** surface, the greater will be the observed angle shift. However, Hg^{2+} ions are not the only origin of the changes on the RI of the solid-liquid interface. Thus, the presence of small changes on the density, ionic strength or even temperature of the analyzed solution media can entail the appearance of a change in the analytical signal measured. In order to avoid the existence of any external influence distinct form the Hg^{2+} ions, the experiments were carried out using buffered solutions (0.1 M NaCl aqueous solution) as the mobile phase. This would avoid any modification of the density or the refractive index of the media during the Hg^{2+} determination. Furthermore, all the measurements were done using a second measurement channel as an internal reference in order to minimize any influence of small temperature modifications during the experiment. All the injections performed for the SPR measurements were done using a constant flow of 100 μl/min.

On a first attempt, aqueous solutions of different concentrations of $Hg(ClO_4)_2$ were directly injected to the SPR system using a freshly cleaned bare gold slide as SPR chip. On an ideal situation, where the Hg^{2+} does not interact with the gold substrate, the injection of Hg^{2+} to a receptor free sensor chip has to present a perfectly stable signal showing no significant variations upon injection of Hg^{2+} solutions.

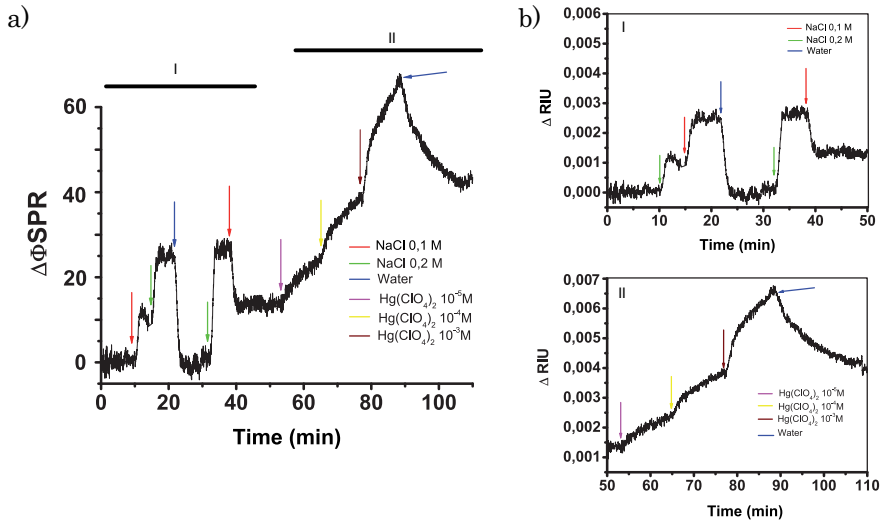

Figure 6.48: SPR sensograms corresponding to the injection of different buffer (0.1 and 0.2 M NaCl aqueous solutions) and $Hg(ClO_4)_2$ solutions to a clean gold sensor chip. a) Zone of the SPR sensogram corresponding to the injection of buffer solutions with different NaCl concentrations (0,1 and 0,2 M) used for the calibration of the SPR signal to refractive index units (RIU). b) Zone of the SPR sensogram corresponding to the injection of aqueous solutions of different Hg^{2+} concentrations, showing the formation of a mercury-gold amalgam.

The obtained sensogram (shown in Figure 6.48) can be divided into two different zones, the first one (I) corresponding to the stabilization and calibration of the chip with the salt buffer solution, and the second one (II) where the Hg^{2+} solutions are injected. As seen on the graph, the injection of different concentrations of NaCl aqueous solutions causes an abrupt increase of the SPR signal, due to the change in RI of the buffer solution. These jumps were used to perform the calibration of the SPR signal ($\Delta\theta_{SPR}$) and its transformation onto refractive index units (RIU). In order to do that, the RI of the different buffer solutions was measured using a refractometer and the difference between those values was used to quantify the jump generated after their injection on the SPR system. This process was repeated twice to minimize the error. Once calibrated, the system was stabilized for 15 minutes under a constant flow of the buffer solution and then aqueous $Hg(ClO_4)_2$ solutions with increasing concentrations, ranging from $1{\cdot}10^{-5}$ to $1{\cdot}10^{-3}$ M, were sequentially injected (Zone II). Although as previously explained, no analytical signal was expected on this case, due to the lack of Hg^{2+} receptor on the sensor surface, it is possible to observe a large increase of the ΔRIU values upon the

Hg^{2+} injections. Such changes showed to be irreversible since washing the SPR chips with the buffer solution did not recovers the original baseline, indicating the existence of some modification of the gold sensor surface. This variation can be attributed to the formation of an amalgam by the spontaneous reduction of the Hg^{2+} in solution to elemental mercury and its mixture with the gold. It is well known that mercury is able to chemically react with the gold sensor chip forming an irreversible Au/Hg amalgam that increases the mass of the sensing layer, and therefore modifies its RI generating the observed analytical signal.

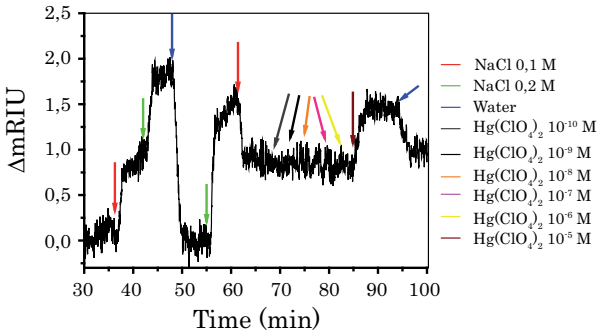

Figure 6.49: SPR sensogram corresponding to the injection of different buffers (0.1 and 0.2 M NaCl aqueous solutions) and $Hg(ClO_4)_2$ solutions to a hexadecylthiol SAM modified gold sensor chip.

With the objective of corroborating this hypothesis, the same experiment was carried out but in this case with a gold substrate modified with an hexadecylthiol SAM as sensor chip. The preparation of such a SAM was carried out following the same procedure as forehead explained for **S1** or **S2** SAMs (section 6.2.4.2). Figure 6.49 depicts the resulting sensogram. On the contrary of the previous case, the injection of increasing concentrations of buffered Hg^{2+} ions aqueous solutions (0.1 M NaCl), ranging from $1{\cdot}10^{-8}$ to $1{\cdot}10^{-4}$ M, to the SPR system using a hexadecylthiol SAM modified gold sensor chip, does not affect the integrity of the sensor, obtaining a stable SPR signal. Furthermore, the absence of analytical signal even injecting salt concentrations of $1{\cdot}10^{-4}$M corroborates the efficiency of the NaCl solution as a RI buffer system. It is worthy to remark that this situation changed when a $1{\cdot}10^{-3}$ M solution of $Hg(ClO_4)_2$ was injected. In such experiment, the SPR signal started to increase and although the washing of the sensing surface reduced the RIU values, the baseline was not totally recovered. Therefore, it is possible to conclude that the use of highly concentrated Hg^{2+} solutions destroys

the hexadecylthiol SAM sensor chip and should be avoided. A schematic representation of the injection of aqueous Hg^{2+} solutions to a hexadecylthiol modified gold substrate is represented on Figure 6.50.

Once the operation protocol was established, we proceed to study the Hg^{2+} recognition using **S1** and **S2** sensing surfaces.

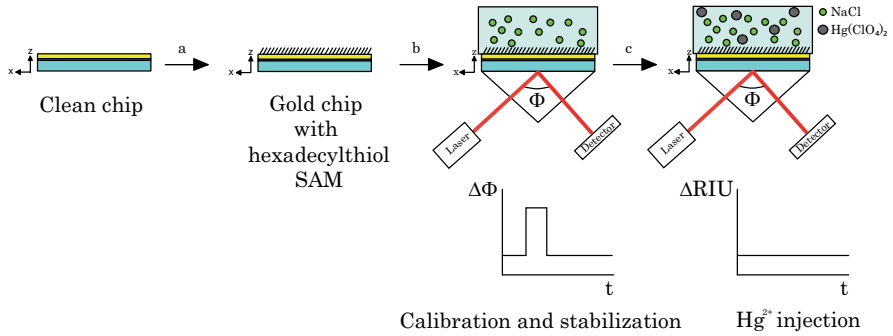

Figure 6.50: Schematic representation of the preparation and use of a hexadecylthiol SAM modified gold substrate as SPR sensor chip, showing; a) formation of the hexadecylthiol SAM, b) stabilization and calibration of the SPR system with the buffer solution (NaCl 0,1M) and c) injection of Hg^{2+} aqueous solutions.

a) Hg^{2+} detection by SPR using S1 SAM modified gold surfaces. SPR recognition studies using freshly prepared **S1** SAM modified SPR chips were carried out in order to further characterize this SAM in front of Hg^{2+}. With the purpose to determine which was the Hg^{2+} concentration range in which this sensor is able to work, a fast screening of the SPR signal vs. Hg^{2+} concentration was performed.

Figure 6.51 depicts the resultant sensogram for the fast screening of the **S1** SAM modified chip upon addition of increasing concentrations of $Hg(ClO_4)_2$. It is observed that, even after the buffer stabilization and calibration steps, the baseline obtained was not constant enough, which can be attributed to a lack of a good monolayer packing. Nevertheless, the addition of small concentrations of Hg^{2+} does not seriously alter the sensor response, as observed for $1{\cdot}10^{-11}$ or $1{\cdot}10^{-10}$ M (green and blue arrows, respectively) Hg^{2+} injections.

This situation changes with an injection at a concentrations of $1{\cdot}10^{-9}$ M where, in addition to a small recognition peak, a change on the baseline trend is also observed. Finally, as showed on the SPR sensogram profile, the injection of a $1{\cdot}10^{-8}$

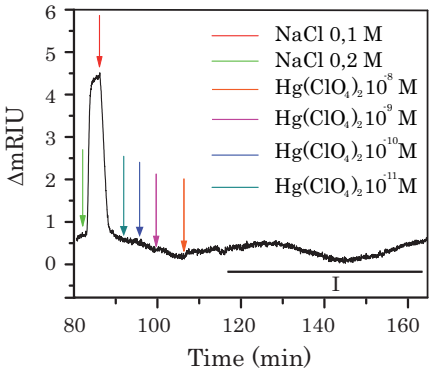

Figure 6.51: SPR sensogram corresponding to the injection of different aqueous buffer concentrations (0.1 and 0.2 M NaCl) and $Hg(ClO_4)_2$ aqueous solutions on a **S1** SAM modified gold chip.

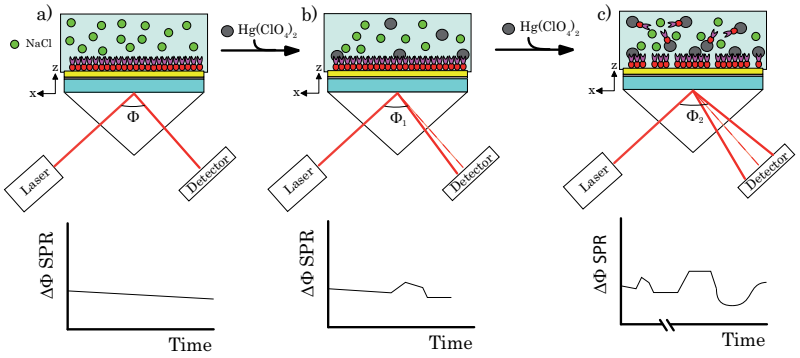

Figure 6.52: Schematic representation of the events occurring after injection of increasing concentration of $Hg(ClO_4)_2$ over a **S1** SAM modified gold chip. a) Before injecting Hg^{2+} ions the monolayer remains stable over the gold substrate; b) when low concentrations of Hg^{2+} are injected, part of the monolayer is complexed without suffering any modification; c) when large concentrations are injected (higher than $1{\cdot}10^{-8}$ M) the monolayer becomes unstable and although more complex is formed, part of the monolayer is desorbed from the gold surface and released to the media, exposing some of the gold unprotected areas to free Hg^{2+} which can react with the gold forming an amalgam.

M $Hg(ClO_4)_2$ solution (orange arrow) ends on the total destabilization of the baseline signal (marked as zone I) making impossible to continue with the analysis. This modification of the baseline can be assigned to an important modification of the surface-liquid properties, caused by the partial desorption of the monolayer and the formation of a Au/Hg amalgam on the uncoated areas. A schematic representation of what might happen with the **S1** SAM during Hg^{2+} injections is represented on Figure 6.52. Once it was established the concentration range (from

$1{\cdot}10^{-11}$ to $1{\cdot}10^{-8}$ M), where the **S1** SAM works properly, the calibration of the SPR response was performed. Therefore, we proceed to inject the Hg^{2+} solutions to freshly prepared sensor chips measuring the generated signal until stabilization (20 minutes). Results obtained for the four concentrations are shown in Figure 6.53 a.

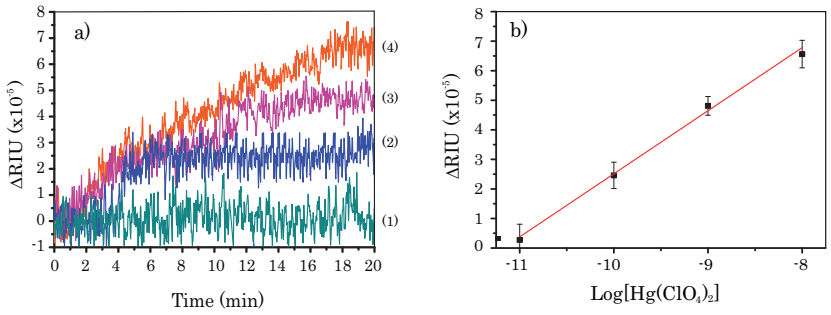

Figure 6.53: a) SPR sensograms obtained for the injection of aqueous Hg^{2+} solutions ranging from $1{\cdot}10^{-11}$ to $1{\cdot}10^{-8}$ M (1-4, respectively) using a gold chip coated with **S1** SAM as Hg^{2+} detecting surface. b) SPR Hg^{2+} detection calibration line of a **S1** sensor chip showing the dependence of the SPR signal (ΔRIU) with the concentration of aqueous Hg^{2+}.

The results obtained for the **S1** SAM SPR gold chip obtained by plotting the maximum ΔRIU values obtained for each concentration vs. the Hg^{2+} concentration are represented on Figure 6.53 b. Despite the good detection limit ($1{\cdot}10^{-10}$ M, hundreds of ppt) the stability problems observed while injecting aqueous solutions with Hg^{2+} concentrations higher than $1{\cdot}10^{-8}$ M, together with the SAM time desorption problems when in contact with Hg^{2+} , previously reported on section 6.2.4.3, make receptor **3** based SPR sensors non suitable for the obtaining of reliable Hg^{2+} sensors.

b) Hg^{2+} detection by SPR using S2 SAM modified gold surfaces. The same experiments were carried out for **S2** SAM modified SPR gold chips. However, in this case prior to the study with the monolayers based on receptor **4** (**S2**), previous control assays with a SPR chip coated with compound **8** (Figure 6.37), based on the same gold anchoring structure as receptor **4** but without the receptor core, were performed. The main objective for this experiment was the identification of any unspecific Hg^{2+} adsorption or desorption effects of the monolayer. The preparation of the SAM of compound **8** over the gold chips was carried out following the same procedure previously described for receptors **3** and **4** (Section 6.2.4.2).

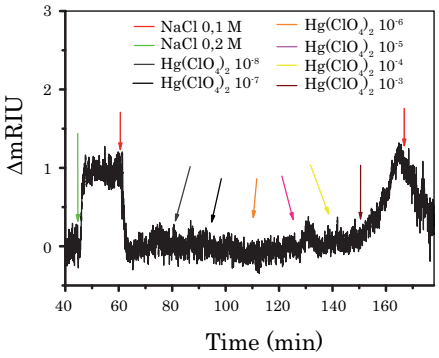

Figure 6.54: SPR sensogram corresponding to the injection of different aqueous buffer concentrations (0.1 and 0.2 M NaCl) and $Hg(ClO_4)_2$ aqueous solutions to a gold chip modified with a SAM of **8**.

Complete SPR sensogram and the SPR signals corresponding to injection of solutions with different Hg^{2+} concentrations for the above described coated SPR chips are shown in Figures 6.54 and 6.55, respectively. In both graphs it is possible to observe a much higher baseline stability, when compared with that obtained for the **S1** coated chip, and the absence of anomalous effects upon Hg^{2+} injection.

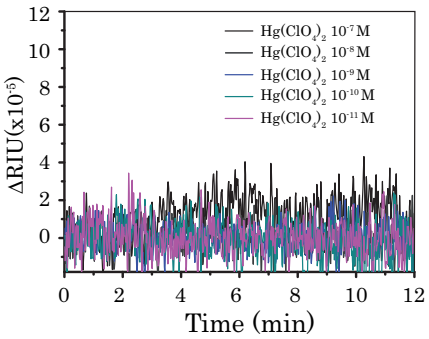

Figure 6.55: SPR sensogram obtained for the injection of aqueous Hg^{2+} solutions ranging from $1{\cdot}10^{-11}$ to $1{\cdot}10^{-8}$ M using a gold sensor chip modified with a SAM of **8**.

It is worthy to remark that a when $1{\cdot}10^{-3}$ M $Hg(ClO_4)_2$ solution is injected, a sudden increase of the SPR signal was observed, probably due to the unstabilization of the monolayer in contact with such a large Hg^{2+} concentration. However this does not represent a problem for the Hg^{2+} detection, as $1{\cdot}10^{-3}$ M (thousands of ppm) is an extremely elevated concentration that will never be present in normal or moderate contaminated areas. A schematic representation of what might happen

with the compound **8** SAM during Hg^{2+} injections is represented on Figure 6.56.

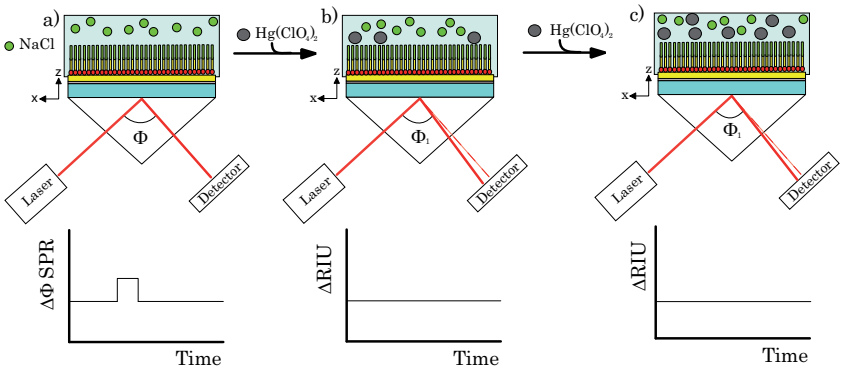

Figure 6.56: Schematic representation of the events occurring after the injection of increasing concentrations of $Hg(ClO_4)_2$ over a SPR gold chip coated with a SAM of compound **8**. a) Stabilization and calibration of the SPR signal with the buffer solution. b) and c) the injection of aqueous Hg^{2+} solutions of different concentrations. The monolayer remains stable over the gold substrate even when high concentrations of mercury are injected.

After probing that SAM of compound **8** present the adequate molecular packing density and stability *vs.* Hg^{2+} ion to be used as anchoring moiety on the formation of SAM based sensors, we proceed to the preparation of **S2** modified SPR gold chips. Results obtained with such chips are shown on Figure 6.57. In this case, as for the compound SAM based on compound **8** (Figure 6.54), the baseline obtained showed a very good stability even with the presence of Hg^{2+}, indicating the absence of any unspecific interaction during the measurements. Corroborating that the presence of the organic aliphatic chain attached to the receptor not only helps on the SAM packing, as previously observed during monolayer characterizations, but also entails a better SPR signal stability and more reduced noise values, if compared with those measurements performed with **S1** sensor chips.

The working scheme of the measurements with the **S2** coated device is represented on Figure 6.58, showing the associated events occurring during injection. As depicted on the cartoon, the monolayer remains invariable in presence of the different salts in the solutions, and the resulting SPR signal only rises upon the sequential injection of increasing concentrations of Hg^{2+} aqueous solutions.

Once determined the stability of the SAM, we proceed to calibrate the SPR response of the **S2** coated chip towards the concentration of Hg^{2+}. Therefore, several Hg^{2+} solutions of concentrations ranging from $1{\cdot}10^{-11}$ to $1{\cdot}10^{-7}$ M were injected

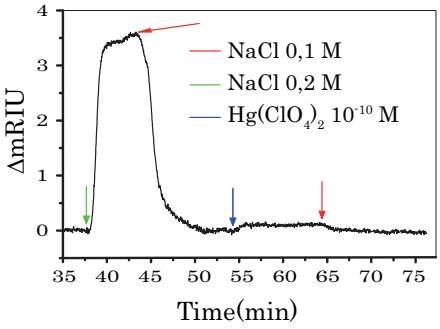

Figure 6.57: SPR sensogram corresponding to the injection of different aqueous buffer concentrations (0.1 and 0.2 M NaCl) and a $1{\cdot}10^{-10}$ M $Hg(ClO_4)_2$ aqueous solutions to a **S2** SAM modified gold sensor chip.

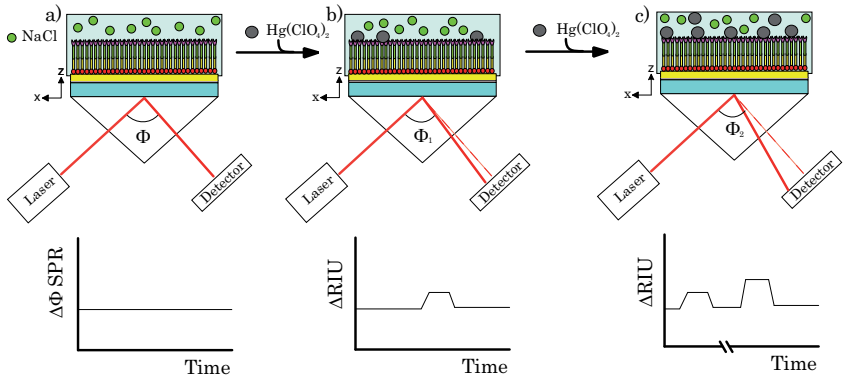

Figure 6.58: Schematic representation of the events occurring after the injection of different concentrations of $Hg(ClO_4)_2$ over a **S2** coated SPR gold chip. The monolayer of compound **4** (**S2**) remains stable all over the experiments independently of the concentration of the $Hg(ClO_4)_2$ injected ($1{\cdot}10^{-11}$ M to $1{\cdot}10^{-7}$ M). a) Stabilization and calibration of the SPR signal with the buffer solution. b) and c) the injection of aqueous Hg^{2+} solutions of different concentrations. The monolayer remains stable over the gold substrate even when high concentrations of mercury are injected.

to freshly prepared and buffer stabilized sensor chips and the resulting SPR signal measured until stabilization (18 minutes).

Calibration of the **S2** modified SPR chips after injection of the different Hg^{2+}solutions is shown on Figure 6.59 a. The analysis of the resulting calibration line, obtained by plotting the maximum ΔRIU values obtained for each concentration *vs.* the Hg^{2+} concentration (Figure 6.59 b), indicates that it is possible to detect the presence of Hg^{2+} in aqueous solutions at concentrations down to $1{\cdot}10^{-11}$ M (ng/l, ppt). This extremely low detection limit obtained is highly remarkable, as it reaches

some atomic absorption techniques and permits to measure with confidence the maximum allowed concentration of Hg^{2+} in drinkable water set by the European Community.[62]

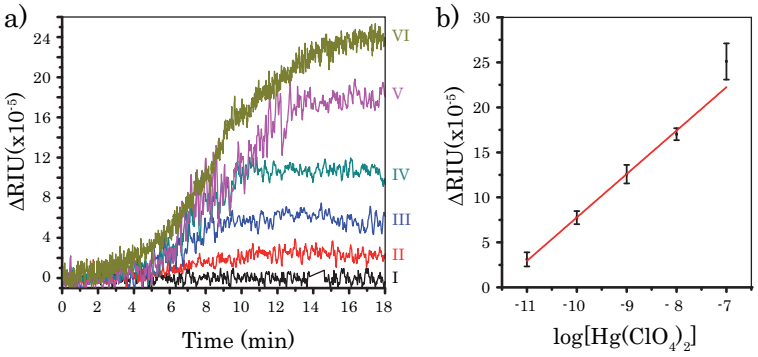

Figure 6.59: a) SPR sensograms obtained for the injection of aqueous Hg^{2+} solutions ranging from $1{\cdot}10^{-11}$ to $1{\cdot}10^{-8}$ M (II-VI, respectively) using a **S2** sensor chip (I sensogram corresponds to the injection of a Hg^{2+} free buffer solution); b) SPR Hg^{2+} detection calibration line of a **S2** sensor chip showing the dependence of the SPR signal (ΔRIU) with the concentration of aqueous Hg^{2+}.

However, the obtaining of an extremely sensitive sensor is not enough, and it has to be also selective to the target analyte. Thus, in order to characterize the selectivity of this new Hg^{2+} sensor, the injection of solutions of different mono-, di- and trivalent cations have been performed. As shown in Figure 6.60 a, the sensor can distinguish Hg^{2+} from all the other mono- and divalent cations, even though its concentration is 100 times lower.

Thus, it is possible to conclude that **S2** based SPR sensors are highly sensitive and selective Hg^{2+} sensing devices that rival with other well established and much more complex systems, such as the inductive coupled plasm mass spectrometry (ICP-MS) or the atomic absorption techniques. However, even though its simplicity, sensing systems based on SAMs are, with punctual exceptions, not very robust systems, and their reusability is still one of their weak points.

In order to check the robustness and re-usability of this Hg^{2+} sensing device, a 10^{-10} M $Hg(ClO_4)_2$ was sequentially injected to the same **S2** coated SPR chips alternating them with buffer washing steps. Results, depicted on Figure 6.60 b, indicate a complete baseline and signal recovery for the first four test, while the fifth one presents a slight signal diminution, entailing the possibility or recycling our sensor up to 4 assays. This is, to the best of our knowledge, the first SPR

Hg^{2+} sensor capable of being reused without loosing any of its detection properties, which supposes an increase of the economic feasibility of the sensor chip if compared with the actual systems.

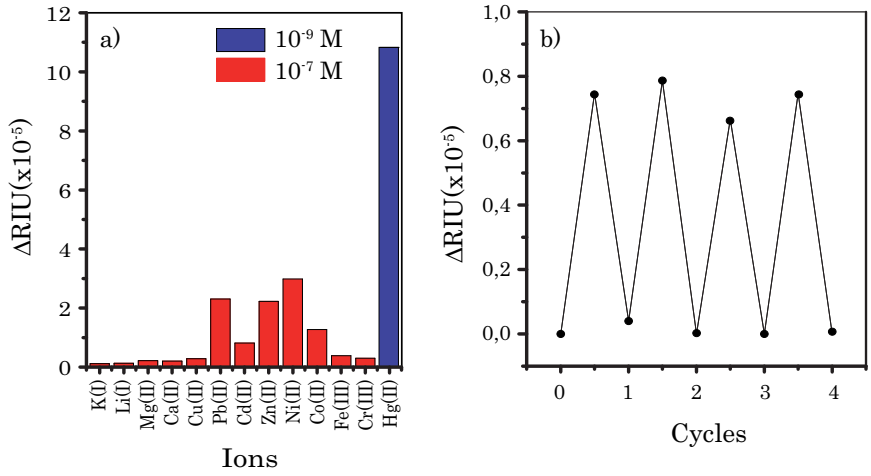

Figure 6.60: a) Selectivity test perform by the injection of different mono- di and trivalent cations onto a **S2** SAM modified SPR sensor chip. The concentration of the different used cation was 100 times higher than the corresponding Hg^{2+} concentration. b) Reusability tests performed to a **S2** SAM modified SPR sensor chip by the cyclic injection of washing buffer solution (NaCl 0.1 M) and a $1{\cdot}10^{-10}$ M aqueous solution of Hg^{2+}. Results indicate the possibility of reusing the SPR sensor up to 4 times without the loose of sensitivity.

c) Determination of the Hg^{2+} recognition kinetic constant by the S2 SAM modified gold surfaces. SPR is a real time detection technique, which means that it is not only possible to determine the concentration of an analyte but also to study how fast does the detection takes place by studying the kinetic properties of the recognition.

On a traditional SPR kinetic study it is needed to know the saturation point of the sensing surface or, in other words, at which point the recognition event is stopped because the active surface has reacted completely. Then, this point will be used as reference for the mathematical calculations and the kinetic fittings. However in our case, this point is unknown because our system does not saturate between the range of Hg^{2+} concentrations tested and therefore, an alternative procedure had to be used.

A general reaction scheme is exploited in order to describe the function of this

analytical system:

$$Hg^{2+}_{(aq)} + L_{(s)} \underset{k_d}{\overset{k_a}{\rightleftharpoons}} HgL_{(s)} \tag{6.5}$$

$$\frac{d[HgL]}{dt} = k_a[Hg^{2+}][L] - k_d[HgL] \tag{6.6}$$

Where L is the receptor monolayer anchored to the Au surface, HgL is the complex formed on the solid surface, and k_a and k_d are respectively, the association and dissociation rate constants of the Hg^{2+} to the receptor (L). The complex formation rate is given by the equation 6.6, where [Hg^{2+}] is the concentration of mercury ions present in the media, [L] the concentration of ligand anchored to the solid surface and [HgL] the concentration of metal-organic complex on the solid surface. Here the concentration of the complex, [HgL], can be approximated to the surface coverage, that is proportional to the SPR signal (ΔRIU). Due to negligibly small concentration differences of the Hg^{2+} analyte during the complexation, concentration of the analyte is assumed to be constant in time; i.e., [Hg^{2+}] = C. Therefore, complex formation can be considered as pseudo first order kinetics in SPR sensors,[163–165] (see Annex SPR) and equation 6.6 can be rewritten as equation 6.7 and rearranged in equation 6.8.

$$\frac{d\Delta RIU}{dt} = k_a C(\Delta RIU_{max} - \Delta RIU_t) - k_d \Delta RIU_t \tag{6.7}$$

$$\frac{d\Delta RIU}{dt} = k_a C \Delta RIU_{max} - (k_a C + k_d)\Delta RIU_t \tag{6.8}$$

Thus, equation 6.8 can be regarded as a straight line:

$$\frac{d\Delta RIU}{dt} = k_s \Delta RIU_t + b;\ with\ k_s = (k_a C + k_d) \tag{6.9}$$

Parameters k_s and b can be determined by linear regression of a plot of ΔRIU/dt vs. ΔRIU values. Where k_s is a concentration dependent parameter obtained from the slope of the plotted line and from which k_a and k_d values can be estimated. The parameter b corresponds to the intersection of the plotted line with the y-axis. This method is called the linearization method,[166] because the relevant parameter k_s can be determined by linear regression.

In our case, the fitting and derivatization of the experimental ΔRIU data, obtained form the injection of different concentrations of Hg^{2+} solutions to a **S2** modified SPR chip in function of time (t) could not be straightly done as the Hg^{2+}absorption regime of the sensor chip does not follow a typical first order Langmuir kinetics but

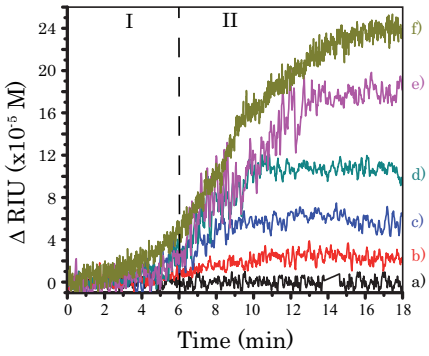

Figure 6.61: Plot of the ΔRIU vs. time for each Hg^{2+} concentration assayed showing the S-type adsorption behavior. a) base line; b) 10^{-11} M; c) 10^{-10} M; d) 10^{-9} M; e) 10^{-8} M; f) 10^{-7} M.

a S-type adsorption behavior, which is indicative of the existence of a cooperative mechanism[167] (Figure 6.61). Then, the Hg^{2+} adsorption can be divided into two different regions (regions I and II in Figure 6.61). While in region I the adsorption rate increases with coverage due to the existence of the cooperative measurement, in region II it follows a Langmuir-type kinetics, being this part the one chosen to perform the kinetic analysis of the system.

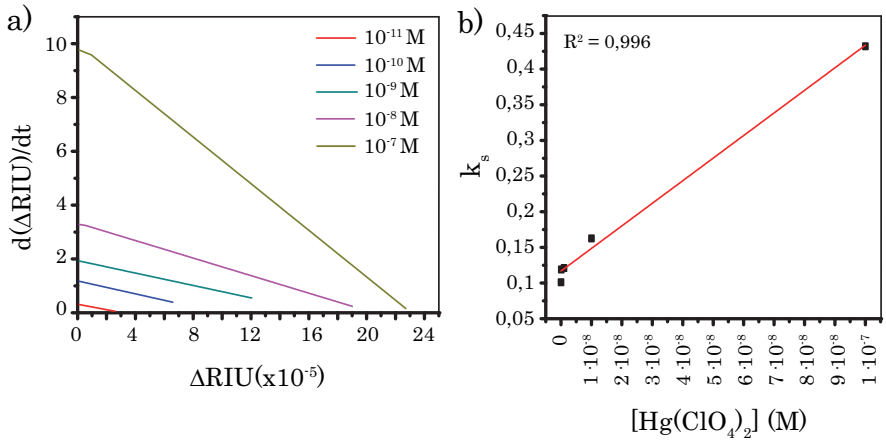

Figure 6.62: a) Plot of the ΔRIU/dt *vs* ΔRIU for each mercury concentration. b) Plot of k_s values *vs.* C obtained from the slopes of the previously plotted lines

The k_s values corresponding to our experimental system were obtained from the slopes of the plotting of the ΔRIU/dt *vs* ΔRIU_t for each mercury concentration (Figure 6.62 a). The kinetic rate constants (k_a and k_d) were determined by a plot

of k_s values *vs.* C. Linear regression reveals the association rate constant (k_a) from the slope of the plotted straight line, and the dissociation rate constant (k_d) from the y-intercept of the plotted line. The k_d and k_a values obtained are 0.1168 s^{-1} and $3.16 \cdot 10^6$ $M^{-1}s^{-1}$, respectively.

It is worth to notice that such values are just an approximation of the real kinetic constants involved in the recognition mechanism and that supposes that all the SPR signal change are due to the anchoring of Hg^{2+} to the receptor core. However, the existence of other factors such as the appearance of fluorescence or a structural change on the monolayer, might also affect the signal and will introduce an error on the kinetic constant values.

6.2.4.5 Conclusions

In summary, a new ultrasensitive, highly selective and recyclable SPR Hg^{2+} sensor chip has been developed. Such a sensor has a detection limit at the picomolar level, which is three orders of magnitude better than the allowable limit specified by the European Community for drinkable water. Furthermore, if compared with other existing techniques, the excellent analytical properties and the estimable cost efficiency of such a SPR sensor make it a good alternative as an "in-field" sensor for the detection of Hg^{2+} ions in water supplies.*

6.3 Hg^{2+} Remediation. New Materials towards Contamination Removal

6.3.1 Introduction

Even though the development of new, fast and reliable mercury sensing systems is the best chance to fight against the appearance of Hg^{2+} contamination in new areas, this is, unfortunately, useless towards the already contaminated sites. Moreover, due to the persistence of mercury in the environment it may take a very long time, perhaps centuries, for mercury-contamination to reach relatively safe levels in both water and soil. Thus, the development of new, efficient and "green" systems to monitor and reduce the residual mercury concentration below the safety limits has become a hot issue for scientists.

*Some of the obtained results with the Hg^{2+} sensing SPR gold chips, based on compound **4**, have been submitted to for publication.

So far, numerous methods have been used for the treatment of aqueous streams contaminated with heavy metals, going from phytoremediation[168] to thermal treatment.[169] However, most of them are either time or cost consuming limiting their feasible use to a small range of contaminated areas.

During the raise of this Thesis we have focused our attention on the developing of cost effective materials able to perform an *in situ* chemical remediation of Hg^{2+} present in water sources. Up to now, artificial polymers[170,171] and mesoporous materials[83,172,173] are the more common ones. Nevertheless, most of these methods have shown several problems such as, a poor selectivity and removal efficiency, the requirement of complicated preparation techniques or weak chemical union within the metals. Moreover, even though some of them are highly efficient, the complexity of its recycling process, the need of non-ecologic chemical substances on its production, or their incompatibility with aqueous environment makes their industrial or *in situ* application rather difficult.

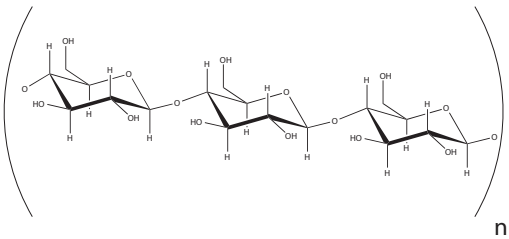

Figure 6.63: Schematic representation of the cellulose chemical structure

Cellulose is a natural, biodegradable, cheap and ubiquitous polymer,[174,175] with exceptional physico-chemical characteristics (Figure 6.63). Properties, like its wettability and stiffness, have made this natural polymer and its derivatives, the basis of several industrial products, such as foodstuffs, polymers or healthcare supplies. On the other hand, the use of cellulose, specially on the development of environmental or biological tests,[106,176,177] has suffered a huge increase during the last years. Particularly interesting is the work of *Martínez et al.*[106] where an optically patterned paper sheet was used as platform for low cost multianalyte biosensors. In agreement with this trend, our group has engaged in the last years on the anchoring of new multifunctional organic molecules able to perform the colorimetric or fluorimetric detection of heavy metals in water supplies using cellulose as solid support.[176,177] Even though, cellulose derivatives have also been used in the past as removal materials,[178,179] its appropriate synthesis and functionalization has

always been a problem. Nevertheless, the total processing of underivatized carbohydrates as cellulose is still quite challenging due to its low solubility in almost all solvents.

From all the plausible processing methodologies the use of ionic liquids, specially the l-3-bismethylimidazolium derivatives salts,[180] have proved to be not only really efficient as cellulose solvent, but also, due to its high solubility in water, they are susceptible to be easily removed from the reaction media, avoiding any purification step, transforming the manipulation and transformation of these kind of organic polymers onto a completely environmental friendly process.

Herein we present a new fluorogenic and chromogenic composite material based on the use of environmentally friendly ionic liquids to combine the highly sensitive and selective Hg^{2+} receptor **2** with a non modified cellulose (Avicel) matrix. The resulting composite material is a highly promising material for the selective remediation of mercury contamination in water supplies.

6.3.2 Preparation and characterization of the cellulose composite based on the receptor 2

Prior to the composite production, the obtaining of an homogeneous solution of all the components was required. While receptor **2** is an organic compound, soluble in a broad range of polar solvents, such as ethanol, tetrahydrofurane or dichloromethane, cellulose presents a completely distinct solubility pattern. Thus, in order to solubilize the cellulose, without breaking its polymeric chain the use of less common solvents, such as ionic liquids is needed.

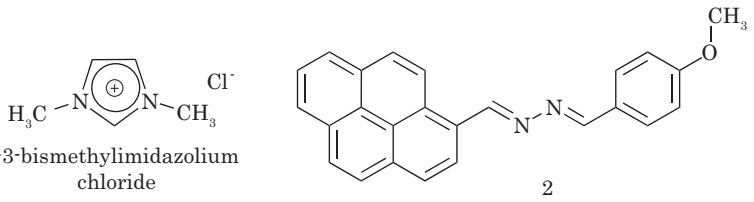

Figure 6.64: Schematic representation of the chemical structures of the ionic liquid used, the l-3-bismethylimidazolium chloride, and the Hg^{2+} receptor **2**.

Therefore, on a first stage we proceed to completely dissolve the cellulose into the selected ionic liquid, l-3-bismethylimidazolium chloride (Figure 6.64), and then the receptor **2** (2% in weight with respect to the cellulose) was added obtaining, after

their complete solution, an homogeneous yellowish and highly viscous solution. On a second step, this solution was drooped onto a beaker full with hot water under stirring. After 2 hours, the resulting solid formed was filtered, copiously washed with water for the removing of the remaining ionic liquid, and dried under vacuum to completely remove the traces of water occluded in the cellulose fibers.

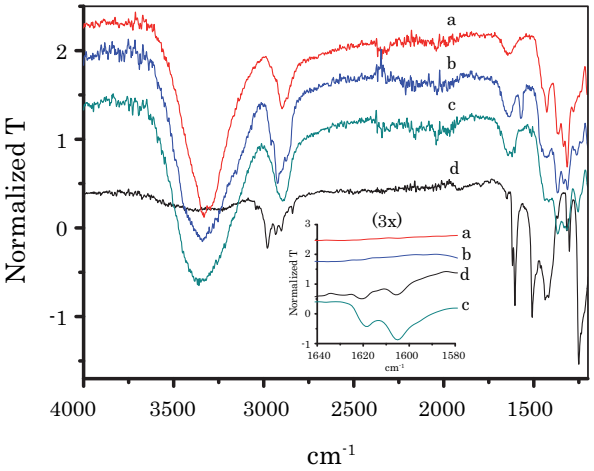

Figure 6.65: FT-IR spectra of a) untreated Avicel cellulose, b) processed Avicel cellulose, c) mercury sensing composite, d) receptor **2**.

Characterization of the freshly prepared composite was carried out by Fourier transform infrared spectroscopy analysis (FT-IR). FT-IR technique not only gives us information about the chemical nature of the analyzed substance but also about the supramolecular interactions between the different components of a composite material.[181] Figure 6.65 shows the IR spectra of all the composite components prior and after its processing with the ionic liquid.

The high cellulose content of the composites (98% weight) makes difficult to observe the bands associated to the receptor molecule (2% weight). However, if we focus our attention to the 1650-1560 cm^{-1} region (Figure 6.65 inset) of the spectra we can see two incipient peaks, at 1618 and 1605 cm^{-1}, characteristics of the stretching of the C=N groups of the used molecular probe. After the composite formation, no significant shift was observed on those signals indicating, therefore, that the cellulose matrix does not interact strongly with the azine groups of the receptor in charge of the mercury recognition.

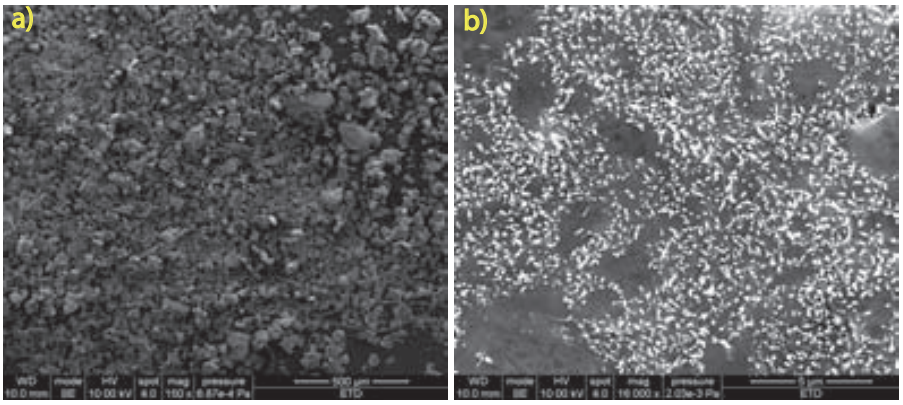

Figure 6.66: SEM images of the freshly milled cellulose composite showing; a) particles of the cellulose composite ranging from 20 to 100 μm and b) zoom image onto one of the particles showing trapped crystals of receptor **2** in the cellulose matrix.

Due to its preparation procedure, the composite particles obtained show sizes ranging from hundreds of microns to even several millimeters. Such a polydisperse and big particle sizes presented a serious problem in order to achieve good Hg^{2+}removal efficiencies, as the real active surface of the composite is reduced with increasing the particle size. Thus, with the objective of maximizing the Hg^{2+} retention an increase of the active surface was required. Among all the available milling techniques, the ball mill was selected due to its simplicity and scaling possibilities. This techniques was applied with a commercial apparatus during 15 minutes at 20 Hz.

Scanning electron microscopy (SEM) images of the freshly milled composite (Figure 6.66) show a much more homogeneous distribution of composite particles, with sizes ranging from 20 to 100 μm on average. Furthermore, a zooming performed onto the surface of one of those particles showed the existence of an homogeneous distribution of compound **2** microcrystals inside the cellulose supporting matrix. In order to establish the possibility to use this novel composite material to perform the removal of Hg^{2+} present in water sources, further analyses to determine the mercury anchoring properties of the composite were developed using home-made remediation columns (Figure 6.67).

ICP-MS was used as reference technique to control the efficiency of the removal of Hg^{2+} from the aqueous samples. ICP-MS analysis were performed before and after the filtration of a $3.8{\cdot}10^{-6}$M $Hg(ClO_4)_2$ (1525 ppb μg/l) aqueous solution through the remediation columns at a flow rate of 2 ml/min. As it can be seen,

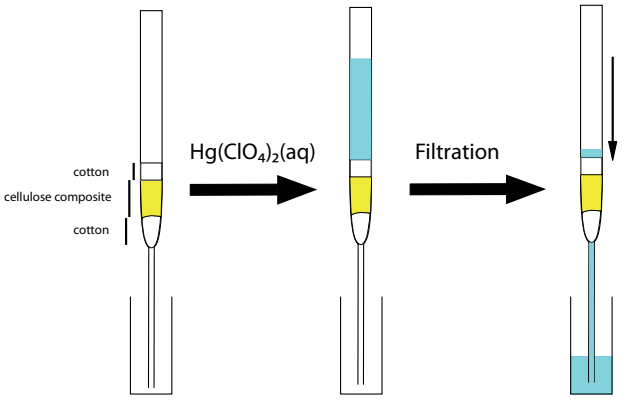

Figure 6.67: Representation of the home-made Hg^{2+} retention columns based on the cellulose composite material

the initial concentration of Hg^{2+} present on the sample was 1525 ppb, thus if we compare this value with those obtained after the filtration through a non treated bare cellulose column, we observe a decrease of the 44% (662 ppb) of the concentration of mercury. This phenomenon might be due to the existence of unspecific interactions between the hydroxyl groups present on the cellulose and the mercury ions, nevertheless this is not a specific process and the retained amount may vary with the presence of different cations in solution.

On the other hand, when the aqueous Hg^{2+} solution is filtered through the composite cellulose column the extraction percentage is increased until the 55% (838 ppb) of the total mercury present in solution, due to the specific anchoring of the metal to our ligand.[87,177] The relatively low retention percentage might also be due to the reduced contact time between the composite and the Hg^{2+} solution when filtered through the column. As a consequence, the same experiment was repeated but this time the cellulose composite (200 mg) were stirred for 4 days in a 10^{-6}M (398 ppb) aqueous solution of $Hg(ClO_4)_2$. ICP-MS results of the filtered solutions show a 48% retention percentage (191 ppb) with respect to the initial Hg^{2+} concentration, in the case of the non treated bare cellulose. On the other hand, results obtained for the composite cellulose increase the retained percentage up to a 94% (376 ppb). Thus, by augmenting the contact time between the cellulose composite and the Hg^{2+} solution it is possible to remove almost completely the presence of Hg^{2+} from aqueous solutions. However, remediation of an analyte does not only implies analyte capture but also this process must be stable enough not to free the contaminant once again. In order to test if the Hg^{2+} anchoring by the

receptor **2** was strong enough, 200 mg of the mercury treated cellulose composite were immersed onto 5 ml of ultrapure water and stirred for 4 days. ICP-MS of the resultant filtrate showed a Hg^{2+} concentration of 7 ppb which correspond to a 1.9% of the total retained. Therefore, it is possible to say that our composite is not only possible to capture up to a 94% of the total mercury but also that this process is irreversible avoiding the returning of the analyte to the media.

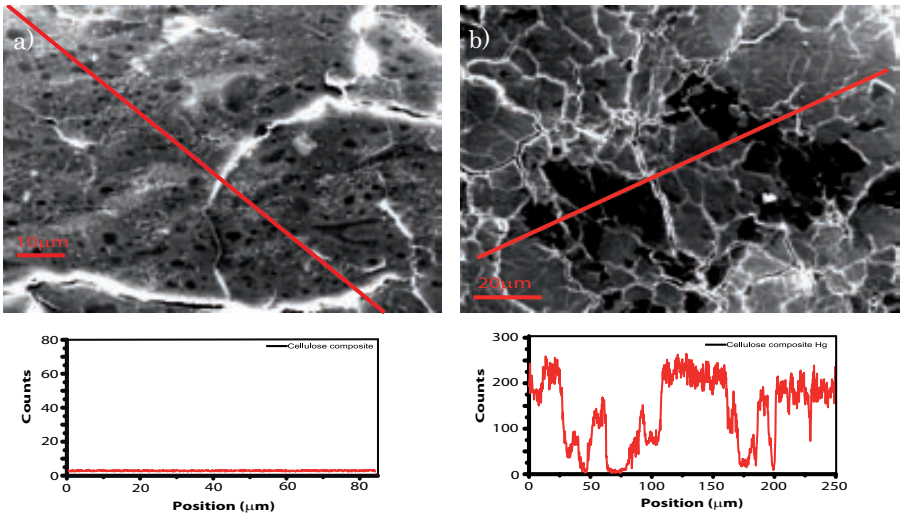

Figure 6.68: SEM images and EDX Hg^{2+} profile analysis (red lines) of freshly prepared compound **2** cellulose composites a) before and b) after immersion for 4 days on a 10^{-6} M $Hg(ClO_4)_2$ aqueous solution. Bellow are the two Hg profiles obtained by EDX.

Distribution analysis of the Hg^{2+} in the cellulose matrix was studied by using EDX analysis as shown in Figure 6.68. Results obtained show an homogeneous dispersion of Hg^{2+} over the cellulose matrix, indicating no segregation of the receptor during the recognition process. Furthermore, while prior to Hg^{2+} treatment it is possible to observe how the ligand is distributed as small microcrystals into the cellulose matrix (Figure 6.66), after being in contact with the heavy metal ions, these crystals are not seen, entailing an increase of homogeniousity of the system during the recognition process.

Mercury indicative properties of the composite were determined by UV-Vis and fluorescence spectroscopies. Figure 6.69 represents the dramatic change suffered by the UV-Vis spectra and the fluorescence emission of the composite prior and after being in contact with a 10^{-3}M $Hg(ClO_4)_2$ aqueous solution. Before contacting with the Hg^{2+} the composite showed an intense band at 375 nm. This

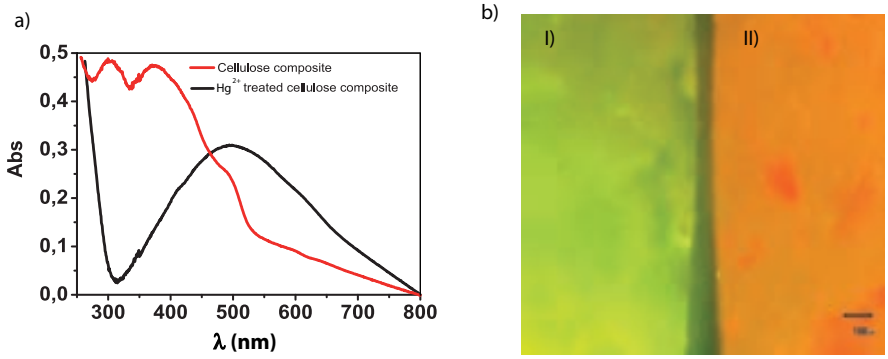

Figure 6.69: a) UV-Vis spectra and b) Fluorescence emission images of the cellulose composite I) before, and II) after mercury complexation.

signal, as well as the green emission observed in the fluorescence image, can be associated with the presence of supramolecular interactions, between the aromatic parts of the free ligand, and the surrounding cellulose matrix,[181] resulting on a bathochromic shift of the spectra from the one obtained in solution.[87] However, once in contact with the analyte, a new band at 515 nm corresponding to the mercury complex, appears upon disappearance of the one at 375 nm. The same shift is observed on the fluorescence image, where the Hg^{2+} treated sample shows an intense red emission in contrast with the green one previously observed. These two facts are related with the change of the electronic properties of the receptor compound after the anchoring of the mercury and allows us not only to know when mercury has been retained by our composite but to do it using simple optical techniques or even with naked eye. Until know, we have probed how the use of the reported composite cellulose material, based on the use of receptor **2** as Hg^{2+} anchoring moiety, is able to drastically reduce the presence of Hg^{2+} present in aqueous media (94% of the total Hg^{2+} present in contaminated water was retained after 4 days of treatment). Furthermore, throughfully washing tests performed to the Hg^{2+} loaded composite showed the release of insignificant amounts Hg^{2+} ions to the clean media, indicating the Hg^{2+} anchoring ocurrs via the formation of strong and stable bonds between the Hg^{2+} and the receptor **2** inside the cellulose matrix. Thus, it is feasible the use of this system not only for the *in situ* static Hg^{2+} remediation but also for the *on flow* Hg^{2+} removal of contaminated water sources.

Nevertheless, the remediation procedure does not finish with the elimination of the

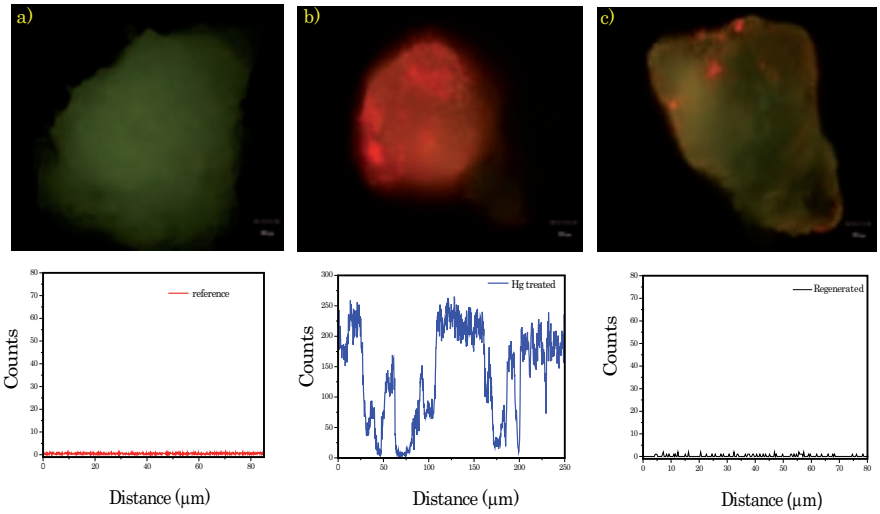

Figure 6.70: Fluorescence image and Hg^{2+} EDX analysis of: a) a particle of freshly prepared cellulose composite, b) Hg^{2+} treated composite particle and c) EDTA regenerated composite particle.

toxic element from the contaminated site, but the adequate disposal of the retained contaminant should be feasible. Recovering assays of the cellulose composite were carried out by slurring of the mercury-rich composite with 3 ml of 1 M aqueous solution of ethylenediaminetetraacetic acid (EDTA). The fluorescence images and EDX analysis line spectra of the initial, Hg^{2+} loaded and regenerated composites are shown in Figure 6.70. Results obtained indicate the almost complete regeneration of the cellulose composite after EDTA treatment and the recovery of the initial characteristics of the composite.

6.3.3 Conclusions

The combined use of an ionic liquid and the organic mercury receptor **2** has allowed to convert a cheap and renewable polymer, such as cellulose, into a promising material able not only of remove the presence of mercury ions in water sources but also to give colorimetric and fluorimetric feedback of the total load. Furthermore, regeneration studies performed on the Hg^{2+} loaded composite, indicate the possibility of releasing the retained Hg^{2+} using a small volume of a concentrated (1 M) EDTA aqueous solution. This result permits not only the re-usability of the composite but also the extraction and concentration of the retained Hg^{2+} in order

to be treated thereafter for its proper elimination. Thus, it is possible to conclude that this composite material supposes an advance on the developing of new, cheap and effective environmental friendly devices, applicable to the remediation of mercury cations in aqueous media.*

*Some of the obtained results, about remediation with the composite material, have been submitted for publication.

Chapter 7

General Conclusions

This part of the Thesis has been focused on the processing of organic functional materials for the development of new systems to fight against Hg^{2+} environmental pollution. Herein we have presented how by the combined use of organic chemistry and different materials processing and structuring techniques it is possible to obtain simple and highly efficient devices with promising properties on the above mentioned field.

First, we have proposed a detection mechanism to explain the bonding process involved on the metal ion recognition by the 1-(4'-metoxyphenyl)-4(2'-pyrenyl)-2,3-diaza-1,3-butadiene (**2**) Hg^{2+} chemosensor molecule that remained still unknown. Furthermore, and taking into account the actual need of fast, cheap and reliable Hg^{2+} determination devices, we have achieved the obtaining of two different Hg^{2+} sensing probes, both based on the use of cellulose derivatives as supporting substrate, but settled on different recognition techniques. Thus, colorimetric cellulose Hg^{2+} probes were developed with the Hg^{2+} chemosensor molecule 1,4-diferrocenyl-2,3-diaza-1,3-butadiene (**1**), and using the "developing technique". Due to its colorimetric origin, *"naked-eye"* and spectrophotometric read-outs of the analytical signal were tested. Although for both approaches, detection limits obtained were higher than the EU or EPA allowed Hg^{2+} concentration in drinkable water, the development of this kind of sensing probes supposes a probe of concept on the use of simple processing techniques for the anchoring of organic sensing molecules onto polymeric organic substrates.

A higher degree of success was obtained using the "reprecipitation method" for the production of nanoparticles of both Hg^{2+} organic receptors **1** and **2**, as highly stable and uniform coatings over cellulose fiber matrix. Hg^{2+} detection tests performed

for both probes showed heterogeneous results. While for the cellulose stripes of compound **1** no analytical response was detected, fluorescence measurements carried out with the compound **2** coated membranes allowed us to sense down to the units of ppb of Hg^{2+} in pure aqueous solutions, matching the legal requirements of the EU and the EPA. Furthermore selectivity assays indicated the absence of any recognition event with any of the 13 tested solutions bearing different cations with various charges and chemical behaviors. Therefore, it is possible to conclude that we succeed on the developing of a new, extremely cost effective and fully reliable system for the fast and the *"in-situ"* control of Hg^{2+} concentrations in water sources. However, the development of a Hg^{2+} sensing device able to compete with the actual extremely sensitive Hg^{2+} detection techniques based on mass spectrometry or atomic absorption, but with the advantage of making continuous and "in-field" measurements was still one of our objectives. Thence, and making use of the group expertise in organic synthesis and surface chemistry we focused our work on the design and synthesis of the new sensing molecule **4**, based of the same 2,3-diazabutadiene sensing unit, to be employed on one of the most sensitive optical detection techniques nowadays available, the surface plasmon resonance (SPR). Results obtained overcome our initial expectancies, as Hg^{2+} detection limits down to the picomolar range were achieved without loosing any selectivity. Moreover, reusability test showed the possibility of recycling the sensor up to four times, a fact that, to the best of our knowledge, was unprecedented on the SPR Hg^{2+} sensors.

Our last objective was based on the preparation of a chemical Hg^{2+} removal system which was tackled with the developing a cellulose composite with receptor **2**. Solved the initial problems to obtain an homogeneous system we succeed on the obtaining of a promising material that not only removes up to the 94% of the Hg^{2+} present in water without the existence of leaking problems but also acts as chromogenic and fluorescent indicator of the presence of such a pernicious metal ion.

Thus, as the final conclusion of this first part of the thesis, it is possible to say that we successfully achieved most of our initial objectives, proving that the use and processing of organic functional materials for the control and removal of environmental pollution is advantageous for the developing of sensing systems.

Bibliography

[1] Janata, J.; Bezegh, A. *Analytical Chemistry* **1988**, *60*, 62–74R.

[2] Wolfbeis, O. S. *Fresenlus Journal of Analytical Chemistry* **1999**, *337*, 522–527.

[3] Janata, J. *Chemical Reviews* **2008**, *108*, 327–328.

[4] Rakow, N. A.; Suslick, K. S. *Nature* **2000**, *406*, 710–713.

[5] Birks, J. B. *Reports on Progress in Physics* **1975**, *38*, 903–974.

[6] Wu, J.-S.; Zhou, J.-H.; Wang, P.-F.; Zhang, X.-H.; Wu, S.-K. *Organic Letters* **2005**, *7*, 2133–2136.

[7] Masson, J.-F.; Battaglia, T. M.; Khairallah, P.; Beaudoin, S.; Booksh, K. S. *Analytical Chemistry* **2007**, *79*, 612–619.

[8] Mancin, F.; Rampazzo, E.; Tecilla, P.; Tonellato, U. *Chemistry - A European Journal* **2005**, *12*, 1844–1854.

[9] de Silva, A. P.; Gunaratne, H. Q. N.; Gunnlaugsson, T.; Huxley, A. J. M.; McCoy, C. P.; Rademacher, J. T.; Rice, T. E. *Chemical Reviews* **1997**, *97*, 1515–1566.

[10] Callan, J. F.; Silva, A. P.; Magri, D. C. *Tetrahedron* **2005**, *61*, 8551–8588.

[11] Lee, J. Y.; Kim, S. K.; Jung, J. H.; Kim, J. S. *The Journal of Organic Chemistry* **2005**, *70*, 1463–1466.

[12] Basudam, A.; Sarmishtha, M. *Progress in Polymer Science* **2004**, *29*, 699–766.

[13] Basabe-Desmonts, L.; Reinhoudt, D. N.; Crego-Calama, M. *Chemical Society Reviews* **2007**, *36*, 993–1017.

[14] Rampazzo, E.; Brasola, E.; Marcuz, S.; Mancina, F.; Tecilla, P.; Tonellato, U. *Journal of Materials Chemistry* **2005**, *15*, 2687–2696.

[15] Onclin, S.; Ravoo, B. J.; Reinhoudt, D. N. *Angewandte Chemie International Edition* **2005**, *44*, 6282–6304.

[16] Murphy, C. J. *Analytical Chemistry* **2002**, *74*, 520–526.

[17] Zheng, Y.; Orbulescu, J.; Ji, X.; Andreopoulos, F. M.; Pham, S. M.; Leblanc, R. M. *Journal of the American Chemical Society* **2003**, *125*, 2680–2686.

[18] Tao, A.; Kim, F.; Hess, C.; Goldberger, J.; R, H.; Sun, Y.; Xia, Y.; Yang, P. *Nano Letters* **2003**, *3*, 1229–1233.

[19] Pallavicini, P.; Yuri, S.; Diaz-Fernandez, A.; Foti, F.; Mangano, C.; Patroni, S. *Chemistry - A European Journal* **2007**, *13*, 178–187.

[20] Edwards, K. A.; Baeumner, A. J. *Talanta* **2006**, *68*, 1421–1431.

[21] Yoshimura, I.; Miyahara, Y.; Kasagi, N.; Yamane, H.; Ojida, A.; Hamachi, I. *Journal of the American Chemical Society* **2004**, *126*, 12204–12205.

[22] Qin, W.; Parzuchowski, P.; Zhang, W.; Meyerhoff, M. E. *Analytical Chemistry* **2003**, *75*, 332–340.

[23] Badr, I. H. A.; Meyerhoff, M. E. *Journal of the American Chemical Society* **2005**, *127*, 5318–5319.

[24] Schulz-Ekloff, G.; Woehrle, D.; van Duffel, B.; Schoonheydt, R. A. *Microporous and Mesoporous Materials* **2002**, *51*, 91–138.

[25] Binning, G.; Quate, C. F. *Physical Review Letters* **1986**, *56*, 930–933.

[26] Wilbur, J. L.; Kumar, A.; Kim, E.; Whitesides, G. M. *Advanced Materials* **1994**, *6*, 600–604.

[27] Thomas, S. W.; Joly, G. D.; Swager, T. M. *Chemical Reviews* **2007**, *107*, 1339–1386.

[28] Crego-Calama, M.; Reinhoudt, D. N. *Advanced Materials* **2001**, *13*, 1171–1174.

[29] Basabe-Desmonts, L.; Beld, J.; Zimmerman, R. S.; Hernando, J.; Mela, P.; García-Parajo, M. F.; van Hulst, N. F.; van den Berg, A.; Reinhoudt, D. N.; Crego-Calama, M. *Journal of the American Chemical Society* **2004**, *126*, 7293–7299.

[30] Duffus, J. H. *Pure and Applied Chemistry* **2002**, *74*, 793–807.

[31] Lutz, H.; Newman, D. K. *Geomicrobiology*; CRC Press, 2008.

[32] Adriano, D. C. *Trace Elements in terrestrial Environments : Biogeochemistryand Bioavailability and Risks of Metals*, second edition ed.; Springerand New York, 2001.

[33] *Technical Background Report to the Global Atmospheric Mercury Assessment*; Tech. Rep.; Arctic Monitoring and Assessment Programme (AMAP) / United Nations Environmental Program (UNEP) Chemicals Branch; 2008.

[34] Environmental; Protection; Agency **2006**, *EPA-HQ-OPPT-2005-0013*.

[35] Cotton, F. A.; Wilkinson, G.; Murillo, C. A.; Bochmann, M. *Advanced Inorganic Chemistry*; Wiley-VCH Verlag GmbH Co. Weinheim, 1999.

[36] Mason, R. P.; Morel, F. M. M.; Hemond, H. F. *Waterand Airand & Soil Pollution* **1995**, *80*, 775–787.

[37] Amyot, M.; Mierle, G.; Lean, D.; Queen, D. J. M. *Geochimica et Cosmochimica Acta* **1997**, *61*, 975–987.

[38] Alberts, J. J.; Schindler, J. E.; Miller, R. W.; Nutter, D. E. J. *Science* **1974**, *184*, 895–897.

[39] Munthe, J. *Atmospheric Environment* **1992**, *26*, 1461–1468.

[40] Fitzgerald, W. F.; Engstrom, D. R.; Mason, R. P.; Nater, E. A. *Environmental Science & Technology* **1998**, *32*, 1–7.

[41] Sung-Chan, C.; Chase, T.; Bartha, T. *Applied and Environmental Microbiology* **1994**, *60*, 4072–4077.

[42] Gilmourand, C. C.; Henry, E. A.; Mitchell, R. *Environmental Science and Technology* **1992**, *26*, 2281–2287.

[43] King, J. K.; Kostka, J. E.; Frischer, M. E.; Saunders, F. M.; Jahnke, R. A. *Environmental Science and Technology* **2001**, *35*, 2491–2496.

[44] Fergusson, J. E. *The Heavy Elements: Chemistryand Environmental Impact and Health effects*; Pergamon Pressand Oxford, 1991.

[45] Kaiser, G. *The Handbook fo Environmental Chemistry*; Springer Verlag, 1980; Vol. 3.

[46] Harada, M. *Critical Reviews in Toxicology* **1995**, *25*, 1–24.

[47] WHO *International Programme on Chemical Safety and Geneva* **1990**.

[48] UNEP, A. *Technical Background Report to the Global Atmospheric Mercury Assessment*; Artic monitoring and Assessment Programeand UNEP Chemical Branch, 2008.

[49] Clarkson, T. *Critital Reviews in Clinical Laboratory Sciences* **1997**, *34*, 369–403.

[50] Placido-Torres, D.; Borges, D. L. G.; Frescura, V. L. A.; Curtius, A. J. *Journal of Analytical Atomic Spectrometry* **2009**, *24*, 1118–1122.

[51] Arpadjan, S.; Vuchkova, L.; Kostadinova, E. *Analyst* **1997**, *122*, 243–246.

[52] Stockwell, P. B.; Corns, W. T.; Allen, J. *Journal of Analytical Atomic Spectrometry* **2009**, *24*, 1026–1033.

[53] Nolan, E. L.; Lippard, S. J. *Chemical Reviews* **2008**, *108*, 3443–3480.

[54] Kim, J. H.; Hwang, A. R.; Chang, S. K. *Tetrahedron Letters* **2004**, *45*, 7557–7561.

[55] Cha, N. R.; Kim, M. Y.; Kim, Y. H.; Choe, J. I.; Chang, S. K. *Jounal of the Chemical Society: Perkin Transactions 2* **2002**, *6*, 1193.

[56] Rurack, K.; Kollmannsberger, M.; Resch-Genger, U.; Daub, J. *Journal of the American Chemical Society* **2000**, *122*, 968–969.

[57] Rurack, K.; Resch-Genger, U.; Bricks, J. L.; Spieles, M. *Chemical Communications* **2000**, 2103–2104.

[58] Mi-Young, C.; Czarnik, A. W. *Journal of the American Chemical Society* **1992**, *114*, 9704–05.

[59] Wang, J.; Qian, X. *Organic Letters* **2006**, *8*, 3721–3724.

[60] Tatay, S.; Gavia, P.; Coronado, E.; Palomares, E. *Organic Letters* **2006**, *8*, 3857–3860.

[61] Murkovic, I.; Wolfbeis, O. S. *Sensors and Actuators B* **1997**, *39*, 246–251.

[62] European-Union, E.; *Council directive 98/83/EC L330/32*.

[63] Coronado, E.; Galan-Mascaro, s. J. R.; Marti-Gastaldo, C.; Palomares, E.; Durrant, J. R.; Vilar, R.; Gratzel, M.; Nazeeruddin, K. *Journal of the American Chemical Society* **2005**, *127*, 12351–12356.

[64] Palomares, E.; Vilar, R.; Durrant, J. R. *Chemical Communications* **2004**, 362–363.

[65] Chen, L.; McBranch, D. W.; Wang, H. L.; Helgeson, R.; Wudl, F.; Whitten, D. G. *Proceedings of the National Academy of Sciences* **1999**, *96*, 12287–12292.

[66] Heeger, P. S.; Heeger, A. J. *Proceedings of the National Academy of Sciences* **1999**, *96*, 12219–12221.

[67] Liu, X.; Tang, Y.; Wang, L.; Zhang, J.; Song, S.; Fan, C.; Wang, S. *Advanced Materials* **2007**, *19*, 1471–1474.

[68] Lee, J. S.; Mirkin, C. A. *Analytical Chemistry* **2008**, *80*, 6805–6808.

[69] Taton, T. A.; Mirkin, C. A.; Letsinger, R. L. *Science* **2000**, *289*, 1757–1760.

[70] Tanaka, Y.; Oda, S.; Yamaguchi, H.; Kondo, Y.; Kojima, C.; Ono, A. *Journal of the American Chemical Society* **2007**, *129*, 244–245.

[71] Zhang, X. B.; Guo, C. C.; Li, Z. Z.; Shen, G. L.; Yu, R. Q. *Analytical Chemistry* **2002**, *74*, 821–825.

[72] Metivier, R.; Leray, I.; Lebeau, B.; Valeur, B. *Journal of Materials Chemistry* **2005**, *15*, 2965–2973.

[73] Lee, J.; Jun, H.; Kim, J. *Advanced Materials* **2009**, *21*, 3674–3677.

[74] Hinton, J.; Veiga, M. In *National Institute for Minamata Disease. Forum 2001. Mar. 19-20, 2001, Minamata, Japan.*

[75] Mulligan, C. N.; Yong, R. N.; Gibbs, B. F. *Engineering Geology* **2001**, *60*, 193–207.

[76] Dbrowski, A.; Hubicki, Z.; Podkoscielny, P.; Robens, E. *Chemosphere* **2004**, *56*, 91–106.

[77] Gavrilescu, M. *Engineering in Life Sciences* **2004**, *4*, 219–232.

[78] Liu, J.; Feng, X.; Fryxell, G. E.; Wang, L. Q.; Kim, A. Y.; Gong, M. *Advanced Materials* **1998**, *10*, 161–165.

[79] Vieira, R. S.; Beppu, M. M. *Water Research* **2006**, *40*, 1726–1734.

[80] Sun, C.; Qu, R.; Ji, C.; Wang, Q.; Wang, C.; Sun, Y.; Cheng, G. *European Polymer Journal* **2006**, *42*, 188–194.

[81] Wagner-Dobler, I.; von Canstein, H.; ; Timmis, K.; Deckwer, W. D. *Environmental Science and Technology* **2000**, *34*, 4628–4634.

[82] Manos, M. J.; Kanatzidis, M. G. *Chemistry - A European Journal* **2009**, *15*, 4779–4784.

[83] Ros-Lis, J.; Casasus, R.; Comes, M.; Coll, C.; Marcos, M. D.; Martinez-Manez, R.; Sancenon, F.; Soto, J.; Amoros, P.; Haskouri, H.; Rurack, K. *Chemistry - A European Journal* **2008**, *14*, 8267–8278.

[84] Molina, P.; Tarraga, A.; Caballero, A. *European Journal of Inorganic Chemistry* **2008**, *2008*, 3401–3417.

[85] Caballero, A.; Lloveras, V.; Tarraga, A.; Espinosa, A.; Velasco, M. D.; Vidal-Gancedo, J.; Rovira, C.; Wurst, K.; Molina, P.; Veciana, J. *Angewandte Chemie* **2005**, *44*, 1977–1981.

[86] Winnik, F. M. *Chemical Reviews* **1993**, *93*, 587–614.

[87] Caballero, A.; Martinez, R.; Lloveras, V.; Ratera, I.; Vidal-Gancedo, J.; Klaus, W.; Tarraga, A.; Pedro, M.; Jaume, V. *Journal of the American Chemical Society* **2005**, *127*, 15666–15667.

[88] So-Youn, M.; Na Jin, Y.; Sang, M. P.; Suk-Kyu, C. *Journal of Organic Chemistry* **2005**, *70*, 2394–2397.

[89] Jong Seung, K.; Duong Tuan, Q. *Chemical Reviews* **2007**, *107*, 3780–3799.

[90] Hamada, F.; Narita, M.; Kinoshita, K.; Makabea, A.; Osa, T. *Journal of Perkin Transactions 2* **2001**, 388–394.

[91] Bichenkova, E. V.; Abdul, G.; Walsh, L.; Savage, H. E.; Rogert, C.; Sardarian, A. R.; Etchells, L. L.; Douglas, K. T. *Organic & Biomolecular Chemistry* **2007**, *5*, 1039–1051.

[92] Nishizawa, S.; Kaneda, H.; Uchida, T.; Norio, T. *Journal of the Chemical Society Perkin Transactions* **1998**, *2*, 2.

[93] Sankaran, N. B.; Nishizawa, S.; Watanabe, M.; Uchida, T.; Teramae, N. *Journal of Materials Chemistry* **2005**, *15*, 2755–2761–.

[94] Bichenkova, E. V.; Sardarian, A. R.; Wilton, A. N.; Bonnet, P.; Bryce, R. A.; Douglas, K. T. *Organic & Biomolecular Chemistry* **2006**, *4*, 367–378–.

[95] Zhang, X.; Cunningham, M. M.; Walker, R. A. *Journal of Physical Chemistry B* **2003**, *107*, 3183–3195.

[96] Kamlet, M. J.; Taft, R. W. *Journal of the American Chemical Society* **1976**, *98*, 377–383.

[97] Kamlet, M. J.; Abboud, J. L.; Taft, R. W. *Journal of the American Chemical Society* **1997**, *99*, 6027–6038.

[98] Taft, R. W.; Kamlet, M. J. *Journal of the American Chemical Society* **1976**, *98*, 2886–2894.

[99] Marcus, Y. *Chemical Society Reviews* **1993**, *22*, 409–416.

[100] Hildebrand, J. H.; Scott, R. L. *The solubility of Non-Electrolytes*; Dover Publications: New York, 1964.

[101] Zhao, Y.; Truhlar, D. G. *Journal of Physical Chemistry A* **2005**, *109*, 5656–5667.

[102] King, R. B. *Encyclopedia of Inorganic Chemistry*; Wiley, Chichester, 2005.

[103] Sun, S.; Bernstein, E. R. *Journal of Physical Chemistry* **1996**, *100*, 13348–13366.

[104] Klemm, D.; Heublein, B.; Fink, H.-P.; Bohn, A. *Angewandte Chemie International Edition* **2005**, *44*, 3358–3393.

[105] Kontturi, E.; Tammelin, T.; Osterberg, M. *Chemical Society Reviews* **2006**, *35*, 1287–1304.

[106] Martinez, A.; Phillips, S.; Butte, M.; Whitesides, G. *Angewandte Chemie International Edition* **2007**, *46*, 1318–1320.

[107] May, K. M. L. M.; Wang, Y.; Bachas, L. G.; Anderson, K. W. *Analytical Chemistry* **2004**, *76*, 4156–4161.

[108] Poplin, J. H.; Swatloski, R. P.; Holbrey, J. D.; Spear, S. K.; Metlen, A.; Graetzel, M.; Nazeeruddin, M. K.; Rogers, R. D. *Chemical Communications* **2007**, *20*, 2025–2027.

[109] Carofiglio, T.; Fregonese, C.; Mohr, G. J.; Rastrelli, F.; Tonellato, U. *Tetrahedron* **2006**, *62*, 1502–1507.

[110] Takahashi, Y.; Kasai, H.; Nakanishi, H.; ; Suzuki, T. M. *Angewandte Chemie International Edition* **2006**, *45*, 913–916.

[111] Freudenberg, U.; Zimmermann, R.; Schmidt, K.; Behrens, S. H.; Carsten, W. *Journal of Colloids and Interface Science* **2007**, *309*, 360–365.

[112] Horn, D.; Rieger, J. *Angewandte Chemie* **2001**, *40*, 4330–4361.

[113] Jian, Y.; Hong-zheng, C.; Mang, W. *Journal of Materials Science* **2003**, *38*, 4021–4025.

[114] Asahi, T.; Sugiyama, T.; Masuhara, H. *Accounts of Chemical Research* **2008**, *41*, 1790–1798.

[115] Kashai, K.; Nalwa, H. S.; Oikawa, S.; Matsuda, H.; Minami, N.; Kakuta, A.; Ono, K.; Nakanishi, H. *Japan Journal of Applied Physics* **1992**, *31*, 1132–1134.

[116] Byeong-Kwan, A.; Soon-Ki, K.; Sang-Don, J.; Soo-Young, P. *Journal of the American Chemical Society* **2002**, *124*, 14410–14415.

[117] Hong-Bing, F.; Jian-Nian, Y. *Journal of the American Chemical Society* **2001**, *123*, 1434–1439.

[118] Ulman, A. *Chemical Reviews* **1996**, *96*, 1533–1554.

[119] Nuzzo, R. G.; Allara, D. L. *Journal of the American Chemical Society* **1983**, *105*, 4481–4483.

[120] Sagiv, J. *Journal of the American Chemical Society* **1980**, *102*, 92–98.

[121] Chechik, V.; Crooks, R. M.; Stirling, C. J. M. *Advanced Materials* **2000**, *12*, 1161–1171.

[122] Bishop, A. R.; Nuzzo, R. G. *Current oppinion in Colloid and Interface Science* **1996**, *1*, 127.

[123] Nuzzo, R. G.; Zegarski, B. R.; Dubois, L. H. *Journal of the American Chemical Society* **1987**, *109*, 733–740.

[124] Gooding, J. J.; Mearns, F.; Yang, W.; Liu, J. *Electroanalysis* **2003**, *15*, 81–93.

[125] Zhang, S.; Cardona, C. M.; Echegoyen, L. *Chemical Communications* **2006**, 4461–4473.

[126] Basabe-Desmonts, L.; Reinhoudt, D. N.; Crego-Calama, M. *Chemical Society Reviews* **2007**, *36*, 993–1017.

[127] Cooper, M. A. *Nature Reviews in drug discovery* **2002**, *1*, 515–528.

[128] Homola, J. *Chemical Reviews* **2008**, *108*, 462–493.

[129] Homola, J. *Surface Plasmon Resonance Sensors*; Springer Verlagand Berlin Springer Series on Chemical Sensors and Biosensors, 2006.

[130] A, C. M. *Nature Reviews Drug Discovery* **2002**, *1*, 515–528.

[131] Frasconi, M.; Deriu, D.; D'Annibale, A.; Mazzei, F. *Nanotechnology* **2009**, *20*, 505501.

[132] Kanoh, N.; Kyo, M.; Inamori, K.; Ando, A.; Asami, A.; Nakao, A.; Osada, H. *Analytical Chemistry* **2006**, *78*, 2226–2230.

[133] Houseman, B. T.; Huh, J. H.; Kron, S. J.; Mrksich, M. *Nature Biotechnology* **2002**, *20*, 270–274.

[134] Mandon, C. A.; Blum, L. J.; Marquette, C. A. *ChemPhysChem* **2009**, *10*, 3273–3277.

[135] Homola, J.; Yee, S. S.; Gauglitz, G. *Sensors and Actuators B: Chemical* **1999**, *54*, 3–15.

[136] Yuan, J.; Deng, D.; Lauren, D. R.; Aguilar, M.-I.; Wu, Y. *Analytica Chimica Acta* **2009**, *656*, 63–71.

[137] Wang, Y.; Brunsen, A.; Jonas, U.; Jakub, D.; Knoll, W. *Analytical Chemistry* **2009**, *81*, 9625–9632.

[138] Yu, Y.; Feng, C.; Caminade, A.-M.; Majoral, J.-P.; Knoll, W. *Langmuir* **2009**, *25*, 13680–13684.

[139] Shankaran, D.; Ravi, G.; Vengatajalabathy, K.; Miura, N. *Sensors and Actuators B: Chemical* **2007**, *121*, 158–177.

[140] Wang, S.; Forzani, E. S.; Tao, N. *Analytical Chemistry* **2007**, *79*, 4427–4432.

[141] Chah, S.; Yi, J.; Zare, R. N. *Sensors and Actuators B: Chemical* **2004**, *99*, 216–222.

[142] Chen, H.; Gal, Y. S.; Kim, S. H.; Choi, H. J.; Oh, M. C.; Lee, J.; Koh, K. *Sensors and Actuators B: Chemical* **2008**, *133*, 577–581.

[143] Kang, T.; Hong, S.; Moon, J.; Oh, S.; Yi, J. *Chemical Communications* **2005**, 3721–3723.

[144] Sigal, G. B.; Bamdad, C.; Barberis, A.; Strominger, J.; Whitesides, G. M. *Analytical Chemistry* **1996**, *68*, 490–497.

[145] Lahiri, J.; Isaacs, L.; Tien, J.; Whitesides, G. M. *Analytical Chemistry* **1999**, *71*, 777–790.

[146] Zwierzak, A.; Slulewska, A. *Synthesis* **1976**, 835–836.

[147] Wadsworth, W. S.; Emmons, E. D. *Journal of Organic Chemistry* **1967**, *32*, 1279–1285.

[148] Wadsworth, W. S.; Emmons, E. D. *Journal of Organic Chemistry* **1964**, *29*, 2816–2820.

[149] Pale-Grosdemange, C.; Simon, E. S.; Prime, K. L.; M., W. G. *Journal of the American Chemica Society* **1991**, *113*, 12–20.

[150] Barrientos, A. G.; delafuente, J. M.; Rojas, T. C.; Fernández, A.; Penadés, D. *Chemistry - A European Journal* **2003**, *9*, 1909–1921.

[151] Fengting, L.; Yu, F.; Blanchard, G. *Spectrochimica Acta Part A: Molecular and Biomolecular Spectroscopy* **2009**, *74*, 991–999.

[152] Adamson, A. W. *Physical Chemistry of Surfaces*; Willey: Chicester, 1993.

[153] Geissler, M.; Chen, J.; Xia, Y. *Langmuir* **2004**, *20*, 6993–6997.

[154] Brito, R.; Tremont, R.; Cabrera, C. R. *Journal of Electroanalytical Chemistry* **2004**, *574*, 15–22.

[155] Brito, R.; Tremont, R.; Feliciano, O.; Cabrera, C. R. *Journal of Electroanalytical Chemistry* **2003**, *540*, 53–59.

[156] Weisser, M.; Nelles, G.; Wohlfart, P.; Wenz, G.; Mittler-Neher, S. *The Journal of Physical Chemistry* **1996**, *100*, 17893–17900.

[157] Moulder, J. F.; Stickle, W. F.; Sobol, P. E.; Bomben, K. D. *Handbook of X-ray photoelectron Spectroscopy*; Eden Prairie, Minnesota, Physical Electronics, Inc., 1995.

[158] Graf, N.; Yegen, E.; Gross, T.; Lippitz, A.; Weigel, W.; Krakert, S.; Terfort, A.; Unger, W. E. *Surface Science* **2009**, *603*, 2849–2860.

[159] Fung, M. K.; Tong, S. W.; Lai, S. L.; Bao, S. N.; Lee, C. S.; Wu, W. W.; Inbasekaran, M.; O'Brien, J. J.; Liu, S. Y.; Lee, S. T. *Journal of Applied Physics* **2003**, *94*, 2686–2694.

[160] Wang, J.; Deng, B.; Chen, H.; Wang, X.; Zheng, J. *Environmental Science and Technology* **2009**, *43*, 5223–5228.

[161] Marin, V.; Baybur, T.; Sligar, S.; Mrksich, M. *Angewandte Chemie International Edition* **2007**, *119*, 8952–8954.

[162] Mrksich, M. *ACS Nano* **2008**, *2*, 7–18.

[163] Malmborg, A.; Michaelson, A.; Ohlin, M.; Jansson, B.; Borrebaeck, C. *Scandinavian Journal of Immunology* **1992**, *35*, 643–650.

[164] Karlsson, R.; Michaelsson, A.; Mattsson, L. *Journal of Immunological Methods* **1991**, *145*, 229–240.

[165] Faegerstam, L. G.; Frostell-Karlsson, A.; Karlsson, R.; Persson, B.; Roennberg, I. *Journal of Chromatography A* **1992**, *597*, 397–410.

[166] Morton, T. A.; Myszka, D. G.; Chaiken, I. M. *Analytical Biochemistry* **1995**, *227*, 176–185.

[167] Taewook, K.; Jungwoo, M.; Seogil, O.; Surin, H.; Soonwoo, C.; Jongheop, Y. *Chemical Communications* **2005**, 2360–2362.

[168] Eapen, S.; D-Souza, S. *Biotechnology Advances* **2005**, *23*, 97–114.

[169] Kunkel, A. M.; Seibert, J. J.; Elliott, L. J.; L., K. R.; Katz, L. E.; Pope, G. A. *Environmental Science and Technology* **2006**, *40*, 2384–2389.

[170] Baumann, T. F.; Reynolds, J. G.; Fox, G. A. *Reactive and Functional Polymers* **2000**, *44*, 111–120.

[171] Alexandratos, S. D. *Journal of Hazardous Materials* **2007**, *139*, 467–470.

[172] Nooney, R. I.; Kalyanaraman, M.; Kennedy, G.; Maginn, E. J. *Langmuir* **2001**, *17*, 528–533.

[173] Olkhovyk, O.; Antochshuk, V.; Jaroniec, M. *Colloids and Surfaces A: Physicochemical and Engineering Aspects* **2004**, *236*, 69–72.

[174] Kontturi, E.; Tammelin, T.; Oesterberg, M. *Chemical Society Reviews* **2006**, *35*, 1287–1304.

[175] Klemm, D.; Heublein, B.; Fink, H.-P.; Bohn, A. *Angewandte Chemie International Edition* **2005**, *44*, 3358–3393.

[176] Díez-Gil, C.; Caballero, A.; Ratera, I.; Tárraga, A.; Molina, P.; Veciana, J. *Sensors* **2007**, *7*, 3481–3488.

[177] Diez-Gil, C.; Martinez, R.; Ratera, I.; Tarraga, A.; Molina, P.; Veciana, J. *Journal of Materials Chemistry* **2008**, *18*, 1997–2002.

[178] Navarro, R. R.; Sumi, K.; Fujii, N.; Matsumura, M. *Water Research* **1996**, *30*, 2488–2494.

[179] Chauhan, G. S.; Guleria, L.; Sharma, R. *Cellulose* **2005**, *12*, 97–110.

[180] Liu, Q.; Janssen, M. H. A.; van Rantwijk, F.; Sheldon, R. A. *Green Chemistry* **2005**, *7*, 39–42.

[181] Fazilova, S. A.; Burkhanova, N. D.; Yugai, S. M.; Pulatova, K. P.; Nikonovich, G. V.; Rashidova, S. S. *Pharmaceutical Chemistry Journal* **2005**, *39*, 658–662.

Part IV

Processing of Molecular Materials for Tissue Engineering

Chapter 8

Objectives

The research work developed and presented on this part has been focused on the study, characterization and structuring of a new family of proteinaceous nanoparticulate aggregates, known as inclusion bodies (IBs), with the objective of studying the influence of these biomaterials as growth vectors for the cell proliferation in tissue engineering.
The experimental work carried out can be divided into three main parts: 1) Complete characterization of bacterial IBs coming from different genetic backgrounds 2) Determination of the influence of the genetic background on the final cell proliferation properties of IBs 3) structuring of IBs onto solid substrates for their final use as biomaterial surface modifying elements. A more detailed description of the posed objectives are:

1. **Characterization of the structural, morphological, mechanical and physico-chemical properties of bacterial IBs coming from different genetic backgrounds**. More specifically we will determine the size, shape, superficial charge, wettability and stiffness values of different IBs produced on regular and genetically deficient bacterias. In order to do that, we will make use of different characterization techniques such as DLS, CA, confocal fluorescence and force spectroscopy atomic force microscopy (FSAFM), among others.

2. **Determination of the influence of the genetic background of IBs on their final cell proliferation properties**. The previously characterized IBs will be submitted to cell proliferation studies (in collaboration with the group of Prof. A. Villaverde; *IBB-Universitat Autòma de Barcelona*) in order

to determine if there is any influence of the initial fabrication process on the final IBs-cell interaction.

3. **2D structuring and cell proliferation studies of IBs onto solid substrates.** A proof of concept of the final use of this novel proteinaceous nanoparticulate biomaterial will be made as new surface modification elements for their application in tissue engineering. The nanostructuring of IBs onto the solid surface will me made by means of soft lithographic techniques, such as μ-CP.

"A stone is simple. But you can build cathedrals of stones"

George Whitesides @TED

Chapter 9

Introduction

9.1 Regenerative Medicine

The history of diseases is vastly older than that of humankind itself. Indeed, disease and parasitism have been inseparable companions since the dawn of life on Earth. The human body has not been an exception to that, as it has been constantly subject to assaults and injuries, invasion by parasites, and infections. Nevertheless, mother nature has also given us the tools to fight against these ubiquitous enemies.

Since beginning of times, man has made use of observation and empirical knowledge to use natural products and materials to develop new substances and methods to heal wounds and to cure illnesses. At the beginning, this medical practice was very basic, reduced to the use of certain plants or fungus as a treatment for mild diseases such as intestinal parasites.[1] However, with the course of time, the gain of experience and the augmentation of the available resources made possible the treatment of much complicated affections or even the developing of a number of rudimentary surgical procedures. Figure 9.1 represents a brief timeline of the evolution of western medicine and the materials related to its practice during the last 5000 years.

Todays medicine is far from being the collection of empirical procedures full of superstitions and fears that was in the past. The abandon of the old prejudices and the establishment of the scientific method, together with the enormous effort developed by scientists of every branch of science, have transformed medicine into an innovative multidisciplinary field. This has been reflected on the impressive increase of the life expectancy of man all over the world and more particularly

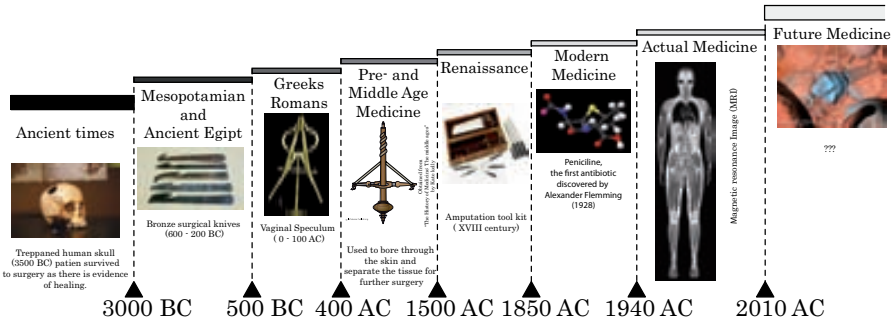

Figure 9.1: Evolution of the paradigm of scientific medicine and the employed materials.

on the developed countries.[2] Nevertheless, there is still work to be done. During ages, our understanding of life has advanced from organs, to tissues, to cells, and finally to molecules, in the 20th century. Nowadays, the ongoing revolution in genomics, proteomics and bioinformatics[3] has provided detailed and precise knowledge of the workings of the human body at the molecular level. This deep molecular familiarity with the human body, along with simultaneous advances in biomaterials science and nanotechnology, will set the stage for a shift from today's medicine in which fundamental new discoveries are constantly being made, to a new medicine era in which the molecular basis of life will be manipulated to produce specific desired results. This is the case of regenerative medicine.

Regenerative medicine is a branch of medicine which aims to restore the function of damaged tissues and organs by helping the body to form new functional tissue to replace lost or defective ones. Much of the recent interest is focused on the late developments in stem cell[4] and biomedical and tissue engineering research.[5]

Depending on the medical approach, regenerative medicine can be divided into four main, but interconnected, research areas:

- **Cell therapies**, based on the use of stem cells for the regeneration of organs and tissues.
- **Tissue engineering**, based on the modification of cells and/or tissues in some way that they can regenerate or replace the damaged tissues in the body by the action of either natural or artificial biomaterials. Most of the times cell therapies and tissue engineering are considered part of one big approach due to their close interconexion.

- **Biomedical engineering**, appeared as another approach to regenerative medicine, it is based in making artificial biomedical devices that mimic the function of a tissue or organ, such as the developing of an artificial pancreas to treat type-1 diabetes.

- **Gene therapy**, based on the recent advances on the understanding of human genome, tries to identify and relate a determined medical condition to the lack or damage of the patient genetic information, solving the problem by delivering the correct gene coding for that protein to the affected cells.[6]

9.2 Processing of Functional Biomaterials

All the presented approaches used for regenerative medicine present exceptional advantages and several possibilities of success. Nevertheless, nowadays the usage of these new medicinal processes is limited by the number of available biomaterials capable of fulfilling all the requirements needed for their correct applications. Therefore, during the last decades, researchers from very different scientific areas such as chemistry, physics, biology or material science, have joint their efforts and focused their attention towards the study and developing of new functional biomaterials capable of interact specifically with biological tissues and to trigger their desired biological responses.
As a consequence, a big number of biomaterial processing and structuring techniques has recently aroused. Depending on the material's final use such techniques can be mainly classified in drug/gene delivery systems, tissue engineering and biosensing materials, among others.

9.2.1 Drug/gene delivery systems

One of the main problems of conventional drug delivery therapies are their limitations to deliver therapeutic drug concentrations to the target tissues and the severe and harmful toxic effects that some drugs can produce on non affected organs and tissues. Therefore, in recent years, a significant effort has been devoted to develop new biomaterials, based on the processing and nanostructuring of drugs, for the controlled drug delivery/targeting.

9.2.1.1 Fabrication of drug/gene delivery biomaterials

Mainly dominated by organic and inorganic nanomaterials, the fabrication processes for drug/gene delivery systems are numerous and very diverse. Among all the possible alternatives it is worthy to remark those related with the synthesis and nanostructuring of polymeric micro- or nanoparticles or with the developing of new funtionalized vesicular structures.

a) Preparation of polymeric micro- or nanoparticles. With the recent advancement in the pharmaceutical technology, new and innovative techniques are being employed in the fabrication of polymeric micro- or nanoparticles. A number of review articles and book chapters describing various aspects of particle preparation and characterization have been published in the last few decades.[7,8] Here we will outline some of the most common techniques used in the preparation of polymeric particles (Figure 9.2).

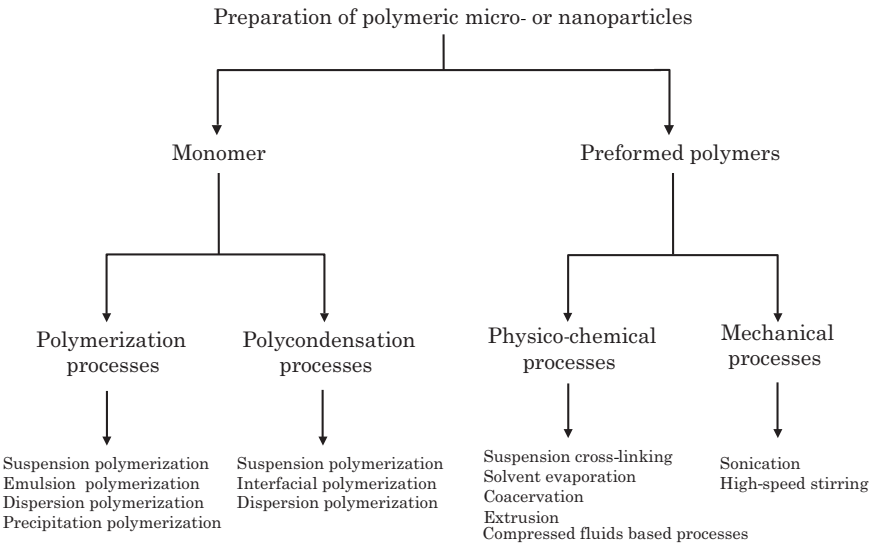

Figure 9.2: Scheme of the commonly employed techniques for the fabrication of polymeric micro- or nanoparticles.

This kind of particulated systems are prepared mainly by two procedures. The first procedure is the "*in situ*" polymerization of monomers to yield polymeric particulates. The most widely used of all of them is the *emulsion polymerization* method. This method is classified into two categories based on the nature of the

continuous phase in the emulsion. In the first case, the continuous phase is aqueous (o/w emulsion), whereas in the other case the continuous phase is organic (w/o emulsion). In either case, the monomer is emulsified in the non-continuous phase with surfactant molecules. The polymerization takes place inside the non-continuous phase triggered by a chemical or physical initiator. The drug to be encapsulated may be incorporated in the reaction medium during the polymerization or can be subsequently added to the preformed particles. The advantage of this technique is that nanoparticles with smaller sizes (50-200 nm) can be obtained. The most used nanoparticles, prepared by this technique, are nanospheres of polymethylmethacrylate, poly(alkyl cyanoacrylate), polyacrylamide, etc.
The second procedure is based on the dispersion of well-characterized preformed polymers of synthetic or natural origin using a suitable physico-chemical processes (Figure 9.2). Between all the plausible techniques, the use of compressed fluids (CFs), such as CO_2, has aroused as an interesting alternative for the polymer processing. These procedures make use of the solvent capability of the liquid or supercritical CO_2 for the material processing, that once employed can be removed from the sample just by a depresurization process. This technique permits to decrease largely the amounts of organic solvent or even to remove completely their need during the fabrication process without altering the particle size ranges. Furthermore, due to their enormous versatility and scale-up properties, CFs appear as a very promising alternative for the industrial production of this kind of nanomaterials for drug-delivery.

b) Preparation of functionalized vesicular structures Since the pioneering observation of *Alec Bangham et al.* roughly 45 years ago, stating that, under determined conditions, phospholipids in aqueous systems can self-assemble forming closed bilayered structures, also know as vesicles, similar to those observed on the lipidic membrane of cells,[9] vesicular systems have become an important topic of research. Thus, they have moved a long way from being just another exotic object of biophysical research to become pharmaceutical carriers of choice for numerous practical applications.[10,11] Vesicular systems constitute very versatile pharmaceutical carriers, since apart from being able to entrap both, hydrophilic and hydrophobic molecules, diverse kinds of changes can be performed in their membrane in order to change their physico-chemical properties and, as a consequence, their performance as drug delivery systems. Ligand-targeted[12] and pH-sensitive[13] vesicles are clear examples in which the membrane composition is

of big importance. Moreover, the extreme processability of this kind of systems allows the functionalization of the vesicular membrane with ligands which specifically interact with the affected tissue or with external stimuli sensitive molecules for a sharp triggering of the drug when necessary. Among all the vesicular systems known, liposomes are, with any doubt, the most studied vesicular systems for drug delivery.

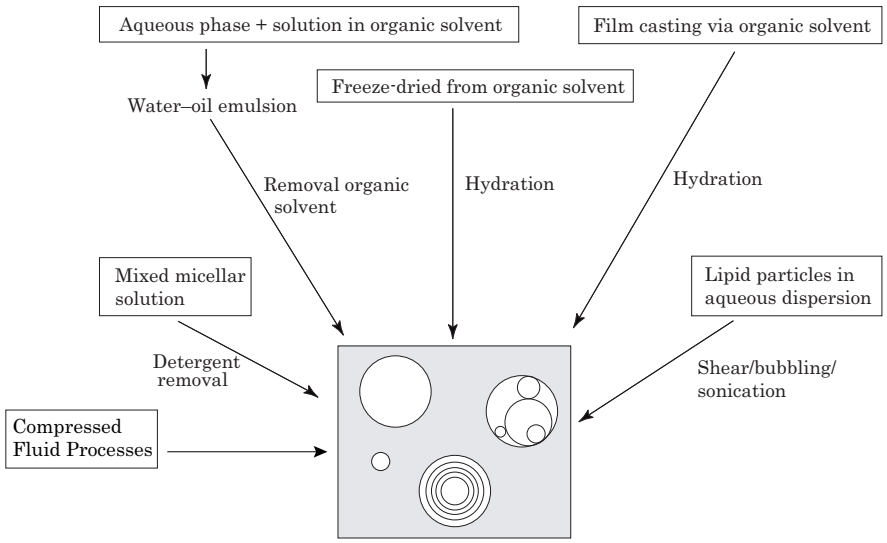

Figure 9.3: Scheme of the commonly employed techniques for the fabrication of vesicular systems.

Figure 9.3 schematically represents the commonly used vesicle preparation techniques, being those involving the hydration or the sonication methods the most used ones. It is possible to remark that depending on the technique used, different kinds of vesicular systems can be obtained, from small unilamelar vesicles to multivesicular and onion-like systems. As in the previous case, CFs have also aroused as an extremely reproducible technique for the large scale production of this kind of systems.

9.2.2 Tissue engineering

Although significant advances have been made in the transplantation of organs or tissues there are many limitations that are difficult to overcome; such as the organ rejection due to immunogenic responses or the shortage of donor organs. Thus,

big efforts have been made to find a feasible solution to such problems. Recently, tissue engineering (TE) which applies methods from materials and life sciences to create artificial constructs to direct tissue regeneration,[14] has attracted many scientists and surgeons with a hope to treat patients in a minimally invasive and less painful way.

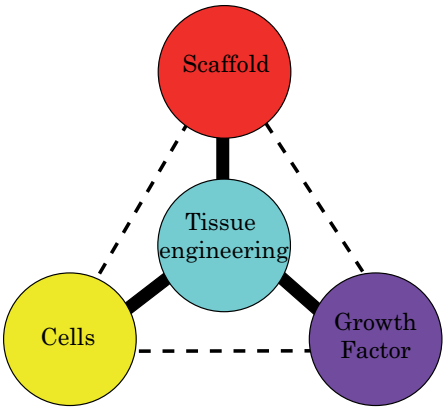

Figure 9.4: Parameters required regenerative medicine based on tissue engineering.

In order to achieve successful regeneration of damaged organs or tissues based on the tissue engineering concept, several critical elements should be considered when designing a new biomaterial. First of all an ideal biomaterial for tissue engineering may serve as mechanical support for cells at the same time that induces, differentiates and channels the tissue growth. Furthermore, it should target cell-adhesion and stimulate the appropriate cellular response providing a wound-healing barrier, and all these aspects without loosing its biocompatibility (Figure 9.4).[15]
Therefore, the number of suitable materials for the developing of this kind of architectures is reduced. Generally, tissue engineering biomaterials are fabricated from biocompatible inorganic materials, like hydroxiapatite scaffolds, or some other bioceramic materials, among others, or from a reduced set of selected natural and synthetic biopolymers, such as chitosane or poly(lactic-co-glycolic acid) (PLGA).[16]
Also combinations of both kinds of materials are used for such purpose.

9.2.2.1 Fabrication of tissue engineering biomaterials

Depending on the nature of the material, fabrication methods can be classified into *inorganic* and *organic*.

a) Fabrication of inorganic biomaterials for tissue engineering. Bioceramics can be produced by a variety of different processes,[17] which, at the same time, may be classified into two main categories: (1) manual-based processing techniques and (2) computer-controlled fabrication processes.[18] Although all of them present promising properties, we will only focus our attention to the manual-based processing techniques and more specifically to the ones based on sol-gel methods.

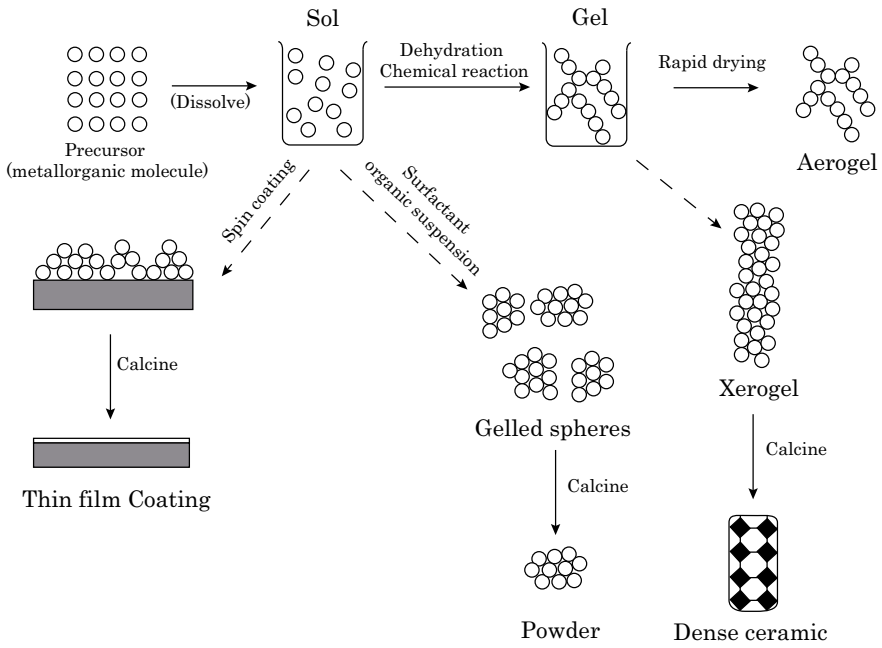

Figure 9.5: Examples of the different final materials that are achievable using the sol-gel method.

The sol-gel process, represented on Figure 9.5 is a well-developed, robust, and versatile wet technique for the synthesis of ceramics and glasses. By applying the sol-gel process, it is possible to fabricate inorganic materials in various forms like ultrafine or spherical shaped powders, thin film coatings, ceramic fibers, microporous inorganic membranes, monolithic ceramics and glasses, and extremely porous aerogel materials.[19] Being the last the most interesting ones from the tissue engineering point of view.

The processing path of aerogel ceramics starts with an alkoxide precursor. Alkoxide precursors, such as tetraethyl orthosilicate and triethoxyl orthophosphate, undergo hydrolysis and condensation reactions to form a sol. In case of silicate precursors, the polymerization of -Si-OH groups continues after the hydrolysis is complete, beginning the formation of the silicate network. The network connectivity increases until it spans throughout the solvent medium. Eventually a "wet gel" is formed. The "wet gel" is then subjected to controlled thermal processes of aging to strengthen the "gel", removing the liquid by-product of the polycondensation reaction. Finally the resulting "gel" is subjected to a thermal stabilization (or sintering) to remove organic species from the surface of the material resulting in the formation of a porous "aerogel".[18]

b) Fabrication of organic polymeric biomaterials for tissue engineering. A large number of fabrication technologies have been applied to process biocompatible polymeric materials for tissue engineering. The conventional fabrication techniques include fiber bonding, solvent casting or particle leaching, among others.[20] Nevertheless, most of these methods require the use of highly toxic organic solvents during the material processing, which increments the time required for solvent evaporation (days-to-weeks) and the difficulty of the fabrication process.[21] As in the case of drug/gene delivery systems, CFs processes have aroused as a interesting alternative for the polymer processing in tissue engineering. When in presence of compressed gases such as, N_2 or CO_2, the polymer granules are plasticized reducing its viscosity and allowing their processing. Furthermore, this approach facilitates the incorporation of heat sensitive pharmaceuticals and biological agents to the biomaterial, as it does not require the use of high temperatures, in contrast to other polymer processing methods, such as the melt molding.[20]

9.2.2.2 Functionalization of surfaces with biomaterials for tissue engineering

Despite the advances performed in the biomaterials field during the last decades, the development of useful biomaterials for tissue engineering is limited due to an incomplete understanding of the specific interface interactions between the biomaterials and the biological systems. When the living organisms are exposed to biomaterials, it is unlikely for cells to directly contact the surface of the material. Despite, the rapid adsorption of biomolecules or physiologic liquids rapidly

translates the composition and properties of the foreign surface into a biological signal. This might lead to a constructive cell response or to cause the isolation or rejection of the implanted material (Figure 9.6).[22] Thus, it is possible to conclude that the first reactions are crucial for the correct developing of the new tissue.

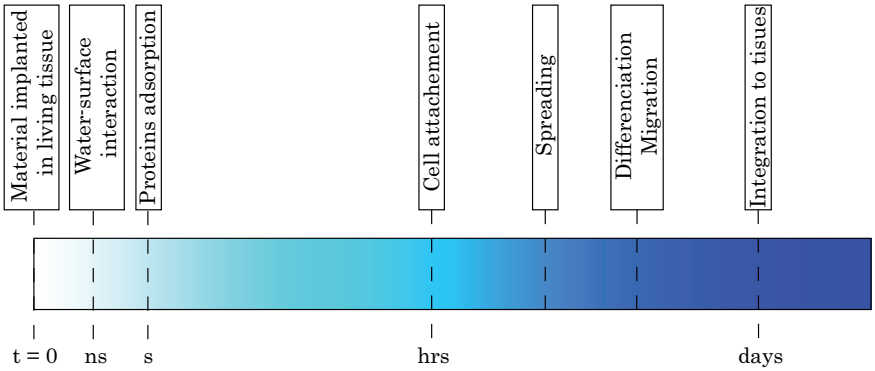

Figure 9.6: Scheme of an ideal biomaterial-tissue interaction timeline.

According to previous works, as the one developed by *Mathieu et al.*[23] these initial interactions of biomaterials with the biological system are determined by a complex set of morphological and physicochemical parameters, such as topography (roughness), stiffness, chemistry or wettability of the top surface layers which are in direct contact with the body fluids and cells. To improve the cell-substrate interaction, different strategies of surface modification have been developed.

a) Surface coating. As previously stated, the first phase of the cell-biomaterial interaction mainly depends on protein adhesion, and more specifically of the presence of two families of proteins, the growth factors[24] and/or adhesion proteins.[25] The pH and the ionic composition of the biological solution together with the temperature, the surface energy and the functional groups present on the surface of the biomaterial are the main factors determining protein adsorption on a specific substrate.[25]

In general, proteins that have a number of charged residues are expected to show a bigger affinity for the opposite charged surfaces due to electrostatic attractions. Thus, by an appropriate pretreatment of the biocompatible substrate, the ionic charges from the surface can be modified, towards the increasing of the affinity of the biomaterial for proteins or other biomolecules.[26] Nevertheless, the situation is not always that easy and the use of deeper surface modification protocols are

required.

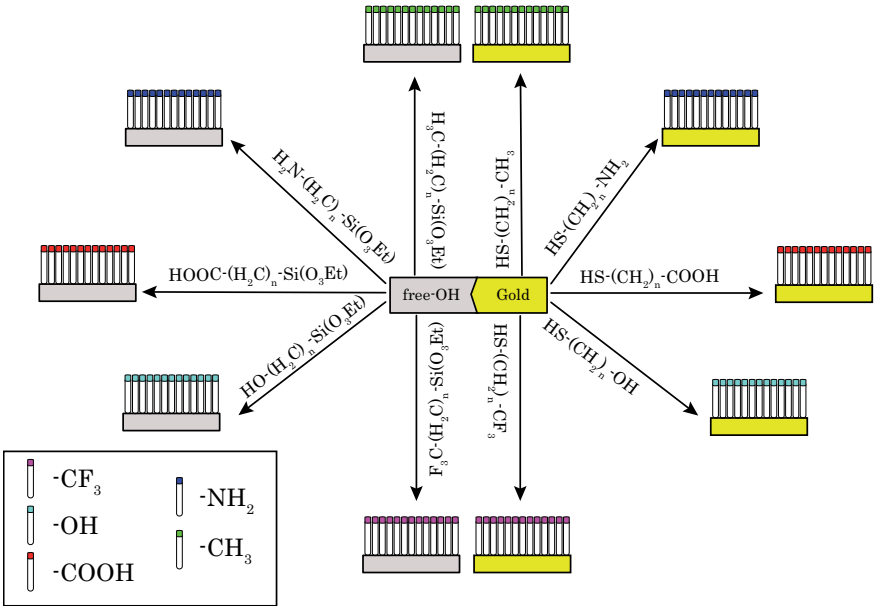

Figure 9.7: Schematic representation of surface chemical modification by means of using self-assembled monolayers.

Surface chemical modifications can be achieved fairly easily at a number of different levels, using plasma or photo induced grafting methods, or more traditional covalent bonding techniques.[27] Nevertheless, when working with metal or silanized surfaces the most common of all of them is to make use of chemical self-assembled monolayers (SAMs) (Figure 9.7).[28] SAMs are well packed two dimensional distributions of molecules covalently attached to specific substrates, such as gold and silicon oxides.[29,30] The main advantage of the use of SAMs *versus* other chemical modification techniques is its extreme versatility together with the simplicity of their preparation method. Thus, only by changing the terminal group of the SAM, the final chemical and wettability properties of the surface can be completely modified. Furthermore, the self organizing properties of this kind of chemical compounds are fundamental to be used in surface structuring techniques such as the microcontact printing (μ-CP) or the replica molding, among others (Figure 9.8). Firstly developed by the group of *G. Whitesides et al.* back in the 1990's, the μ-CP technique is based on the use of a patterned elastomeric stamp, usually made of polydimethylsiloxane (PDMS), to structure molecules onto a target surface.

Patterned sizes obtained with this technique range from 3 nm to 100 μm. In the biomaterials field the μ-CP technique has been mainly used to selectively modify surfaces of determined biomaterials increasing their chemical versatility.[31]

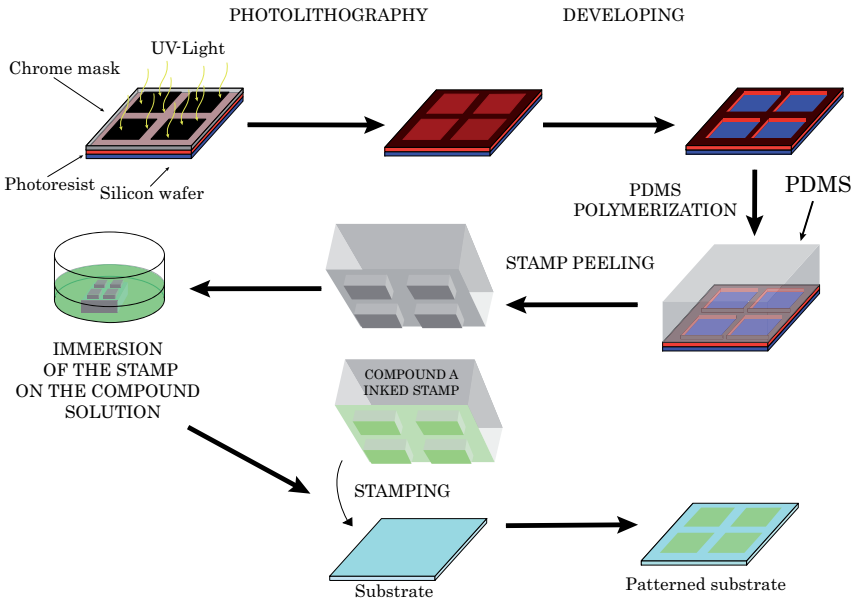

Figure 9.8: Schematic representation of a μ-CP process for direct stamping of chemical substances onto a surface. On a first step the negative of the desired pattern is defined on the surface of a silicon wafer by means of photolithography. Then, the pattern is transfered to a elastomeric polymer, usually PDMS, by thermally curing the polymer precursor in contact with the patterned silicon surface. Once obtained, the PDMS stamp is peeled and inked on a solution of the target molecule and directly used to pattern the organic molecule onto the target surface (Image reproduced from *Liu et al. Materials Today*, **2005**, *8*, 28-35).

Figure 9.8 depicts an schematic representation of a μ-CP process, from the preparation of the PDMS elastomeric stamp to the pattern of the chemical compound onto the surface of the material to be modified.[32]

Another strategy to improve the cell-scaffold interaction is coating the substrate with a biodegradable polymer.[33] Moreover, the strong interfacial adhesion between the ceramic biomaterial of the scaffold and the organic polymer is a key parameter in generating composites with good mechanical properties. A wide variety of polymers have been investigated for this purpose, including polylactic acid or polyglycolic acid, among others. Furthermore, it has been also anticipated

that the combination of ceramic scaffolds and appropriate biodegradable polymer coatings can enhance the interfacial adhesion of proteins.

b) Topography and roughness modification. The cell and protein adhesion to biomaterials can also be enhanced by modifying the morphological properties of the surface. Numerous chemical and physical methods have been developed to generate nanoscale surface patterns suitable for both, the construction of biocompatible materials for tissue engineering and for in vitro investigations on molecular mechanism of cell-surface interactions.[34]

Traditionally, the methods employed for the modification of the morphological properties of the biomaterial's surface involved the use of aggressive techniques such as sandblasting, heat treatments or acid etching, among others. Although, positive results were obtained by the use of these processes[35] the final control of the geometry of the patterned features is still a problem.

In order to be able to solve this situation the use of nanostructuring techniques with high lateral resolution is required. Several different techniques have been used to perform these geometrically defined surface patterns, from traditional lithographic methods, like electron-beam lithography, photolithography or colloidal lithography[36] to modern soft lithographic techniques such as the dip-pen[37,38] or the imprint lithography.[39]

9.2.2.3 Biological responses to the characteristics of the biomaterial surface

As stated before, the nature of the surface of a determined biomaterial plays an important role on its final characteristics as tissue engineering substrate. Indeed, a lot of cell behaviors such as attachment, migration, differentiation or proliferation, are strongly dependent on the chemical and physical properties of the surface. Therefore, the understanding and developing of new biomaterials with controlled surface properties has become a priority during the last decade.

The final quality of a biomaterial is determined by a set of factors including, biocompatibility, the presence of structural features (such as stripes or pores), physical properties (roughness, pattern, stiffness, etc) and chemical properties (hydrophilicity, free energy, charge, ionic interaction, etc). However, nowadays it is not possible to conclude which of them is the one influencing more the response

of cells, as it strictly depends on the specific cell and biomaterial we are dealing with.

a) Influence of the surface chemical properties. The surface chemistry of an implanted material is of extreme importance on the first stages of the tissue regeneration. It has been shown that by controlling the functional groups of the substrate it is possible not only to tune the protein adsorption, but also to determine the adsorbed protein conformation.[40,41]

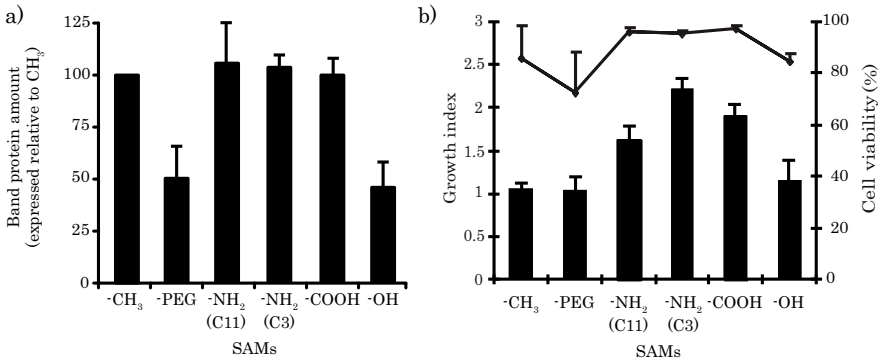

Figure 9.9: a) Total adsorbed protein (relative to the -CH_3-terminated SAMs) on the chemically modified silicon substrates. b) Viability (dots) and growth (bars) of human fibroblasts on SAMs after incubation for 48 h at 37°C. The cell viability was evaluated by trypan blue exclusion. The cell viability at time zero was higher than 95%. (Data obtained from *Faucheux et al.*, *Biomaterials*, **2004**, *25*.)

One example of protein adhesion dependence with the surface chemical properties of a surface is the work developed by *Xu et al.*[42] In this case, they use glow discharge plasma to oxidize the surface of a low density polyethylene substrate producing different wettability values. Adhesion forces of three different proteins -bovine serum albumina, fibrinogen and human FXII- were tested by the use of an atomic force microscope indicating an increase of cell attachment when the contact angle of the substrate was over 60-65°.

More ambitious is the work developed by *Faucheux et al.*,[28] where the protein adsorption and cell proliferation properties of modified silicon surfaces with SAMs exhibiting different chemical ending groups were compared. On a first step, they proceeded to modify the chemical properties of the silicon oxide surfaces using highly reactive organosilane molecules bearing different chemical functional ending

groups like methyl, hydroxyl, amine and carbonyl, among others. Such organosilane molecules are capable of reacting with the free -OH groups present on the silicon surface forming a well packed SAM. Then, in order to study how the chemical nature of the substrate influences the protein adhesion, the substrates were immersed on a bovine serum solution. After surface analysis it was possible to determine that the presence of ending groups such as polyethyleneglycol (PEG) or -OH on the substrate surface entailed a decreasing of the total adsorbed protein, while in the case of -COOH, NH_2 or CH_3 maxima coverage values were obtained. According to the authors, this effect can be attributed to the resistance that non-ionic and proton acceptors groups, such as -OH, present to protein adsorption (Figure 9.9 a). This was not a new phenomena as it had been previously reported by *Ostuni et al.*[43]

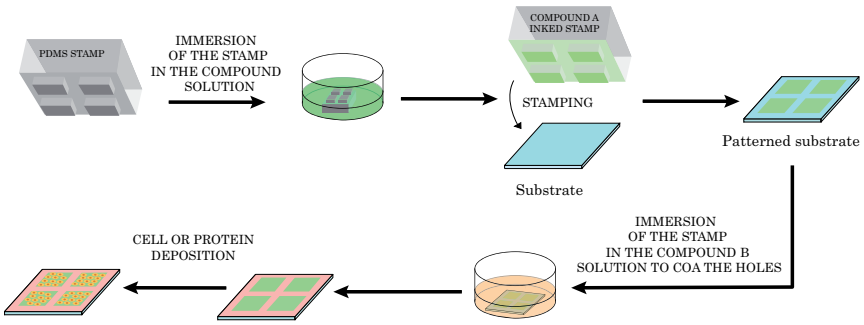

Figure 9.10: Schematic of the use of μ-CP process for the zone selective modification of the surface of a determined biomaterial for the enhancement of protein or cell adhesion (Image reproduced from *Liu et al. Materials Today*, **2005**, *8*, 28-35).

Cell growth studies (Figure 9.9 b) indicated a tight relationship between the previously observed results and the final cell proliferation. Thus, those surfaces coated by moderate wettable surfaces (NH_2 and -COOH) present a higher growth ratio than those bearing non-ionic hydrophilic surfaces (PEG, -OH). On the other hand, the reduced proliferation observed for the -CH_3 coated surface is assigned to the generation of conformational changes on the tridimensional structure of the attached proteins, that inhibits the appropriate cell growth.[44]

As explained on the previous section, the use of soft lithographic techniques, such as μ-CP, allows the local functionalization of surfaces. Therefore, once the desired molecule pattern has been transfered to the surface of the target biomaterial, the non covered parts of the surface can be selectively coated by a second molecule

having different functionality, permitting the fully surface chemical functionalization. This allows to distinctly modify the chemical nature of different areas of the same substrate, achieving a mayor control of the protein and cell proliferation (Figure 9.10).[31] One clear example of this is the work developed by *Offenhausser et al*,[45] where they demonstrate the efficacy of the μ-CP method for the developing of protein patterned surfaces for the growth of neurones with a defined geometry (Figure 9.11).

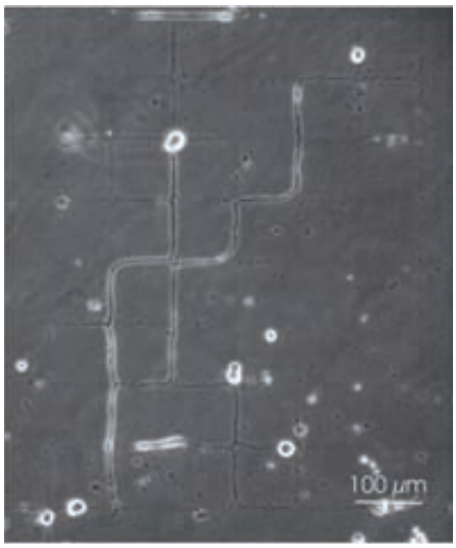

Figure 9.11: Phase contrast micrograph of a cricket neuron growing on a concanavalin A grid pattern with 20 μm wide lines on a background of star-PEG. Image obtained from *Offenhaeusser et al. Soft Matter*, **2007**, *3*, 290-298

Therefore, it is possible to conclude that by controlling the chemical nature of a surface it is possible to affect not only the number and conformation of the adsorbed proteins, but also to modify the cell proliferation regime and shape the cell growth on the top of it.

b) Influence of the surface physical properties. While much effort in developing new materials for biological applications has been focused on their chemical properties, the study of the influence of their structural and physical properties has been less usual. For many years, it has been recognized that the use of substrates with different physical or structural properties for cell proliferation can act as a guide making cells to preferentially grow on one determined direction. Nevertheless, due to technical limitations, the research was limited to study the

influence of these properties at the macro or microscopic level. Due to the recent advances on preparation and characterization techniques at the nanoscale, an increasing interest on the study of the cell-substrate interactions at the nanoscopic level, specially in those related with the nanoscopic structuring of the substrate topography and superficial stiffness, has appeared.

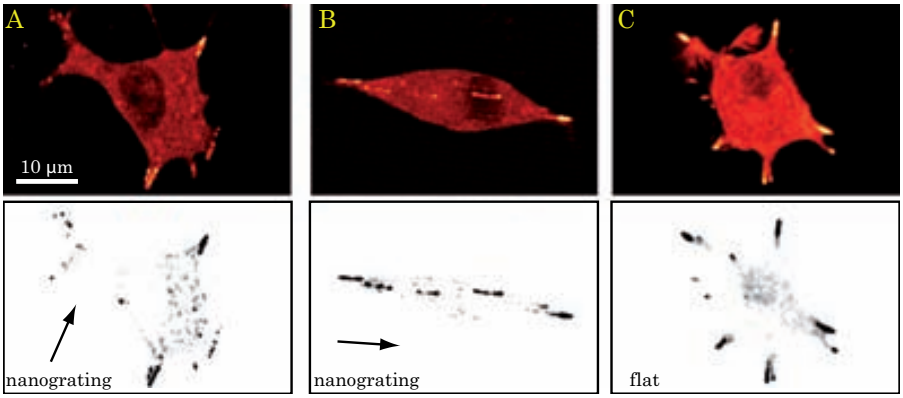

Figure 9.12: A) and B) Distribution of paxillin-EGFP fluorescent signal in PC12 cells differentiating on nanogratings (250 nm deepth and 500 nm wide), and C) on flat substrate. In the lower row is shown the inverted fluorescent signal at the cell-substrate interface pointing the regions with more paxillin-EGFP accumulation (black spots). Black arrows indicate the direction of the nanograting (Image reproduced from *Ferrari et al.*, *Biomaterials*, **2010**, *31*, 4682-4694)

Recent works have demonstrated that by the use of this kind of modified substrates it is possible not only to variate the cell-surface adhesion profiles but also, in some cases, to modify the cell morphology or some other complex functions, such as their differentiation or growth.[46] Once deposited over the surface, the cell response depends upon many factors, including cell type,[46] feature size and geometry of the substrate,[47] and the physical properties of the bulk substrate material, including substrate stiffness.[48] From all these properties, the influence of substrate morphology on cell properties is probably the most representative,[46] being perhaps, its impact upon cell geometry the most palpable response.

Figure 9.12 represents the final morphology of PC12 neural cells grown on two nanostructured and one flat substrates. It is possible to observe how cells in contact with the nanoscopic gratings modify their shape and adapt to the substrate morphology, while those cultivated over a flat substrate do not present any shape anisotropy. The possibility of inducing and maintaining a stable directionality upon cell growth has a clear impact on the use of biomaterials as scaffolds aimed

at the controlled regeneration or the replacement of highly anisotropic tissues. Nevertheless, the influence of the morphology of the substrate on cell geometry can not be taken as an absolute parameter and, although many cells (including fibroblasts, endothelial cells, stem cells, among others) respond to nanogratings by simultaneously aligning and elongating in the direction of the grating axis, several others (human-derived leukocytes, keratinocytes, and monocytes) do not present any response when grown onto the same kind of patterned surfaces.
Therefore, morphology is not the only characteristic of the substrate influencing on the final cell behavior, since substrate stiffness is also another of the most influencing studied parameters.

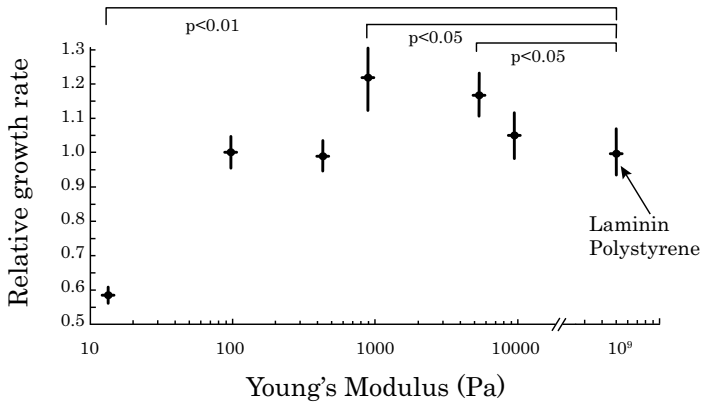

Figure 9.13: Growth rate of undifferentiated stem cells as a function of substrate Young's modulus. Growth rates were normalized to laminin polystyrene substrates. Error bars are 95% confidence intervals, and p-values, 0.05, based on Students t-test under laminin-coated polystyrene surface conditions, are also shown. Image obtained from *Saha et al*, *Biophysical Journal*, **2008**,*9* ,4426-4438

As a cell binds to a substrate and adheres to it, intense forces are generated from the cell cytoskeleton to these adhesive bonds, allowing the cell to spread. Nevertheless, the properties of the substrate might determine the magnitude of these adhesion forces and the extent of cell spreading that ensues.[49] Nowadays, most of our understanding of cell adhesion and growth is derived from experiments on cells cultured on very hard surfaces, like plastic culture dishes or glass substrates, however tissues within our bodies have present a very different range of stiffnesses. Subsequently, the study and comprehension of the influence of the stiffness of a substrate on the final cell growth is of extreme importance for the obtaining of better biomaterials.

The stiffness of the surface of a material is given by the Youngs modulus* that for stiff tissues, such as bones is in the range of GPa, and for soft tissues like brain, the Young modulus values are in the range of kPa.
Figure 9.13, obtained from the work developed by *Saha et al*,[51] clearly represents what previously stated. It is possible to observe how just by modifying the Young's modulus of the biomaterial severe alterations on the final cell proliferation are produced. In this case, such authors made use of hydrogel based cell culture system bearing variable Young's moduli values (from 10 Pa to 1 GPa) for the study of neural stem cell proliferation. Results obtained indicate that softer gels (100-500 Pa) greatly favored neurons proliferation, whereas harder gels (1,000-10,000 Pa) promoted glial cell cultures. In contrast, cell spreading and differentiation were inhibited on substrates with moduli of approximately 10 Pa, demonstrating that the mechanical properties of biomaterials can be tuned to regulate the differentiation of neural stem cells.
In summary, it is possible to say that the complexity behind the biomaterials applied for tissue engineering has been significantly increased from both, materials and surface science directions. Thus, for a medical implant it is not only important to take into account its bulk physicochemical properties but also the surface coatings that gives it the defined chemical, topographical and physical properties required in order to direct the desired cellular response.

9.2.3 Biosensing materials

As previously explained in the first part of this Thesis, sensors play an important role in several different aspects of our live, from environment monitoring to food analysis or even clinical detection, among others. The recent advances achieved in the biomaterials field has profound a direct impact on the development of new biosensors with excellent properties and improved selectivity for clinical applications. Amongst the many biorecognition materials that can be used, those involving the use of enzymes, DNA, or antigensantibodies are the most employed ones. Nevertheless, the direct application of this biomaterials is usually not sufficient to achieve the desired sensing properties and the use of intermedia materials and adequate surface processing and structuring processes is required.

*The young's modulus is the ratio of the uniaxial stress over the uniaxial strain in the range of stress in which Hooke's Law holds[50]

9.2.3.1 Biorecognition materials

a) Enzymes. Enzymes have been used as analytical reagents for selective detection of special materials since 1940s because of their special catalysis to substrates and selective recognition of coenzymes and inhibitors correspondingly. Furthermore, due to their physico-chemical characteristics, enzymes are easily linked to several different substrates such as electrochemical electrodes, optical fibers or even field-effect transistor (FET) facilities, being the preferred materials for the preparation of biosensors.
Enzyme based biosensors are fast, precise, and extremely sensitive devices that are now widely used in the fields of clinical detection, environment monitoring, and also in pharmaceutical biochemical research.[16] Nevertheless, the enzymes are also very sensitive biomolecules which require specific temperature, pH, or ionic strength conditions to properly perform their sensing role. This is severely limits the application of enzymes in biosensors and is one of the most important tasks to overcome in the development of enzyme biosensors.

b) DNA. DNA can also be used as molecular recognition element in biosensors. Based on the types of DNA used in biosensors and the mechanisms of action, there are in total two kinds of DNA biosensors, namely, single-strand DNA (ssDNA) biosensor and double-strand DNA (dsDNA) biosensor. The ssDNA biosensor uses an immobilized ssDNA as a probe to detect its own complementary ssDNA series by the interaction of DNA bases. The dsDNA biosensor is used to detect some molecules or ions that can interact with immobilized dsDNA based on the signals produced in the interaction. Depending on the signal transduced DNA based biosensors can be classified into electrochemical, optical and surface plasma DNA biosensors, among others.

c) Antigen-antibody. Based on the special reaction of antigen with antibody, antigens (antibodies) can be used to prepare immunobiosensors for the qualitative or quantitative determination of corresponding antibodies (antigens) or even their accelerators and inhibitors by the changes of some physical or chemical signals such as optical, electrochemical, quality, and thermal signals during the reaction. Till now, lots of antigens (antibodies) have been used to construct immunobiosensors.

9.2.3.2 Fabrication of biosensing materials

As previously stated, the presence of a biorecognition material is not always sufficient for the obtaining of a proper biosensing device, and most of the times intermedia materials and correct processing and structuring techniques are also required.

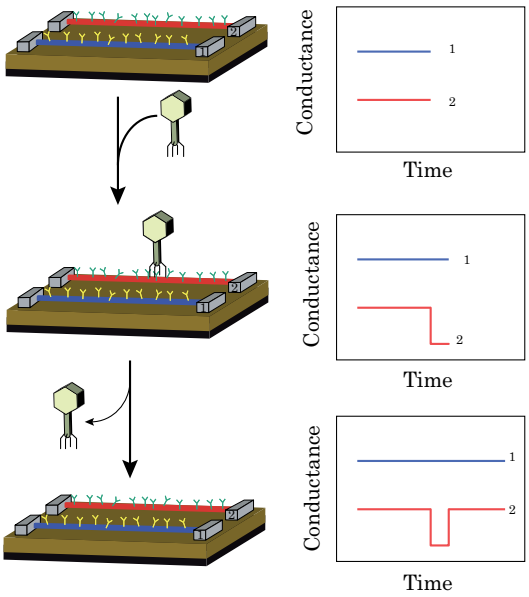

Figure 9.14: Nanowire-based detection of single viruses. (Left) Schematic shows two nanowire devices, 1 and 2, where the nanowires are modified with different antibody receptors. Specific binding of a single virus to the receptors on nanowire 2 produces a conductance change (Right) characteristic of the surface charge of the virus only in nanowire 2. When the virus unbinds from the surface the conductance returns to the baseline value. Image reproduced from *Patlosky et al. PNAS*, **2004**, *101*, 14017-14022

One clear example of this is the work developed by *Patlosky et al.*[52] (Figure 9.14), where a highly selective device, based on the use of antibodies-antiviruses coated nanowire arrays, permits the real-time electrical detection of single virus particles via a field effect mechanism. Moreover, further studies indicate that these kind of devices can be used not only to detect the presence of viruses but also to rapidly determine isoelectric points and variations in receptor-virus binding kinetics. Nevertheless, sensing devices based on bomaterials are not limited to the electrosensors field being possible to find examples of mass sensitive, or optical

biosensors, among others.

Figure 9.15 represents and scheme of a label-free optical biosensor developed by *Nath et al.*.[53] The method relies on the change in the absorbance spectrum of a SAM of colloidal gold on glass, as a function of biomolecular binding to the surface of the immobilized colloids. In this case a the detection limit of 16 nM for streptavidin was observed. The main advantages of this kind of biosensors relies on their easy fabricate, reproducibility and minimal technological requirements which maintain their cost effectiveness.

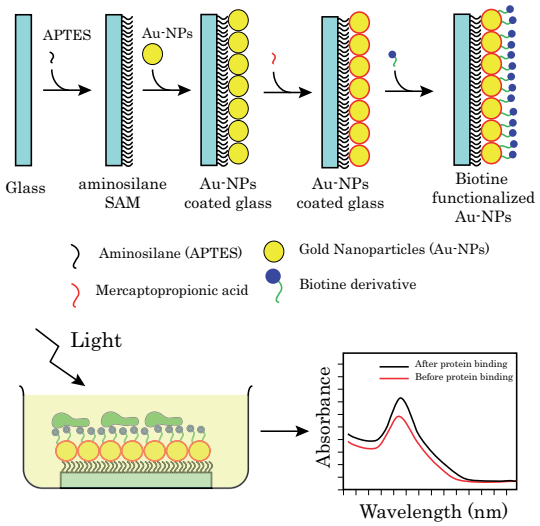

Figure 9.15: (Top) Schematic of the steps involved in the fabrication of the immobilized colloidal gold sensor chip on glass. Glass substrate was functionalized with Aminopropyltriethoxysilane (APTES) to provide an amine-terminated surface for formation of a monolayer of gold nanoparticles (Au-NPs). SAM of mercaptopropionic acid on gold nanoparticles provides a reactive carboxyl group that can be further modified by biotin to study specific binding of streptavidin. (Down) Biomolecular binding at the surface of the functionalized gold monolayer results in a shift in peak wavelength as well as an increase in intensity. Image reproduced from *Nath et al. Anal. Chem*, **2002**, *74*, 504-509.

9.2.4 Inclusion bodies as functional biomaterial

As previously stated, during the last decades, scientists from the fields of material science, surface engineering, chemistry, physics, biology, biochemistry and medicine have attempted to develop new biomaterials capable of controlling the specific cell surface interactions, resulting on an important increase of the number

of available biomaterials for medical applications.

Today, most of the more commonly used biomaterials have sufficient mechanical resistance, elasticity as well as the desired stability towards degradation to be applied in tissue engineering. However, a large number of them are limited by the non sufficient biocontact of the material with the surrounding biological media.[54] To overcome this situation, several approaches are currently under intense investigation. These approaches are based on the control of the chemical composition -functional groups, hydrophilic/hydrophobic character- and the nanoscopic properties -topography, roughness, stiffness- of the material surface.[55] It is also under investigation the incorporation of different biomolecules, such as short amino acid sequences, carbohydrates and/or functional parts of hormones, enzymes or growth factors, onto the material surface.[56] Despite these research, it is also worthy to mention that the mechanisms of protein adsorption and bioadhesion remain also not fully understood, being sometimes difficult to make predictions.

During the last years, our group, in collaboration with the group of Prof. A. Villaverde at the IBB (*Universitat Autònoma de Barcelona*), has been working on the characterization and use of a new kind of proteinaceous biomaterial, known as inclusion bodies (IBs), as a new kind of biomaterial for cell proliferation enhancement.

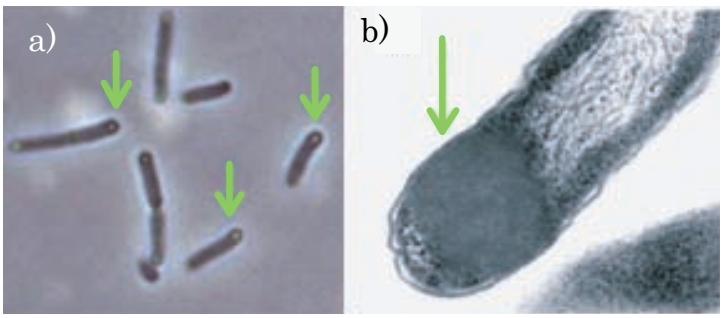

Figure 9.16: Confocal microscopy (a) and transmission electron microscopy (b) images of *E. coli* BL21(DE3) expressing human leptin. Inclusion bodies of the target molecule are formed in the cytoplasm indicated with an arrow (Image obtained from *http://mbel.kaist.ac.kr*)

IBs are non-enveloped and mechanically stable nanoparticulate entities mainly constituted by proteins, which are generated in vivo during the production and further deposition of a wide catalog of recombinant polypeptides[57] (Figure 9.16). Once produced, IBs can be easily extracted and purified from the rest of the cytosolic components of the bacteria by the use of the appropriate sequence of lysis

buffers and centrifugation steps obtaining a highly pure IBs solid deposits. For long, IBs have been seen as undesirable by-products to be discarded for further applications, as believed to be formed by misfolded, nonfunctional polypeptides escaping the cells quality control machinery.[58] However, a dramatic turn in the understanding of the bacterial control of protein aggregation at the cell systems level has recently shown inclusion bodies as formed by properly folded, functional species.[59] Furthermore, IB formation has not been associated to any particular protein sequence, being the production of IBs with diverse functionalities possible. This has prompted the straightforward use of IBs on several different applications such as catalytic processes (IBs formed by enzymes)[60] or drug delivery systems.[61] Moreover, in recent research works, it has been found that IBs possess an unexpected amyloid-based molecular architecture structurally comparable to that observed in a growing number of neurological diseases such as Alzheimer.[62] Thus, from another point of view, these aggregates can be considered an interesting and convenient model to investigate the molecular basis of protein folding and aggregation, which is not only important for the production of functional proteins, but also to solve the molecular mechanism of the above mentioned diseases, that have also become the object of intense research.
The intrinsic characteristics of IBs made thought to use them as possible biomaterials to modify the surface properties of materials in order to enhance cell proliferation. For this reason, this Thesis introduces a detailed investigation of such an application.

9.3 Present and Future Trends

The development of new biomaterials requires that the materials designed are not only bio-inert but also that they interact and even respond to the biological environment. Among all the possible modifications it has been observed that the tunning of the physical and chemical properties of the material surface has an enormous influence on the cell behavior once the material is in contact with the biological environment.

Thus, it is possible to conclude, that understanding and correlating the effect of materials processing with their physicochemical and in vitro properties should permit the development of more efficient biomedical devices able to respond to specific

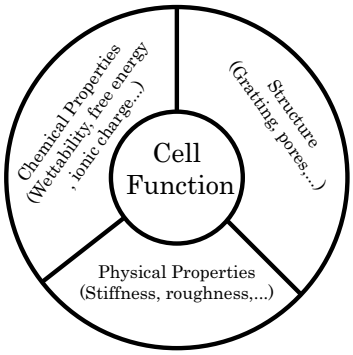

Figure 9.17: Schematic diagram of factors determining cell fate

requirements for each problem. However, due to the enormous complexity of the task, this would never be accomplished without the and collaboration between scientists from different areas, such as physics, chemistry, biology and materials science.

Chapter 10

Results and Discussion

10.1 Characterization of IBs

As previously described, bacterial IBs are highly pure deposits of a certain protein formed in recombinant bacteria† subjected to stress upon protein production. Composition studies performed in freshly prepared and purified IBs indicate that they are highly hydrated, chemically pure particles formed by the expressed protein up to around 95% of the protein therein,[63,64] while the 5% remaining is formed by other cell components, such as RNA, DNA, and lipids, entrapped during the IB formation.[65] Although protein aggregation is usually linked to missfolding phenomena, IBs are belived to contain an important extent of polypeptides with native-like secondary structure and are thereby biologically active.[66] Nevertheless, how functional species can coexist with the amyloid-like pattern (cross molecular beta-sheet rich structures, generally associated with non functional proteins) is still unsolved.

The chemical composition is not the only factor influencing the final structure and properties of the IBs, as the influence of environmental conditions on the folding state of IB proteins[59,67] indicates an important degree of molecular flexibility. In addition, being the IB protein quality tightly surveyed by the quality control system of the bacteria,[68] it is not unexpected that the modification or removal of any fragment of genetic information of the IBs producer bacteria might allow the tunning of the final properties of the these protein aggregates.[69]

A clear example of this is the work developed by *Villaverde et al.*[70] In this work,

†Bacteria that have undergone genetic engineering. This means that their DNA has been altered by the introduction of new DNA.

the fluorescence intensity of green fluorescent protein (GFP) IBs produced in different genetic deficient bacteria affecting certain cytosolic chaperones and proteases was determined, indicating the presence of different fluorescent activity depending on the recombinant bacteria used. Thus, it was demonstrated that the use of recombinant bacteria with different genetic background does not perturb the amyloid-like architecture of the IBs, but allows the tunning of the final properties of the IBs (Figure 10.1).

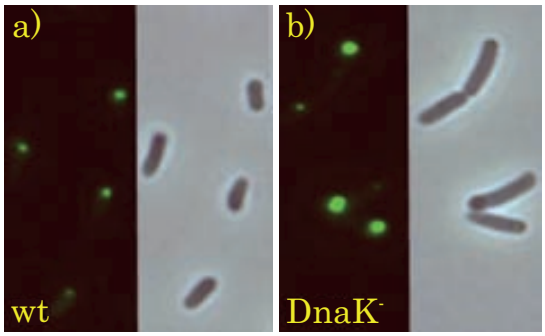

Figure 10.1: Confocal fluorescence microscopy images (left) and optical microscopy images (right) of a) non modified or wild type (wt) *E. Coli* bacteria and b) DnaK deficient ($DnaK^-$) *E. Coli* bacteria during GFP IBs production. IBs coming from genetically modified bacteria present a much higher fluorescence indicating the presence of more active GFP inside the IB structure.

Recent studies on the functionality and applications of IBs have shown their enormous potential, not only from the industrial catalysis point of view, but also in the field of biomaterials. Indeed, their fully biocompatible and nanostructured nature make IBs a highly promising material for the structuring and engineering of surfaces to be further applied on regenerative medicine, and more specifically in tissue engineering. Nevertheless, despite their enormous potential as a non-cytotoxic nanomaterial produced by cost effective and scalable procedures, the chemical and mechanical properties of IBs remained essentially unexplored. In this regard, very little was known about their structural or physicochemical properties, being only some bibliographic references about their density,[63] hydratation level[71] or pH responsiveness,[72] available in the literature.

To deeper explore these issues, our group in collaboration with the group of *A. Villaverde* has, for the first time, characterized the structural and physicochemical properties of a set of GFP IBs. IBs formed by this fluorescent protein are very convenient models for these kind of structural and functional analyses due to their

high fluorescence. Such IBs were produced in a conventional *K-12 wild type* (wt) *E. Coli* strain, and in derived genetic backgrounds showing deficiencies in the protein quality control network, that is known to regulate not only protein folding but also aggregation. In order to have a better insight of the influence of the genetic background of the recombinant bacteria on the final properties of the IBs, three paradigm mutations affecting different arms of the quality control system were chosen. The first mutation involves the existence of deficiencies of the DnaK protein, known to be the main cytosolic chaperone acting as a negative regulator of the heat shock system and as a potent proteolytic stimulator showing also folding, holding and disaggregase activities[73]. The second one was a mutation that gives rise to a deficiency in ClpA, an ATPase subunit of ClpP that possesses intriguing foldase-like properties[74]. And finally, the last mutation chosen was that yielding deficiencies in the ClpP (protease enzime), also with foldase like properties.

10.2 Characterization of IBs

10.2.1 Structural characterization of IBs

In the context of potential nanomedical applications, the production of IBs with tailored sizes and morphologies would be highly convenient. However, due to the characteristics of the production process, this must necessarily be done during their in vivo fabrication, by the controlled modification of the conditions that affect their construction.

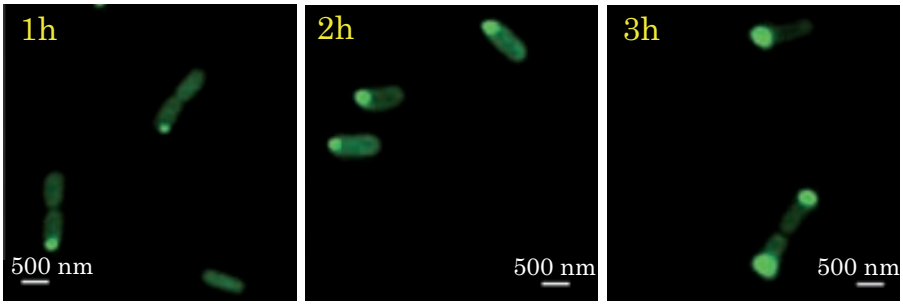

Figure 10.2: Confocal fluorescence microscopy images of GFP IBs at different times of production showing the increase of size of the IB with the pass of time.

The formation of IBs is a fast and efficient procedure, nevertheless, very few details are known about how processing parameters such as production time or the

existence of cellular genetic deficiencies might influence the final properties of the IBs.

Time dependence studies of IBs production on a non modified *E. Coli* strain, or wild type (wt), were developed using a confocal fluorescence microscope (Figure 10.2). Results obtained showed the presence of clearly visible IBs only 1 hour after induction of gene expression. Furthermore, it was possible to observe IBs grew volumetrically with time reaching almost the 40-50% of the total cell volume after only 3 hours of production.

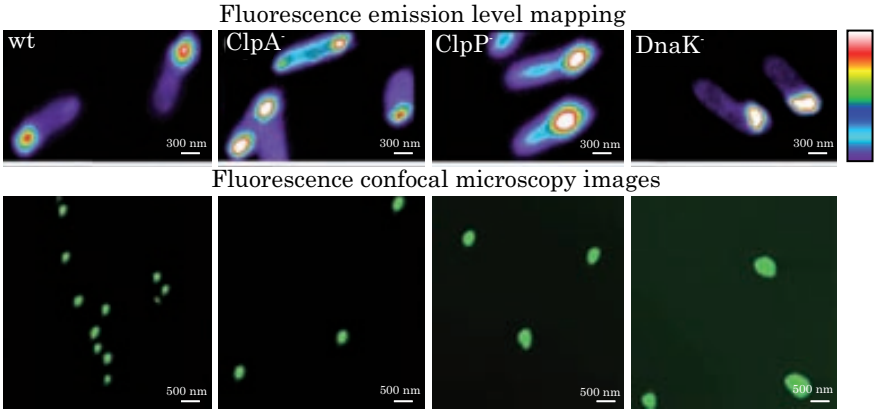

Figure 10.3: Fluorescence intensity mappings (top) and confocal microscopy images (bottom) of IBs coming from different bacterial strains.

The same experiment was carried out using different modified *E. Coli* strains presenting deficit of the previously depicted chaperones or proteases encoding genetic sequences.

As in the previous case, the presence of IBs was evident after a few minutes of GPF gene expression, being more and more clear with the pass of production time. After 3 hours of production, results indicated the existence of discrepancies on the size and fluorescence intensity of the IBs depending on their genetic background (Figure 10.3). Thus, wt IBs appeared as the smallest and the less fluorescent of all of them, while DnaK$^-$ and ClpP$^-$ IBs were the biggest and the most fluorescent. A closer look to the fluorescence emission levels allowed us to determine that IBs sizes and fluorescence intensities were not directly related. For instance, IBs obtained in ClpA and ClpP deficient cells, with very similar particle sizes, showed different fluorescence emission levels (71 and 184 mean FL1 units per particle, respectively) as observed in Figure 10.3 top. The fluorescence mapping of GFP IBs was, however, comparable in all strains, showing a common homogeneously

fluorescent core pattern (Figure 10.3 top). These results can be explained by the presence of different conformations of the aggregated proteins depending on the producer cellular strain.

Nonetheless, fluorescent confocal microscopy is an imaging technique and only qualitative information about the particle size can be obtained. In order to further characterize these differences, IBs produced after 3 hours of gen induction, coming form the four different cellular strains were purified (see Experimental Part) and resuspended on a phosphate buffer solution (PBS) at pH = 7.4 in order to emulate, as much as possible, the intracellular media conditions. Once purified, the samples were subject to DLS particle size distribution analysis (Figure 10.4).

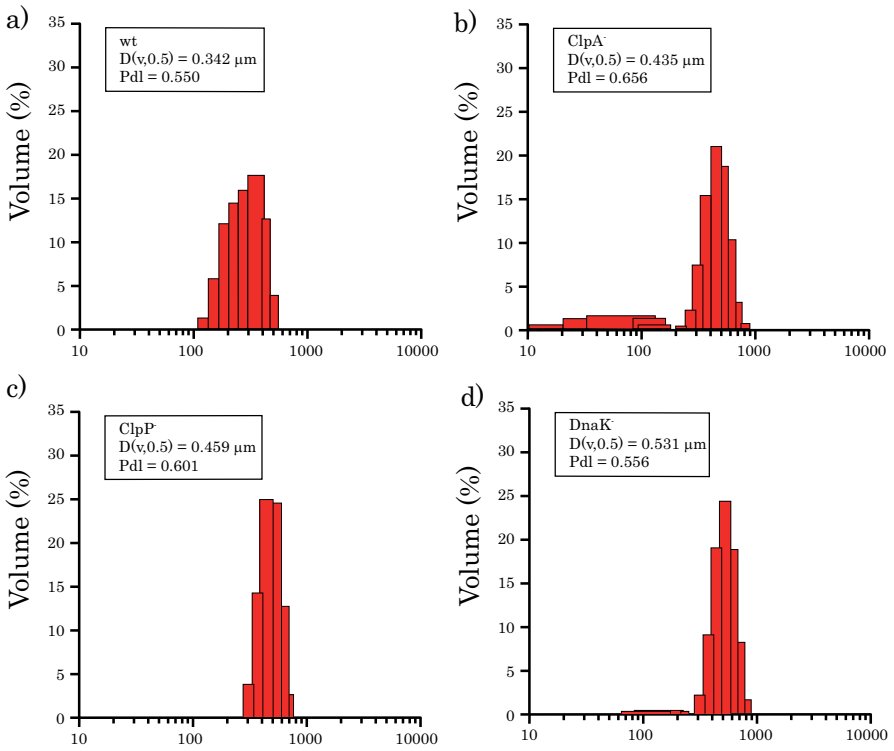

Figure 10.4: Dynamic light scattering volumetric particle size distribution analysis of GFP IBs suspensions in phosphate buffer solution (PBS, pH = 7.4) coming from a) wt, b) ClpA$^-$, c) ClpP$^-$ and d) DnaK$^-$ cellular strains. D(V, 0.5) indicates the mean volumetric particle size diameter while PdI is the polydispersity index.

Results obtained indicate that while mature IBs purified from wild type cells showed an average diameter of 340 nm, this value can be increased progressively

up to more than 500 nm in DnaK$^-$ deficient cells (Figure 10.4 d), maintaining a relatively low polydispersity index[‡] in all analyzed samples.
Nevertheless, particle size distributions obtained from DLS give only information about the average particle present in liquid media, and gives no detail about particle morphology. For this reason, SEM images of freshly produced IBs from the four different cellular strains were obtained after deposition on a polycarbonate membrane (0.1 μm pore size). Prior to measurement, the IBs treated membranes were subject to a gold metalization process in order to avoid sample charging during the imaging.
In the case of wt, DnaK$^-$ and ClpA$^-$ (not shown) produced IBs, the recorded images (Figure 10.5 a and b) depict the presence of spherical or oval entities with rough surfaces and sizes matching those previously observed by DLS. In contrast, results obtained for ClpP$^-$ produced IBs show the formation of morphologically abnormal, tear-shaped IBs (Figure 10.5 c).

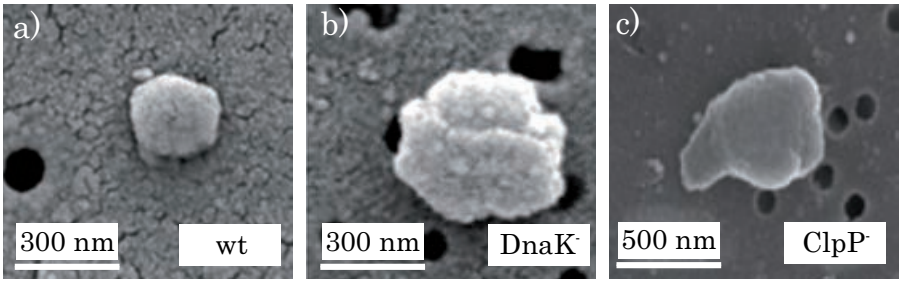

Figure 10.5: Scanning electron micrographs of freshly prepared IBs after deposition onto polycarbonate membranes (0.1 μm pore size) a) wt, b) Dnak$^-$ and c) ClpP$^-$.

In order to eliminate any influence of the SEM sample preparation procedure to the final morphological results, AFM operated in dynamic mode was also employed to obtain images of wt and ClpP$^-$ produced IBs. Sample preparation was performed as follow. A 20 μg/ml suspension of IBs in PBS solution was drop-casted onto a freshly cleaved mica surface and air dried. Once dried the sample was washed carefully with 500 μl of ultrapure water in order to remove the physisorbed phosphate salts. Results obtained are depicted in Figure 10.6.
In the case of wt IBs it is possible to observe the presence of cylindrical entities with average sizes of 300 nm length, 170 nm wide and 180 nm height, according to cross-sectional measurements performed (Figure 10.6), which are more or less

[‡]Polidispersity index (PdI) gives information about the dispersion of sizes. The lower the PdI index the more monodisperse the sample.

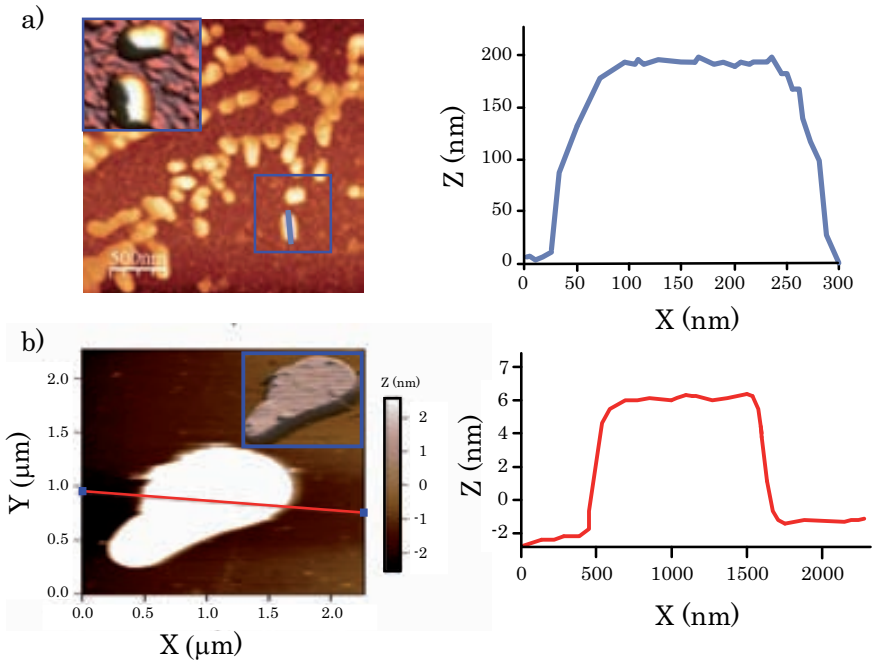

Figure 10.6: Topographycal AFM images operating in dynamic mode of a) wt and b) ClpP$^-$ IBs drop-casted over a mica surface. Cross sections (right) and 3D reconstructions (insets) of the selected IBs are also shown.

in agreement with the DLS and SEM experiments. Results obtained with ClpP$^-$ samples (Figure 10.6 b) also confirm the presence of the tear-shaped IBs. It is important to remark the reduced height observed (only 6 nm) for the ClpP$^-$ IBs, that might be a consequence of a strong aggregate-surface interaction which forces the IB to maximize the contact surface and could also explain its tear-shaped form.

The observed differences in size, fluorescence intensity and morphology between IBs coming for different genetic background can be assigned to the existence of distinct dynamics of the in vivo protein deposition occurring in the different cellular strains tested. On a non-modified cell, *de novo* produced recombinant polypeptide chains interact with each other through stereo-specific hydrophobic contacts[75] that allow the creation of seeding nuclei (usually one or two per cell),[64] on which additional protein molecules or proto-aggregates are progressively deposited.[76] Since polypeptides forming IBs are also steadily removed from these clusters by a combination of chaperones and proteases (the constituents of the cell protein

quality control network),[70] the volumetric growth of IBs inside bacteria is due to an unbalanced equilibrium between these opposite activities, resulting on a protein deposition rate higher than the protein removal.[77] Thus, depending on the genetic background of the bacteria this unbalanced equilibrium will be displaced to the obtaining of IBs with different final properties.

Therefore, it is possible to conclude that by the appropriate combination of time of harvesting (determining IB growth stage) and the producing strain (determining both biological activity and upper size limit) it is possible to define particular particle dimensions and biological activities like the fluorescence, that could be appropriate for different applications.§

10.2.2 Mechanical characterization of the IBs

It is known that the mechanical properties of a substrate biomaterial are critically affecting relevant features of mammalian cells growing on it, such as cell morphology,[78,79] proliferation,[78,79] motility[80] and differentiation.[79,81] Therefore, the study of the IBs mechanical properties and how the genetic modification of the producing bacteria affects them is crucial for their future application in nanomedicine.

To determine how the different genetics of IB bioproduction affects their elasticity, we made use of the force spectroscopic atomic force Microscopy (FSAFM) (See annex A-3). During the last decade, AFM, and particularly FSAFM, has proved its value not only for imaging biological samples,[51,82] but also for measuring inherent properties of biological structures and aggregates, like local interaction forces, mechanical properties or dynamics in natural (physiological) environments,[83] all of them very interesting properties from the biomedical point of view.

An scheme of a FSAFM measurement is depicted in Figure 10.7. In this technique an AFM tip is pressed into the target object with a defined force (F) at the same time that the deflection (d) of the tip cantilever is monitored. If the object is hard (blue line) the tip will not be able to produce any deformation on its surface and all the movement of the tip in the Z direction will be reflected on a deflection of the tip cantilever, represented with a straight line on the force *vs.* distance graph (blue curve part III). Nevertheless when a soft object is pressed, the cantilever produces the subsequent indentation on the object's surface (red

§In order to normalize the IBs production procedure for further characterizations, it was decided to standardize the IBs fabrication time to 3 hours

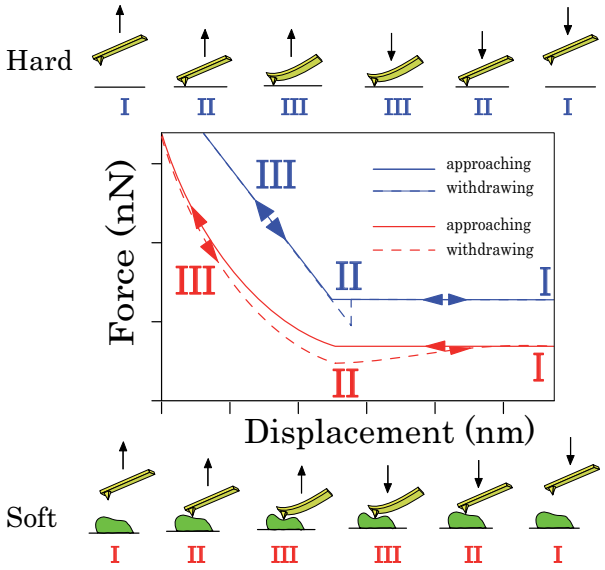

Figure 10.7: Representation of the approaching and withdrawing curves of a force spectroscopic atomic force microscopy (FSAFM) measurement on a hard (blue) and a soft (red) sample.

line part II). This will be reflected on a smaller cantilever deflection, as part of the force applied will be used to perform the indentation. This is represented with the curved line of smaller slope (red line part III). Thus, by fitting the obtained curve with one of the existent indentation mathematical models such as the Hertz,[84–89] the JKR[90] or the DMT[91], among others, it is possible to extract information about the mechanical properties (stiffness) of the indented object. Although not used in this work, tip withdrawal (doted lines) can also be used to extract useful information about the target, such as the adhesion forces.

FSAFM technique and proteins are very sensitive to the environment where the spectroscopic measurement is performed, a fact that might have serious influence on the final result. Therefore, in order to preserve the natural state of the protein aggregates and to mimic the natural cell environment, the spectroscopical measurements of the different IBs were performed in liquid media (PBS buffer, pH = 7.4). Figure 10.8 represent an example of a real force *vs.* distance curve obtained from an AFM spectroscopical measurement over an IB.

The next step, in order to calculate the desired mechanical parameters of interest it is needed to fit the obtained curves to one of the theoretical models above mentioned. Among the different theories describing the elastic deformation of a

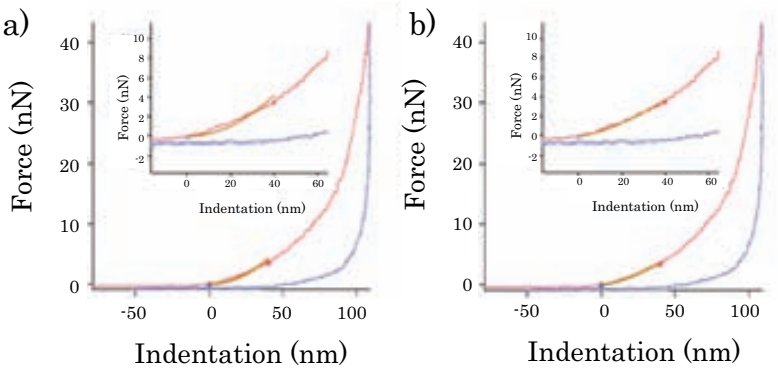

Figure 10.8: a) Conical and b) spherical fitting of a selected approaching curve measurement over a selected IB. In red is represented the curve resulting from the approaching and indentation of the tip on the IB. In blue is represented the withdrawing curve generated while moving the AFM tip to its initial position.

soft sample by a rigid indenter,[92] the Hertzian model[93] has been one of the more used in similar systems[89,94,95]. Depending on the geometrical shape of the indenter used the Herztian model can be expressed using a conical or a spherical approach (Equations 10.1).

Therefore, from the obtained force (F) *vs.* distance (d) plot and using the Hertz model (see appendix III), it was possible to fit the experimental data with the behavior expected for a conical and a spherical indenter, obtaining the Young modulus of the sample,¶

$$Conical\ F = \left[\frac{2E^{*}tan\alpha}{\pi(1-\nu^{2})}\right]\delta^{2} \quad Spherical\ F = \left[\frac{2E^{*}R^{1/2}}{3(1-\nu^{2})}\right]\delta^{2/3} \tag{10.1}$$

where F corresponds to the force applied with the AFM tip over the sample, E* to the reduced Young modulus of the sample,‖ α is the half opening angle of the conical tip, ν the Poisson ratio of the IBs (assumed to be 0.33 for biological samples[86,89]), δ the indentation produced by the tip on the sample and R the tip radius.

Due to the local nature of the measurements, this procedure was repeated several times in different points for each IB studied, recording a large number of curves

¶Although its simplicity, the Hertzian model has demonstrated to be one of the most effective and widely used models for the mathematical analysis of the F *vs.* d curves obtained with FSAFM in biological samples[84–89]

‖The reduced modulus (E*) is related to Young's modulus (E) of the test specimen through the following relationship $1/E^{*} = (1 - \nu_i^2)/E_i + (1 - \nu_s^2)/E_s$ where E_i, ν_i, E_s, ν_s are the Young's modulus and the Poisson ratio of the indenter and the sample, respectively

(at least 200) representative for each IB strain. The big number of indentations performed on each IB subjects them to a high level of stress, which might lead to the rupture of the aggregate and the subsequent alteration of the measurement. Thus, with the objective of controlling if the measured IB has been destroyed during the realization of the force spectroscopy curves, AFM images before and after the analysis were obtained. Images obtained show no serious deformation on the IB, which kept its initial shape and structure (Figure 10.9).

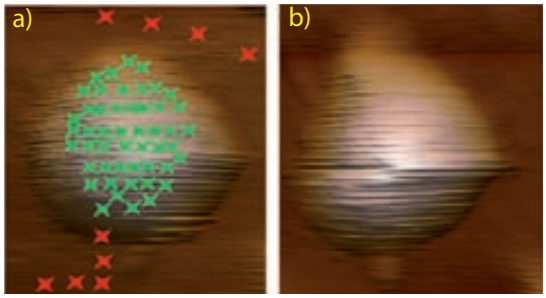

Figure 10.9: AFM imageof an IB a) before and b) after indenting. Green crosses represent the spectroscopical measurements performed on the IB while red ones are the ones executed over the clean mica surface. It is possible to observe how no damage was produced to the integrity of the studied IB while spectroscopical measurements were carried out.

In our case, from the two plausible tip geometries (conical or spherical) associated with the hertzian fitting, the one related with a spherical tip presented the higher agreement with the experimental data (Figure 10.8 b). This compatibility of the experimental data with the model was verified for the most part of the experimental curves.

Table 10.1: Elasticity distribution values obtained for the different IBs after statistical analysis of the FSAFM measurements

IB	**Young's modulus**			(MPa)
wt	3.73±0.05			
Dnak$^-$	3.56±0.56		7.75±0.99	
ClpA$^-$	5.01±0.25		10.99±0.30	
ClpP$^-$	3.33±0.21	7.10±0.09	13.45±2.28	22.07±0.168

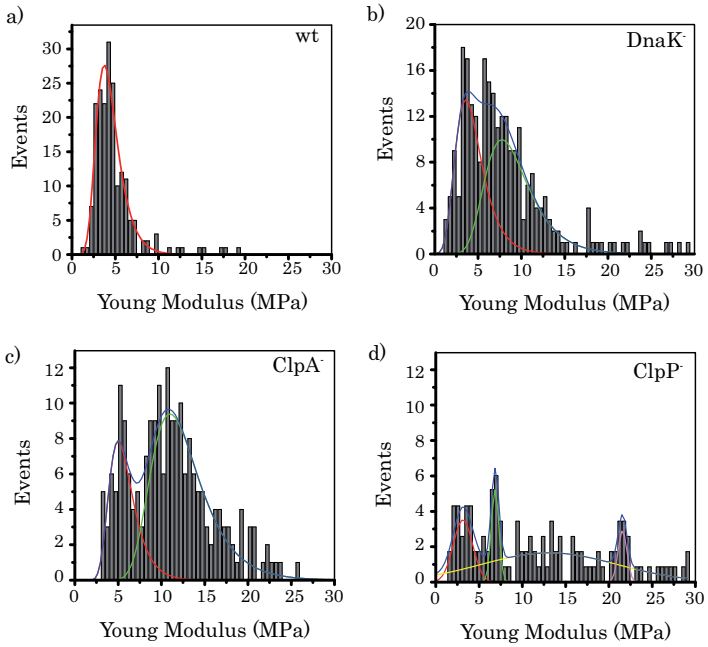

Figure 10.10: Histogram representation of the number of events *vs.* Young modulus obtained for IBs produced in different bacterial mutants. a) Wt IBs showing only one peak at 3.73 MPa, b) DnaK$^-$ IBs show two overlapped Young modulus distributions centered at 3.56 and 7.75 MPa, c) ClpA$^-$ IBs show the presence of two different Young modulus distributions, at 5.01 and 10.99 MPa and d) ClpP$^-$ IBs show the presence of an inhomogeneous distribution of elasticity with four Young modulus distributions at 3.33, 7.10, 13.45 MPa and 22.07 MPa.

Statistical studies, presented in Figure 10.10 and sumarized in Table 10.1, indicate the existence of different Young modulus distributions according to the IB origin. Stiffness data obtained for wt IBs, represented on Figure 10.10 a, depicted a monomodal elasticity distribution with a main peak value of 3.73±0.05 MPa and an full width at half maximum (fwhm) of 2.9±0.05 MPa. On the other hand, for DnaK$^-$ and ClpA$^-$ IBs results indicate the presence of two elasticity populations. In the case of DnaK$^-$ IBs (Figure 10.10 b), the peak at lower strength values was situated at 3.56±0.56 MPa with an fwhm of 3.6±0.48 MPa matching the one obtained for wt particles. However the second population, shifted to harder areas, was placed at 7.75±0.99 MPa with a broader shape with a fwhm of 5.8±0.37 MPa. For ClpA$^-$ IBs (Figure 10.10 c), the peak distribution was shifted, for both populations, to harder areas with mean peak values of 5.01±0.25 and 10.99±0.30 MPa and fwhm of 3.2±0.28 and 6.6±0.25 MPa, respectively. Results obtained after the

analysis of ClpP$^-$ IBs depict the presence of four different stiffness populations (Figure 10.10 d) two of them situated in the range previously observed for the ClpA$^-$ IBs, (3.33±0.21 and 7.10±0.09 with fwhm of 2,67±0.59 and 1,05±0.39, respectively) and other two at higher Young modulus values, (13.45±2.28 MPa and 22,07±0,168 MPa with fwhm of 18,75±2.59 MPa and 1,21±0,468 MPa, respectively).

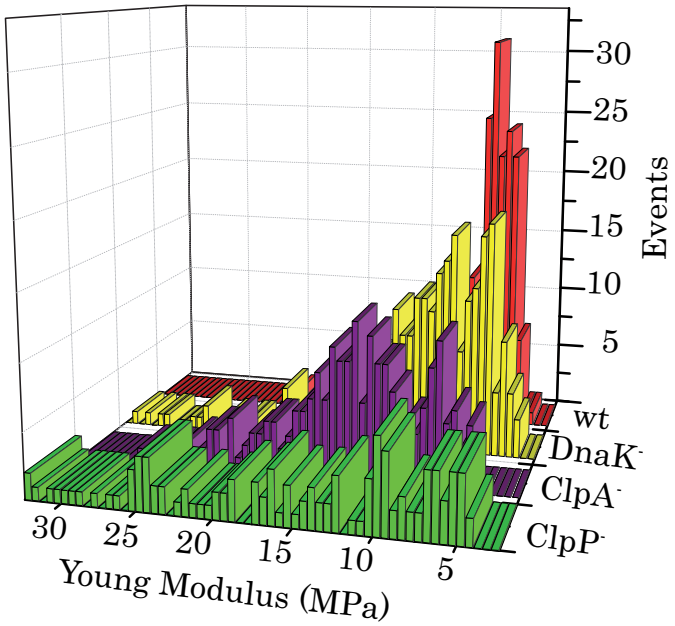

Figure 10.11: 3D Histogram representation of the number of events vs. Young modulus for IBs produced in the different bacterial mutants.

Although, Young modulus values obtained after mathematical treatment of the FSAFM measurements performed onto ClpP$^-$ IBs indicate the appearance of harder elasticity distributions, if compared with the other IBs. The presence of one peak at 22.07 MPa can not be explained just by the modification of the protein stiffness as it differs almost 10 MPa with the previous distribution from the same IB. Therefore, and taking into account the reduced height previously observed on ClpP$^-$ IBs (Figure 10.6) this peak can be assigned to the influence of the substrate on the AFM tip during the FSAFM measurement. In order to easily compare the results obtained for all the IBs tested, a 3D representation of the stiffness histograms obtained for all the IBs tested is depicted in Figure 10.11. In summary, it is possible to observe how, by the modification of the genetic background of

the IBs, not only a general shift to higher stiffness on the Young modulus of the IBs can be observed, but also an increase on the number of different elasticity populations is present, indicating the appearance of hardness differences between the proteins conforming the IBs.

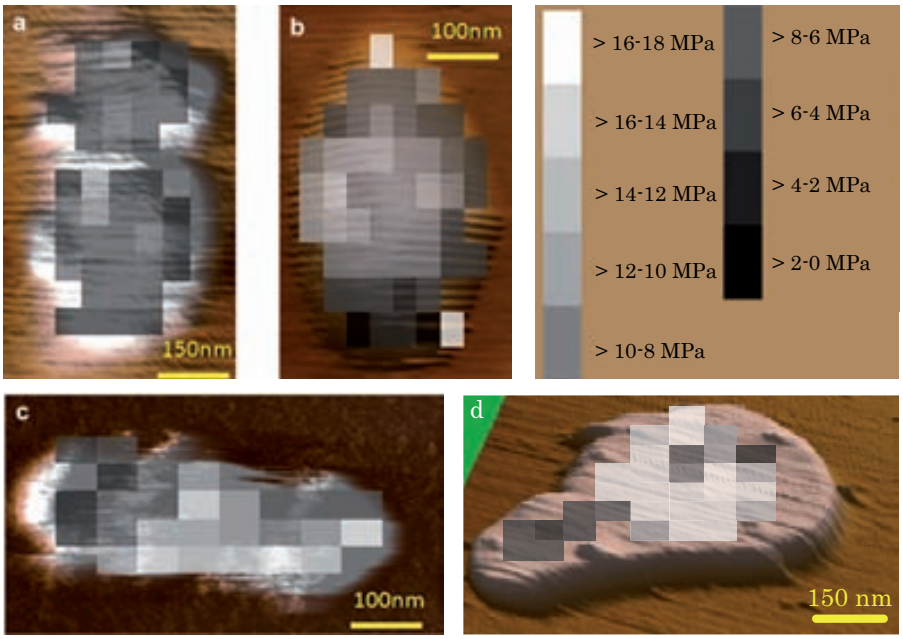

Figure 10.12: 2D software reconstruction of the elasticity maps of IBs from different genetic backgrounds. a) wt IBs, b) DnaK$^-$ IBs, c) ClpA$^-$ and d) ClpP$^-$ IBs. Observations infer the existence of an homogeneously spread distribution of Young modulus values over the wt IBs. On the other hand, maps obtained for DnaK$^-$, ClpA$^-$ and ClpP$^-$ IBs indicate the existence of two elasticity populations, with the harder areas segregated and localized on the center of the DnaK$^-$ IBs and on the right side of ClpA$^-$ and ClpP$^-$ particles.

However, FSAFM is not only a extremely sensitive technique that allow us to obtain the nanoscale mechanical properties of an object but it also counts with the excellent lateral resolution of an AFM. Therefore, and by the use of an AFM equipped with a closed loop tracking system,** it was possible to obtain the spatial distribution of the elasticity regimes over one IB and to develop stiffness maps (Figure 10.12), where each force (F) vs. indentation (d) measurement was spatially localized over the target IB. Figure 10.12 a shows how the Young modulus is homogeneously spread over the wt IBs, with mean values of 3.6±0.56 MPa.

**X and Y positioning system that allows the AFM tip to overcome the hysteresis and temperature drift problems introducing complete spatial resolution of the measurement

As previously shown in the Young modulus determination, in DnaK$^-$ and ClpA$^-$ IBs two elasticity populations could be observed, as entailed in Figure 10.12 b and i, with the harder areas segregated and localized on the center of the DnaK$^-$ IBs and on the right side of ClpA$^-$ particles. ClpP$^-$ particles show similar distributions (Figure 10.12 d) than ClpA$^-$ IB. The above described data indicated that, the genetics of IB fabrication, determines not only the final size, folding and content of active protein, but also the coexistence of more rigid structures and softer ones in the same IB. Furthermore, it seems that these different structures are localized on determined areas of individual IB, confirming the existence of structural diversity inside the protein aggregates. Therefore, it is possible to affirm that the use of modified bacteria for IB production might also imply the possibility to tune their mechanical properties, which as previously depicted on the Introduction (Section 9.2.2.3) is of extreme importance for the maximization of the bioregenerative properties of biomaterials.

10.2.3 Physico-chemical characterization of the IBs

Another characteristic of the IBs that can influence their final use in biomedical applications is their surface physico-chemical properties. Model surfaces with known physico-chemical properties have been widely employed for studying not only material surface properties but also complex events such as protein adsorption or cellular responses. Previous studies have already shown how different surface properties entail variations on the macroscopic behavior of a biomaterial,[28] being those related with changes on the electrical charges and on wettability among the most influencing.[96,97]

The surface charge of a material is not an absolute value, as it is seriously affected by the surrounding media. Therefore, in order to obtain information about the surface charge of the different IBs in the same media, Z-potential[††] measurements of freshly prepared IBs suspended in buffer solutions (PBS, pH = 7.4) were performed using the dynamic light scattering (DLS) technique.

Results obtained, Table 10.2, showed that IBs from the different genetic backgrounds present a very similar and slightly negative charged surfaces, which is indicative not only of the unstablility of IBs suspensions, that will tend to coagulate forming larger aggregates with time (Section 6.2.3.1), but also reveals a

[††]Z-potential of a dispersed particle gives information about the potential difference between the dispersion medium and the stationary layer of fluid attached to the dispersed particle, indicating the charge of the particle in suspension

tendency to interact with positively charged surfaces.

IB	**Z-Potential** (mV)	St. Dev.
wt	-16.7	1.7
Dnak$^-$	-18.2	1.7
ClpA$^-$	-17.8	1.7
ClpP$^-$	-26.5	1.3

Table 10.2: Z-potential values of the freshly prepared IB suspensions coming form different genetic backgrounds as determined by DLS

Nevertheless, the small differences observed do not permit to establish whether the origin of the IBs has any influence on their adhesion onto a determined surface.
As stated before, the wettability of the surface of a determined biomaterial plays a crucial role on its final adhesive properties. In order to study the wettability properties of IB variants (namely those produced in DnaK$^-$, ClpA$^-$ and ClpP$^-$ mutants *vs.* wt strain), six SAMs on gold substrates were obtained by functionalizing them with different molar ratios (X) of -OH terminated (hydrophilic) and -CH_3 terminated (hydrophobic) alkanethiols. As a result, an array of modified gold surfaces bearing controlled contact angles, ranging from 110° to 20°, were fabricated (see Experimental Part). Afterwards, the different arrays of modified gold surfaces were immersed in suspensions (20 mg/mL) of the different IB variants in PBS (pH = 7.4) for 2 hours and subsequently, contact angle (CA) and IB coverage counting of the different functionalized gold substrates were determined before and after IB deposition (See Experimental Part).
Results obtained are schematically shown in Figure 10.13. While prior to IB deposition, an increase of 10% in the concentration of the hydroxyl terminated thiol with respect to the -CH_3 terminated ones, implied a decrease of 6±1° on the contact angle of the functionalized surface, the measurements performed after the deposition of IBs presented a much smaller reduction (Figure 10.13 left). This fact was more intense for Dnak$^-$ and ClpA$^-$ IBs where the decrements were 2.4±0.8° and 1.9±0.5° (Figure 10.13 b, c left), respectively, than for wt or ClpP$^-$ IBs where the diminutions were 4.5±0.8° and 5.9±0.8°, respectively (Figure 10.13 a, d left). Thus, it is possible to say that the presence of IBs on the functional surface, buffers

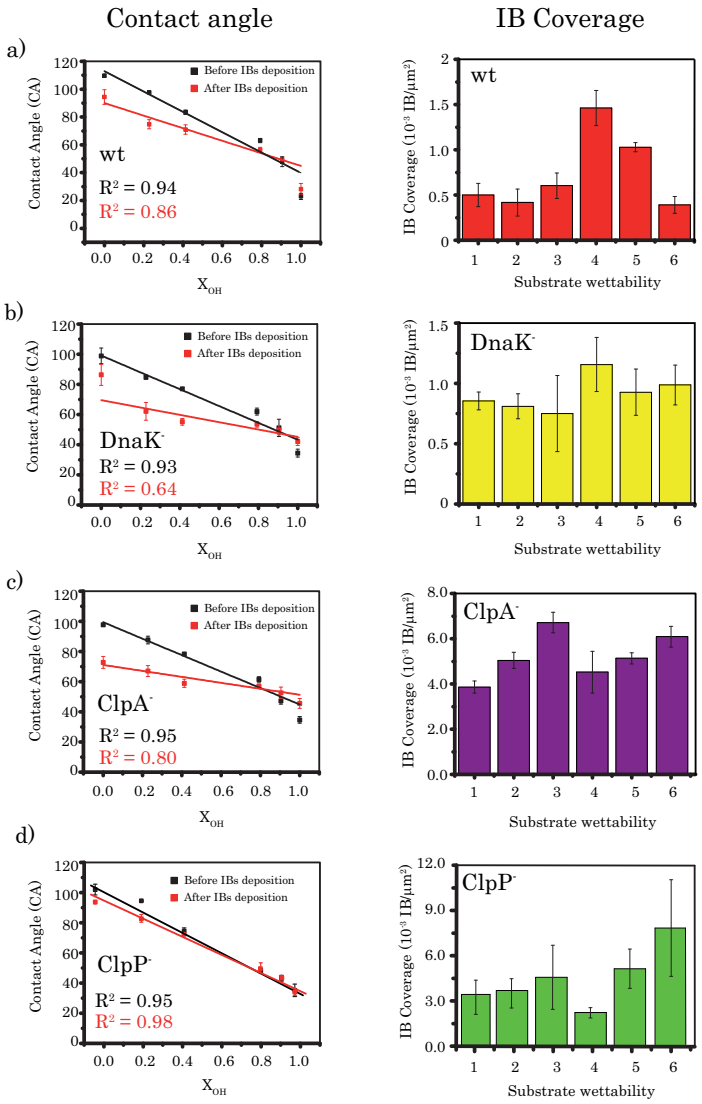

Figure 10.13: Left; Contact angles of the 6 different -CH_3 terminated gold surfaces, containing different molar ratio of -OH terminated (X_{OH}) alkanethiols, gold surfaces before and after deposition of IBs. Right; Dependence of the IBs coverage on the functionalized gold substrate wettability a) wt, b) DnaK$^-$, c) ClpA$^-$ and d) ClpP$^-$. Substrate wettability ranging from 20-30° (1), 40-50°(2), 60-70° (3), 70-80° (4), 80-90° (5) and 100-110° (6).

the change of wettability of the substrate at different extent deppending on their genetic background.

IBs surface coverage dependence with the substrate contact angle was also determined by measuring the density of aggregates per μm^2 using an optical fluorescence microscope connected to a CCD camera. Fluorescence images obtained were treated with the ImageJ 1.38 software[‡‡] in order to count the observed IBs, as fluorescent dots. Results obtained for wt IBs (Figure 10.13a right) showed the existence of a maximum of IBs coverage reaching absolute values of 0.0015 IB/μm^2, for a surface contact angle of approximately 80°. Therefore, it is possible to establish a preference of these IBs to join slightly hydrophobic surfaces.

On the other hand, data obtained for the other IBs tested, Dnak$^-$, ClpA$^-$ and ClpP$^-$ (Figure 10.13 b, c right and d, respectively), exhibited significantly different tendencies. In all the cases, the maximum of interaction was slightly shifted to lower contact angles (75° for DnaK$^-$ and 60° for both ClpA$^-$ and ClpP$^-$) and a gradual increase of the covering of IBs on the modified surfaces for higher contact angles (>90°) could also be observed, pointing to the existence of more amphiphilic behaviors of the DnaK$^-$, ClpA$^-$ and ClpP$^-$ IB surfaces. Thus, it is possible to observe how, by changing the IB variant, the dependence of the substrate contact angle with the maximum coverage varies from monomodal, with a single maximum at 80° (wt), to bimodal, with two peaks, one at lower angles (between 75° and 60°) and the other one at higher values (>90°), for DnaK$^-$ and ClpA$^-$ respectively, indicating the existence of two different wettability populations. However, looking at the absolute IBs coverage values, Dnak$^-$ IBs showed extreme similarity to those obtained with wt IBs, reaching a maximum coverage of 0.0012 IB/μm^2, while ClpA$^-$ and ClpP$^-$ IBs depict coverage levels up to 5 times higher (0.007 IB/μm^2 for ClpA$^-$ and for ClpP$^-$). This fact is of extreme importance, as an increase on the IBs density entails not only the subsequent increase on the amount of deposited biomaterial, but also the enhancement of the final roughness of the treated surface, usually related to cell proliferation properties modification.[98]

Therefore, it was possible to establish that the wettability of surfaces decorated with IBs is dependent of their genetic background where they were produced, and that the modification of this parameter allow us not only to tune the interaction of IBs with the media, but also to modify the density of deposited IBs and, therefore, the final roughness of the covered material. Being, all of them, factors which have a direct relationship with the tissue regeneration abilities.

[‡‡]GNU license

10.2.4 Conclusions

The conformation status of the recombinant proteins forming the IBs, as regulated by the protein quality control machinery of bacteria, defines the nanoscale, structural and physicochemical properties of IBs. Such proteinaceous particulate biomaterials exhibit a range of sizes, wettability and stiffness when obtained from wt, DnaK$^-$, ClpA$^-$ and ClpP$^-$ strains, associated to the style of protein packaging occurring in absence of each of these elements of the heat shock machinery. The inhibition of proteolysis allowing the deposition of otherwise degraded protein species and the associated condensation of the IB cross-β-sheet architecture in DnaK$^-$, ClpA$^-$ and ClpP$^-$ backgrounds can account for the up shift of particle size (from 342 to 530 nm) and stiffness (from around 2 up to 13 MPa) as well as the change in wettability and fluorescence properties of IBs. Furthermore, such results are in agreement with previous Fourier transformed infrared spectroscopy analyses (FTIR) of IBs from modified cellular strains, in which a downshift in the β-sheet peaks (at 1627 and 1693 cm^{-1}) was observed,[99] indicating a more compact and therefore stiffer cross-β-sheet architecture than in wt IBs. In addition, recombinant proteins are stabilized in these backgrounds as a result of a global inhibition of the proteolytic activity of the quality control machinery,[70] leading to the incorporation of otherwise degraded protein species into IBs. This dual deposition could be related to the heterogeneous stiffness maps obtained for DnaK$^-$, ClpA$^-$ and ClpP$^-$ IBs, and indicates that the conformational status of the aggregated polypeptides determines the consistence of the protein clusters at the nanoscale level.

All these aspects are of extreme importance, as permit us, just by the modification of the genetic background of the IBs, to selectively tune the structural, morphological, mechanical and other physicochemical properties of IBs, which are clue for the correct interaction between proteins, cells and biomaterials when applied to regenerative medicine.*

10.3 IBs as cell proliferation vectors

As explained before, in tissue engineering the cell binding and proliferation can be stimulated through a set of different approaches being the topographical[47]

*The different structural and physico-chemical properties of IBs obtained from different strains and their influence on surface adhesion have been published at *Biomaterials*, **2010**, *31*, 5802-5812.

or physicochemical[28,48] modification of the material surface properties the most employed. For this purpose different techniques have been used, from materials etching to soft lithography methods, depending on the nature of the material itself. Recently, approaches based on surface functionalization with biomaterials[100–105] or decoration with nanoparticles have also permitted a fine tuning of the surface and roughness irrespective of the support material.[104,105] For instance, silica and ceramic nanoparticles between 24 and 1500 nm in diameter can positively modulate the cell proliferation.[104,106] Nevertheless, not all the nanoparticles are suitable to be used as decoration motives on biomaterials for tissue engineering as they have to accomplish severe requirements of biocompatibility, toxicity and stability among others.

Previous studies have already pointed IBs as cost effective noncytotoxic nanomaterials which sizes and physicochemical properties, as beforehand explained, can be easily tuned. Therefore, they were thought to be good candidates for the biomaterials surface decoration. Nevertheless, prior to further experimental work, it was needed to test the stability of IBs not only with time but also *versus* storage under diverse environmental conditions.

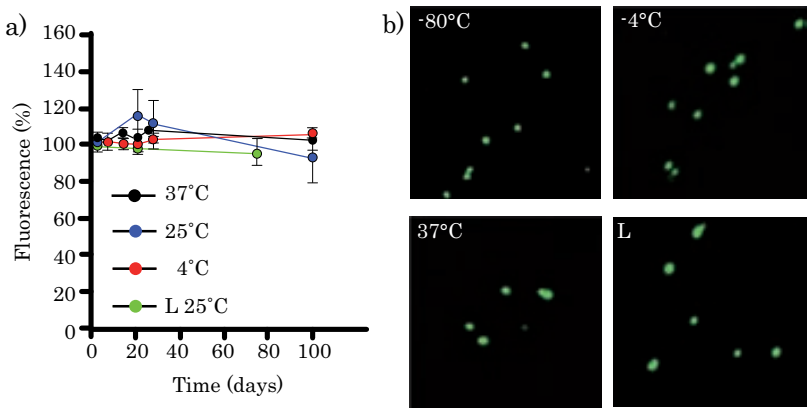

Figure 10.14: a) IBs stabilities measured as the lose of fluorescence activity of GFP IBs stored in aqueous buffer at 37°C, 25°C, and 4°C, or lyophilized (L) and further stored at 25°C for 100 days; b) Confocal microscopy of purified IBs kept for one month at 37°C, -4°C and -80°C. Stability after lyophilization/reconstitution was also measured (L).

Results obtained indicate that GFP IBs are fully stable for long periods of time with respect to both fluorescence emission (Figure 10.14 a) and architecture at all the different conditions tested (Figure 10.14 b), allowing both the conservation and a convenient manipulation of IBs under assay conditions. Interestingly, IBs

were also mechanically and functionally stable during lyophilization, extending even more their potential since they can be kept for long periods of time (months or even years).

As previously explained on the introduction, the succeed of a determined biomaterial when employed in tissue engineering lies on the formation of the correct interactions between the material surface and the proteins and cells present on the media. Thus, the use of surface coatings or modification systems for the better adaptation of the biomaterial surface to its function is a common procedure. During the previous section we have thoroughfuly studied and characterized the structural, morphological and physicochemical properties of different IBs, with results that fit on the range of interest of the biomaterials surface modification field. Therefore, once established the stability and resistance of the IBs under different conditions we proceed to explore their applicability as cell growth promoters. In a first proof of concept, to determine if IBs could be used as proliferation vector for tissue engineering, we drop-casted a suspension of DnaK$^-$ GFP IBs in PBS (pH = 7.4) on tissue-culture-treated polystyrene plates* and tested the growth of baby hamster kidney (BHK21) mammalian cells for 75 hours. All the cell proliferation measurements were performed by Dr. Esther Vázquez from the IBB Institute of *Universitat Autònoma de Barcelona*. A non-treated polystyrene surface and a treated surface with vitronectin† were used in control experiments.

Drop casting of the IBs resulted on a random distribution of the IBs over the polystyrene surface, as shown in Figure 10.15 a. IB counting results, performed using the same protocol used for the coverage *vs.* surface wettability analysis, indicate a IB density of 0.05 IBs/μm^2 (calculated as in Section 10.2.3).

Once decorated, the freshly prepared polystyrene surfaces were cultured during 75 hours in the presence of BHK21 cells. Results, depicted on Figure 10.15 b, show a relevant growth of the BHK21 cells that appear intimately attached to the GFP IBs, as observed by the merging of the cell membrane staining (red label) and IB fluorescence (green label) (Figure 10.15 c).

Intriguingly, cell number quantification experiments, performed using the same surfaces, indicate that in the polystyrene surface, which is largely optimized for cell adhesion and growth, the conventional cell-binding agent vitronectin did not have a detectable effect (Figure 10.16 a) and a signal similar to the reference was

*These polystyrene plates are the traditionally used as substrates for cell proliferation and culture studies

†Vitronectin is a cell adhesion and spreading promoter protein which is very common in serum and the extracellular matrix

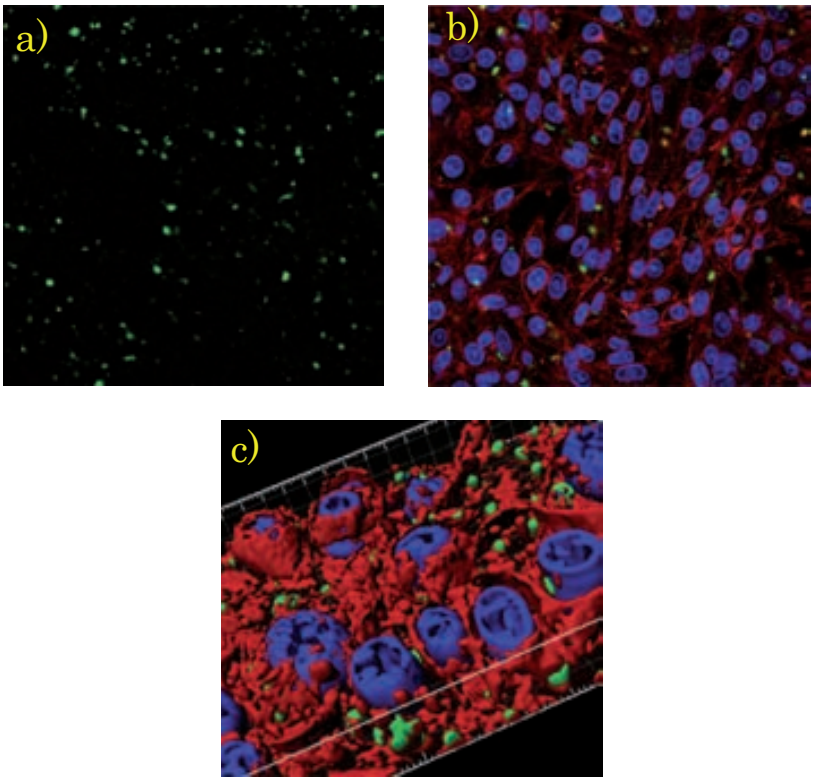

Figure 10.15: Stimulated BHK21 mammalian-cell proliferation by the presence of IBs on the surface. a) Confocal image of a 35 mm polystyrene plate coated with 240 μg of GFP IBs produced in wt cells (green) prior to cell proliferation experiment; b) For the same field, the BHK cell overlay of the 0.6 mm section 75 h after cell deposition, showing a big number of cells (in blue the nucleous and in red the cytoplasm) over the IBs (green) treated surface; c) 3D reconstruction of a confocal xyz stack of 22 sections processed with Imaris 3D software by applying the isosurface module.

obtained. On the other hand, results obtained for the IBs decorated surfaces show a dramatic stimulation of cell proliferation (Figure 10.16 a), more remarkable after 72 hours of culturing.

In order to discard any other contribution to the cell proliferation, this results were repeated using polystyrene surfaces decorated with different amounts of IBs. Results obtained depicted an IBs dose dependency of the cell proliferation (Figure 10.16 b), which not only corroborates the influence of IBs on the cell growth but also opens the door to the tunable setting of the proliferation. Moreover, no cytopathic effects were observed in cells cultured, independently of the number of IBs on the treated surfaces.

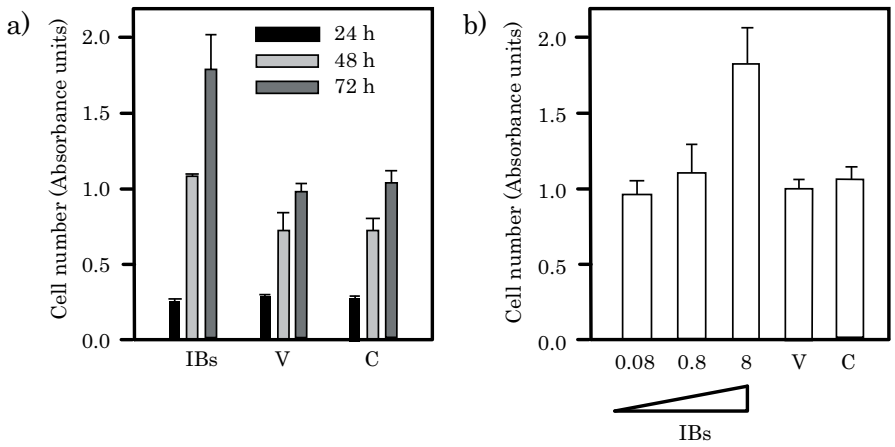

Figure 10.16: a) BHK cell growth on IB-coated plates (IB), vitronectin-coated plates (V), and control plates (C); b) BHK cell growth on plates coated with different concentrations of IBs (in IBs/μm^2) compared to vitronectin-coated plates (V) and control plates (C).

Once demonstrated that random surface decoration and patterning with inclusion bodies has a significant and positive impact on cell growth, we wanted to study how the rational modification of the structural and physicochemical characteristics of IBs may influence their macroscopic impact on living cells in IB-cell interfaces. To determine if these alterations in the IBs nanoscale properties could be sensed by biological systems, we comparatively explored the promotion of the proliferation of two different mammalian cells -the previously used BHK21 strain and the PC12*- cultured on the same kind of polystyrene surfaces decorated with IBs of different genetic origins. For this experiment, IBs produced on wt, DnaK$^-$ and ClpA$^-$ were used. The preparation of the polystyrene culture plates was carried out under the same conditions previously employed and the cell proliferation was determined following the MTT method (see Experimental Part).

Interestingly, the proliferation of BHK21 cells was favored by all IB variants although at different extents (Figure 10.17 a). While for the first 48 hours a significant cell proliferation increase is detected for the coated substrate with respect to the non coated (control) one, it is not possible to distinguish between the different IBs. However, at 72h after the initiation of the culture the cell density in plates decorated with wt and Dnak$^-$ IBs was about twice than in plates without IBs and both types of IBs rendered cell density values statistically indistinguishable

*Cellular line coming from a pheochromocytoma of the rat adrenal medulla, often used as a model system for neuronal differentiation

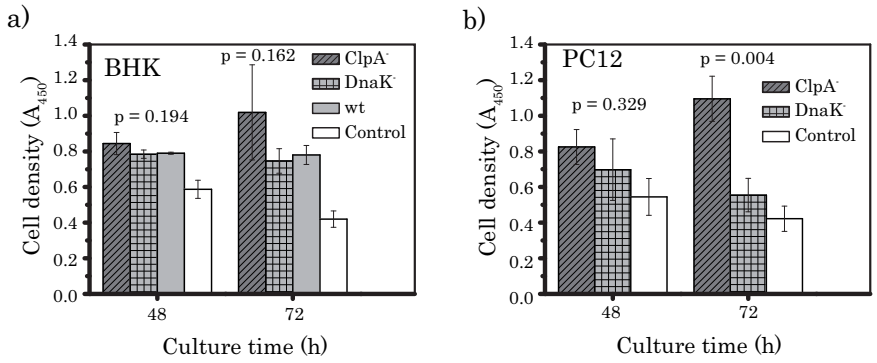

Figure 10.17: Cell proliferation determined by a conventional MTT assay monitored in polystyrene plates. Plates were untreated (control) or decorated with $2.65 \cdot 10^8$ IBs per well of different IB variants. The analysis was done in triplicate using a) BHK and b) PC12 cell lines. Differences of cell density between IB-decorated wells and IB-free wells (control) were always significant ($p<0.006$, not shown) in all the experiments. As an exception, growth of PC12 cells on DnaK IBs was stimulated over the control in the limits of statistic significance ($p<0.132$ at 48 h and $p<0.047$ at 72 h). The significance as p values of the differences between growth on ClpA$^-$ and DnaK$^-$ IBs are depicted over the corresponding bars.

($p<0.538$)* between them. ClpA$^-$ IBs dramatically enhanced cell density over the values achieved by other IB variants, although at levels still out of significance level ($p<0.162$ when comparing with Dnak$^-$ IBs and $p<0.203$ when comparing with wt IBs).

To confirm the differential properties of ClpA$^-$ IBs in stimulating cell proliferation, we extended the study to rat pheochromocytoma (PC12) cells, that tend to grow as floating clusters rather than as firmly attached monolayers. In this model, ClpA$^-$ IBs enhanced cell proliferation over Dnak$^-$ IBs and control surfaces in a still more evident way, even after only 48 hours of cell culture and becoming more and more evident with the pass of time (Figure 10.17 b; $p<0.004$). On the other hand, although DnaK$^-$ IBs do produce an enhancement of the cell proliferation after 72 hours of cell culture, if compared to control measurements, p values indicate that both results (DnaK$^-$ and control cell proliferation) are not significantly different.

These results confirm that through the modification of the genetic background

*The p value, more known as "statistical significance", indicates the probability that the observed relationship or a difference in a sample occurred by chance. p-Values below 0.05 p-values indicate that there is a 5% probability that the relation between the variables found in our sample is a obtained by chance[107]

of the IBs, it is possible to achieve IB nanoparticles displaying improved tissue engineering characteristics which are directly linked to their structural and physicochemical properties. Furthermore, the progressive temporal increase of the proliferation observed with the MTT assays promoted by the IB variants indicate that they act stimulating cell proliferation rather than cell adhesion. Interestingly, the similarity between the macroscopic eco of Dnak$^-$ and wt IBs in IB-cell interfaces and the divergent behavior of ClpA$^-$ IBs is highly coincident with the profile of the nanomechanical and physicochemical properties (stiffness and wettability, respectively) exhibited by the IB variants, again very proximal when comparing IBs produced by wt and Dnak$^-$ cells.

10.3.1 2D microstructuring of IBs for cell directionality

Until now it has been demonstrated that IBs are highly efficient as tunable growth vectors which can be easily deposited on surfaces of different nature. Nevertheless, for some biomedical applications a localized cell growth is needed, being the local structuring of the proliferation vector required.

Despite other available biomaterials such as polymers or hydrogels, which chemical structure forces the use of more expensive and aggressive structuring techniques, IBs are nanoparticulate entities which can be easily processed using a suspension in a buffer solution (PBS, pH = 7.4), opening the door to their use in cost effective and softer techniques such as soft lithography or dip pen lithography, among others. Therefore, as a proof of concept in order to corroborate the versatility of IBs as surface modification element, we proceed to their microstructuring onto a solid substrate by means of the μ-CP technique. In this case, and with the objective of reducing the patterning difficulties, the surface chosen was SiO_2 due to its flatness and reduced intrinsic roughness together with its easy functionalization with proper SAMs. An schematic representation of the followed procedure is represented on Figure 10.18.

As previously stated, IBs nanoparticles are slightly negatively charged when suspended in PBS buffer (Section 10.2.3), therefore and as SiO_2 surfaces present free -OH groups, the first stage for the IBs structuring was the chemical functionalization of the surface with an appropriate chemical group to maximize IBs anchoring. Among all the plausible chemical modifications the use of amine terminated silanes, and more specifically of N-[3-(trimethoxysilyl)propyl]ethylenediamine(TPEDA),

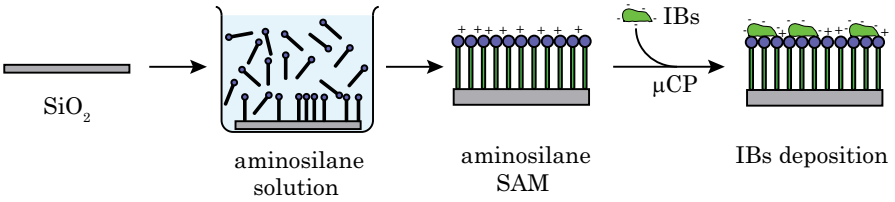

Figure 10.18: Schematic representation of the procedure used for the IBs μ-CP onto a solid substrate

appeared as the most reliable option.[108] SAMs of this compound does not only present a contact angle in the range of maximum coverage of DnaK$^-$ IBs (60-70°), but also a terminal amino group that can be easily positively charged increasing the interactions between the SAM and the negatively charged IBs surfaces entailing an increment of the coating by the appearance of electrostatic interactions. Furthermore, the TPEDA SAMs satisfy other of the key points of the SiO_2 functionalization which is the obtaining of a versatile and stable SAM that provides the substrate with the sufficient reliability for the further processing and cell culture. The preparation of the SAM coated silicon oxide substrate is explained in the Experimental Part.

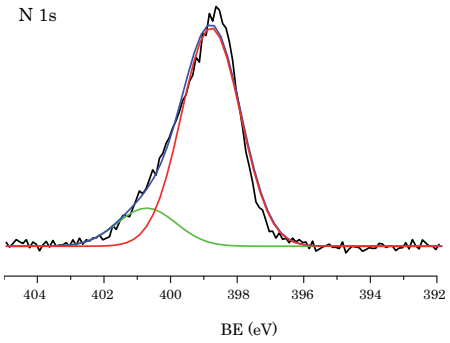

Figure 10.19: XPS spectra of the N1s peak of the aminosilane SAM modified silicon oxide surface

After preparation, and prior to the IBs structuring, the freshly prepared SAM modified surface was characterized by CA and XPS techniques. CA results indicate the presence of an average static contact angle of 64.5±5.5°, which is in

agreement with the values observed on the literature for this kind of amino terminated layers.[109] N1s XPS results, depicted on Figure 10.19, show the presence of one main peak at 398.7 eV, which can be assigned to the overlapped signals of the -NH- and -NH_2 peaks present on the TPEDA chemical structure, and a small shoulder to higher energies (400.7 eV) coming from the protonated amines (NH_2^+ and NH_3^+) that will render a positive charge to the SAM surface.

Therefore, once the correct formation of the TPEDA SAM over the SiO_2 was corroborated, we proceed with the μ-CP of the IBs. As previously described on the introduction, the μ-CP is a soft lithography technique based on the use of a decorated elastomeric stamp to transfer the pattern of the substance which want to be deposited directly onto the target substrate as a print. In our case a 30 μm stripes decorated PDMS stamp (see Experimental Part for PDMS stamp production and patterning processing) were inked with a $DanK^-$ IBs PBS buffer (pH 7.4) suspension for 40 min, dried under nitrogen flow, and placed onto a clean negatively charged amine-terminated silicon substrate. After 1 min contact time the stamp was carefully removed and the patterned surface gently rinsed with ultrapure water to remove the non adhered IBs.

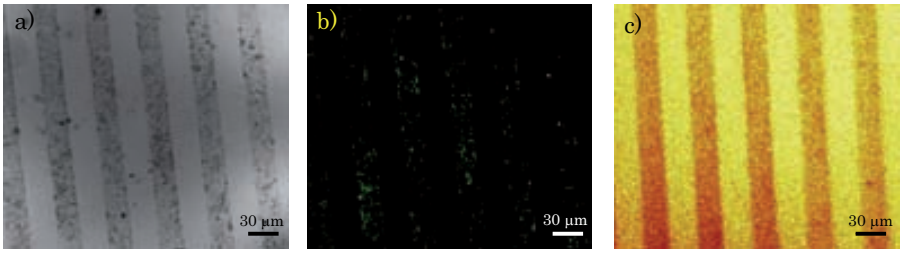

Figure 10.20: Images of the 30 μm lined IB-patterned amino-terminated silicon surfaces taken by a) conventional b) confocal microscopy and c) -CN ions ToF-SIMS analysis

The patterned surfaces were analyzed using fluorescence confocal microscopy and time of flight second ion mass spectrometry (ToF-SIMS) techniques. The optical and confocal microscope images (Figure 10.20 a and b, respectively) clearly show the presence of 50 μm IBs arranged on stripes on the silicon surface. Furthermore, the intense fluorescence observed indicates that IBs remain intact after the imprinting process. Coverage studies performed following the same protocol previously depicted (Section 10.2.3) indicate a IBs density of 0.04 IBs/μm^2, four times higher that the maximum coverage obtained for the $DnaK^-$ IBs with the wettability controlled surface, and reaching the levels observed for the $ClpA^-$ or the $ClpP^-$.

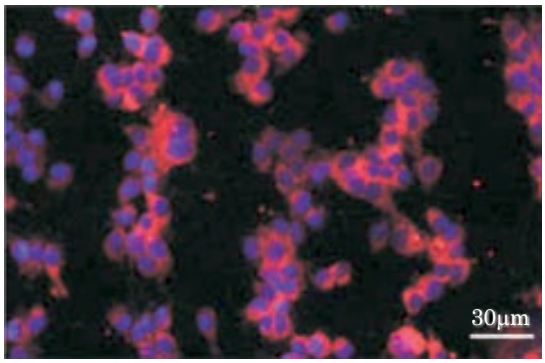

Figure 10.21: Image of the 30 μm lined IB-patterned amino-terminated silicon surfaces taken by confocal microscopy after 48 hours of growth of BHK21 cells

The presence of IBs was confirmed by ToF-SIMS. This spectrometrical technique consists on the use of energy controlled Ga^{3+} atoms to locally ionize the sample surface and the ions released are analyzed on a time of flight detector. Thus, it is possible not only to obtain information about the chemical composition of the studied sample but also to obtain spatial resolution of this information. Figure 10.20 c depicts a CN^- ion ToF-SIM image obtained from a 50 μm $DnaK^-$ IBs stripes decorated TPEDA silicon oxide surface. The brighter color corresponds to a CN^- richer areas.
Once determined that the IBs patterning process was successful we proceed to culture of BHK21 cells on the modified surface. Results, shown in Figure 10.21, clearly indicate a line-shaped stimulation of cell proliferation in the regions decorated with IBs, while no cell growth is detected on the IBs free areas. This result not only stresses again the ability of IBs to stimulate cell proliferation on surfaces that are initially not suitable for cell growth but also demonstrates that in combination with structuring techniques it is possible to obtain cell proliferation patterns, localizing the presence of cell growth to the selected areas.

10.4 Conclusions

Therefore, it has been demonstrated that the IBs are stable and versatile nanoparticulate biomaterials, whose fine structuring onto a solid substrate can be easily achieved by the use of efficient and cost effective soft lithographic techniques such

as μ-CP. Furthermore, cell proliferation studies performed with these IBs patterned surfaces have shown the excellent properties of this kind of proteinaceous nanoparticulate material as surface modification element for tissue engineering.*

*The use and structuring of IBs onto different kinds of biomaterials as cell proliferation enhancer has been object of an international patent accepted with number WO2010076361A1 and a publication in *Adv. Mat.*, **2009**, *21*, 4249-4253.

Chapter 11

General Conclusions

This second part of the Thesis has been focused on the study, characterization and structuring of a novel kind of proteinaceous nanoparticulated material, known as inclusion bodies (IBs), which are generated in vivo during the expression of a wide catalogue of recombinant peptides. Since bacterial inclusion bodies are fully biocompatible materials that can be obtained at large scale by cost-effective procedures, their physiological modification during biofabrication in selected genetic backgrounds can be observed as a possibility to generate specific tailored biological interfaces. The tuning opportunities offered through adjusting the quality control machinery of bacteria, might expand the spectrum of biomedical applications of this novel bacterial nanomaterial.

Characterization experiments have demonstrated how the final conformation status of recombinant proteins in *E.Coli* defines the nanoscale structural, physicochemical and mechanical properties of IBs. Such proteinaceous particulate biomaterial exhibit a range of sizes, wettability and stiffness when obtained in wt, $DnaK^-$, $ClpA^-$ and $ClpP^-$ strains, associated to the style of protein packaging occurring in absence of each of the elements of the protein quality control cell machinery.

The inhibition of proteolysis allows the deposition of the otherwise degraded protein species, which is reflected on an increase of the particle size distribution of IBs from the 342 nm of the non modified wt IBs to the 531 nm of the $DnaK^-$ IBs. This lack of protein quality control might also be associated to the condensation of the protein cross-β-sheet architecture in $DnaK^-$, $ClpA^-$ and $ClpP^-$ backgrounds, which can account from the modification of particle stiffness from around 3 up to 22 MPa. Furthermore, FSAFM analysis report an increase on the bulk stiffness

value of the IBs, together with the emergence of bi- and multimodal stiffness distributions ($DnaK^-$ and $ClpA^-$ IBs and $ClpP^-$ IBs, respectively). Additionally, 2D stiffness maps developed on different IBs indicate, that the spatial positioning of the distinct stiffness zones does not respond to a randomized distribution, but to the appearance of segregation between the different stiffness regions inside the same inclusion body.

The same argument can be applied to bulk wettability and wettability dependent surface coverage results. It is possible to observe how the deposition of IBs produces a decrease on the contact angle of the surface, which extension would be determined by the genetic background of the used IB. It is also observed how the maximum surface coverage is increased and shifted from one unimodal distribution placed at contact angle values between 70-80° to bimodal distributions with relative maxima at contact angle values between 70-80° and >90° for $DnaK^-$ IBs and 60-70° and >90° for $ClpA^-$ and $ClpP^-$ IBs.

Interestingly, when using different IBs for bottom-up decoration of surfaces for tissue engineering, such range of structural, physicochemical and mechanical properties could be sensed by cultured mammalian cells, resulting in a tunable stimulation of cell proliferation. This result was implemented by the structuring of the IBs on a solid substrate by the use of μ-CP, which resulted on the zone selective enhancement of cell growth, opening the doors to the obtaining of tunable materials for biomedical applications.

Bibliography

[1] Spindler, K. *The Man in the Ice: The Preserved Body of a Neolithic Man Reveals the Secrets of the Stone Age*; Harmony Books, 1994.

[2] CIA *The World Factbook*; Central Intelligence Agency, 2010.

[3] Baxevanis, A. D.; Ouellette, B. F. *Bioinformatics: A Practical Guide to the Analysis of Genes and Proteins*; Wiley-Interscience, New York, 1998.

[4] Reya, T.; Morrison, S.; Clarke, M.; Weissman, I. *Nature* **2001**, *414*, 105–111.

[5] Shin, H.; Jo, S.; Mikos, A. G. *Biomaterials* **2004**, *4*, 743–765.

[6] Smith, A. E. *The Lancet* **1999**, *S1*, S1–S4.

[7] Barratt, G. *Polymeric Biomaterials*; Marcel Dekker, New York, 2002.

[8] Allemann, E.; Gurny, R.; Doelker, E. *European Journal of Pharmacy and Biopharmacy* **1993**, *39*, 173.

[9] Bangham, A.; Standish, M.; Watkins, J. *Journal of Molecular Biology* **1965**, *13*, 238–252.

[10] Torchilin, V. *Nature Reviews Drug Discovery* **2005**, *4*, 145–160.

[11] ElBayoumi, T.; Torchilin, V. *Current Trends in Liposome Research* **2010**, *1*, 1–27.

[12] Sapra, P.; Allen, T. *Progress in Lipid Research* **2003**, *42*, 439–462.

[13] Drummond, D.; Zignani, M.; Leroux, J. *Progress in Lipid Research* **2000**, *39*, 409–460.

[14] Vacanti, J. P.; Langer, R. R. *The Lancet* **1999**, *S1*, S32–S34.

[15] Khang, G.; Kim, M. S.; Lee, H. B. *A manual for biomaterials: Scaffold fabrication technology*; World Scientific, 2007.

[16] Chen, Q.-Z.; Bretcanu, O.; Boccaccini, A. R. *Biomaterials Fabrication and Processing Handbook*; Taylor and Francis, 2008.

[17] Jones, J.; Boccaccini, A. *Cellular Ceramics: Structure, Manufacturing, Processing and Applications*; Wiley-VCH Verlag GmbH Co. Weinheim, 2005.

[18] Leong, K.; Cheah, C.; Chua, C. *Biomaterials* **2003**, *24*, 2363–2378.

[19] Wen, J.; Wilkes, G. L. *Chemistry of Materials* **1996**, *8*, 1667–1681.

[20] Hutmacher, D. W. *Biomaterials* **2000**, *21*, 2529 – 2543.

[21] Mikos, A.; Thorsen, A.; Czerwonka, L.; Bao, Y.; Langer, R.; Winslow, D.; Vacanti, J. *Polymer* **1994**, *35*, 1068–1077.

[22] Roach, P.; Eglin, D.; Rohde, K.; C., P. C. *Journal of Materials Science: Materials in Medicine* **2007**, *18*, 1263–1277.

[23] Mathieu, H. J. *Surface and Interface Analysis* **2001**, *32*, 3–9.

[24] Singhatanadgit, W.; Salih, V.; Olsen, I. *Journal of Cellular Physiology* **2006**, *209*, 912–922.

[25] Curran, J.; Chen, R.; Hunt, J. *Biomaterials* **2005**, *26*, 7057 – 7067.

[26] Zurlinden, K.; Laub, M.; Jennissen, H. *Materialwissenschaft und Werkstofftechnik* **2005**, *36*, 820–827.

[27] Jiao, Y.-P.; Cui, F.-Z. *Biomedical Materials* **2007**, *2*, R24–R37.

[28] Faucheuxa, N.; Schweiss, R.; Luetzow, K.; Werner, C.; Groth, T. *Biomaterials* **2004**, *25*, 2721–2730.

[29] Nuzzo, R. G.; Allara, D. L. *Journal of the American Chemical Society* **1983**, *105*, 4481–4483.

[30] Sagiv, J. *Journal of the American Chemical Society* **1980**, *102*, 92–98.

[31] Goubko, C. A.; Cao, X. *Materials Science and Engineering C* **2009**, *29*, 1855–1868.

[32] Xia, Y.; Whitesides, G. M. *Angewandte Chemie International Edition* **1998**, *37*, 550–575.

[33] Chen, Q.; Boccaccini, A. *Journal of Biomedical Materials Research A* **2006**, *77A*, 445–457.

[34] von der Mark, K.; Park, J.; Bauer, S.; Schmuki, P. *Cell and Tissue Research* **2010**, *339*, 131–153.

[35] Lampin, M.; Warocquier-clerout, R.; Legris, C.; Degrange, M.; Sigot-Luizard, M. *Journal of Biomedical Materials Research* **1997**, *36*, 99–108.

[36] Dalby, M.; Riehle, M.; Sutherland, D.; Agheli, H.; Curtis, A. *European Cells and Materials* **2005**, *9*, 1–8.

[37] Huo, F.; Zheng, Z.; Zheng, G.; Giam, L. R.; Zhang, H.; Mirkin, C. A. *Science* **2008**, *321*, 1658–1660.

[38] Lee, S. W.; Oh, B. K.; Sanedrin, R. G.; Salaita, K.; Fujigaya, T.; Mirkin, C. A. *Advanced Materials* **2006**, *18*, 1133–1136.

[39] Schmidt, R. C.; Healy, K. E. *Journal of Biomedical Materials Research Part A* **2009**, *90A*, 1252–1261.

[40] Sigal, G. B.; Mrksich, M.; Whitesides, G. M. *Journal of the American Chemical Society* **1998**, *120*, 3464–3473.

[41] Srivastava, S.; Verma, A.; Frankamp, B. L.; Rotello, V. *Advanced Materials* **2005**, *17*, 617–621.

[42] Xu, L.-C.; Siedlecki, C. A. *Biomaterials* **2007**, *28*, 3273–3283.

[43] Ostuni, E.; Chapman, R. G.; Holmlin, R. E.; Takayama, S.; Whitesides, G. M. *Langmuir* **2001**, *17*, 5605–5620.

[44] Iuliano, D. J.; Saavedra, S. S.; Tmskey, G. A. *Journal of Biomedical Materials Research* **1993**, *27*, 1103–1113.

[45] Offenhaeusser, A.; Boecker-Meffert, S.; Decker, T.; Helpenstein, R.; Gasteier, P.; Groll, J.; Moeller, M.; Reska, A.; Schaefer, S.; Schulte, P.; ; Vogt-Eisele, A. *Soft Matter* **2007**, *3*, 290–298.

[46] Bettinger, C. J.; Langer, R.; Borenstein, J. T. *Angewandte Chemie - International Edition* **2009**, *48*, 5406–5415.

[47] Flemming, R.; Murphy, C.; Abrams, G.; Goodman, S.; Nealey, P. *Biomaterials* **1999**, *20*, 573–588.

[48] Discher, D. E.; Janmey, P.; Wang, Y.-L. *Science* **2005**, *310*, 1139–1143.

[49] Discher, D. E.; Janmey, P.; Wang, Y.-L. *Science* **2005**, *310*, 1139–1143.

[50] McNaught, A. D.; Wilkinson, A. *IUPAC Compendium of Chemical Terminology*; Blackwell Scientific Publications, Oxford, 1997.

[51] Saha, K.; Keung, A. J.; Irwin, E. F.; Li, Y.; Little, L.; Schaffer, D. V.; Healy, K. E. *Biophysical Journal* **2008**, *95*, 4426–4438.

[52] Patolsky, F.; Zheng, G.; Hayden, O.; Lakadamyali, M.; Zhuang, X.; Lieber, C. M. *Proceedings of the National Academy of Sciences* **2004**, *101*, 14017–14022.

[53] Nath, N.; Chilkoti, A. *Analytical Chemistry* **2001**, *74*, 504–509.

[54] Hersel, U.; Dahmen, C.; Kessler, H. *Biomaterials* **2004**, *24*, 4385–4415.

[55] Zhang, L.; Webster, T. J. *Nanotoday* **2009**, *4*, 66–80.

[56] Sakiyama-Elbert, S. E.; Hubbell, J. A. *Annual Review of Materials Science* **2001**, *31*, 183–201.

[57] A, M. F. *The Biochemical Journal* **1986**, *240*, 1–12.

[58] Baneyx, F.; Mujacic, M. *Nat Biotech* **2004**, *22*, 1399–1408.

[59] Garcia-Fruitos, E.; Gonzalez-Montalban, N.; Morell, M.; Vera, A.; Ferraz, R.; Aris, A.; Ventura, S. a. V. A. *Microbial Cell Factories* **2005**, *4*, 27–33.

[60] Martinez-Alonso, M.; Gonzalez-Montalban, N.; Garcia-Fruitos, E.; Villaverde, A. *Microbial Cell Factories* **2009**, *8*, 4.

[61] Kesik, M.; Saczynska, V.; Szewczyk, B.; Pluciennicza k, A. *Immunology Letters* **2004**, *91*, 197–204.

[62] Hardy, J.; Selkoe, D. J. *Science* **2002**, *297*, 353–356.

[63] Bowden, G. A.; Paredes, A. M.; Georgiou, G. *Nature Biotechnology* **1991**, *9*, 5.

[64] Carrio, M. M.; Corchero, J. L.; Villaverde, A. *FEMS Microbiology Letters* **1998**, *169*, 9–15.

[65] Neubauer, P.; Fahnert, B.; Lilie, H.; Villaverde, A. *Microbiology Monographs, Springer, Berlin* **2006,**, *1*, 237–292.

[66] Ventura, S.; Villaverde, A. *Trends in Biotechnology* **2006**, *24*, 179–185.

[67] Garcia-Fruitos, E.; Aris, A.; Villaverde, A. *Appl Environ Microbiol* **2007**, *73*, 289–294.

[68] Gonzalez-Montalban, N.; Garcia-Fruitos, E.; Villaverde, A. *Nat Biotech* **2007**, *25*, 718–720.

[69] Carrio, M. M.; Villaverde, A. *FEBS Letters* **2003**, *537*, 215–221.

[70] Garcia-Fruitos, E.; Martinez-Alonso, M.; Gonzalez-Montalban, N.; Valli, M.; Mattanovich, D.; Villaverde, A. *Journal of Molecular Biology* **2007**, *374*, 195–205.

[71] Foguel, D.; Silva, J. L. *Biochemistry* **2004**, *43*, 11361–11370.

[72] Peternel, S.; Jevsevar, S.; Bele, M.; Gaberc-porekar, V.; Menart, V. *Biotechnology and Applied Biochemistry* **2008**, *49*, 239–246.

[73] Rodriguez, F.; Arsene-Ploetze, F.; Rist, W.; Ruediger, S.; Schneider-Mergener, J.; Mayer, M.; Bukau, B. *Molecular Cell* **2008**, *32*, 347–358.

[74] Mogk, A.; Deuerling, E.; Vorderwuelbecke, S.; Vierling, E.; Bukau, B. *Molecular Microbiology* **2003**, *50*, 585–595.

[75] Speed, M. A.; Wang, D. I.; King, J. *Nature Biotechnology* **1996**, *14*, 1283–1287.

[76] Carrio, M.; Gonzalez-Montalban, N.; Vera, A.; Villaverde, A.; Ventura, S. *Journal of Molecular Biology* **2005**, *347*, 1025–1037.

[77] Carrio, M.; Villaverde, A. *FEBS Letters* **2001**, *489*, 29–33.

[78] Yeung, T.; Georges, P.; Flanagan, L.; Marg, B.; Ortiz, M.; Funaki, M.; Zahir, N.; Ming, W.; PA, W. V. . J. *Cell Motility and Cytoskeleton* **2005**, *60*, 24–34.

[79] Chen, C.-C.; Hsieh, P. C.-H.; Wang, G.-M.; Chen, W.-C.; Yeh, M.-L. *Materials Letters* **2009**, *63*, 1872–1875.

[80] Hadjipanayi, E.; Mudera, V.; Brown, R. A. *Journal of Tissue Engineering and Regenerative Medicine* **2009**, *3*, 77–84.

[81] Cheung, Y. K.; ; Azeloglu, E. U.; Shiovitz, D. A.; Costa, K. D.; Seliktar, D.; Sia, S. K. *Angewandte Chemie International Edition* **2009**, *48*, 7188–7192.

[82] Teixeira, A. I.; Ilkhanizadeh, S.; Wigenius, J. A.; Duckworth, J. K.; Inganeas, O.; Hermanson, O. *Biomaterials* **2009**, *30*, 4567–4572.

[83] Engel, A.; Muller, D. J. *Nat Struct Mol Biol* **2000**, *7*, 715–718.

[84] Jaeger, M. S.; Uhlig, K.; Clausen-Schaumann, H.; Duschl, C. *Biomaterials* **2008**, *29*, 247–256.

[85] Koenders, M. M. J. F.; Yang, L.; Wismans, R. G.; van der Werf, K. O.; Reinhardt, D. P.; Daamen, W.; Bennink, M. L.; Dijkstra, P. J.; van Kuppevelt, T. H.; Feijen, J. *Biomaterials* **2009**, *30*, 2425–2432.

[86] Vinckier, A.; Semenza, G. *FEBS Letters* **1998**, *430*, 12–16.

[87] Heuberger, M.; Dietler, G.; Schlapbach, L. *Nanotechnology* **1995**, *6*, 12–23.

[88] del Mercato, L. L.; Maruccio, G.; Pompa, P. P.; Bochicchio, B.; Tamburro, A. M.; Cingolani, R.; Rinaldi, R. *Biomacromolecules* **2008**, *9*, 796–803.

[89] Radmacher, M.; Fritz, M.; Cleveland, J. P.; Walters, D. A.; Hansma, P. K. *Langmuir* **1994**, *10*, 3809–3814.

[90] Johnson, K. L.; Kendall, K.; Roberts, A. D. *Proccedings of the Royal Society of London A* **1971**, *324*, 301–313.

[91] Derjaguin, B. V.; Muller, V. M.; Toporov, Y. P. *Journal of Colloids and Interface Sciences* **1975**, *53*, 314–326.

[92] Pietrement, O.; Troyon, M. *Journal of Colloid and Interface Science* **2000**, *226*, 166–171.

[93] Hertz, H. *J reine angew Math 92* **1896**, *92*, 15.

[94] Parra, A.; Casero, E.; Lorenzo, E.; Pariente, F.; Luis, V. *Langmuir* **2007**, *23*, 2747–2754.

[95] Afrin, R.; Alam, M. T.; Ikai, A. *Protein Science* **2005**, *14*, 1447–1457.

[96] Webb, K.; Hlady, V.; Tresco, P. A. *Journal of Biomedical Materials Research* **1998**, *41*, 422–30.

[97] Andrade, J.; Hlady, V. In *Biopolymers/Non-Exclusion HPLC*; Berlin: Springer, 1986; pp 1–63–.

[98] Washburn, N.; Yamada, K.; Simon, C.; Kennedy, S.; Amis, E. *Biomaterials* **2004**, *25*, 1215–1224.

[99] Piszczek, G.; Rozycki, J.; Singh, S.; Ginsburg, A.; Maurizi, M. J. *Biological Chemistry* **2005**, *280*, 12221–12230.

[100] Suci, P. A.; Klem, M. T.; Arce, F. T.; Douglas, T.; Young, M. *Langmuir* **2006**, *22*, 8891–8896.

[101] Uchida, M.; Klem, M. T.; Allen, M.; Suci, P.; Flenniken, M.; Gillitzer, E.; Varpness, Z.; Liepold, L. O.; Young, M.; Douglas, T. *Advanced Materials* **2007**, *19*, 1025–1042.

[102] Yanker, D. M.; Maurer, J. A. *Molecular BioSystems* **2008**, *4*, 502–504.

[103] Ludden, M. J. W.; Mulder, A.; Tamp, R.; Reinhoudt, D. N.; Huskens, l. J. *Angewandte Chemie* **2007**, *46*, 4104–4107.

[104] Lipski, A. M.; Pino, C. J.; Haselton, F. R.; Chen, I.-W.; Shastri, V. P. *Biomaterials* **2008**, *29*, 3836–3846.

[105] El-Ghannam, P., A. R.and Ducheyne; Risbud, M.; Adams, C. S.; Shapiro, I. M.; Castner, D.; Golledge, S.; Composto, R. J. *Journal of Biomedical Materials Research A* **2004**, *68*, 615–627.

[106] Dulgar-Tulloch, A. J.; Bizios, R.; Siegel, R. W. *Journal of Biomedical Materials Research Part A* **2009**, *90*, 586–594.

[107] http://www.statsoft.com/textbook/elementary-concepts-in-statistics/.

[108] Hsu, S.-H.; Reinhoudt, D. N.; Huskens, J.; Velders, A. H. *Journal of Materials Chemistry* **2008**, *18*, 4959–4963.

[109] Bia, X.; Wong, W. L.; Jia, W.; Agarwal, A.; Balasubramanian, N.; Yang, K.-L. *Biosensors and Bioelectronics* **2008**, *23*, 1442–1448.

Part V

Experimental Part

Chapter 12

Experimental Part

12.1 Instrumentation and Sample Preparation

- **Atomic force microscopy (AFM).** Atomic force microscopy (AFM) images were taken with a commercial AFM (MFP-3D-SA, Asylum Research, Santa Barbara, USA). Samples were analyzed in dynamic mode working at 8 kHz of frequency and in a liquid environment (PBS buffer solution pH = 7.4) in order to mimic the cytoplasmic environment of the cell. Pyramidal NSC35/AlBS silicon tips (Mikromash, USA) having nominal spring constants of 0.28 N/m were used. Sample preparation was done by drop casting 100μL of an IBs suspension in the same PBS buffer (20 mg/mL) over freshly cleaved mica. Before measuring the mica was rinsed twice with the same PBS buffer to remove the excess of IBs.

- **Column chromatography.** Silica 60 A. C. C. 35-70 μm (flash silica) supplied by SDS was employed as stationary phase on the column chromatography separations.

- **Confocal microscopy.** Confocal microscopy images of the IBs were developed by Dr. Elena García Fruitos using a Leica TSC SP2 AOBS confocal fluorescence microscope (Leica Microsystems Heidelberg GmbH, Mannheim, Germany) after excitation at 488 nm, and images were recorded at emission wavelengths between 500 and 600 nm (63x, NA 1.4, oil) using a Plan-Apochromat objective (zoom 8; 1024x1024 pixels). Bacterial cells were fixed with formaldehyde (0.2%) in PBS solution and isolated IBs were also resuspended in PBS.

Confocal microscopy of the cell cultures were examined by Dr. Esther Vázquez using a spectral confocal Leica TCS SP5 AOBS (Leica Microsystems, Mannheim, Germany) using a Plan-Apochromat 63x, NA 1.4 lens. All images were obtained from living cells grown in glass bottom dishes (MatTek Corporation, Ashland, MA, USA). Finally, the argon laser 488nm line was used for imaging the IBs (emission at 500-537 nm). For the 3D Z-series of 22 optical sections were collected at 0.6 mm intervals. Z-stacks were acquired with LAS AF software (Leica Microsystems) and 3D models were generated using Imaris software (Bitplane, Zurich, Switzerland.

- **Contact angle.** All contact angle measurements were carried out at room temperature by the sessile drop method using an OCA 15+ (Dataphysics, Germany) contact angle goniometer. Four sets of static contact angles, at different positions on each sample, were measured and averaged. A 3 μl drop of MilliQ water was placed on a freshly prepared sample using a Hamilton micro-syringe. The measurements involve the fitting of the liquid-solid interfacial angle of a drop picture or movie (in the case of the advancing and receding angles) with the software SCA20 (Dataphysics, Germany).

- **Cyclic voltammetry.** The cyclic voltammograms of the freshly prepared gold samples were recorded using a VersaSTAT 3 potentiostat (Princetown Applied Research, USA). Gold slides were connected to the potenciostat via crocodile clamps and used as working electrode. A 1 mM aqueous solution of $Fe(CN)_6^{-3}$, in a 0.1 M aqueous solution of KCl was used as electrolyte for the measurements. A platinum wire was used as counter electrode, while a Ag/AgCl one was used as reference electrode. Clean gold and SAM modified gold electrodes were subjected to 5 potential cycles between 0.0 V and 0.6 V at a scan rate of 100 mV/s.

- **Dynamic light scattering.** Particle size studies of the receptor nanoparticles were performed using dynamic light scattering (DLS) Malvern Nanosizer S from Malvern (Worcestershire, UK). DLS measurements were performed at 25°C using 1 mL of a freshly prepared nanoparticle suspension into a disposable plastic cuvette.
  Determination of the size of IBs was carried out after dispersion of the freshly prepared aggregates in PBS buffer (pH = 7.4, IB final concentration was 20 mg/mL). To facilitate the dispersion in the liquid, 2 mL of the mixture were

sonicated for 1 min. DLS measurements were carried out at 37°C using 1 mL of freshly prepared IBs suspension into a disposable plastic cuvette. Each sample was analyzed by triplicate averaging thirty single measurements.
Z-Potential measurements of the receptor nanoparticles and the IBs were measured using a dynamic light scattering (DLS). Z-potential measurements were developed using a disposable plastic cuvette equipped with two electrodes using 1 mL of suspension.

- **Fourier Transform infrared attenuated total reflectance Spectroscopy (FT-IR-ATR)** The IR spectra were recorded under identical conditions by using a FT-IR Spectrum One (Perkin Elmer, USA) spectrometer with an Universal ATR Sampling Accessory. The abbreviations used for the description of the IR spectra are: weak intensity band (w), medium intensity band (m), strong intensity band(s).

- **Nuclear magnetic resonance (NMR)** The spectra were registered at the nuclear magnetic resonance service of the Universidad Autónonoma de Barcelona with a Bruker Avance 250 MHz and Avance 400 MHz equipment. The same solvent was used as internal reference for the spectra. The abbreviations employed on the NMR spectra are: s (singlet), d (doblet), t(triplet), q (quadruplet), m (multiplet). Deuterated $CDCl_3$ solvent was used for the preparation of the samples.

- **Force spectroscopy atomic force microscopy (FSAFM).** FSAFM measurements were done with a commercial AFM (MFP-3D-SA, Asylum Research, Santa Barbara, USA) equipped with a close loop tracking system and working in liquid environment. Pyramidal NSC35/AlBS silicon tips (Mikromash, USA) having nominal spring constants of 0.28 N/m were used. The spectroscopic calibration of the raw cantilever in liquid media (PBS buffer solution pH = 7.4) was developed by measuring force vs. distance curves, on freshly cleaved mica. The force curves, consisting of 2048 data points, were obtained imposing a maximum applied force of 50 nN at a frequency of 8 kHz. The mechanical properties of the substrate data were calculated from force (f) *vs.* distance (d) curves according to the procedures described in references[1] and[2]. Sample preparation was done by drop casting 100μL of an IB suspension of the same PBS buffer (20 mg/mL) over freshly cleaved mica. Before measuring, the mica was rinsed twice with the same PBS buffer

to remove the excess of IBs.

In order to achieve spatial resolution of the spectroscopic measurements, dynamic AFM images of the studied IBs were developed prior and after force vs. distance measurements. Differences observed between the images before and after the f *vs.* d curves allowed us to follow any movement or deformation produced on the sample during the experiment (see appendix III).

- **Fluorescence spectroscopy** spectra were carried out using a Perkin Elmer LS45 Fluorescence spectrometer. All solvents employed were degassed with a stream of N_2 prior to use.

- **Luminescence stereomicroscope.** Luminescence measurements of the Hg^{2+} treated cellulose sensing probes were performed using a commercial luminescence stereomicroscope (Leica MLZIII) with an incorporated CCD digital camera (Leica DC 250). Images were then software treated (Metamorph 7.5, Universal Imaging, 2007) acquiring thus the total luminescence intensity data from the images.

- **Matrix assisted laser desorption/ionization mass spectrometry with time of flight detection (MALDI-ToF).** Spectrograms were carried out by Amable Bernabé (NANOMOL-ICMAB-CISC) using a mass spectrometer Ultraflex (Bruker) operating at pulsed ion extraction in positive or negative mode at high power. The same equipment was used to develop the **surface assisted laser desorption/ionization mass spectrometry (SAMDI)** by attaching the modified gold surface to the MALDI holder with double size scotch film.

- **Mixer mill.** Receptor **2**:cellulose composite powder was milled using a mixer mill MM 400 (Retsch Inc., USA) for 5 minutes at 50% of the maximum power of the mill.

- **Melting point.** The melting points (Mp) of the synthesized compounds, expressed as a temperature range, were measured using a Melting point SMP10 BIBBY from Stuart Scientific (Stanfordshire, UK).

- **Optical microscopy.** Optical microscope and fluorescence images of the deposited IBs were performed using an OLYMPUS Bx51 microscope with an OLYMPUS DP20 camera with 3 s shutter time, and an OLYMPUS U-RFL-T mercury lamp accessory. In order to remove the background light a

GFP pass filter was used. ImageJ (GNU) software was utilized to perform the particle counting from the fluorescence images recorded.

- **Scanning electron microscopy (SEM) and energy dispersive X-ray analysis (EDX).** Imaging of the polymeric membranes was performed using a scanning electron microscope Hitachi S-570.
  Cross section imaging and qualitative Hg^{2+} detection of the the functionalize cellulose membranes were carried out on a SEM JEOL JSM-6300 (JEOL LDT, Tokyo, Japan) with a dispersive energy spectrometer EDX-LINK ISIS 200 (Oxford Instruments, Bucks, England).
  SEM images of the receptor **2**:cellulose composite were performed on a SEM FEI QUANTA 200 FEG-ESEM equipped with a dispersive energy spectrometer EDX-LINK ISIS 200 (Oxford Instruments, Bucks, England).
  All the samples were metalized with either carbon or gold by means of a K550 Sputter Coater K250 Carbon Coating Attachment (Emitech, Ashford, U.K.) prior to the development of the experiment, in order to avoid charging of the sample.

- **Secondary ions mass spectroscopy with time of flight detection (ToF-SIMS).** The spectra were recorded by Dr. Raúl Pérez from the Parc Científic de Barcelona (UB) using a ToF-SIMS IV (ION-TOF) operating at $5{\cdot}10^{-9}$ mbar using Bi_3^{2+} as primary ions of 25 keV. It works applying clusters pulses of primary ions of 15 ns. With this conditions the sample (125 x 125 μm^2) is scanned for 30 s. The equipment bares an ionic charge neutralizer that allows to avoid the materials' overload. The desorbed secondary ions are accelerated to 2 keV, the mass is analyzed in the flight tube and after the detection they are further accelerated to 10 keV. The scanned area allows a mass resolution around 10000 *m/z*. The abundance of the ions was normalized to the total ions in order to compensate the differences in the number of Bi soots that every sample receives apart to other instrumental factors.

- **Surface plasmon resonance.** Time-resolved SPR measurements were carried out using a Biosuplar 6 SPR (Analytical Microsystems, Regensburg, Germany). A freshly prepared sensor chip was placed into the biosensor system by exposing the gold film side to the flow cells. The prism was attached

via a matching oil of identical refractive index (n=1.52) (see apendix II for more information).

- **Thin layer chromatography (TLC)** The control of the chemical reactions was done using aluminium sheets covered with silica gel 60 F_{254} by Merck. The sheets were developed under a UV lamp and/or using a $KMnO_4$ solution.

- **UV-Vis spectroscopy (UV-Vis).** Spectra of the compound **1** Hg^{2+}sensing probes were developed on a Shimadzu UV-2101 PC equipped with a reflectance absorption accessory (integrating sphere), while spectra of the receptor 2-cellulose composite were carried out using freshly prepared KBr-composite pellets and were acquired on a Varian Cary 300 equipped with a reflectance absorption accessory (integrating sphere). KBr was thoroughly dried prior to use.

- **X-ray photoelectron spectroscopy (XPS)** The XPS measurements were performed using an PHI 5500 Multitechnique System (Physical Electronics) photoelectron spectrometer with the monochromatic $Al_{K\alpha}$ X-ray source ($h \cdot \nu$ = 1486.6 eV) situated perpendicularly to the analyzer and calibrated to the Ag 3d5/2 line. The energy resolution (*full with at half maximum*, FWHM) measured was set to 0.8 eV. The base pressure in the spectrometer was between $2 \cdot 10^{-8}$ and $5 \cdot 10^{-9}$ Torr. The studied area has 0.8 mm^2 of diameter and a pass energy of 187.5 eV with an interval of 0.8 eV was used for the general spectra, while a pass energy of 23.5 eV. An interval of 0.1 eV was employed for the spectra of the different elements. Spectral analysis were carried out using the Multipack software (V6.0A 1998) from Physical Electronics, Inc. Since in practice XPS may not distinguish between the various types of atoms of the same element present in a molecule, there is a need of a fitting procedure consisting of reconstructing the XPS spectrum with a minimum number of peaks consistent with the raw data (the experimental resolution and the molecular structure). In this fitting, atoms of the same element under very similar chemical environments, i.e. very close in binding energy, are considered equivalent and represented by one peak. All the measurements were accomplished on freshly prepared samples in order to guarantee the reproducibility of the results. See Appendix I for a brief description of the XPS technique.

12.2 X-ray Crystalline Structure of Compound 2

The resolution of the crystalline structure of **2** was carried out by Dr. Klaus Wurst from the University of Insbruck (Austria).

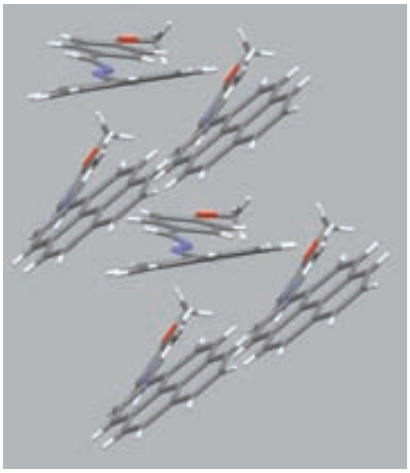

Figure 12.1: Representation of the crystallographic structure of the compound **2**

Receptor **2** crystals were obtained by slow evaporation at 21 °C of a saturated solution of **2** in ethanol. The crystallographic measurements were developed at 233(2) K. A diffractometer Nonius Kappa charge-coupled device (CCD) with a monochromatic $Mo_{k\alpha}$ ($\lambda = 0.71073$ Å) was employed. Crystallographic data from crystals of compound **2** are shown in Table 12.1 and Figure 12.1.
If we first focus our attention to the molecule Hg^{2+} receptor moiety (diaza bridge), it is possible to observe how the angle values between the atoms forming part of the diaza bridge (N(1)-C(1)-C(2) 120.1(4)°; N(2)-C(18)-C(19) 123.4(4)°; C(1)-N(1)-N(2) 112.7(4)°; C(18)-N(2)-N(1) 110.4(4)°) are close to 120°, indicating their sp2 character (angles observed for the N atoms are a bit smaller due to the presence of free pair of electrons). Therefore, it is possible to conclude that as single crystal receptor **2** molecules do not present a large electronic delocalization, as it was expected. Another important data for defining the geometry of the crystallogafic structure of receptor **2** is the molecule planarity. In contrast to what the chemical structure of **2** let us think, in Figure 12.1 it is clearly shown how the three constituents of the molecule (benzene, pyrene and the diaza bridge) are not

Table 12.1: Crystallographic data of the compound **2**

Compound	**2**
Empirical formula	$C_{25}H_{18}N_2O$
Molecular weight	362.41
Crystalline system	Monoclinic
Spatial group	$P2_{1/c}$
Crystal colour	Yellow
a (Å)	30.058(2)
b (Å)	7.4134(7)
c (Å)	8.2753(6)
α (°)	90
β (°)	91.191(5)
γ (°)	90
V$\AA^3$	1843.6(3)
ρ_{calcd} (g/cm^3)	
F(000)	760
Z	4
R (F_0)	0.0668
Rw ($F_0{}^2$)	0.1637
F^2	1.061

placed in the same plane but slightly twisted, being the dihedral angle between those of 18.86°. This result is in agreement with the sp2 character of the atoms present on the diaza bridge.

In which respects to the intermolecular interactions, it is possible to observe that both pyrene and benzene moieties presents short intermolecular interactions. In the case of pyrene four contacts are detected, corresponding to $\pi - \pi$ interactions between itself and another pyrene unit of the closest layer (3.326 Å). Furthermore, the interacting pyrenes are not in the same plane but forming an angle of 33.28°. On the other hand, the benzene moiety also presents only two short intermolecular interactions, one of them involving the methyl group present on the methoxyle that interacts with the π electrons of the benzene unit present in the closer layer (interaction distance 2.537 Å), while the oxygen of the same methoxyle group interacts with the closer -H of the benzene present in the closer layer (interaction distance 2.572 Å).

The study of the interaction of the molecules in the same layer revels the presence of dimmers with confronted benzene units and stabilized by the interaction of the oxygen of the methoxyle moiety with one of the -H of the methyl group of the closest molecule (interaction distance 2.336 Å). Nevertheless, no lateral interaction between the pyrene units was detected.

12.3 Theoretical Calculations of the Structure of the Hg^{2+}:Ligand Complex

For insight into a plausible structural characterization of the complex, DFT quantum chemical calculations were performed (Arturo Espinosa University of Murcia) using the Truhlar hybrid metafunctional mPW1B95[3] that has been recommended for general purpose applications. It was developed in order to produce a better performance where weak interactions are involved, such as those between ligands and heavy metals.[4]

The reliably accurate description of weak interactions like hydrogen bonds and other found in supramolecular complexes generally requires a treatment of electron correlation. Density functional theory[5] (DFT) has proved to be quite useful in this regard offering an electron correlation correction frequently comparable to the second-order Mller-Plesset theory (MP2) or in certain cases, and for certain purposes, even superior to MP2, but at considerably lower computational cost. Due to the size of the systems investigated in the present study the cost advantage that offers the DFT $mPW1B95$ method in comparison with MP2 was significant. Calculated geometries at the DFT level were fully optimized in the gas-phase with tight convergence criteria using the Gaussian 03 package.[6] The $6-31G^{**}$ basis set was employed in the optimizations for all atoms except mercury, for which the Stuttgart relativistic small-core basis set (StRSC) with effective core potential (ecp)[7] was used. From these gas-phase optimized geometries all reported data were obtained by means of single-point (SP) calculations at the $mPW1B95/6-31G^{**}/StRSC-ecp$ level.

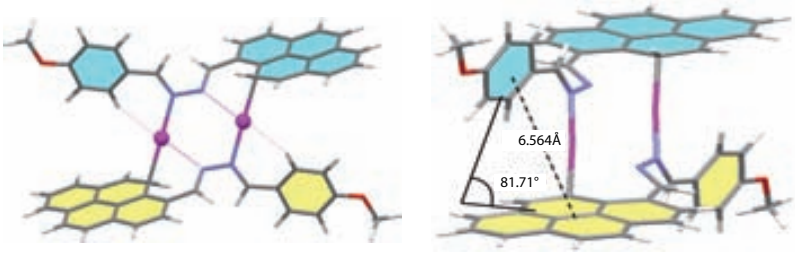

Figure 12.2: Calculated (mPW1B95/6-31G**/StRSC-ecp) structures for the 2:2 **2**Hg^{2+} :**2** complex

DFT calculations performed for both stoichiometries. In the case of the 2:2 complex such calculation depicted the existence of a single energy minimum corresponding to a C_i-symmetric 2:2 Hg^{2+} :**2** complex (Figure 12.2). This structure presents two wquivalent Hg atoms that are essentially linearly di-coordinated (N-Hg bonds d_{N-Hg} = 2.182 Å, N-Hg bonds d_{C10-Hg} = 2.263 Å, N-Hg-C10 angle 176.5°) by the action of the pyrene C-10 atom of one ligand and a N atom belonging to the other ligand bridge. As a consequence of the bonding of the pyrene to the metal, the C-10 atom is pyramidalized as evidenced by the high value (34.0°) of the dihedral angle formed by the C10-H bond with the pyrene mean plane. Electrostatic interactions between the two positively charged mercury atoms seem not to be important since the intermetallic distance between them is large enough ($d_{Hg\cdots Hg}$ = 4.166 Å) to significantly contribute to the formation of the complex. The pyrenyl and phenyl mean planes lie almost orthogonal (81.7°) to each other and the distance between their centroids the geometric centers of each of the aromatic moieties is R_{cent} = 6.564 Å.

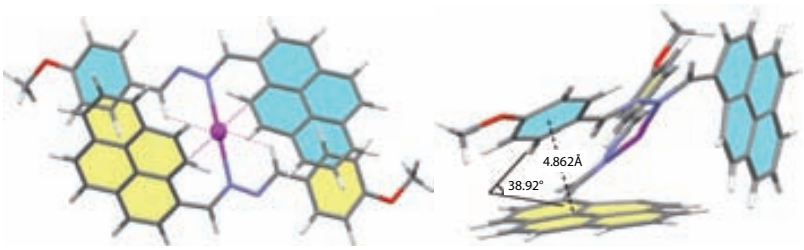

Figure 12.3: Calculated (mPW1B95/6-31G**/StRSC-ecp) structures for the 2:1 Hg^{2+}:**2** complex.

For the 2:1 complex DFT calculations show in the potential energy surface two minima close in energy (Δ E = 5.34 kcal· mol^{-1}). The absolute minimum has a C_2-symmetric structure with both ligand molecule showing an extended conformation ($dihedral_{CH=N-N=CH}$ = 168.6°) with the Hg^{2+} ion linearly bonded to two N atoms (one from each ligand molecule, N-Hg bonds d_{N-Hg} = 2.278 Å, N-Hg-N' angle 166.32°, Figure 12.3) almost aligned with the C_2 axis. Furthermore, both a smaller torsion angle between the aromatic pyrene and phenyl rings of θ = 38.92° and a closer centroids intermolecular distance R_{cen}=4.862 Åare found.

Complex $[L_2Hg_2]^{4+} E = -2600.53203042$ au

Table 12.2: Cartesian coordinates (in Å) for the modeled complex $[L_2Hg_2]^{4+}$

Atom	X	Y	Z	Atom	X	Y	Z
C	0.0000	0.0000	0.0000	C	5.9236	-0.9053	-1.7767
N	1.3204	0.0000	0.0000	N	4.6031	-0.9053	-1.7767
N	1.9277	1.2668	0.0000	N	3.9958	-2.1722	-1.7767
C	1.5038	2.1731	0.8947	C	4.4197	-3.0784	-2.6715
H	-0.5138	0.9641	-0.1438	H	6.4374	-1.8694	-1.6328
H	0.8649	1.7553	1.6857	H	5.0586	-2.6607	-3.4624
C	-0.8438	-1.1687	0.0915	C	6.7674	0.2634	-1.8682
C	-0.4414	-2.4324	0.6179	C	6.3650	1.5270	-2.3947
C	0.8405	-2.6345	1.3169	C	5.0830	1.7291	-3.0937
C	1.1321	-3.9053	1.9158	C	4.7914	3.0000	-3.6925
C	0.2679	-5.0007	1.7907	C	5.6556	4.0954	-3.5674
C	0.5719	-6.2579	2.3955	C	5.3516	5.3525	-4.1722
C	-0.3405	-7.3031	2.3304	C	6.2641	6.3978	-4.1071
C	-1.5704	-7.1196	1.6710	C	7.4940	6.2142	-3.4478
C	-1.9257	-5.8882	1.0694	C	7.8493	4.9829	-2.8461
C	-3.2028	-5.7011	0.4401	C	9.1264	4.7957	-2.2168
C	-3.5540	-4.4823	-0.0864	C	9.4776	3.5770	-1.6903
C	-2.6571	-3.3705	-0.0298	C	8.5807	2.4652	-1.7469
C	-3.0380	-2.0906	-0.4986	C	8.9616	1.1852	-1.2780
C	-2.1643	-1.0199	-0.4209	C	8.0879	0.1146	-1.3558
C	-0.9982	-4.8044	1.1179	C	6.9218	3.8990	-2.8947
C	-1.3480	-3.5374	0.5540	C	7.2716	2.6320	-2.3307
H	1.2366	-1.7632	1.8620	H	4.6869	0.8578	-3.6387
H	2.0275	-3.9976	2.5390	H	3.8961	3.0923	-4.3157
H	1.5210	-6.3810	2.9234	H	4.4025	5.4756	-4.7001
H	-0.1160	-8.2621	2.8004	H	6.0396	7.3568	-4.5771
H	-2.2854	-7.9461	1.6336	H	8.2090	7.0407	-3.4103
H	-3.9013	-6.5401	0.4064	H	9.8249	5.6348	-2.1831
H	-4.5364	-4.3402	-0.5416	H	10.4600	3.4348	-1.2350
H	-4.0386	-1.9500	-0.9125	H	9.9622	1.0447	-0.8642
H	-2.4830	-0.0391	-0.7824	H	8.4067	-0.8661	-0.9943
C	1.8155	3.5523	0.9853	C	4.1080	-4.4577	-2.7620
C	2.3622	4.3469	-0.0710	C	3.5613	-5.2522	-1.7056
C	2.6313	5.6844	0.1166	C	3.2923	-6.5897	-1.8933
C	2.3598	6.3062	1.3766	C	3.5637	-7.2115	-3.1534
C	1.7890	5.5425	2.4303	C	4.1345	-6.4479	-4.2070
C	1.5179	4.2027	2.2241	C	4.4056	-5.1081	-4.0009
H	2.4858	3.9264	-1.0750	H	3.4377	-4.8317	-0.7016
H	3.0064	6.3173	-0.6891	H	2.9172	-7.2227	-1.0875
H	1.5538	6.0056	3.3885	H	4.3697	-6.9110	-5.1652
H	1.0756	3.6206	3.0371	H	4.8479	-4.5260	-4.8139
O	2.6498	7.5971	1.4388	O	3.2738	-8.5024	-3.2156
C	2.3670	8.3585	2.6494	C	3.5565	-9.2638	-4.4262
H	2.6904	9.3786	2.4231	H	3.2331	-10.2840	-4.1999
H	2.9438	7.9543	3.4937	H	2.9797	-8.8597	-5.2704
H	1.2885	8.3405	2.8615	H	4.6350	-9.2459	-4.6383
Hg	2.4016	-2.3709	-0.2998	Hg	3.5219	1.4655	-1.4768

Complex $[L_2Hg]^{4+} E = -2448.33791554$ au

Table 12.3: Cartesian coordinates (in Å) for the modeled complex $[L_2Hg]^{2+}$

Atom	X	Y	Z	Atom	X	Y	Z
Hg	0.0000	0.0000	0.0000	H	0.2120	9.3088	-0.9915
C	3.1699	0.0000	0.0000	C	-3.1318	0.0635	-0.4860
N	2.1255	0.8184	0.0000	N	-2.0835	-0.7484	-0.5351
N	2.3946	2.1346	-0.1715	N	-2.2967	-1.9714	-1.0765
C	1.3924	2.9419	-0.4042	C	-1.2547	-2.7123	-1.3514
H	4.1314	0.4806	-0.2167	H	-4.0388	-0.3263	-0.9632
H	0.3587	2.5258	-0.4492	C	-3.1493	1.4104	0.0196
C	3.1367	-1.4314	0.1410	C	-2.2859	1.9097	1.0472
C	2.1361	-2.1594	0.8619	C	-1.5481	1.0472	1.9399
C	1.2530	-1.5391	1.8214	C	-0.6727	1.5668	2.8797
C	0.2545	-2.2640	2.4514	C	-0.4706	2.9750	3.0108
C	0.0630	-3.6546	2.1856	C	0.4391	3.5230	3.9434
C	-0.9678	-4.4044	2.7962	C	0.5425	4.9060	4.1040
C	-1.0669	-5.7801	2.5801	C	-0.2692	5.7674	3.3560
C	-0.1329	-6.4379	1.7704	C	-1.1993	5.2663	2.4211
C	0.9193	-5.7332	1.1487	C	-2.0691	6.1283	1.6727
C	1.9106	-6.3925	0.3474	C	-2.9826	5.6213	0.7814
C	2.9397	-5.6930	-0.2336	C	-3.0817	4.2124	0.5471
C	3.0452	-4.2732	-0.0819	C	-4.0233	3.6653	-0.3562
C	4.1030	-3.5324	-0.6600	C	-4.0573	2.3024	-0.6105
C	4.1483	-2.1507	-0.5492	C	-1.2920	3.8510	2.22505
C	1.0125	-4.3169	1.3376	C	-2.2118	3.3219	1.2675
C	2.0574	-3.5792	0.6998	H	-1.8148	-0.0144	1.9779
H	1.4894	-0.5280	2.1700	H	-0.1627	0.8977	3.5799
H	-0.3701	-1.7861	3.2127	H	1.0503	2.8512	4.5513
H	-1.6784	-3.8982	3.4545	H	1.2464	5.3180	4.8291
H	-1.8652	-6.3497	3.0590	H	-0.1952	6.8479	3.5014
H	-0.2066	-7.5179	1.6217	H	-2.0054	7.2057	1.8435
H	1.8431	-7.4763	0.2252	H	-3.6569	6.2880	0.2391
H	3.7024	-6.2123	-0.8183	H	-4.7186	4.3325	-0.8701
H	4.8821	-4.0598	-1.2145	H	-4.7601	1.9060	-1.3474
H	4.9477	-1.5933	-1.0435	C	-1.3501	-4.0072	-1.9586
C	1.5538	4.3468	-0.6381	C	-2.6089	-4.6050	-2.2569
C	2.8312	4.9757	-0.57718	C	-2.6695	-5.8417	-2.8649
C	2.9595	6.3252	-0.8321	C	-1.4744	-6.5289	-3.2092
C	1.8178	7.1015	-1.1682	C	-0.2161	-5.9513	-2.9166
C	0.5414	6.4936	-1.2296	C	-0.1670	-4.7078	-2.2979
C	0.4230	5.1345	-0.9644	H	-3.5244	-4.0697	-1.9998
H	3.7070	4.3742	-0.3282	H	-3.6223	-6.3163	-3.1040
H	3.9280	6.8260	-0.7928	H	0.7081	-6.4670	-3.1760
H	-0.3423	7.0768	-1.4870	H	0.8047	-4.2555	-2.0829
H	-0.5610	4.6619	-1.0238	O	-1.6515	-7.7180	-3.8085
O	2.0608	8.4004	-1.4093	C	-0.4962	-8.4709	-4.2245
C	0.9682	9.2577	-1.7910	H	-0.8925	-9.3789	-4.6906
H	1.4129	10.2465	-1.9430	H	0.0971	-7.9033	-4.9583
H	0.5058	8.9085	-2.7275	H	0.1291	-8.7399	-3.3585
H	-0.2348	-2.3193	-1.1294				

12.4 Synthesis

12.4.1 Reactives and solvents

All commercial chemicals were obtained from usual suppliers (SDS, Panreac, Fluka, Aldrich Chemical and Merck) and used without further purification. All organic anhydrous solvents used for the synthesis of the products were obtained following the usual procedures.[8] All the HPLC solvents and those used for the surface chemistry were of super purity degree (ROMIL-SpS) purchased to Teknokroma (Barcelona, Spain). Column chromatography purifications were performed on silica gel (35-70 μm).

12.4.2 Preparation of 1,4-diferrocenyl-2,3-diaza-1,3-butadiene (1)

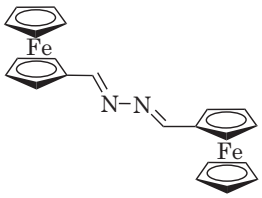

This product was synthesized by Dr. Antonio Caballero at the Universidad de Murcia. To a solution of formylferrocene (0.250 g, 1.17 mmol) in ethanol (50 ml) hydrazine hydrate (28.3 ml, 0. 585 mmol) was dropped and the resulting solution was stirred at room temperature for 10 h. After cooling, the precipitated solid was filtered, air-dried and recrystallized from ethanol to give **1** as orange crystals.

- *Yield* 70%. *Mp*: >260°C.
  IR (Nujol), $\nu(cm^{-1})$: 1682, 1663, 1629, 1464, 1408, 1300, 1245, 1103, 1041, 1021, 1000, 827, 812.
  ^{1}*H-NMR ($CDCl_3$, ppm)*: δ 4.24 (10H, s), 4.45 (4H, st), 4.70 (4H, st), 8.48 (2H, s).
  ^{13}*C-NMR ($CDCl_3$, ppm)*: δ 68.6, 69.3, 70.9, 78.0, 161.2.
  EIMS, m/z (%): 424 (M^+), 211, 184, 121.
  Anal. Calc. for $C_{22}H_{20}Fe_2N_2$: C = 62.31; H = 4.75; N = 6.61.
  Found: C = 62.55; H = 4.51; N = 6.88.

12.4.3 General Procedure for the preparation of 1,4 unsymmetrically disubstituted 2,3-diaza-1,3-butadienes (2, 3 and 5)

.

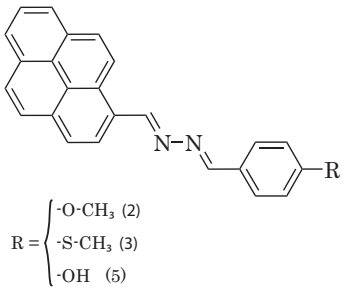

The synthesis and characterization of this compounds was carried out by Dr. Rosario Martínez at the Universidad de Murcia. *n*-Butyllithium (1.6 M in hexane ; 0.70 ml) was dropped to a solution of N-(diethoxyphosphinyl)hydrazone of 1-pyrenecarboxaldehyde[9] (0.410 g, 1.08 mmol) in dry THF (20 ml), at -78°C and in atmosphere of nitrogen. Then, a solution of the appropriate aldehyde (1.08 mmol) in dry THF (10 ml) was added dropwise and the mixture was stirred for 30 min. The reaction mixture was allowed to reach room temperature and stirred overnight. The solvent was evaporated under reduced pressure and the resulting solid was slurried with diethyl ether (25 ml) to give the corresponding disubstituted 2,3-diaza-1,3-butadiene which were recrystallized from dichloromethane/diethyl ether (1/10).

- **1-(*p*-Methoxyphenyl)-4-(1-pyrenyl)-2,3-diaza-1,3-butadiene (2)**.
  Yield 70%. *Mp:* 155-157°C.
  IR (Nujol), $\nu(cm^{-1})$: 1619, 1604, 1509, 1301, 1251, 1184, 1164, 1027, 854, 835, 715.
  ^{1}*H-NMR ($CDCl_3$, ppm)*: δ 3.89 (s, 3 H), 7.02 (d, J = 8.7 Hz, 2H), 7.89 (d, J = 8.7 Hz, 2H), 8.05 (t, J = 7.6 Hz, 1H), 8.10 (d, J = 8.9 Hz, 1H), 8.15 (d, J = 8.9 Hz, 1H), 8.22-8.26 (m, 4 H), 8.72 (d, J = 8.1 Hz, 1H), 8.82 (s, 1 H), 8.91 (d, J = 9.3 Hz, 1H), 9.73 (s, 1 H).
  ^{13}*C-NMR ($CDCl_3$, ppm)*: δ 55.43, 114.28, 122.77, 124.60, 124.95, 125.03, 125.85, 126.05, 126.09, 126.22, 126.81, 126.94, 127.45, 128.83, 1283.85, 130.10,

130.35, 130.61, 131.25, 133.24, 160.22, 162.02, 162.18.
EIMS, m/z(%): 361 (M^+), 227, 201, 133.
Anal. Calc. for $C_{25}H_{18}N_2O$: C = 85.85; H = 5.01; N = 7.73.
Found: C = 82.70; H = 5.20; N = 7.50.

- **1-(*p*-Methylthiophenyl)-4-(1-pyrenyl)-2,3-diaza-1,3-butadiene (3)**.
  Yield 85%. *Mp:* 224-226°C.
  IR (Nujol), $\nu(cm^{-1})$: 1614, 1594, 1245, 1068, 962, 848, 804, 719.
  ^{1}*H-NMR (*$CDCl_3$*, ppm)*: δ 2.52 (s, 3 H), 7.30 (d, J = 8.3 Hz, 2H), 7.81(d, J = 8.3 Hz, 2H), 8.00 (t, J = 7.6 Hz, 1H), 8.06 (d, J = 8.8 Hz, 1H), 8.12 (d, J = 8.8 Hz, 1H), 8.20-8.22 (m, 4 H), 8.69 (d, J = 8.1 Hz,1H), 8.78 (s, 1 H), 8.87 (d, J = 9.29 Hz, 1H), 9.69 (s, 1 H).
  ^{13}*C-NMR (*$CDCl_3$*, ppm)*: δ 15.4, 122.7, 124.6, 124.9, 125.0, 125.8, 125.9, 126.1, 126.2, 126.2, 126.6, 127.4, 128.9, 130.5, 130.6, 130.7, 131.2, 133.4, 143.1, 160.7, 161.9.
  EIMS, m/z(%): 378 (M^+), 227, 201, 150, 137.
  Anal. Calc. for $C_{25}H_{18}N_2S$: C = 79.33; H = 4.79; N = 7.40.
  Found: C = 79.55; H = 4.56; N = 7.55.

- **1-(*p*-Hydroxyphenyl)-4-(1-pyrenyl)-2,3-diaza-1,3-butadiene (5)**.
  Yield 55%. *Mp*: 238-240°C.
  IR (Nujol), $\nu(cm^{-1})$: 3399, 1605, 1270, 1164, 1107, 960, 878, 845, 825, 719.
  ^{1}*H-NMR (*$CDCl_3$*, ppm)*: δ 6.89 (d, J = 8.36 Hz, 2H), 7.80 (d, J = 8.36 Hz, 2 H), 8.13 (t, J = 7.68 Hz, 1H), 8.24 (d, J = 8.86 Hz, 1H), 8.30 (d, J = 8.82 Hz, 1H), 8.34-8.40 (m, 4 H), 8.69 (d, J = 8.09 Hz, 1 H), 8.79 (s, 1 H), 9.12 (d, J = 9.31 Hz, 1 H), 9.66 (s, 1 H). ^{13}*C-NMR (*$CDCl_3$*, ppm)*: δ 116.2, 137.7, 124.1, 124.6, 124.8, 125.6,126.4, 126.7, 126.9, 127.1, 127.2, 127.8, 129.3, 129.4, 130.0, 130.6, 131.0, 131.2, 133.0, 159.7, 162.0, 162.4.
  EIMS, m/z (%): 348 (M^+), 320, 228, 201, 121.
  Anal. Calc. for $C_{24}H_{16}N_2O$: C, 82.74; H, 4.63; N, 8.04.
  Found: C, 82.53; H, 4.90; N, 7.88.

12.4.4 Synthesis of 1-(4-alkoxyphenyl)-4-(1-pyrenyl)-2,3-diaza-1,3-butadiene derivative (4)

.

Diisopropyl azodicarboxylate (28 mg, 0.14 mmol, 27.6 μg/l) was added dropwise

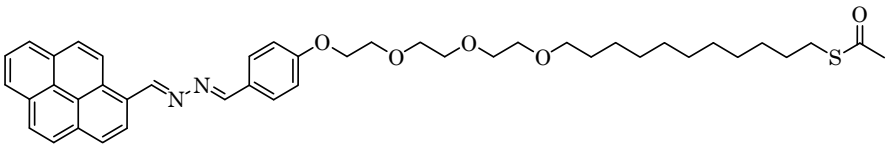

to a solution of triphenylphosphine (44.5 mg, 0.17 mmol), 1-(thioacetyl-undec-11-yl)tri(ethylene glycol)[10,11] (100 mg, 0.14 mmol) and 1-(p-hydroxyphenyl)-4-(1-pyrenyl)-2,3-diaza-1,3-butadiene (50.6 mg, 0.14 mmol) in freshly distilled ethyl ether (20 ml). The mixture was stirred overnight at room temperature and the solvent was removed under reduced pressure. The yellow solid obtained was purified by column chromatography on silica gel, using ethyl ether as the eluent. R_f=0.8 (SiO_2; ethyl ether).

- *Yield:* 30%. *Mp*: 81-83°C.
  IR (ATR) $\nu(cm^{-1})$: 3045, 2921, 2852, 1687, 1620, 1605, 1512, 1352, 1109.
  ^{1}*H-NMR (250 MHz, $CDCl_3$, ppm)*: δ 9.78-9.64 (m, 1H), 8.4 (d, J = 8.90 Hz, 1H), 8.82 (s, 1H), 8.73 (d, J = 8.72 Hz, 1H), 8.30-8.00 (m, 7H), 7.95-7.78 (m, 2H), 7.12-6.93 (m, 2H), 4.30-4.12 (m, 8H), 3.96-3.85 (m, 2H), 3,81-3.54 (m, 8H), 3.45 (t, J = 6.31, 6.31 Hz, 2H), 2.84 (t, J = 6.87, 6.87 Hz, 2H), 2.31 (s, 3H), 1.25 (s, 18H).
  ^{13}*C-NMR (63 MHz, $CDCl_3$, ppm)*: δ 195.8, 161.7, 161.2, 159.9, 133.0, 131.0, 130.4, 130.1, 130.0,128.6, 128.6, 127.2, 126.8, 126.6, 126.0, 125.9, 125.8, 125.6, 124.8, 124.7, 124.6, 122.5, 114.7, 71.3, 70.7, 70.4, 70.4, 69.8, 69.4, 67.3, 30.4, 29.4, 29.4, 29.3, 29.2, 29.1, 29.2, 28.9, 28.89, 28.59, 25.89.
  MS (MALDI-TOF) 709 (M^+).
  Anal. Calcd. for $C_{43}H_{52}N_2O_5S$: C = 72.85; H = 7.39; N = 3.95; S = 4.52.
  Found: C = 72.93; H = 7.51; N = 3.93; S = 4.43.

12.5 Preparation of the Hg^{2+} Sensing Probes

12.5.1 "Developing technique"

The probes were fabricated with ALBET, Θ = 142 mm, pore size 0.20 μm regenerated cellulose mixed ester paper. For the preparation of the mercury ion indicator paper, regenerated cellulose mixed ester paper with 0.20 μm pore size have been

chosen as our fiber substrate due to its high surface porosity which gives a high surface coverage area to interact with the sensing molecule, for the preparation of a mercury ion indicator paper. Preparation of the probes was carried out in several steps. Firstly the 142 mm in diameter (Θ) disks of paper were introduced for 20 s into acetonitrile solutions of different concentrations of $Hg(ClO_4)_2$ (from 10^{-6}M to 10^{-2}M). Then the paper was left to air dry for 40 s and once dried, carefully introduced for 2 s and immediately removed from a toluene solution of **1** (10^{-3} M) and then homogeneously dried. Indeed, it is also possible to use CH_3CN/H_2O (7:3, v/v) of $Hg(ClO_4)_2$.

12.5.2 Nanocomposite probes

Nanoparticles of the mercury receptor molecules were prepared by the reprecipitation method.[12] 100 ml of a 10^{-3} M THF or NMP solution of the mercury indicator molecules were slowly dropped into 10 ml of vigorously stirred ultra-pure water. The antisolvent water effect, together with the miscibility of the THF and NMP in water and the strong stirring, make possible the generation of the nanoparticle suspension. The coated membranes were prepared by vacuum filtering, at a flux of 35 ml/min, 30 ml of nanoparticle suspension of mercury receptor molecule through a mixed cellulose ester (Advantec, Θ = 47 mm, 0.1 μm pore) yielding a final load of $2.4{\cdot}10^{-8}$ mol/cm^2 of molecular probe on the surfaces that were left to air dry.

12.5.3 SPR gold sensor chips

Gold slides cleaning

All the glass material employed for the preparation of the self assembled monolayers was firstly extensively cleaned using a Hellmanex II solution, 2% v/v, in distilled water. Then the material was rinsed several times with MilliQ water and dried in the oven at 150°C. The SPR gold substrates used were purchased from SSens (Hengelo, Netherland), while normal gold slides were bought to Arrandee (Werther, Germany). This substrates are composed by a borosilicate glass base (approx. 0.7 mm width) over which a adhesive chrome layer from 1 to 4 nm has been deposited. This layer warrants the correct adhesion of the gold layer deposited afterwards. The gold layer has a width of 50 nm in the case of the SPR slides and between 200 and 300 nm for the Arrandee ones.
The cleaning procedure of these substrates is the following: firstly each substrate is

plentifully washed with organic solvents (CH_2Cl_2, acetone, heptane, ethanol). After rinsing with clean HPLC ethanol and drying with a stream of N_2, each substrate is immersed for 20 s on a piranha solution (H_2SO_4/H_2O_2 7:3 v/v, CAUTION! HANDLE WITH EXTREME CARE!, PIRANHA SOLUTION IS DANGEROUS AND SOME CASES OF EXPONTANEOUS EXPLOSION HAVE BEEN REPORTED). Then the substrates are rinsed with MilliQ water and ethanol and dried under a stream of N_2.

Preparation of the receptor 3 and 4 SAMs (S1 and S2)

SAMs (**S1** and **S2**) were prepared following the procedure depicted on Figure 12.4. On a first step, the freshly cleaned gold substrates were immersed into a 10^{-3} M ethanolic solution of receptor (**3** or **4**) at 35° C. This treatment was prolonged for at least 48 hour in order to obtain a good surface coverage. Then, substrates were removed from the solution and rinsed with copious amounts of clean ethanol, to remove the non bonded remaining material, and dried under N_2.

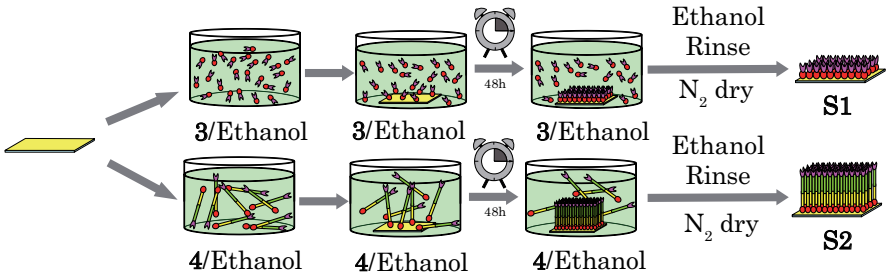

Figure 12.4: Scheme of the receptor **3** and **4** SAM formation.

12.6 IBs Preparation and Studies

12.6.1 IBs production

IBs production was performed by the group of Prof. Villaverde at the IBB (Universidad Autónoma de Barcelona). The *Escherichia Coli* strains used in this study were streptomycin resistant MC4100 strain (araD139 Δ(argF-lac) U169 rpsL150 relA1 flbB5301 deoC1 ptsF25 rbsR),[13] as a wild-type, and its derivative streptomycin resistant strain JGT4 strain (clpA::kan) and tetracycline and streptomycin

resistant JGT20 strain (dnak756 thr::Tn10), lacking ClpA ATPase and DnaK chaperone, respectively.[14] All strains were transformed with an IPTG-inducible pTVP1GFP plasmid, encoding a green fluorescent protein (GFP) fused to the VP1 capsid protein of foot-and-mouth disease virus.[15] Bacterial cultures were performed with shake flask cultures growing at 37°C and 250 rpm in lysis buffer rich medium[13] plus the required antibiotic. Gene expression was induced with 1mM IPTG at OD_{550nm} = 0.5. 20 mL culture samples were taken 3 h post-induction and were processed for further analysis. All experiments were done by triplicate.

12.6.2 IBs purification

IBs purification was performed by the group of Prof. Villaverde at the IBB (Universidad Autónoma de Barcelona). Samples of bacterial cultures (20 mL) were centrifuged at 4°C at 5000 g for 5 min, resuspended in lysis buffer (20 mL, 50 mM TrisHCl (pH 8.1), 100 mM NaCl, and 1 mM EDTA) and frozen at -80°C. After that, samples were defrozen and phenylmethanesulphonylfluoride (PMSF) (100 μL, 100 mM) and lysozime (400 μL, 1 mg/mL) were added and incubated for 2h at 37°C. Then, 100 μ of Triton X-100 were added (0.5% Triton X-100). After 1h incubation at room temperature, the sample was ice-jacketed, and sonicated 5 cycles of 10 min each at 40% amplitude under 0.5 s cycles. Next, the mixture was incubated with DNase (12 μL, 1 mg/mL) and $MgSO_4$ (12 μL, 1 M) for 45 min at 37°C. Finally, samples were centrifuged at 4°C at 15000 g for 15 min, the pellet was washed once with 1 mL of lysis buffer containing Triton X-100 (0.5%) and the sample was centrifuged again at 15000 g for 15 min at 4°C. Pellets containing pure inclusion bodies were stored at -80°C until analysis. All incubations were done under gently agitation.

12.6.3 IBs size and Z potential determination by dynamic light scattering (DLS)

The particle sizes and Z potential of IB were determined in a dynamic light scattering (DLS) device (Malvern, Nanosizer Z), in suspension on PBS buffer (pH = 7.4, IB final concentration was 20 mg/mL). To facilitate the dispersion on the liquid, 2 mL of the mixture were sonicated for 1 min. Both measurements were

carried out at 37°C using 1 mL of freshly prepared IBs suspension into a disposable plastic cubette. Each IBs sample was analyzed by triplicate averaging thirty single measurements.

12.6.4 IBs stability analyses

IBs aged for 5 h and obtained in DnaK$^-$ cells, in PBS with 10 g/L bovine serum albumin (BSA), sucrose (60 g/L), gentamicin (40 mg/L), penicillin (100 μg/L), and streptomycin (10 mg/mL), were incubated at different temperatures for different times. Samples were frozen at 80°C until fluorescence determination at 510 nm in a Cary Eclipse fluorescence spectrophotometer (Variant, Inc., Palo Alto, C.A) using an excitation wavelength of 450 nm. Results are given as the percentage of remaining activity or fluorescence with respect to fully stable samples at 80°C. Another set of samples was lyophilized in a Cryodos-80 Telstar lyophilizer and stored at 4°C until analysis.

12.6.5 Preparation of the SAM modified gold surfaces for IBs characterization

Different molar ratios of hydrophilic (-OH terminated) and hydrophobic (-CH_3 terminated) alkanethiols were used to obtain mixed self assembled monolayers (SAMs) with different degree of hydrophobicity, as shown by static contact angle measurements (Table 12.4). SAMs with different proportions of 1-undecenethiol (-CH_3 terminated) and 11- mercapto-1-undecanol (-OH terminated) were prepared by immersion of the freshly cleaned gold substrates (1 mM) in an ethanolic solution of the organic thiols with the appropriate molar ratio for 24 h. Then, substrates were rinsed with clean ethanol and sonicated for 5 min in ethanol to remove the physisorbed molecules. Afterwards the substrates were dried under a stream of N_2 and immediately used.

12.6.6 Contact angle measurements

Wettability of the self assembled monolayer of the mixed thiols before and after being in contact with IBs was determined with an OCA 15 (Dataphysics, Germany) contact angle goniometer. Data treatment and angle determination were

Table 12.4: f_{-OH} and total concentration of the 6 different CH_3/OH mixed monolayer solutions

Substrate	mg -OH	mM -OH	μl CH_3	mM CH_3	Tot. [C]	f_{-OH}
1	0	0	6.7	1.99	1.99	0
2	1.442	0.47	5.35	1.59	2.06	0.228
3	2.586	0.84	4.0	1.19	2.03	0.414
4	4.678	1.53	1.35	0.40	1.93	0.793
5	5.540	1.81	0.65	0.19	2	0.905
6	6.116	2.0	0	0	2	1

carried out with the software SCA20 (Dataphysics, Germany). Four sets of static contact angles, at different positions on each sample, were measured.

12.6.7 Coverage study of the IBs

Freshly prepared mixed monolayers of the thiols were immersed for 2 h into an IB suspension in PBS buffer (IB suspension was sonicated for 5 min prior to the introduction of the substrate). Afterwards, the IBs covered substrates were gently rinsed with ultrapure water (18.2 MΩ) and dried under a stream of N_2. Optical fluorescence microscope images of the deposited IBs were performed using an OLYMPUS Bx51 microscope with an OLYMPUS DP20 camera with 3 s shutter time, and an OLYMPUS U-RFL-T mercury lamp accessory. In order to remove background light a GFP pass filter was used. ImageJ (GNU) software was used to perform the particle counting.

12.6.8 Atomic force microscopy (AFM) of the IBs

Atomic force microscopy (AFM) images were taken with a commercial AFM (MFP-3D-SA, Asylum Research, Santa Barbara, USA). Samples were analyzed in dynamic mode working at 8 kHz of frequency and in a liquid environment (PBS buffer media pH = 7.4) in order to mimic the cytoplasmic environment of the cell. Pyramidal NSC35/AlBS silicon tips (Mikromash, USA) having nominal spring constants of 0.28 N/m were used. Sample preparation was done by drop casting of an IBs suspension in the same PBS buffer (20 mg/mL) over freshly cleaved mica.

12.6.9 Force spectroscopy AFM of the IBs

AFM indentation measurements were done with a commercial AFM (MFP-3D-SA, Asylum Research, Santa Barbara, USA) equipped with a close loop tracking

system and working in a liquid environment. Pyramidal NSC35/AlBS silicon tips (Mikromash, USA) having nominal spring constants of 0.28 N/m were used. The spectroscopic calibration of the raw cantilever in liquid media (PBS buffer solution pH =7.4) was developed by measuring force vs. distance curves, on freshly cleaved mica. Sample preparation was done by drop casting of an IB suspension in the same PBS buffer (20 mg/mL) over freshly cleaved mica. The force curves, consisting of 2048 data points were obtained imposing a maximum applied force of 50 nN at a frequency of 8 kHz. AFM mechanical properties data were calculated from force *vs.* distance curves according to the procedures described in Annex III .

12.6.10 Preparation of the aminosilane SAM modified silicon slides for IBs characterization

Prior to monolayer formation, the silicon (100) substrates were treated with oxidizing solution ($NH_4OH/H_2O_2/H_2O$ in 1:1:5 ratio) for 30 min at 80°C and gently rinsed with ultrapure water (ω 18.2 MΩ cm). Subsequently, the substrates were placed in piranha solution for 15 min (concentrated H_2SO_4 and 33% aqueous H_2O_2 in a 3:1 ratio), copiously rinsed with ultrapure water, and dried under a stream of nitrogen. Then the substrates were exposed under controlled atmosphere (Ar) to a solution of N-[3-(trimethoxysilyl)propyl]ethylenediamine (5 mM) in dry toluene for 3 h. Subsequently, substrates were rinsed with toluene and ethanol to remove the excess of silanes.

12.6.11 μ-contact printing of the IBs

The μCP of IBs onto the amino-terminated silicon substrate was performed using polydimethylsiloxane (PDMS, Sylgard 184, Dow Corning, USA) stamps. Stamps were fabricated by casting a 10:1 (v/v) mixture of PDMS and curing agent (Sylgard 184, Dow Corning) against a photolithographically patterned silicon master, curing for 18 hours at 60°C. For the μCP-patterned IBs, the stamps were inked in a IBs PBS buffer (pH 7.4) suspension (20 μg/l) for 40 min, dried under nitrogen flow, and placed on the clean amine-terminated silicon substrate. After 1 min contact time the stamp was carefully removed and the patterned surface gently rinsed with ultrapure water to remove the non adhered IBs.

12.6.12 Cell proliferation studies with IBs

IBs cell proliferation assays were developed by *Dr. Esther Vázquez* from the *IBB-Universidad Aut ònoma de Barcelona*. IBs produced and purified from different bacterial strains were sterilized by exposure to a 253 nm UV light germicidal lamp for 4 h. The IBs were resuspended in PBS, and $2.65 \cdot 10^8$ IBs (particles) were added per well to coat untreated Costar 3370 plates, which were left overnight at 4°C. Wells were washed in PBS and blocked with 3% BSA in PBS for 1 h at 37°C. Afterwards, $3 \cdot 10^3$ newborn hamster kidney (BHK) cells or $2 \cdot 10^4$ rat pheochromocytoma (PC12) cells were added per well and incubated in Dulbeccos Modified Eagles Medium (DMEM) supplemented with nonessential amino acids and fetal calf serum (5%), at 37°C for different times. Blank wells underwent exactly the same treatment as described but without IBs. After incubation, cell proliferation was determined using the EZ4U kit (Biomedica GmbH) following the manufacturers instructions, and analyzed in the multilabel reader iEMSMF (Labsystems, Helsinki, Finland). The reading absorbances were 450 nm and 620 nm as reference, and the values were standardized with respect to medium containing wells. A pre-test to select incubation time before saturation was carried out with the kit reagents. All assays were done in triplicate. Data were expressed as the mean ± standard error of the mean (SEM) of the values obtained per condition and evaluated statistically by a T-test analysis. Cultured cell pictures under different conditions were taken with a Nikon Eclipse TS100 inverted microscope by using NIS-Elements F 3.00 imaging software.

Bibliography

[1] Domke, J.; Radmacher, M. *Langmuir* **1998**, *14*, 3320–3325.

[2] Parra, A.; Casero, E.; Lorenzo, E.; Pariente, F.; Luis, V. *Langmuir* **2007**, *23*, 2747–2754.

[3] Zhao, Y.; Truhlar, D. G. *Journal of Physical Chemistry A* **2005**, *109*, 5656–5667.

[4] Muńiz, J.; Sansores, L. E.; Martínez, A.; Salcedo, R. *Journal of Molecular Structure: THEOCHEM* **2007**, *820*, 141–147.

[5] Becke, A. D. *Journal of Chemical Physics* **1993**, *98*, 5648–5652.

[6] Frischand, M. J.; et al.; *Gaussian 03*.

[7] Schuchardt, K. L.; Didier, T. B.; Elsethagen, T.; Sun, L.; Gurumoorthi, V.; Chase, J.; Li, J.; Windus, L., Theresa *Jounal of Chemical Information and Modeling* **2007**, *47*, 1045–1052.

[8] Gordon, A. J.; Ford, R. A. *The chemistfs companion: A handbook of practical data, techniques, and references*; John Willey and Sons: New York, 1972.

[9] Martínez, R.; Ratera, I.; Tárraga, A.; Molina, P.; J., V. *Chemical Communication* **2006**, 3809–3811.

[10] Pale-Grosdemange, C.; Simon, E. S.; Prime, K. L.; M., W. G. *Journal of the American Chemica Society* **1991**, *113*, 12–20.

[11] Barrientos, A. G.; delafuente, J. M.; Rojas, T. C.; Fernández, A.; Penadés, D. *Chemistry - A European Journal* **2003**, *9*, 1909–1921.

[12] Kashai, K.; Nalwa, H. S.; Oikawa, S.; Matsuda, H.; Minami, N.; Kakuta, A.; Ono, K.; Nakanishi, H. *Japan Journal of Applied Physics* **1992**, *31*, 1132–1134.

[13] Sambrook, J.; Fritsch, E.; T, M. *Molecular Cloning: A Laboratory Manual*; Cold Spring Harbor: New York, 1989.

[14] Thomas, J. G.; Baneyx, F. *The Journal of Bacteriology* **1998**, *180*, 5165–5172.

[15] Garcia-Fruitos, E.; Gonzalez-Montalban, N.; Morell, M.; Vera, A.; Ferraz, R.; Aris, A.; Ventura, S. a. V. A. *Microbial Cell Factories* **2005**, *4*, 27–33.

Part VI

Annexes

Annexes A

Annexes

A.1 X-Ray Photoelectron Spectroscopy (XPS)

A.1.1 General description

The development of the X-ray photoelectron spectroscopy (XPS) emerged from the discovery of the photoelectric effect by *Henrich Hertz* in 1887, in which X-rays were used as exciting photon source.[1] Twenty years later, in 1907, *P. D. Innes* was able to record broad bands of emitted electrons as a function of velocity. However, he erroneously concluded that the most probable theory (of the photoelectric effect) is atomic disintegration and he did not refer to the Einsteins explanation of the photoelectric effect.[2,3] Several years later, *Kai Siegbahn* and his group in Upsala (Sweden) reached several significant instrumental improvements and in 1954 recorded the first high-energy resolution XPS spectrum of cleaved sodium chloride, which revealed the potential of XPS. The first commercial XPS was developed by Hewlett-Packard in the USA in 1969. *Siegbahn* received the Nobel Prize in 1981 for his wide efforts to develop XPS into a useful analytical tool. Since then, XPS is one of the most important techniques for surface analysis.

XPS is a spectroscopic technique that measures the elemental composition, chemical state and electronic state of the elements that exist within a material. In XPS, a beam of monochromatic X-rays is used to irradiate the sample inducing the ejection of electrons due to the photoelectric effect. The kinetic energy of the ejected photoelectrons is measured with an electron energy analyzer to be finally displayed as a spectrum. Only those photoelectrons originated within tens of angstroms below the solid surface are able to leave it without energy loss. This

is why XPS is an analytical technique sensitive to the top-most layers of a surface. The measured kinetic energy of the electrons can be transformed into their binding energy (E_b), energy required to remove an electron from a certain atom, trough Equation A.1.

$$h\nu = E_b + E_k + \Theta_{spec} \tag{A.1}$$

where $h\nu$ is the energy of the incident photon, E_b is the binding energy, E_k the kinetic energy of the emitted electron and Θ is the spectrometer work function.

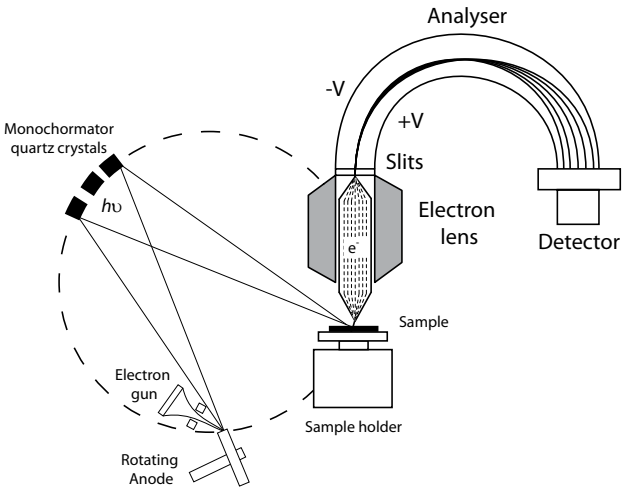

Figure A.1: Scheme of an XPS instrument. Reproduction of an image taken form *Pavlovic E. et al.*, *Acta Univaersitatis Upsaliensis*, **2003**

Figure A.1 depicts a schematic representation of a XPS instrument. The essential parts of the instrument consist of an X-ray source (electron gun, rotating anode, monochromator, quartz crystals, etc), an analysis chamber,an electron lens, an analyzer and a detector. All the system must be placed under ultra high vacuum regime (10^{-10} mbar) to allow the appropriate measurement, avoiding scattering of the emitted electrons, and the contamination of the sample.

A.1.2 Chemical shift

The exact binding energy of an electron in a given element depends on the chemical environment that surrounds it. Each element produces a different set of XPS peaks at characteristic binding energies, allowing the identification of the chemical

elements present in the sample.

Table A.1: Binding energies for some common chemical elements. Chemical shifts values have been obtained from *G. Beamson et al. "High resolution XPS of organic polymers: the Scienta ESCA 300 Database"*, **1992**.

Orbital	**Group**	E_b (eV)
C1s	C-H/C-C	285.0-285.5
	C-O	286.5-287
	O-C=O	289-289.5
	C-N	285.5-286.5
	N-C=O	288.0-288.6
N1s	C-N	399.1-400.2
	NH_3^+	401-402
	N-C=O	399.8
O1s	SiO_x	532.0
	C-O	532.7-533.8
S2p3/2	-SH/-S-S-	164-165
	S=O (sulfinyl)	166.6
	O=S=O (sulphonyl)	168.4
Hg4f5/2, 7/2	Hg^{2+}	100-105

Furthermore, changes on the chemical state or environment of a same element are also reflected on its XPS spectra. This effect causes the so called chemical shift of the binding energy of an element from the reference value. Thus, XPS can not only be used to determine the element nature but also it is a very useful technique to identify the oxidation state and chemical surroundings of a chemical compound. Table A.1 depicts some of the chemical shifts values for the most representative chemical elements, such as C, O ,N and other specially used during the developing of this work like Hg.

A.2 Surface Plasmon Resonance (SPR)

A.2.1 General Description

SPR is an evanescent field optical sensing technique based on the detection of small variations of the refractive index (Δn) of a medium adjacent to a metallic surface. The origin of the surface plasmon resonance (SPR) spectroscopy dates from the beginning of the last century with the finding of *R.W. Wood* anomaly seen for the reflected light from diffraction gratings[4] further investigated by *Ritchie et al.*[5] Since then, there has been a considerable amount of work done on the fundamental properties and applications of plasmons and specially on the developing of a wide variety of optical sensors.[6]

The physical phenomena behind the SPR is based on the interaction between an incident beam of light and the plasmons present on a thin metal layer. At the interface of two transparent media having different refractive indexes, the incident light gets reflected and refracted. If the angle of incidence is greater than a certain angle, called the critical angle (ϕ_c), no light is refracted and the incident light undergoes total internal reflection. However not all the radiation is reflected and part of the electromagnetic field penetrates a very short distance into the medium, generating an exponentially decreasing electromagnetic filed that propagates perpendicular to the surface, known as evanescent filed (EF). Due to its nature, the distance at which this EF is active is really low being almost negligible at distances higher than 200 nm from its origin (Figure A.2).

Furthermore, apart form the EF, the presence of free electrons at the interface of this two materials is essential for the appearance of SPR. Thus, the interface between the media is coated with a thin layer of metal (usually gold or silver) where free conduction electrons are abundant. When these two conditions are matched there is an angle (ϕ_{SPR}) at which the generated EF enters in resonance with the plasmons present in the metal surface. Then, a big part of its energy is transfered and dispersed through the metal surface producing a significant reduction of the intensity of the reflected light, that can be easily detected. SPR technique make use of the modification of this resonance settings to monitor changes on the surface properties of gold.

Figure A.3 depicts a schematic representation of an SPR detecting system based on a continuous flow system consisting on a monochromatic light source (LASER),

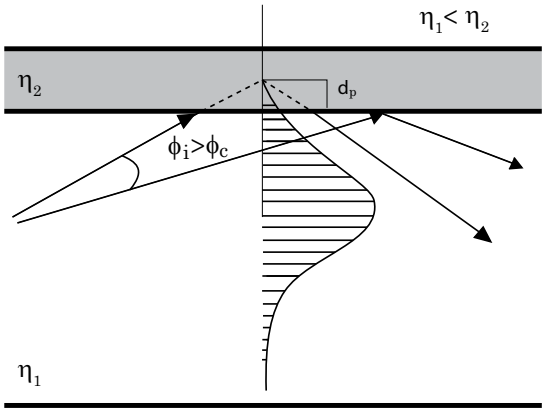

Figure A.2: Schematic representation of the evanescent field phenomenon, being $\eta_2 > \eta_1$ and $\theta_i > \theta_c$

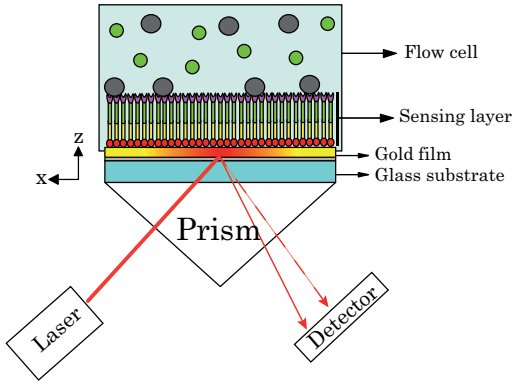

Figure A.3: Schematic representation of a continuous flow SPR system

an optical detector, a prism of controlled refractive index, a gold coated glass slide and a flow cell. In this case the variations of the ϕ_{SPR} are monitored while a solution is pumped over the gold layer.

As said before, SPR is extremely sensitive to small changes on the properties of the, here, metal-liquid interface properties, specially its refractive index. Therefore, even a small modifications on the metal-liquid interface will alter the ϕ_{SPR} at which the SPR phenomena takes place. The number of phenomena able to generate an SPR response is quite numerous, from conformational changes, to modifications of the colorimetric or fluorescent properties of the substrate, nevertheless the adsorption of molecules is the most common of all of them.

A.2.2 SPR Sensor Modification

Due to its high sensitivity, SPR has aroused as one of the most interesting optical sensing techniques in the last decades. However, despite its advantages SPR selectivity is rather low, meaning that any molecule adjacent to the metallic surface that changes η will induce an SPR response. Nevertheless, the selectivity of an SPR sensor platform can be more or less easily tunned by the appropriate modification of the sensor gold surface.
During the last years, several innovative recognition elements have been developed and deposited on Au thin films for SPR sensing. Depending on the study two different immobilization methods can be identified, the *direct* and the *capture* methods.

- **Direct immobilization method**. Due to its simplicity it is the most used approach. There, the ligand is covalently attached onto the sensor surface by chemical modification, mainly by the use of thiol groups. The main drawback of this approach lays on the controlling of the orientation of the analyte receptor upon anchoring to the surface. Thus, it is important to carefully design and characterize the ligand prior to immobilization.

- **Capture immobilization method**. Its provides an alternative to the direct covalent immobilization. In this case a "bridge" molecule is firstly anchored to the metal surface to assure a good packing and stability of the gold coating, then the receptor ligand will be attached to the first layer preparing the surface for analyte sensing. The main disadvantage of this technique is the increase in complexity of the sensor preparation, however, better packed and oriented surfaces can be obtained.

A.2.3 SPR Kinetic Studies

An important application of a SPR sensor is the possibility to perform kinetic analysis of the interaction between a molecule A and a ligand B attached to a metallic surface, normally gold. The binding kinetics of such a molecular interaction is quantitatively characterized by the rate constants and the equilibrium constants involved. An SPR interaction plot is the experimental output given by this technique which generally contains three phases: a) the association phase, where the molecule A is injected to the system and interacts with the ligand B

attached to the surface, b) the dissociation phase, where the injection of the analyte A is stopped but the solvent continuous to flow, releasing the molecule A previously complexed on the surface, and c) the regeneration phase, where the solvent is continuously flowing and the surface is free of the analyte A (Figure A.4). The association and the dissociation phases can be used to determine the rate constants and thereby the equilibrium constants.

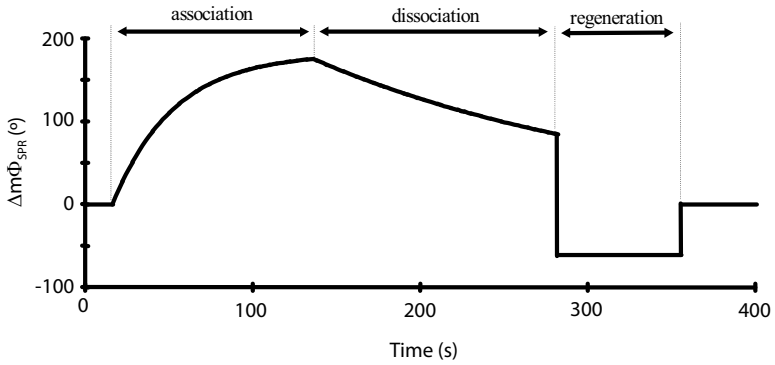

Figure A.4: Schematic representation of the three phases of an SPR injection plot.

Therefore, for a binding reaction between two compounds, A and B, that gives a one to one complex AB, as in Equation A.2, where A is the injected analyte and B the ligand attached to the surface, the processes are controlled by k_a and k_d which are the association rate constant in ($M^{-1}s^{-1}$) and the dissociation rate constant (in s^{-1}), respectively.

$$A + B \underset{k_d}{\overset{k_a}{\rightleftharpoons}} AB \tag{A.2}$$

Considering an equilibrium situation, the above described rate constants can be rewritten as the subsequent equilibrium constants, given by Equation A.3

$$K_A = \frac{k_a}{k_d} = \frac{[AB]}{[A]\,[B]} \quad K_D = \frac{k_d}{k_a} = \frac{[A]\,[B]}{[AB]} \tag{A.3}$$

where K_A is the association equilibrium constant (in M^{-1}) and K_D is the dissociation constant (in M).

The binding reaction in the association phase is given by Equation A.4, since we can assume that the concentration of AB complex is very small in this phase of

the interaction plot and, therefore the dissociation reaction is not significant.

$$A + B \xrightarrow{k_a} AB \tag{A.4}$$

$$\frac{d\,[AB]}{dt} = k_a\,[A]\,[B] \tag{A.5}$$

On the contrary the binding reaction in the dissociation phase is controlled by Equation A.6, where both reactions compete and must be taken into account.

$$AB \underset{k_d}{\overset{k_a}{\rightleftharpoons}} A + B \tag{A.6}$$

$$\frac{d\,[AB]}{dt} = k_a\,[A]\,[B] - k_d\,[AB] \tag{A.7}$$

The concentration of the ligand B at a given time t, $[B]_t$, is given by Equation A.8, where $[B]_{t=0}$ is the concentration of B at the initial time.

$$[B]_t = [B]_{t=0} - [AB]_t \tag{A.8}$$

Substituting this equation into Equation A.7 results in

$$\frac{d\,[AB]}{dt} = k_a\,[A]\,([B]_{t=0} - [AB]_t) - k_d\,[AB]_t \tag{A.9}$$

The formation of the complex AB on the surface of the chip is measured with the SPR instrument, being its concentration directly proportional to the output signal R; i.e., $[AB]$ = R. Due to negligibly small concentration differences of analyte A during the association phase, it can be assumed that its concentration is constant along time, being $[A]_{t=0}$ = C. Therefore, the complex formation reaction can be considered as pseudo first order reaction in SPR sensors[7–9], and the Equation A.9 can be rewritten as:

$$\frac{dR}{dt} = k_a C(R_{max} - R_t) - k_d R_t \textit{ which can be arranged as} \tag{A.10}$$

$$\frac{dR}{dt} = k_a C R_{max} - (k_a C + k_d) R_t \tag{A.11}$$

Equation A.11 can be regarded as a straight line dR/dt = b - $k_s R_t$ with k_s = (k_aC +k_d) and b = k_aCR_{max}. Parameters k_s and b therefore can be determined by a linear regression of the plot of dR/dt values versus R_t values, being the

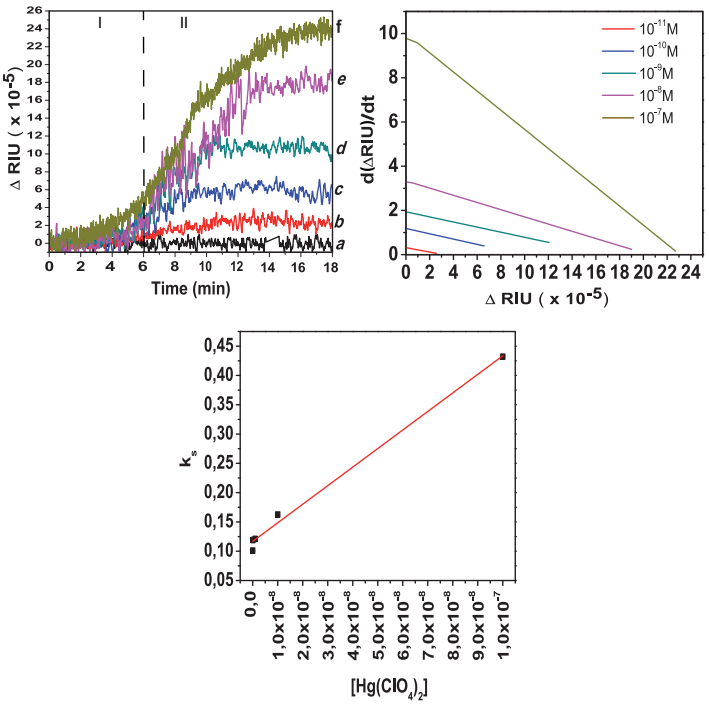

Figure A.5: Schematic representation of the kinetics of a chemical recognition process followed by SPR and the plot normally used for determining the association and dissociation rate constants.

resulting k_s value a concentration-dependent parameter. This method is called the linearization method, because the data are presented in such a way and the relevant parameter k_s can be determined by linear regression (Figure A.5).
Finally the Kinetic rate constants, k_a and k_d are determined by a plot of k_s values versus concentration of the analyte A. A linear regression provides the association rate constant k_a from the slope of the plotted straight line and the dissociation rate constant, k_d from the y-intercept of the plotted line.

A.3 Force Spectroscopy Atomic Force Microscopy (FSAFM)

A.3.1 General information

Invented in 1981 by *Binnig G.* and *Rohrer H.*[10] and 1986 by *Binnig G.*, *Quate C. F.* and *Gerber Ch.*,[11] Scanning tunneling microscope (STM) and the atomic force microscope (AFM) are the two first components of a complex set of scanning probe microscopies (SPMs) which use has changed the way of understanding the nanoworld.

The principle by which all SPMs function, is based on the mapping of weak interactions between a sharp tip and a sample, while scanning its surface from a close distance (Å). Thus, depending on the measured properties it is possible to talk about different types of SPMs, such as surface topography, friction, charge distribution or magnetism. The resolution of the technique is dependent on the accuracy by which the tip follows the sample surface, which means that an exact positioning of the tip is extremely important. In order to achieved the required exactitude piezoelectric actuator tubes, capable of positioning tip and specimen within a few Angstroms or less, are used to control the measuring elements.

There is a continuous growth in the number of new types of instruments sharing important features with STM and AFM, which are comprehensively referred to as Scanning Probe Microscopes (SPMs). Among these it is worthy to remark the magnetic force microscope (MFM),[12] which is essentially an AFM operating in non-contact and with a magnetic tip, enabling it to probe the magnetic properties of a surface; the scanning near-field optical microscope (SNOM),[13] based on an AFM system using an optical probe with an aperture of about 10 nm, the SNOM technique allow us to overcome the resolution limit of traditional optical techniques by pacing the detector very close (distance much closer than the wavelength) to the specimen surface; charge force microscope (CFM),[14] where the interaction between surface charges gives an image of charge induced by the tip utilized.

Table A.2: SPMs techniques.

Instrument	**Acronym**	Measured parameter
Scanning tunneling microscope	STM	electron tunneling current
Atomic force microscope	AFM	surface force/force gradient
Charge force microscope	CFM	electrostatic force
Magnetic force microscope	MFM	magnetic force
Tunneling stabilized magnetic force microscope	TSMFM	magnetic force
Scanning near-field optical microscope	SNOM	near-field optical reflection
Scanning ion conductance microscope	SICM	ion current

A.3.1.1 Atomic force microscopy (AFM)

Atomic force microscopy (AFM) is a high resolution scanning probe microscopy technique that relies on the measurement of ultra-small forces (less than 1nN) present between a tip and a sample surface.

In AFM a sharp tip at the end of a flexible cantilever is brought in contact with, or near, the surface to be imaged. Information gathered by AFM is limited to a very reduced area of the sample (approx. maximum scanned area 150X150 μm), and only "flat" samples (no more than 20 μm of roughness) can be analyzed. The force measured by the AFM is composed of all the attractive and repulsive forces acting between the tip and the sample. Thus, the resultant of all these forces will produce a proportional positive or negative bending of the flexible cantilever. By detecting the size of the bending the existent force may be measured. The forces involved in the process are very difficult to be identify as they depend very much on the material of the tip and the sample respectively. Generally speaking the forces can be divided into long range and short-range. When scanning in contact with the sample surface the short-range forces dominate, while at larger distances from the surface the long-range forces, such as van der Waals, capillary, magnetic or electrostatic forces, will dominate.

As previously explained, the accurate control of the tip or sample positioning is carried out by several piezoelectric elements that facilitate the very precise scanning, while the relative displacement between the cantilever surface and the reference surface is determined by a laser reflected on the top of the cantilever whose movement is recorded on a position sensitive detector (PSD) (Figure A.6).

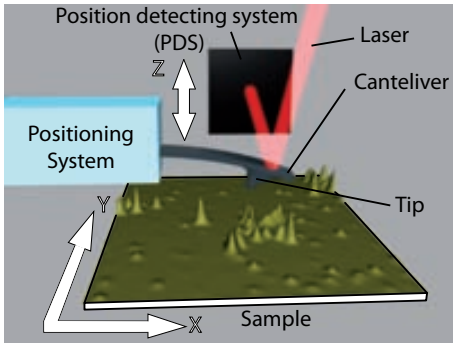

Figure A.6: Scheme of an AFM

AFM can be operated using two different modes, the contact and the non-contact modes.

- **Contact mode.** In the contact mode the tip is dragged over the surface while keeping a constant contact with it, thus, it follows the orography of the substrate as scanning the sample. Moreover, information about the friction between the tip and the sample can also be obtained. However, this fact also turns to be also the main disadvantage of this AFM mode as the friction of the tip might also damage the surface of soft samples.

- **Non-contact mode.** In the non-contact mode the cantilever is oscillated by a vibrating piezocrystal and changes on the amplitude of the oscillating movement are recorded while the surface is scanned. This mode is much less damaging than the previous one as the tip does not contact the sample surface, however no information about the friction forces of the substrate can be obtained.

A.3.1.2 Force spectroscopy AFM

Due to its spatial resolution and sensitivity to weak forces, AFM technique is ideal for studying the mechanical properties of materials at a very localized nanometric scale. For this method, the AFM tip is extended towards and retracted from the surface as the deflection of the cantilever is monitored as a function of piezoelectric displacement.

$$F = -kd_c \tag{A.12}$$

where k corresponds to the cantilever spring constant and d_c to the cantilever deflection.

The plotting of the resulting cantilever deflection vs. sample distance can be transformed, upon calibration trough the Hooke's law (Equation A.12), to the force applied generating a force (f) *vs.* distance (d) curve, from which would be possible to obtain information about the mechanical properties, chemical bonds strength,... of the studied substrate.

Figure A.7 depicts two theoretical examples of force vs. distance curves. The

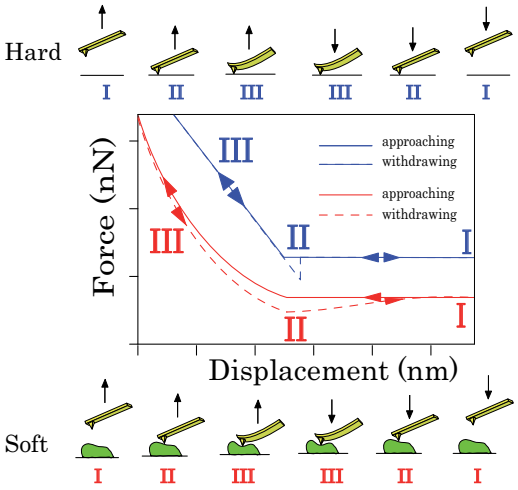

Figure A.7: Representation of the approaching and withdrawing curves of a FSAFM measurement on a hard (blue) and a soft (red) samples.

blue lines correspond to the experiment performed to a hard sample, while the red one corresponds to a soft sample.

In the first case, the stiffness of the measured substrate is very high and the tip will generate almost indentation on the substrate surface during the approaching process, thus the force curve obtained can be represented by a straight line where each nm of the z-piezo movement is reflected on a deflection of the cantilever. This situation is repeated on the withdrawing of the tip. However, it can be observed how, even when the tip is not contacting the sample, the cantilever is deflected towards the surface until a point were it suddenly reaches the initial position. This phenomena is due to the existence of adhesion forces between the tip and the sample and it is more pronounced when the measurements are done in air, as the tip has to overcome the force performed by water meniscus formed between

itselve and the sample.

For the soft sample the situation is completely different, in this case the approach movement of the tip generates a big indentation of the sample, expressed on a lower deflection of the cantilever and the appearance of a non linear behavior of the force vs. displacement curve. Furthermore, adhesion of the tip to the sample will also be bigger and this will be reflected on the withdrawing curve.

In order to calculate the desired mechanical parameters of interest it is needed to fit the obtained curves to a theoretical model. Among the different theories describing the elastic deformation of a soft sample by a rigid indenter,[15] the Hertzian model[16] has been one of the more used one.[17–19]

For the Hertzian model, the applied force and the indentation of a soft sample by a hard tip, are related through Equation A.2;

$$F = A\left[\frac{E^*}{(1-\nu^2)}\right]\delta^m \tag{A.13}$$

where E^* is the reduced Young's modulus of the sample, ν is the Poisson ratio of the sample, and A and m are a constants that depend on the indenter radius and shape.[20]

$$F = \left[\frac{4E^*R^{1/2}}{(3(1-\nu_s^2))}\right]\delta^{3/2}\,;\delta = \left[\frac{(3(1-\nu_s^2))}{4E^*R^{1/2}}\right]^{2/3}F^{2/3} \tag{A.14}$$

$$F = \left[\frac{2E^*tan(\alpha)}{(\pi(1-\nu_s^2))}\right]\delta^{2}\,;\delta = \left[\frac{(\pi(1-\nu_s^2))}{2E^*tan(\alpha)}\right]^{1/2}F^{1/2} \tag{A.15}$$

Assuming a spherical geometry for our indenter, the relationship between the applied force (F) and the indentation (δ) is reduced to Equation A.14; where R is the tip radius. While in the case of a conical indenter the expression is shown on Equation A.15; where α is the half opening angle of the conical tip.

Indentation (δ) values for each sample were calculated by computing the lateral deviation (along the X axis of the graph) of the piezo movement (z) vs. deflexion (d) graph respect to the one obtained for the reference mica surface.[21] Assuming a typical Poisson ratio value of 1/3,[18,21] it is possible to obtain the reduced young modulus (E^*) for each experiment by the fitting of the F versus δ plots, to the conical or spherical approximations. Real Young modulus of our sample can be easily obtained from the reduced one following the relationship shown on Equation A.16, where ν_s, E_s and ν_t, E_t correspond to the Poisson ratio (ν) and

the young modulus (E) of the sample and the tip respectively.

$$E^* = \left[\frac{(1-\nu_s^2)}{E_s} + \frac{(1-\nu_t^2)}{E_t} \right] \tag{A.16}$$

All the F *vs.* d fittings performed in this thesis were handled using the IGOR PRO 6 software (Wavemetrics, USA).

Bibliography

[1] Briggs, D.; Seah, M. P. *Practical Surface Analysis by Auger and X-ray Photoelectron Spectroscopy*; John Wiley & Sons, Norwich, 1983.

[2] Einstein, A. *Annalen der Physick* **1905**, *322*, 132–148.

[3] Jenkin, J. G.; Leckey, R. C. G.; Liesegang, J. *Journal of Electron Spectroscopy and Related Phenomena* **1977**, *12*, 1–35.

[4] Wood, R. W. *Philosophical Magazine* **1902**, *4*, 396–403.

[5] Ritchie, R. H. *Physical review* **1957**, *106*, 874–881.

[6] Homola, J. *Surface Plasmon Resonance Sensors*; Springer Verlagand Berlin Springer Series on Chemical Sensors and Biosensors, 2006.

[7] Karlsson, R.; Michaelsson, A.; Mattsson, L. *Journal of Immunological Methods* **1991**, *145*, 229–240.

[8] Malmborg, A.; Michaelson, A.; Ohlin, M.; Jansson, B.; Borrebaeck, C. *Scandinavian Journal of Immunology* **1992**, *35*, 643–650.

[9] Faegerstam, L. G.; Frostell-Karlsson, A.; Karlsson, R.; Persson, B.; Roennberg, I. *Journal of Chromatography A* **1992**, *597*, 397–410.

[10] Binnig, G.; Rohrer, H. *Helvetica Physica Acta* **1982**, *55*, 726–735.

[11] Binning, G.; Quate, C. F. *Physical Review Letters* **1986**, *56*, 930–933.

[12] Martin, Y.; Rugar, D.; Wickramasinghe, H. K. *Applied Physics Letters* **1988**, *52*, 244–245.

[13] Pohl, D. W.; Denk, W.; M., L. *Applied Physics Letters* **1984**, *44*, 651–655.

[14] Stern, J. E.; Terris, B. D.; Mamin, H. J.; Rugar, D. *Applied Physics Letters* **1988**, *53*, 2717–2719.

[15] Pietrement, O.; Troyon, M. *Journal of Colloid and Interface Science* **2000**, *226*, 166–171.

[16] Hertz, H. *J reine angew Math 92* **1896**, *92*, 15.

[17] Parra, A.; Casero, E.; Lorenzo, E.; Pariente, F.; Luis, V. *Langmuir* **2007**, *23*, 2747–2754.

[18] Radmacher, M.; Fritz, M.; Cleveland, J. P.; Walters, D. A.; Hansma, P. K. *Langmuir* **1994**, *10*, 3809–3814.

[19] Afrin, R.; Alam, M. T.; Ikai, A. *Protein Science* **2005**, *14*, 1447–1457.

[20] Weisenhorn, A. L.; Khorsandi, M.; Kasas, S.; Gotzos, V.; Butt, H. J. *Nanotechnology* **1993**, *4*, 106–113.

[21] Vinckier, A.; Semenza, G. *FEBS Letters* **1998**, *430*, 12–16.

Part VII

Patents and Publications

MINISTERIO DE INDUSTRIA, TURISMO Y COMERCIO

Oficina Española de Patentes y Marcas

(12) SOLICITUD DE PATENTE DE INVENCIÓN

(21) Nº SOLICITUD: 200603285

(22) FECHA DE PRESENTACIÓN: 27 DIC 2006

(43) FECHA DE PUBLICACIÓN DE LA SOLICITUD:

(51) Clasificación Internacional:

(30) Datos de prioridad: (31) Número (32) Fecha (33) País

(71) Solicitante(s):
CONSEJO SUPERIO DE INVESTIGACIONES CIENTIFICAS
UNIVERSIDAD DE MURCIA
Domicilio: C/ SERRANO, 117
28006 MADRID
Nacionalidad: ESPAÑOLA

(72) Inventor(es): Díez Gil, Cesar; Ralera Bastardas, Imma; Veciana Miró, Jaume; Martínez, Rosario; Zapata, Felipe; Caballero, Antonio; Tarraga, Alberto; Molina, Pedro.

(74) Agente:

GRÁFICO SELECTIVO PARA PUBLICACIÓN

(54) Título de la invención:
PROCEDIMIENTO PARA LA FUNCIONALIZACIÓN DE UN SUSTRATO, SUSTRATO FUNCIONALIZADO Y DISPOSITIVO QUE LO CONTIENE

(57) Resumen:

PROCEDIMIENTO PARA LA FUNCIONALIZACIÓN DE UN SUSTRATO, SUSTRATO FUNCIONALIZADO Y DISPOSITIVO QUE LO CONTIENE

La invención se refiere a un procedimiento para la funcionalización de un sustrato a partir de un compuesto molecular, donde dicho sustrato es una membrana porosa, orgánica o inorgánica, insoluble en medio acuoso, y dicho compuesto molecular es un compuesto funcional insoluble en medio acuoso y soluble en un disolvente orgánico miscible en agua, comprendiendo dicho procedimiento preparar una suspensión acuosa de nanopartículas de dicho compuesto molecular funcional, donde el tamaño de las nanopartículas es igual o inferior al tamaño de poro de dicha membrana, y filtrar dicha suspensión a través de dicho sustrato, de manera que dichas nanopartículas coalescen entre sí y con el sustrato quedando ambos íntimamente unidos.
La invención también se refiere al sustrato así obtenido, a su utilización y al dispositivo que lo comprende.

OFICINA ESPAÑOLA DE PATENTES Y MARCAS

Sensors **2007**, *7*, 3481-3488

sensors

ISSN 1424-8220

www.mdpi.org/sensors

Full Research Paper

Naked-eye and Selective Detection of Mercury (II) Ions in Mixed Aqueous Media Using a Cellulose-based Support

César Díez-Gil [1], Antonio Caballero [2], Imma Ratera [1], Alberto Tárraga [2], Pedro Molina [2,*] and Jaume Veciana [1,*]

1 Institut de Ciència de Materials de Barcelona (CSIC)-CIBER-BBN, Campus Universitari, 08193 Bellaterra, Catalonia, Spain. Fax: 34 93 5805729; Tel: 34 93 580 1853. E-mail: vecianaj@icmab.es
2 Departamento de Química Orgánica, Facultad de Química, Universidad de Murcia, Campus de Espinardo, 30100 Murcia, Spain. E-mail: pmolina@um.es; vecianaj@icmab.es

* Author to whom correspondence should be addressed.

Received: 8 November 2007 / Accepted: 20 December 2007 / Published: 21 December 2007

Abstract: A test paper for high-selectivity detecting Hg^{2+} ions in mixed acetonitrile-water solutions has been achieved using a bis(ferrocenyl) azine, as chromogenic chemosensor molecule, and a solid cellulose fibre, as a substrate. Depending on the amount of mercury ions in contact with the detecting molecule a spectacular color change in the cellulose indicator is produced, being possible to determine the concentration of Hg^{2+} ions either by naked eye or spectroscopically.

Keywords: mercury (II) ions detection, bis(ferrocenyl) azine, chromogenic chemosensor, cellulose–based probe

1. Introduction

The sensitive detection of heavy and transition- metal ions, such as mercury is currently a task of prime importance for environmental or biological applications. Mercury, one of the most toxic elements in the world, represents a major toxicity to microorganism and environment even in low concentration. Inorganic mercury has been reported to produce harmful effects at 5 μg/l in a culture medium.[1] Once introduced into the marine environment, microorganisms convert it into methylmercury, a form of mercury being even more toxic to aquatic organisms and birds than the inorganic mercury, which eventually reaches the top of the food chain and accumulates in higher

organisms, especially in large edible fish.[2] When consumed by humans, methylmercury triggers several serious disorders including sensory, motor and neurological damage.[3] The development of methods for the determination mercury is, therefore, of significant importance for environment and human health. In the last decade researchers have done a big effort to develop new mercury sensors. An important number of selective Hg^{2+} chemosensors have been devised using redox,[4] chromogenic,[5] or fluorogenic[6] changes in organic media as detection channels. However, Hg^{2+} cations are relatively easy to be chelated and detected in organic solvents, they are rather difficult to be recognized directly in aqueous environments due to their strong hydrations. Consequently, developing simple and practical Hg^{2+} chemosensors in aqueous media is still a challenge.[7] Although instrumental analyses such as atomic absorption or atomic emission spectroscopy are currently used in the detection of metal ions, there is still a need to develop novel methods for the detection of toxic ions that offer high sensitivity, short response times, and high selectivity.[8] Among all these sensing approaches, the optical detectors that allow on-site, real-time qualitative or semiquantitative detection without the use of any complex spectroscopic instrumentation have received a great deal of attention.[9] Even though there are several molecules detecting mercury ions, only a few of them are available to be anchored or firmly physisorbed to a solid substrate and most of them have important short-comings for real applications, such as a lack of selectivity and high price. Firm fixation on solid substrates of colorimetric or fluorimetric reagents for heavy metal detection has been attempted by several techniques: polymer-bound chemosensors,[10] incorporation into PVC-based liquid membranes, covalent anchoring with cross-linked copolymers, layer-by-layer accumulation methods such as Langmuir-Blodgett films or alternate deposition of oppositely charged polyelectrolytes.[11] However, they have some drawbacks including complicated synthetic procedures, insufficient sensitivity and requirements for auxiliary additives.

Cellulose is an abundant, inexpensive, biodegradable and renewable biopolymer exhibiting very good mechanical properties and is also water-absorbing. Cellulose can be modified to alter and tailor its chemical and physical properties.[12] The use of cellulose-based materials could thus be extended to new applications by the incorporation of functional detecting molecules onto its fiber surface. In this context, paper strips have recently been used in biomedical assays,[13] and for heavy-metal ions detection,[14] although with low selectivity towards mercury ions. We present here a new cellulose based colorimetric mercury indicator using a simple procedure that allow its use for on-site selective mercury detection in mixed water environments which is one of the major drawbacks of most of the previously reported mercury chemosensors.

2. Results and Discussion

Recently we have reported a highly selective chromogenic mercury detector based on the 1,4-disubstituted azine bearing two end-capped ferrocene groups **1** (Figure 1). The optical activity of this molecule suffers from important changes when complexed with mercury ions enabling an optical-based mercury detector. A preliminary study[4b] in CH_3CN/H_2O mixtures toward Hg^{2+} ions have been previously reported showing no interaction with other common cations, such as Mg^{2+}, Ca^{2+}, Ni^{2+}, Zn^{2+}, Cd^{2+}, Pb^{2+}, and Cu^{2+} (Figure 1). Remarkable is this molecular detector since it suffers an important colour change in sensing which can be used for a naked-eye detection of Hg^{2+} ions in solution.

However, this application is limited to mixtures of polar organic solvents with water because of the poor solubility of **1** in pure water.

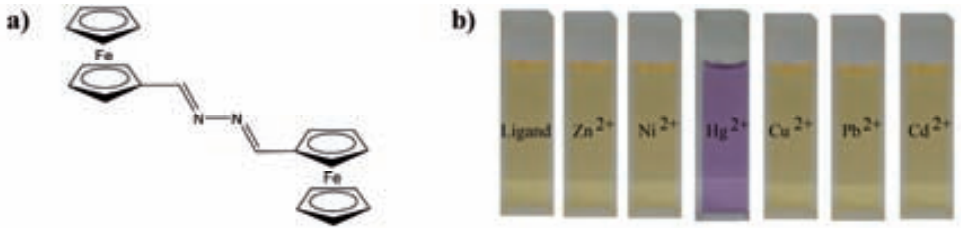

Figure 1. a) Highly selective and chromogenic mercury sensor based in a 1,4-disubstituted azine bearing two ferrocene groups. b) Colour change due to binding of **1** in CH_3CN/H_2O (7/3, v/v) (c = 1 x 10^{-3} M) with Hg^{2+}in comparison with other divalent metal cations.

To confirm the potential application of this ligand for detecting Hg^{2+}metal ions on a solid support, cellulose based probes were prepared in two steps. Firstly the cellulose disk was introduced into a mercury ion solution, using either an acetonitrile/water mixture (7:3) or pure acetonitrile, and after drying it introduced into the solution of the bis(ferrocene)azine **1** sensor. For the initial impregnation of the paper disks with the mercury ions it is also possible to use only water for the deposition of Hg(II) on the cellulose but then the sensitivity decreases considerably due to the poor solubility of the bis(ferrocene) azine in the stagnant water inside the cellulose fibers giving a poor homogeneity of the colour change. It is worth mentioning that the reverse procedure for the impregnation process, consisting firstly in soaking the cellulose with an organic solution of the detecting molecule and then with mercury ion solutions, does not provide positive results. This may be attributed to the better interaction of the mercury ions with the cellulose. In fact, it has been recently found that the cellulose is, on average, negatively charged, [15] so the interaction between the mercury cation and the surface is driven by very strong electroatractive forces that may change with the media.

The quantitative detection measurements of the cellulose probes were made using an UV-Vis spectrophotometer with an integrating sphere expansion pack, which allowed us to determine the absorption spectra of our solid substrates by light reflectance. An untreated cellulose paper was set as reference sample during the measurements. The measurements were performed from 400 to 700 nm. The resulting spectra were normalized showing that a neat interconversion between the uncomplexed and the mercury complexed species derived from **1** occurs on the surface of the indicator by the increasing amount of mercury ions present in the analyzed solutions.

The increasing concentration of mercury ions in the tested solution caused the apparent shift of the band initially appearing at 485 nm and shifted up to 565 nm (Figure 2). The band at 485 nm corresponds to the UV-Vis absorption spectrum of the cellulose indicator paper coated only with the free ligand **1** while the band at 565 nm corresponds to the UV-Vis absorption spectrum of the completely complexed ligand **1**·Hg^{2+}. For the intermediate mercury concentrations, when the free ligand **1** deposited on the paper is not completely complexed, there is the simultaneous presence of both bands at 485 nm and 565 nm with different intensities depending on the amount of mercury ions

in the tested solution. The large bathochromic shift of 80 nm observed for this band is responsible of the spectacular color change from orange (neutral azine **1**) to deep purple (complexed azine **1**·Hg^{2+}) suffered by the cellulose indicator paper (Figure 2). This impressive color change as well as the high reproducibility and the large persistence (days) of the coloration of the cellulose probes permit a "naked-eye" detection of Hg^{2+} ions similar to the well known *pH* paper indicator, as shown in Figure 2. Taking into account that the colour of **1**·Hg^{2+} complex in solution is not very persistent, since it is less intensive and disappears after about 20 min, these results clearly demonstrate the higher stability and sensitivity of the complex in solid state than in solution (Figure 2). The spectra obtained in Figure 3 can be quantified by their deconvolutions into two different Gaussian bands (Figure 3); one at 485 nm that corresponds to the absorption maximum for the free ligand **1** and another band corresponding to the mercury complex **1**·Hg^{2+} at 565 nm.

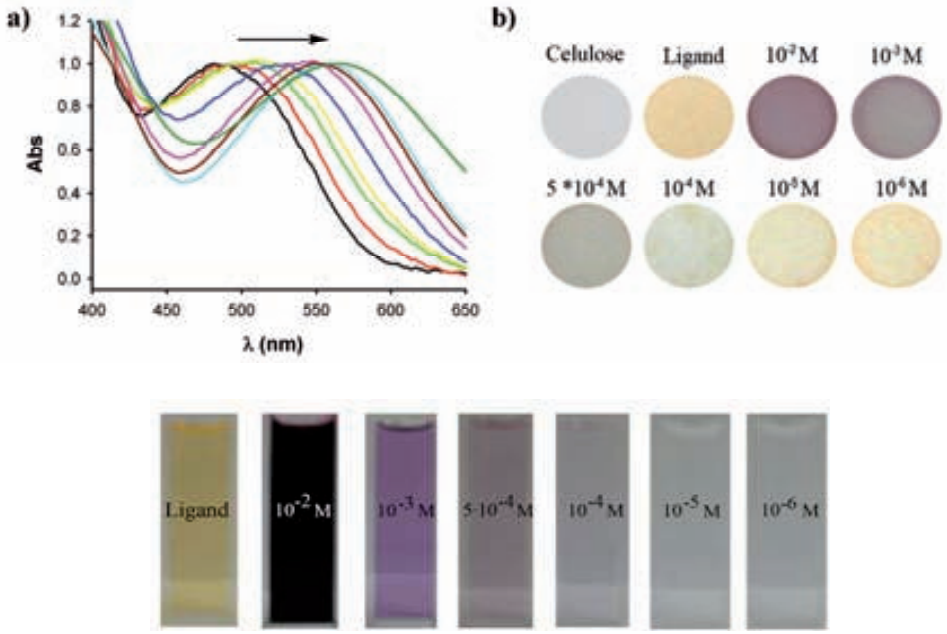

Figure 2. a) Normalized reflectance UV-Vis spectra of the cellulose indicator papers upon dipping onto increasing concentration of $Hg(ClO_4)_2$ in acetonitrile. b): "Naked-eye" detection of different concentations of Hg^{2+} cation using the cellulose indicator papers. c) Colour changes of azine **1** with different concentration of Hg^{2+} in CH_3CN/H_2O (7:3, v/v)

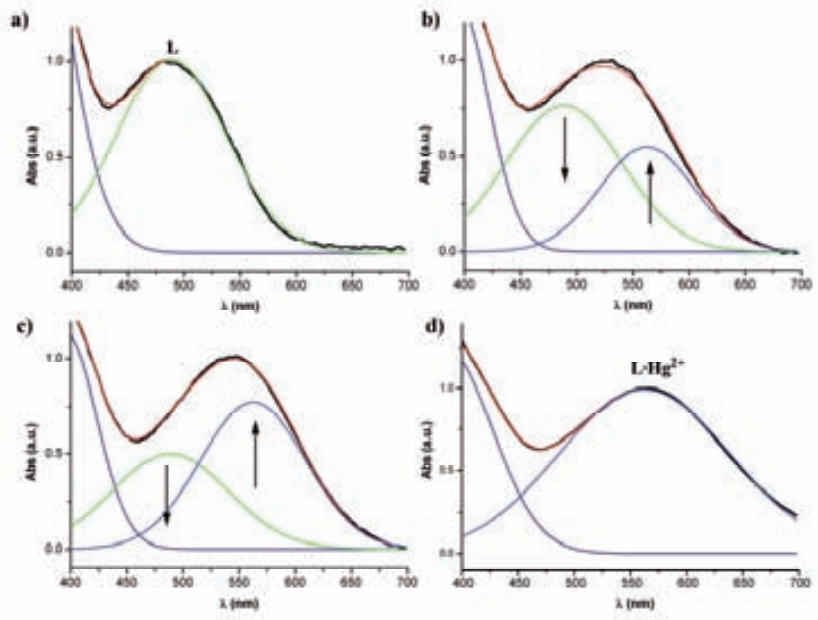

Figure 3. Deconvolution of the observed UV-Vis band in two Gaussian bands after soaking the cellulose paper into solution of increasing concentration of mercury ions: a) before soaking and after soaking with b) $7.5 \cdot 10^{-4}$ M, c) $2.5 \cdot 10^{-3}$ M, and d) $1.0 \cdot 10^{-2}$ M of Hg^{2+} in acetonitrile.

With this treatment a perfect image over the decreasing of the free ligand band and the increasing of the **1**·Hg^{2+}complex band upon increasing amounts of mercury ions is observed. Thus, measuring the area below the complex curve at each mercury concentration it has been possible to calibrate the cellulose-based optical indicator (Figure 4) with a high reproducibility. The detection limit of the presented mercury indicator papers is calculated by interpolation from the graph reaching a concentration limit down to tens of ppm.

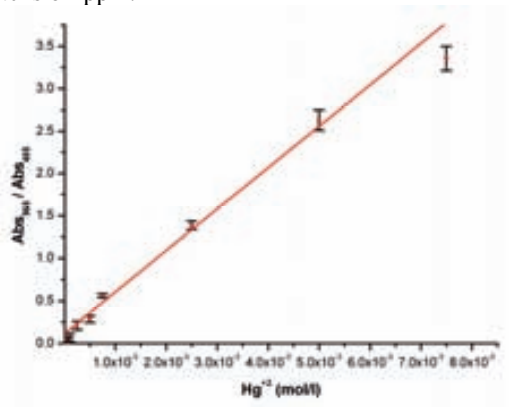

Figure 4. Calibration curve of the responses of the cellulose paper with **1** by fitting the area ratio data of the deconvoluted Gaussian bands (see Fig 3) with maxima at these two wavelengths - area(565nm)/area(485nm)- vs. the Hg^{2+} concentration. The error bars obtained from data replication at each concentration are also shown.

Further experiments with other divalent cations, like Mg^{2+}, Ca^{2+}, Ni^{2+}, Zn^{2+}, Cd^{2+}, Pb^{2+}, and Cu^{2+}, in CH_3CN/H_2O mixtures have also been performed showing a lack of any optical change of the indicator papers. This result demonstrates a high selectivity toward mercury ions of the reported cellulose-based optical indicator.

In summary, the developing of a new selective and highly sensitive heterogeneous indicator of mercury ions in acetonitrile-water solutions by the combined use of a cellulose substrate and a molecule with excellent detecting characteristics is presented. Depending on the amount of mercury ions in contact with the cellulose indicator papers a gradual color change is produced, being possible to determine by naked eye its concentration, with a detection limit of tens of ppm. Additionally, and no less important, this protocol takes advantage of surpassing the drawback of the low solubility in water of most of the reported Hg^{2+} chemosensors, allowing them to be used for detecting Hg^{2+} cations in water solutions. We are now working in order to decrease the detection limit down to ppb which is the limit acceptable for the EPA (United States Environmental Protection Agency) in potable water.

3. Experimental Section

The probes were fabricated with ALBET, 142 mm Ø, pore size 0.20μm regenerated cellulose mixted ester paper. ^1H and ^{13}C NMR spectra were recorded at 400 MHz on a Brucker AC400 spectrometer. The EI mass spectrum was recorded on a Fisons AUTOSPEC 500 VG spectrometer. Microanalyses was performed on a Carlo Erba 1108 instrument. The UV-Vis measurements were followed using a Shimadzu UV-2101 PC equipped with a reflectance absorption accessory (integrating sphere) and a Hitachi S-570 scanning electron microscope was used to perform SEM imaging of the samples. The camera used to take the pictures of the membranes was a Canon Power Shot A530 and Microsoft Paint software was used as a imaging treatment program.

3.1. Preparation of 1,4-diferrocenyl-2,3-diaza-1,3-butadiene.

To a solution of formylferrocene (0.250 g, 1.17 mmol) in ethanol (50 ml) hydrazine hydrate (28.3 ml, 0. 585 mmol) was dropped and the resulting solution was stirred at room temperature for 10 h. After cooling, the precipitated solid was filtered, air-dried and recrystallized from ethanol to give **1** as orange crystals in 70% yield. M. p. > 260 ºC (decomposes). ^1H NMR ($CDCl_3$): δ= 4.24 (10 H, s), 4.45 (4 H, st), 4.70 (4 H, st), 8.48 (2 H, s). ^{13}C NMR ($CDCl_3$): δ 68.6 (4xCH, Fc), 69.3 (10xCH, Fc), 70.9 (4xCH, Fc), 78.0 (2xq, Fc), 161.2 (2xCH=N). EIMS, m/z (%): 424 (M^+, 67), 211 (74), 184 (55), 121 (100). Anal Calc for $C_{22}H_{20}Fe_2N_2$: C, 62.31; H, 4.75; N, 6.61. Found: C, 62.55; H, 4.51; N, 6.88.

3.2. Preparation of the mercury ion indicator paper

Regenerated cellulose mixed ester paper with 0,2 μm pore size have been chosen as our fiber substrate due to its high surface porosity which gives a high surface coverage area to interact with the sensing molecule **1**, for the preparation of a mercury ion indicator paper. Preparation of the probes was carried out in several steps. Firstly the 40mm Ø disks of paper were introduced for 20s into acetonitrile solutions of different concentrations of $Hg(ClO_4)_2$ (from 10^{-6}M to 10^{-2}M). Then the paper was left to air dry for 40s and once dried, carefully introduced for 2s and immediately removed from a toluene

solution of **1** (10^{-3} M) and then homogeneously dried. Indeed, it is also possible to use acetonitrile/water mixtures (7:3, v/v) of $Hg(ClO_4)_2$ which is worth mentioning due to the fact that the possibility to use water environments for selective Hg^{+2} metal ion detection is one of the major drawbacks of most of the reported chemosensors.

Acknowledgements

This work was supported in part by the Ministerio de Educación y Ciencia (Spain), under the project ejeC-Consolider EMOCIONa (CTQ2006-06333/BQU) and CTQ 2004-02201 project, the European Science Foundation EUROCORES Programme SONS (project Fun-Smarts-2), the Generalitat de Catalunya (2005SGR00362), the Fundación Séneca (CARM) (02970/PI/05) and the Instituto de Salud Carlos III, through "Acciones CIBER". I.R. and A.C. are grateful to Ministerio Educación y Ciencia for a ''Ramón y Cajal'' contract and a predoctoral grant, respectively.

References and Notes

1. Boening, D. W. *Chemosphere* **2000**, *40*, 1335-1351.
2. Krishna, M. V. B.; Ranjit, M.; Karunasagar, D.; Arunachalam, J. *Talanta* **2005**, *67*, 70-80.
3. Clarkson, T. W.; Magos, L.; Myers, G. J. *N. Engl. J. Med.* **2003**, *349*, 1731-1737.
4. (a) Jiménez, D.; Martínez-Mañez, R.; Sancenón, F.; Soto, J. *Tetrahedron Lett*. **2004**, *45*, 1257-1259. (b) Caballero, A.; Martínez, R.; Lloveras, V.; Ratera, I.; Vidal-Gancedo, J.; Wurst, K.; Tárraga, A.; Molina, P.; Veciana, J. *J. Am. Chem. Soc.* **2005**, *127*, 15666 -15667.
5. (a) Choi, M. J.; Kim, M. Y.; Chang, S.-K. *Chem. Commun*. 2001, 1664-1665. (b) Tatay, S.; Gaviña, P.; Coronado, E.; Palomares, E. *Org. Lett.* **2006**, *8*, 3857-3860. (c) Coronado, E.; Galán-Mascarós, J. R.; Martí-Gastaldo, C.; Palomares, E.; Durrant, J. R.; Vilar, R.; Gratzel, M.; Nazeeruddin, Md. K. *J. Am. Chem. Soc.* **2005**, *127*, 12351-12356.
6. (a) Nolan, E. M.; Lippard, S. J. *J. Am. Chem. Soc.* **2003**, *125*, 14270-14271. (b) Ono, A.; Togashi, H. *Angew. Chem. Int. Ed.* **2004**, *43*, 4300-4302. (c) Guo, X.; Qiuan, X.; Jia, L. *J. Am. Chem. Soc.* **2004**, *126*, 2272-2273. (d) Hennrich, G.; Walther, W.; Resch-Genger, U.; Sonnenschein, H. *Inorg. Chem.* **2001**, *40*, 641-644. (e) Zhang, G.; Zhang, D.; Yin, S.; Yang, X.; Shuai, Z.; Zhu, D. *Chem. Commun.* **2005**, 2161-2162. (f) Wang, J. B.; Qian, X. H. *Org. Lett.* **2006**, *8*, 3721-3724. (g) Zhu, X. J.; Fu, S. T.; Wong, W. K.; Guo, H. P.; Wong, W. Y. *Angew. Chem. Int. Ed.* **2006**, *45,* 3150-3154. (h) Nolan, E. M.; Racine, M. E.; Lippard, S. *J. Inorg. Chem.* **2006**, *45*, 2742-2749. (i) Ko, S.-K.; Yang, Y.-J.; Tae, J.; Shin, I. *J Am Chem Soc* **2006**, *128*, 14150-14155., (j) Yoon, S.; Albers, A.; Wong, A. P.; Chang, C. J. *J Am Chem Soc* **2005**, *127*, 16030-16031 (k) Wu, D.; Huang, W.; Duan, C.; Lin, Z.; Meng, Q. *Inorg. Chem*. **2007**, *46*, 1538-1540.
7. (a) Nolan, E. M.; Racine, M. E.; Lippard, S. J. *Inor. Chem.* **2006**, *45*, 2742-2749. (b) Zhao, Y.; Zhong, Z. Q. *Org. Lett.* **2006**, *8*, 4715-4717. (c) Ou, S. J.; Lin, Z. H.; Duan, C. Y.; Zhang, H. T.; Bai, Z. P. *Chem. Commun*. **2006**, 4392-4392. (d) Meng, X. M.; Liu, L.; Hu, H. Y.; Zhu, M. Z.; Wang, M. X.; Shi, J.; Guo, Q. X. *Tetrahedron Lett.* **2006**, *47*, 7961-7964. (e) Ko, S. K.; Yang, Y. K.; Tae, J.; Shin, I. *J. Am. Chem. Soc.* **2006**, *128*, 14150-14155.
8. (a) Wang, X.; Drew, C.; Lee, S. H.; Senecal, K. J.; Kumar, J.; Samuelson, L. A. *Nano Lett.* **2002**, *2*, 1273-1275. (b) Metivier, R.; Leray, I.; Valeur, B. *Chem. Eur. J.* **2004**, *10*, 4480-4490.

9. (a) Palomares, E.; Vilar, R.; Durrant, J. R. *Chem. Commun*. **2004**, 362-363. (b) Liu, J.; Lu, Y. *J. Am. Chem. Soc*. **2004**, *126*, 12298-12298. (c) Liu, J.; Lu, Y. *Anal. Chem.* **2004**, *74*, 1627-1632. (d) Balaji, T.; El-Safty, S. A.; Matsunaga, H.; Hanaoka, T.; Mizukami, F. *Angew. Chem. Int. Ed.* **2006**, *45*, 7202-7208.
10. Mello, J. V.; Finney, N. S.; *J. Am. Chem. Soc*. **2005**, *127*, 10124-10125.
11. (a) Orellana, G.; Gomez-Carneros, A. M.; Dios, C. D.; Garcia-Martinez, A. A.; Moreno-Bondi, M. C. *Anal. Chem*. **1995**, *67*, 2231-2238. (b) Caminati, G.; Margheri, E.; Gabrielli, G. *Thin Solid Films* **1994**, *244*, 905-908. (c) Zheng, Y.; Orbulescu, J.; Ji, X.; Andreopoulos, M. F.; Pham, M. S.; Leblanc, M. R. *J. Am. Chem. Soc*. **2003**, *125*, 2680-2686. (d) Lee, S.-H.; Kumar, J.; Tripathy, S. K. *Langmuir* **2000**, *16*, 10482-10489. (e) Pearson, C.; Nagel, J.; Petty, M. C. *J. Phys. D: Appl. Phys.* **2001**, *34*, 285-291.
12. Klemm, D.; Heublein, B.; Fink, H-P.; Bohn, A. *Angew. Chem. Int. Ed.* **2005**, *44*, 3358-3393.
13. Martinez, A. W.; Phillips, S. T.; Butte, M. J.; Whitesides, G. M. *Angew. Chem. Int. Ed.* **2007**, *46*, 1318-1320.
14. Takahashi, Y.; Kasai, H.; Nakanishi, H.; Suzuki, T. M. *Angew. Chem. Int. Ed.* **2006**, *45*, 913-916.
15. Freudenberg, U.; Zimmermann, R.; Schmidt, K.; Behrens, S. H.; Ca. Wener *J. Colloid Interf. Sci*. **2007**, *309*, 360-365.

Nanocomposite membranes as highly selective and sensitive mercury(II) detectors

César Díez-Gil,[ab] Rosario Martínez,[c] Imma Ratera,[ab] Alberto Tárraga,[c] Pedro Molina*[c] and Jaume Veciana*[ab]

Received 15th January 2008, Accepted 26th February 2008
First published as an Advance Article on the web 13th March 2008
DOI: 10.1039/b800708j

A new solid-state membrane filter was prepared by filtering nanoparticles of a fluorophoric mercury(II) detecting molecule dispersed in water through a nanopore size cellulose membrane. By this method, nanoparticles are uniformly coated onto the membrane fibres to form a nanocomposite membrane for selective detection of mercury(II) ions in water allowing trace analysis—down to the ppb level—of this highly toxic metal.

1. Introduction

Mercury is a highly toxic element and its contamination has become severe in some parts of the world, resulting in health damage to their inhabitants.[1] Aquatic microorganisms can convert mercury ions into methylmercury, which subsequently bioaccumulates into the adipose tissues of fishes and marine mammals,[2] to be later spread out into the nutritional chain affecting, therefore, all the ecosystem. Methylmercury has a high potential neurotoxic activity and is involved in several mercury-pollution-related diseases[3] (*e.g.* prenatal brain damage, cognitive and motion disorders and Minamata disease). As a consequence of such risks mercury(II) ion levels in water are continually monitored by government agencies, and regulatory commissions are dictating increasingly stringent regulations for the maximum permitted limits of mercury ions in water. Thus, the United States Environmental Protection Agency (EPA) has dictated 2 ppb as an acceptable limit for mercury(II) ions in drinking water.[1]

In order to monitor continuously large and disperse water resources, efforts are being made in developing new, cheap, efficient, and selective solid mercury-sensing devices able to measure trace amounts of this heavy metal ion in water. An important number of those devices are based on molecules which can selectively recognize such metal ions and transduce their presence into an output signal, such as a change in the redox property,[4] or in their chromogenic[5] or fluorogenic[6,7] behaviours. Although there are several mercury detecting molecules, the number of those able to detect such an ion when supported on a solid substrate is very limited.[8] In addition, most of them have significant short-comings for their real application, such as a lack of selectivity, water insolubility, large structural complexity, and high price. Consequently, the development of practical, selective, sensitive, and reliable solid-state mercury sensors or detectors could represent a great advance for the *in situ* control of contaminated water, allowing therefore more effective remediation responses. One of the main problems found in this area is the firm fixation of mercury molecular probes on solid substrates. In order to solve this problem different methods such as Langmuir–Blodgett films,[9] covalent bonding[10] or composite formation have been assayed.[11] Nevertheless, severe disadvantages like the lack of sensitivity, the need of auxiliary additives, or complicated synthetic procedures are always found. Another simple procedure to deposit a mercury indicator molecule on a surface is the "dip-coating" method, which consists of soaking a solution of the molecule onto the surface of a solid support and drying the solvent. Although it is the easiest way of supporting molecules on solid substrates, the resulting lack of homogeneity and the ease of leakage of deposited molecules make the devices prepared with this method useless.

Herein we present a novel method for homogeneously supporting a mercury molecular indicator on commercial nanopore size membranes.[12] This method consists of the coating of a membrane surface by means of the filtration of an aqueous suspension of nanoparticles of the detecting molecule. Remarkably, this procedure promotes the coalescence of the suspended nanoparticles on the membrane surface yielding a nanocomposite membrane that can be used as a cheap analytical test filter for the highly selective and reliable quantitative detection of Hg^{2+} in water at concentrations down to the ppb level.

2. Results and discussion

For this study we chose 1-(4′-methoxyphenyl)-4-(1′-pyrenyl)-2,3-diaza-1,3-butadiene **1** as a fluorescent and highly selective mercury molecular probe since it detects mercury ions in aqueous environments (Fig. 1).[6] Upon complexation of the unsymmetrical azine **1** with the mercury ions, the lone pair of electrons of the nitrogen atom no longer participates in the quenching process of the fluorophoric pyrenyl group, causing the appearance of an intense fluorescence. Thus, addition of small amounts of Hg^{2+} ions to a solution of the indicator molecule dramatically increases the excimer emission band at 510 nm (see Fig. 1) and also changes its optical absorption properties.[6] Moreover, selectivity studies in solution towards Hg^{2+} showed no interaction of the compound with several other common

[a]*Institut de Ciència de Materials de Barcelona (CSIC)-CIBER-BBN, Campus Universitari, 08193 Bellaterra, Catalonia, Spain. E-mail: vecianaj@icmab.es; Fax: +34 93 5805729; Tel: +34 93 580 1853*
[b]*Networking Research Center on Bioengineering, Biomaterials and Nanomedicine (CIBER-BBN), Barcelona, Spain*
[c]*Departamento de Química Orgánica, Facultad de Química, Universidad de Murcia, Campus de Espinardo, 30100 Murcia, Spain*

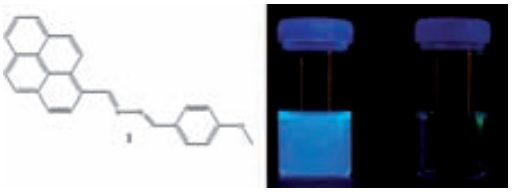

Fig. 1 Left: molecular structure of the unsymmetrical azine **1**. Right: fluorescence emission from an aqueous solution (CH_3CN–H_2O, 7 : 3) of the mercury molecular probe **1** with 1 equivalent of Hg^{2+} and without Hg^{2+} ions.

mono-, di-, and trivalent ions, like Li^+, Na^+, K^+, Mg^{2+}, Ca^{2+}, Cu^{2+}, Zn^{2+}, Cd^{2+}, Ni^{2+}, Pb^{2+}, Sm^{3+}, Eu^{3+}, Yb^{3+}, and Lu^{3+}.

The sensitivity and reproducibility of a detecting device based on molecules fixed on solid supports depend on several factors, such as the nature of the indicator molecule, the pathway through which the molecular probe interacts with the mercury ions present in water, the aggregation state of the molecules, the homogeneity and amount of compound deposited on the support, and the area of contact between the molecules and the solution containing the metal ion. Consequently, a key issue for developing a heterogeneous mercury detector with azine **1** is to achieve a firm and uniform coating of this signalling molecule onto an appropriate nanoporous membrane with a large surface area. This was achieved by a simple process that uses the "reprecipitation method"[13] for preparing aqueous nanodispersions of solid azine **1** and their deposition on the surface of a commercial membrane with *ca.* 100 nm pore size by filtering the suspensions through the membrane.

2.1 Prepartion of nanoparticles of the probe molecule

In order to control the homogeneity and the loading of azine **1** on the membranes, the use of nanoparticles with average diameters similar to those of the membrane pores was critical. It is important to mention here that the matching of pore sizes with the particle sizes, as well as the narrow polydispersity of the suspensions, played a key role in maximizing the loading of the membrane with the mercury detecting probe, as well as in attaining more homogeneous coatings. Particles with such characteristics allowed a deeper penetration of the indicator into the membrane, avoiding, at the same time, the clogging of the membrane pores. Consequently, the first goal was to find the experimental conditions to obtain particles of azine **1** with *ca.* 100 nm average diameters. Since sizes and size distributions of particles obtained with the reprecipitation method usually depend on external factors such as temperature, nature of the water-miscible organic solvent and the mixing efficiency of solvents,[14] these variables were tested by choosing two different water-miscible solvents and two distinct mixing procedures. Thus, nanoparticles suspended in water were obtained by dropping 100 μl of 10^{-3} M organic solutions (in THF or NMP) of azine **1** onto 10 ml of vigorously mixed ultra-pure water at a fixed temperature. Results and conditions of some representative experiments for obtaining aqueous suspensions of **1** are given in Table 1, entries 1–8.

Table 1 Experimental conditions and particle characteristics of azine **1** obtained by the reprecipitation method

		Mix. cond.			Particle diameter/ nm[b]			
Entry	Solv.[a]	Stirr.	Sonic.	*T*/K	10%	50%[c]	90%	ZP/mV[d]
1	NMP	Yes	No	298	91	171	342	−20
2	THF	Yes	No	298	91	249	825	−19
3	NMP	Yes	No	273	44	78	164	−14
4	THF	Yes	No	273	68	111	190	−22
5	NMP	No	Yes	298	91	222	295	−11
6	THF	No	Yes	298	142	267	342	−18
7	NMP	No	Yes	273	68	106	164	−25
8	THF	No	Yes	273	68	136	255	−21

[a] NMP, *N*-methylpyrrolidone; THF, tetrahydrofuran. [b] Volumetric particle size distributions, measured with dynamic light scattering technique are given as 10, 50, and 90% quantiles. [c] Values corresponding to the medians of the particle size distributions. [d] *Z*-potential values.

Dynamic light scattering (DLS) measurements of the obtained particle suspensions showed particle sizes between 80 and 250 nm with low polydispersities, the exact values of which depended on the conditions used for their preparation. Table 1 shows that lowering the temperature of the reprecipitation experiment promotes smaller particle sizes. This effect was also observed when the organic solvent was changed, obtaining smaller particle sizes for NMP than for THF. To check the influence of the mixing method of water and the organic solution of azine **1**, sonication and mechanical stirring were used. As is shown in Table 1, the particle sizes obtained with sonication are much larger than with mechanical stirring. Therefore, the latter procedure turns out to be much more efficient for mixing the two solutions, leading thereby to a faster nucleation process due to the antisolvent effect of water, where the azine **1** is not soluble. *Z*-Potential measurements were also performed for all obtained suspensions. In all cases, the absolute value obtained for *Z*-potentials was lower than 30 mV, which is indicative of the formation of unstable particle suspensions in water with a high tendency to aggregate with time.

2.2 Nanocomposite membranes loaded with azine 1

To achieve and maximize the loading of molecular probe inside the membrane, nanoparticle suspensions of azine **1** with *ca.* 100 nm mean sizes (entry 4, Table 1) were filtered through 100 nm pore size commercial membranes of different nature; *i.e.*, polycarbonate, nylon, polyester and mixed cellulose ester. Fig. 2 shows SEM images of the polycarbonate and mixed cellulose ester membranes coated with the molecular probe **1**. It is clear from Fig. 2a that particles of azine **1** were deposited on the top of the polycarbonate membrane as plate-like structures without any well-defined shapes, showing mean sizes that noticeably exceed those observed by the DLS technique. This result can be explained by the coalescence of the nanoparticles into larger plate-like particles instead of isolated deposition on the surface of the polycarbonate fibers. The tendency of such nanoparticles to aggregate during the filtration process is in good agreement with the low *Z*-potential values measured for their suspensions ($\leq$30 mV in all cases; Table 1) and could

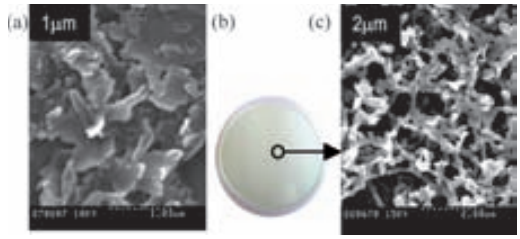

Fig. 2 (a) SEM image of a polycarbonate membrane surface after filtering a suspension of nanoparticles (entry 4, Table 1). (b) Photograph of a mixed cellulose ester membrane loaded by filtering a suspension of nanoparticles of **1** (entry 4, Table 1), showing an homogeneous light-green coloured surface due to the uniform distribution of the mercury indicator. (c) SEM image of a mixed cellulose ester membrane loaded with **1**, showing the high homogeneity of the coating of the fibres of cellulose.

probably be due to the lack of electrostatic repulsions between the particles. It is worth mentioning that most of filtered particles of the probe **1** were retained in the membrane since no particles were detected in the filtered water. Similar results were also obtained using other commercial 100 nm pore size synthetic membranes made of nylon and polyester. Coatings with characteristics very similar to those of the polycarbonate membrane were obtained, since all these synthetic organic membranes have similar morphological features, such as flat top surfaces. However, the coating process was considerably improved with a 100 nm pore size mixed cellulose ester membrane, because in this fibrillar membrane the filtered nanoparticles were retained in the membrane, not only by coalescing between them on the top of the membrane, but also around the cellulose fibers inside the membrane, as revealed by Fig. 2c.

Consequently, the deeper penetration of the nanoparticles into the pores yields a more efficient loading of the membrane, both at the top of its surface and inside, without blocking the pores of the filter, as occurs with the synthetic organic membranes. In addition, this loading procedure made it possible to get a more homogeneous coverage of the membrane. In order to study the influence of the amount of filtered nanoparticles through the membrane, increasing amounts of nanoparticle suspensions on a mixed cellulose ester membrane were filtered. Thus, 5, 10, 20 and 25 ml of a nanoparticle suspension of the indicator, prepared as previously described (entry 4, Table 1), were filtered through a mixed cellulose ester membrane with 100 nm pore size. SEM images (Fig. 3) show significant variations from an almost non-covered surface to a partially shuttered membrane, as the quantity of filtered nanoparticles was increased. The increase of the amount of filtered particles entailed an increase of the loading of the molecules that coat the membrane without blocking the pores. In highly loaded membranes the nanoparticles coalesce on the top of the membrane forming clearly visible plates as well as inside the membrane around its fibres (*vide infra*).

2.3 Hg^{2+} binding ability of nanocomposite membranes

An in-depth study of the binding ability of azine **1** to Hg^{2+} ions when the molecular probe is coating the fibres of the cellulose

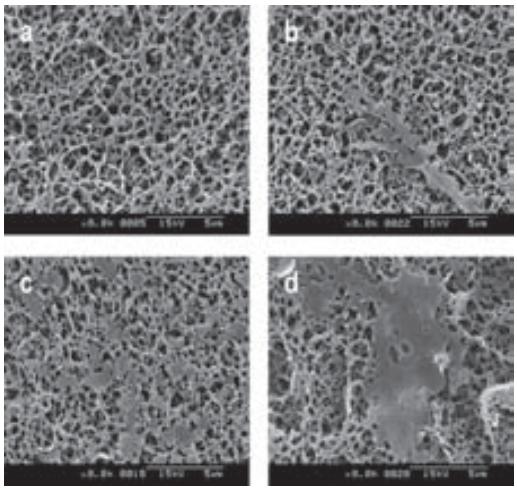

Fig. 3 SEM images of mixed cellulose ester membranes after filtering increasing amounts of nanoparticle suspension. Images a, b, c and d correspond, respectively, to the filtration of 5, 10, 20 and 25 ml of nanoparticle suspensions of the detecting molecule (entry 4, Table 1).

membrane, as well as the level of penetration of the detecting molecule inside the membrane, was undertaken by SEM imaging with mercury energy dispersive X-ray (EDX) analysis. This study was performed after filtering 10 ml of a 10^{-2} M $Hg(ClO_4)_2$ aqueous solution through the coated membrane, prepared by filtering 30 ml of nanoparticle suspension (entry 4, Table 1). The cross-sectional SEM image (see Fig. 4) indicate that solid azine **1** is able to complex Hg^{2+} ions from water and that the thickness of the layer where the mercury indicator is fixed is around 10 μm, as shown by the mercury peak of the EDX analysis. Thus, the composite membrane shows a remarkably concentrated region located at its surface containing the molecular probe **1**. Moreover, the layer of such molecules was firmly anchored to the membrane since it was not easy to remove from the membrane either by rubbing or by immersion in water, as revealed by optical microscopy and SEM. EDX analysis of

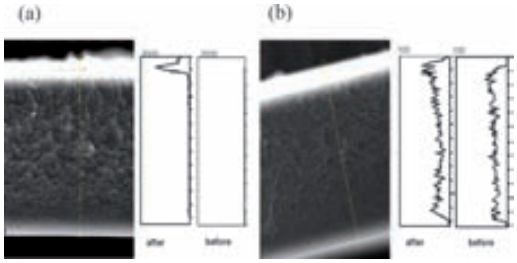

Fig. 4 Cross section image and SEM EDX images: (a) of a coated cellulose membrane with nanoparticle suspension of **1** after and before filtering 10 ml of 10^{-2} M mercury(II) aqueous solution and (b) of a dip-coated cellulose membrane with **1** after and before the treatment with a 10^{-2} M mercury(II) aqueous solution.

a cellulose membrane loaded with solid azine **1** by means of the dip-coating technique is also shown in Fig. 4 for comparison purposes. It is clear from Fig. 4 that there was a much higher mercury signal on the top of the membrane prepared by nanoparticle filtration compared to the dip-coated one. The latter membrane showed only a slight increase of the mercury signal along all the cross section, with slightly more intensity on the top and the bottom of the membrane. In addition, the line profile for the dip-coated membrane showed a mercury signal 200 times smaller than that obtained by nanoparticle filtration, which implies a poorer efficiency of the former method for coating the cellulose fibres.

Once the complexing ability of a mixed cellulose ester membrane coated with the probe **1** to Hg^{2+} ions in water was confirmed, the efficiency of these solid-state devices as potential mercury detectors was evaluated. For such a study, 100 ml of aqueous solutions with different concentrations of mercury(II) ions were filtered through the coated membranes. The interaction of the covering layer and the mercury ions should produce a change in the fluorogenic properties of the detector proportional to the concentration of mercury salt in each of the aqueous solutions. The luminescence of membranes was measured with a stereomicroscope, using an excitation wavelength of 360 nm and reading the emission at 420 nm. A digital camera was adapted for imaging the luminescence responses coming from the surfaces. Indeed, the resulting total luminescence of the membranes increased upon increasing of the concentration of mercury ions present in the analysed water (see Fig. 5), and a detection of mercury concentrations ranging from 1.0×10^{-8} M to 2.0×10^{-3} M was possible.

The total luminescence intensities measured for each assayed concentration were used to calibrate the response of the membranes to Hg^{2+} ions. Calibration curves in two different concentration ranges of mercury(II) ions were performed (Fig. 6).

Linearity of the luminescence responses with respect $\log[Hg^{2+}]$ were found for both concentration ranges, although the standard deviations were somewhat larger for the lower concentration range. Remarkable is the detection limit of 2 ppb of Hg^{2+} reached in these quantitative measurements. This amount matches the limit of mercury content of drinking water allowed by the EPA.[1] Even more outstanding is the fact that this lower limit can be decreased considerably by filtering two- or five-fold amounts of mercury solutions reaching limits well below 2 ppb of mercury ions in water.

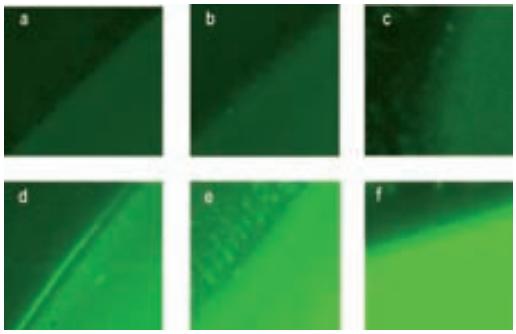

Fig. 5 Representative optical microscope fluorescence images of the contours of sensing membranes after filtration of 100 ml of aqueous solutions with concentrations of: (a) 0 M, (b) 10^{-6} M, (c) 10^{-5} M, (d) 10^{-4} M, (e) 10^{-3} M, and (f) 10^{-2} M of mercury(II) ions.

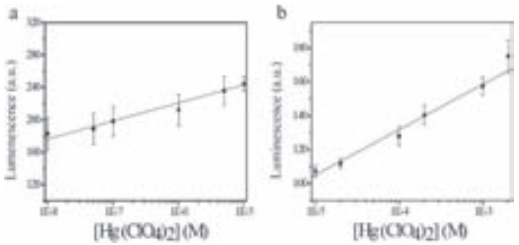

Fig. 6 Calibration curves of the luminescence responses to Hg^{2+} ions of sensing membranes after filtering 100 ml of aqueous mercury solutions with $[Hg(ClO_4)_2]$ concentrations between (a) 1.0×10^{-5} M and 1.0×10^{-8} M and (b) between 2.0×10^{-3} M and 1.0×10^{-5} M.

2.4 Selective detection of aqueous mercury(II) ions

Although selectivity studies previously made in CH_3CN–H_2O solutions showed no interaction of the probe molecule **1** with other cations normally present in drinking water,[6] further experiments were also carried out to confirm the absence of interference of other cations in the response of the cellulose-based detecting probes to mercury(II) ions. For this purpose 10 ml of 10^{-2} M aqueous solutions of salts of Na(I), K(I), Li(I), Mg(II), Ca(II), Ni(II), Zn(II), Cu(II), Cd(II), Co(II), Pb(II), Al(III), Cr(III) and also a mixture of all of them and tap water were filtered through the composite membrane. The luminescence intensity measurements of each assay are shown in Fig. 7, together with the resulting measurements after filtering different solutions with much lower concentrations (10 mL of 10^{-4} M solutions) of mercury(II) ions using different mercury salts to see if there was any influence of the counteranions (chloride, acetate, triflate,

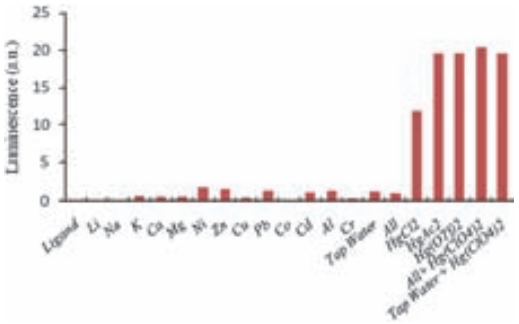

Fig. 7 Luminescence intensity measurements on the cellulose-based detecting membranes after filtering 10 ml of 10^{-2} M solutions of Li (I), Na(I), K(I), Ca(II), Mg(II), Ni(II), Zn(II), Cu(II), Pb(II), Cd(II), Co(II), Al(III), Cr(III) metallic salts. The influence of the counteranions of mercury(II) salts was also tested by filtering 10^{-4} M aqueous solutions of different mercury(II) salts.

and perchlorate). Although the concentrations of all tested cations were 100 times higher than those of Hg^{2+}, no significant increase of fluorescence signals was detected, proving the high selectivity of the developed mercury probe coated onto the membrane.

3. Conclusions

In conclusion, it has been demonstrated that the filtration of water-suspended nanoparticles of azine **1** through a nanoporous cellulose-based membrane provides a nanocomposite membrane that can be used as an analytical quantitative sensor able to selectively detect by fluorescence mercury(II) ions in water with a high sensitivity down to the ppb trace level. This practical, reliable, selective, and sensitive solid-state mercury detecting probe may represent a great advance for the *in situ* detection of contaminated water. Adaptation of the method herein reported to produce mercury sequestering materials that can be used as filters for remediation of contaminated water resources is in progress. It is possible to conclude that the results here described fill a void in the field of detection of mercury(II) ions in water that may provide advantageous for our environment.

4. Experimental

4.1 Nanocomposite membrane preparation

Nanoparticles were prepared by the reprecipitation method.[14] 100 μl of a 10^{-3} M THF or NMP solution of the mercury indicator molecule **1** were slowly dropped into 10 ml of vigorously stirred ultra-pure water. The antisolvent water effect, together with the miscibility of the tetrahydrofuran in water and the strong stirring, make possible the generation of the nanoparticle suspension. The coated membranes were prepared by vacuum filtering three times, at a flux of 35 ml min^{-1}, 10 ml of nanoparticle suspension of mercury detecting probe **1** (entry 4, Table 1) through a mixed cellulose ester (Advantec, Ø = 47 mm, 0.1 μm pore) yielding a final load of 2.4×10^{-8} mol cm^{-2} of molecular probe on the surfaces that were left to air dry.

4.2 Particle size studies

Particle size studies of the nanoparticles were performed using dynamic light scattering (DLS) (Malvern Nanosizer S). DLS measurements were performed at 25 °C using 1 ml of freshly prepared nanoparticle suspension (Table 1) into a disposable plastic cuvette. The temperature of the stirred water was maintained constant at 273 or 298 K with an external thermostatic bath.

4.3 Scanning electron microscopy

Imaging of coated membranes with mercury molecular probe **1** was performed using a scanning electron microscope (Hitachi S-570). Freshly prepared stripes were cut and metallised with gold for 3 minutes with a K550 Sputter Coater K250 Carbon Coating Attachment (Emitech, Ashford, U.K.) before the experiment was done.

4.4 Energy dispersive X-ray analysis composition studies

Cross section imaging and qualitative mercury(II) detection of coated membranes with mercury molecular probe **1** were carried out on a scanning electron microscope JEOL JSM-6300 (JEOL LDT, Tokyo, Japan) with a dispersive energy spectrometer EDX-LINK ISIS 200 (Oxford Instruments, Bucks, England). Freshly prepared stripes were cut and metallised with gold for 3 minutes with a K550 Sputter Coater K250 Carbon Coating Attachment (Emitech, Ashford, U.K.) before the experiment was done.

4.5 Dip coated membrane preparation

0.1 μm pore and 47 mm Ø (Advantec) mixed cellulose ester membranes were dipped for 10 seconds into a 1 mM dichloromethane solution of azine **1** and subsequently air dried. The freshly prepared indicator membranes were soaked in aqueous solutions of different concentrations (10^{-6} M to 10^{-3} M) of mercury(II) perchlorate and also air dried.

4.6 Luminescence measurements

Aqueous solutions of different concentrations (2.0×10^{-3} M and 1.0×10^{-8} M) of mercury perchlorate were vacuum filtered, at a flux of 35 ml min^{-1}, through the mercury molecular probe **1** coated membranes. Luminescence measurements were performed using a commercial luminescence stereomicroscope (Leica MLZIII) with an incorporated CCD digital camera (Leica DC 250). Images were then software treated (Metamorph)[15] acquiring thus the total luminescence intensity data from the images.

4.7 Selectivity measurements

10 ml of 10^{-2} M Na(I), K(I), Li(I), Mg(II), Ca(II), Ni(II), Zn(II), Cu(II), Cd(II), Co(II), Pb(II), Al(III), Cr(III) aqueous solutions were filtered through different membranes loaded with 30 ml of the mercury molecular probe **1** nanoparticle suspension (entry 4, Table 1), at a flux of 35 ml min^{-1}, and left to air dry. Luminescence studies of the resulting treated membranes were carried out as explained in Section 4.6. Moreover, 10 ml of 10^{-4} M of different mercury salts were used as positive tests.

Acknowledgements

This work was supported in part by the Ministerio de Educación y Ciencia (Spain), through the Consolider-C project EMOCIONa (CTQ2006-06333/BQU) and CTQ 2004-02201 project, the European Science Foundation EUROCORES Programme SONS (project Fun-Smarts-2), the Generalitat de Catalunya (2005SGR00362), Fundación Séneca (CARM) (02970/PI/05), and the Instituto de Salud Carlos III, through "Acciones CIBER". I.R. is grateful to Ministerio Educación y Ciencia for a "Ramón y Cajal" contract.

References

1 R. P. Mason, W. F. Fitzgerald and F. M. M. Morel, *Geochim. Cosmochim. Acta*, 1994, **58**, 3191; *United States Environmental Protection Agency Roadmap for Mercury*, 2006, EPA-HQ-OPPT-2005-0013.

2 D. W. Boening, *Chemosphere*, 2000, **40**, 1335; H. H. Harris, I. J. Pickering and G. N. George, *Science*, 2003, **301**, 1203; S. Jensen and A. Jernelov, *Nature*, 1969, **223**, 753.
3 P. Grandjean, P. Weihe, R. F. White, F. Debes, S. Araki, K. Yokohama, K. Murata, N. Sorensen, R. Dahl and P. J. Jorgensen, *Neurotoxicol. Teratol.*, 1997, **19**, 417; S. de Flora, C. Bennicelli and M. Bagnasco, *Mutat. Res.*, 1994, **317**, 57; P. B. Tchounwou, W. K. Ayensu, N. Ninashvili and D. Sutton, *Environ. Toxicol.*, 2003, **18**, 149; N. J. Langford and R. E. Ferner, *J. Hum. Hypertens.*, 1999, **13**, 651.
4 S. S. M. Hassan, M. B. Saleh, A. A. A. Gaber, R. A. H. Mekheimer and N. A. A. Kream, *Talanta*, 2000, **53**, 285; M. H. Mashhadizadeh and I. Sheikhshoaie, *Talanta*, 2003, **60**, 73.
5 E. Coronado, J. R. Galán-Mascarós, C. Martí-Gastaldo, E. Palomares, J. R. Durrant, R. Vilar, M. Gratzel and Md. K. Nazeeruddin, *J. Am. Chem. Soc.*, 2005, **127**, 12351; S. Tatay, P. Gavina, E. Coronado and E. Palomares, *Org. Lett.*, 2006, **8**, 3857; S. Y. Moon, N. R Cha, Y. H. Kim and S. K. Chang, *J. Org. Chem.*, 2004, **69**, 181; J. V. Ros-Lis, R. Martinez-Manez, K. Rurack, F. Sancenon, J. Soto and M. Spieles, *Inorg. Chem.*, 2004, **43**, 5183; L. Jae-Seung, H. Min Su and C. A. Mirkin, *Angew. Chem., Int. Ed.*, 2007, **46**, 4093; D. E. Wylie, L. D. Carlson, R. Carlson, F. W. Wagner and S. M. Schuster, *Anal. Biochem.*, 1991, **194**, 381.
6 A. Caballero, R. Martínez, V. Lloveras, I. Ratera, J. Vidal-Gancedo, K. Wurst, A. Tárraga, P. Molina and J. Veciana, *J. Am. Chem. Soc.*, 2005, **127**, 15666.
7 L. Prodi, C. Bargossi, M. Montaltí, N. Zaccheroni, N. Su, J. S. Bradshaw, R. M. Izatt and P. B. Savage, *J. Am. Chem. Soc.*, 2000, **122**, 6769; S. Yoon, A. E. Albers, A. P. Wong and C. J. Chang, *J. Am. Chem. Soc.*, 2005, **127**, 16030; E. M. Nolan and S. J. Lippard, *J. Am. Chem. Soc.*, 2003, **125**, 14270; Y. Zhao and Z. Zhong, *J. Am. Chem. Soc.*, 2006, **128**, 9988; A. Ono and H. Togashi, *Angew. Chem., Int. Ed.*, 2004, **43**, 4300; S. H Kim, J. S. Kim, S. M. Park and S. K. Chang, *Org. Lett.*, 2006, **8**, 371; K. C. Song, J. S. Kim, S. M. Park, K. C. Chung, S. Ahn and S. K. Chang, *Org. Lett.*, 2006, **8**, 3413; J. Wang, X. Qian and J. Cui, *J. Org. Chem.*, 2006, **71**, 4308; Y. Tang, M. Yu, F. Feng, L. An, H. Sun, S. Wang, Y. Li and D. Zhu, *Macromol. Rapid Commun.*, 2006, **27**, 389; E. M. Nolan and S. J. Lippard, *J. Mater. Chem.*, 2005, **15**, 2778; E. M. Nolan, M. E. Racine and S. J. Lippard, *Inorg. Chem.*, 2006, **45**, 2742; Y. Yu, L. R. Lin, K. B. Yang, X. Zhong, R. B. Huang and L. S. Zheng, *Talanta*, 2006, **69**, 103; O. Selifonova, R. Burlage and T. Barkay, *Appl. Environ. Microbiol.*, 1993, **59**, 3083; Z. G. Can-Cheng, L. Zhi-Zhang, S. Guo-Li and Y. Ru-Qin, *Anal. Chem.*, 2002, **74**, 821; M. Matsushita, M. M. Meijler, P. Wirsching, R. A. Lerner and K. D. Janda, *Org. Lett.*, 2005, **7**, 4943.
8 I. Oehme and O. S. Wolfbeis, *Microchim. Acta*, 1997, **126**, 177; Z. Xiao-Bing, G. Can-Cheng, L. Zhi-Zhang, S. Guo-Li and Y. Ru-Qin, *Anal. Chem.*, 2002, **74**, 821; I. Murkovic and O. S. Wolfbeis, *Sens. Actuators, B*, 1997, **38–39**, 246; M. K. Nazeeruddin, D. Di Censo, R. Humphry-Baker and M. Grätzel, *Adv. Funct. Mater.*, 2006, **16**, 189; G. Orellana, A. M. Gómez-Carneros, C. de Dios, A. A. Garcia-Martínez and M. C. Moreno-Bondi, *Anal. Chem.*, 1995, **67**, 2231; C. Díez-Gil, A. Caballero, I. Ratera, A. Tárraga, P. Molina and J. Veciana, *Sensors*, 2007, **7**, 3481.
9 G. Caminati, E. Margheri and G. Gabrielli, *Thin Solid Films*, 1994, **244**, 905; Y. Zheng, J. Orbulescu, X. Ji, M. F. Andreopoulos, M. S. Pham and M. R. Leblanc, *J. Am. Chem. Soc.*, 2003, **125**, 2680.
10 N. M. Hanumegowda, I. M. White and F. Xudong, *Sens. Actuators, B*, 2006, **120**, 207; T. Balaji, M. Sasidharan and H. Matsunaga, *Analyst*, 2005, **130**, 1162; A. A. Ensafi and M. Fouladgar, *Sens. Actuators, B*, 2006, **113**, 88; Y. Tang, F. He, M. Yu, F. Feng, L. An, H. Sun, Y. Li and D. Zhu, *Macromol. Rapid Commun.*, 2006, **27**, 389.
11 H. M. Rowe, W. Y. Xu, J. N. Demas and B. A. DeGraff, *Appl. Spectrosc.*, 2002, **56**, 167; H. Chun-Lian, R. Feng-Lian, Z. Xiao-Bing and H. Zhi-Xiang, *Talanta*, 2006, **70**, 364; L. Soo-Hyoung, J. Kumar and S. K. Tripathy, *Langmuir*, 2000, **16**, 10482; N. A. Gavrilenko, N. V. Saranchina and G. M. Mokrousov, *J. Anal. Chem.*, 2007, **62**, 923; N. L. Dias-Filho and D. Ribeirio-do-Carmo, *Talanta*, 2006, **68**, 919; X. Liu, Y. Tang, L. Wang, J. Zhang, S. Song, C. Fan and S. Wang, *Adv. Mater.*, 2007, **19**, 1471; M. K. Nazeeruddin, D. di-Censo, R. Humphry-Baker and M. Grätzel, *Adv. Funct. Mater.*, 2006, **16**, 189; C. Cano-Raya, M. Dm Dernández-Ramos, J. Gómez-Sánchez and L. F. Capitán-Vallvey, *Sens. Actuators, B*, 2006, **117**, 135.
12 J. Veciana, I. Ratera, C. Díez-Gil, P. Molina, A. Tárraga, R. Martínez, A. Caballero and F. Zapata, Spanish Patent, ES 200603285, 2006.
13 F. Hong-Bing and Y. Jian-Nian, *J. Am. Chem. Soc.*, 2001, **123**, 1434; H. S. Nalwa, H. Kasai, S. Okada, H. Oikawa, H. Matsuda, A. Kakuta, A. Mukoh and H. Nakanishi, *Adv. Mater.*, 1993, **5**, 758; E. Van Keuren, E. Georgieva and J. Adrian, *Nano Lett.*, 2001, **1**, 141.
14 Y. Zheng, J. Orbulescu, X. Ji, M. F. Andreopoulos, M. S. Pham and M. R. Leblanc, *J. Am. Chem. Soc.*, 2003, **125**, 2680; Y. Takahashi, H. Kasai, H. Nakanishi and T. M. Suzuki, *Angew. Chem., Int. Ed.*, 2006, **45**, 913; H. Kasai, H. S. Nalwa, S. Oikawa, H. Matsuda, N. Minami, A. Kakuta, K. Ono, A. Muco and H. Nakanishi, *Jpn. J. Appl. Phys.*, 1992, **31**, 1132.
15 Image analysis software: *Metamorph 7.5*, Universal Imaging, 2007.

(12) SOLICITUD INTERNACIONAL PUBLICADA EN VIRTUD DEL TRATADO DE COOPERACIÓN EN MATERIA DE PATENTES (PCT)

(19) Organización Mundial de la Propiedad Intelectual
Oficina internacional

(43) Fecha de publicación internacional
8 de julio de 2010 (08.07.2010)

PCT

(10) Número de Publicación Internacional
WO 2010/076361 A1

(51) Clasificación Internacional de Patentes:
C12P 21/02 (2006.01) *C07K 14/00* (2006.01)
C12N 15/62 (2006.01)

(21) Número de la solicitud internacional:
PCT/ES2009/070616

(22) Fecha de presentación internacional:
22 de diciembre de 2009 (22.12.2009)

(25) Idioma de presentación: español

(26) Idioma de publicación: español

(30) Datos relativos a la prioridad:
P200900045
30 de diciembre de 2008 (30.12.2008) ES

(71) Solicitantes *(para todos los Estados designados salvo US)*: **CONSEJO SUPERIOR DE INVESTIGACIONES CIENTÍFICAS** [ES/ES]; C. de Serrano, 117, E-28006 Madrid (ES). **UNIVERSITAT AUTÒNOMA DE BARCELONA** [ES/ES]; Edifici A - Campus Universitari, E-08193 Bellaterra, Bercelona (ES). **CENTRO DE INVESTIGACIÓN BIOMÉDICA EN RED EN BIOINGENIERIA, BIOMATERIALES Y NANOMEDICINA** [ES/ES]; C. Maria de Luna, 11, Módulo 3, E-50018 Zaragoza (ES).

(72) Inventores; e

(75) Inventores/Solicitantes *(para US solamente)*: **VECIANA MIRO, Jaume** [ES/ES]; C. de Serrano, 117, E-28006 Madrid (ES). **RATERA BASTARDAS, Inmaculada** [ES/ES]; C. de Serrano, 117, E-28006 Madrid (ES). **DÍEZ GIL, César** [ES/ES]; C. de Serrano, 117, E-28006 Madrid (ES). **VILLAVERDE CORRALES, Antonio Pedro** [ES/ES]; Campus UAB, E-08193 Bellaterra, Barcelona (ES). **VÁZQUEZ GÓMEZ, Esther** [ES/ES]; Campus UAB, E-08193 Bellaterra, Barcelona (ES). **GARCÍA FRUITÓS, Elena** [ES/ES]; C. Maria de Luna, 11, Módulo 3, E-50018 Zaragoza (ES).

(74) Mandatario: **PONTI SALES, Adelaida**; C. Consell de Cent, 322, E-08007 Barcelona (ES).

(81) Estados designados *(a menos que se indique otra cosa, para toda clase de protección nacional admisible)*: AE, AG, AL, AM, AO, AT, AU, AZ, BA, BB, BG, BH, BR, BW, BY, BZ, CA, CH, CL, CN, CO, CR, CU, CZ, DE, DK, DM, DO, DZ, EC, EE, EG, ES, FI, GB, GD, GE, GH, GM, GT, HN, HR, HU, ID, IL, IN, IS, JP, KE, KG, KM, KN, KP, KR, KZ, LA, LC, LK, LR, LS, LT, LU, LY, MA, MD, ME, MG, MK, MN, MW, MX, MY, MZ, NA, NG, NI, NO, NZ, OM, PE, PG, PH, PL, PT, RO, RS, RU, SC, SD, SE, SG, SK, SL, SM, ST, SV, SY, TJ, TM, TN, TR, TT, TZ, UA, UG, US, UZ, VC, VN, ZA, ZM, ZW.

(84) Estados designados *(a menos que se indique otra cosa, para toda clase de protección regional admisible)*: ARIPO (BW, GH, GM, KE, LS, MW, MZ, NA, SD, SL, SZ, TZ, UG, ZM, ZW), euroasiática (AM, AZ, BY, KG, KZ, MD, RU, TJ, TM), europea (AT, BE, BG, CH, CY, CZ, DE, DK, EE, ES, FI, FR, GB, GR, HR, HU, IE, IS, IT, LT, LU, LV, MC, MK, MT, NL, NO, PL, PT, RO, SE, SI, SK, SM, TR), OAPI (BF, BJ, CF, CG, CI, CM, GA, GN, GQ, GW, ML, MR, NE, SN, TD, TG).

Declaraciónes según la Regla 4.17:

— *sobre la identidad del inventor (Regla 4.17(i))*

— *sobre el derecho del solicitante para solicitar y que le sea concedida una patente (Regla 4.17(ii))*

— *sobre la calidad de inventor (Regla 4.17(iv))*

Publicada:

— *con informe de búsqueda internacional (Art. 21(3))*

(54) **Title**: INCLUSION BODIES, BACTERIAL CELLS AND COMPOSITIONS CONTAINING THEM AND USES THEREOF

(54) **Título** : CUERPOS DE INCLUSIÓN, CÉLULAS BACTERIANAS Y COMPOSICIONES QUE LOS CONTIENEN Y SUS USOS

(57) **Abstract**: The present invention relates to an isolated inclusion body comprising a polypeptide, characterised in that such inclusion body is in particulate form. The present invention also refers to a bacterial cell comprising said inclusion body. The present invention additionally refers to a composition comprising said inclusion body and a eukaryotic cell. The present invention moreover refers to a composition comprising said inclusion body and animal or plant tissue. The present invention furthermore refers to the uses of said inclusion body as medicaments and cell-proliferation stimulators and tissue regenerators.

(57) **Resumen**: La presente invención se refiere a un cuerpo de inclusión aislado que comprende un polipéptido caracterizado porque el cuerpo de inclusión está en forma particulada. La presente invención también se refiere a una célula bacteriana que comprende dicho cuerpo de inclusión. La presente invención se refiere además a una composición que comprende dicho cuerpo de inclusión y una célula eucariota. La presente invención se refiere también a una composición que comprende dicho cuerpo de inclusión y un tejido de animal o planta. La presente invención se refiere también a los usos de dicho cuerpo de inclusión como medicamentos y estimuladores de la proliferación celular y regeneradores de tejido.

WO 2010/076361 A1

Biomaterials 31 (2010) 5805–5812

Contents lists available at ScienceDirect

Biomaterials

journal homepage: www.elsevier.com/locate/biomaterials

The nanoscale properties of bacterial inclusion bodies and their effect on mammalian cell proliferation

César Díez-Gil [a,b], Sven Krabbenborg [a], Elena García-Fruitós [b,c], Esther Vazquez [b,c,d], Escarlata Rodríguez-Carmona [b,c], Imma Ratera [a,b], Nora Ventosa [a,b], Joaquin Seras-Franzoso [b,c,d], Olivia Cano-Garrido [b,c], Neus Ferrer-Miralles [b,c,d], Antonio Villaverde [b,c,d,*], Jaume Veciana [a,b,*]

[a] Departament de Nanociència Molecular i Materials Orgànics. Institut de Ciència de Materials de Barcelona (ICMAB-CSIC), Bellaterra, 08193 Barcelona, Spain
[b] Networking Research Centre on Bioengineering, Biomaterials and Nanomedicine, CIBER-BBN, 08193 Barcelona, Spain
[c] Institut de Biotecnologia i de Biomedicina, Universitat Autònoma de Barcelona, Bellaterra, 08193 Barcelona, Spain
[d] Department of Genetics and Microbiology, Universitat Autònoma de Barcelona, Bellaterra, 08193 Barcelona, Spain

ARTICLE INFO

Article history:
Received 23 February 2010
Accepted 4 April 2010
Available online 8 May 2010

Keywords:
Inclusion bodies
Cell growth
Nanoparticles
Stiffness
Wettability
Tissue engineering

ABSTRACT

The chemical and mechanical properties of bacterial inclusion bodies, produced in different *Escherichia coli* genetic backgrounds, have been characterized at the nanoscale level. In regard to wild type, DnaK$^-$ and ClpA$^-$ strains produce inclusion bodies with distinguishable wettability, stiffness and stiffness distribution within the proteinaceous particle. Furthermore it was possible to observe how cultured mammalian cells respond differentially to inclusion body variants when used as particulate materials to engineer the nanoscale topography, proving that the actual range of referred mechanical properties is sensed and discriminated by biological systems.

The data provide evidence of the mechanistic activity of the cellular quality control network and the regulation of the stereospecific packaging of partially folded protein species in bacteria. This inclusion body nanoscale profiling offers possibilities for their fine genetic tuning and the resulting macroscopic effects when applied in biological interfaces.

1. Introduction

Inclusion bodies are non-enveloped and mechanically stable nanoparticulate entities mainly constituted by proteins, which are generated in vivo during the production and further deposition of a wide catalogue of recombinant polypeptides [1]. Early after the implementation of recombinant DNA technologies in both pharma and biotech industries, the formation of inclusion bodies has been observed as a major obstacle in protein production processes [1,2], as important amounts of target polypeptides commonly precipitate as such water-insoluble protein clusters. For long, inclusion bodies have been seen as undesirable by-products to be discarded for further application, as believed to be formed by misfolded, nonfunctional polypeptides escaping the cell's quality control machinery [2]. However, a dramatic turn in the understanding of the bacterial control of protein aggregation at the cell systems level has recently shown inclusion bodies as formed by properly folded, functional species [3] that are not excluded from cell surveillance regarding their conformational quality [4,5]. This has prompted the straightforward use of inclusion bodies formed by enzymes in different kind of catalytic processes [6]. In addition, inclusion bodies have shown to possess an unexpected amyloid-based molecular architecture structurally comparable to that observed in eukaryotic amyloids [7].

At a nanoscale level, inclusion bodies are pseudo-spherical, quite pure proteinaceous particles ranging from around 50–500 nm [8]. Their mechanical stability is high enough to preserve the integrity and morphology upon mechanical, chemical and enzymatic cell disruption (or combined treatments) and upon long term storage under different conditions, including lyophilisation [9]. Being the size of inclusion bodies within the range of mammalian cell micro- and nano-environment topology influencing mammalian cell proliferation, random surface decoration and patterning with inclusion bodies has a significant and positive impact on cell growth, making them promising biomaterials for tissue engineering [9]. Despite their enormous potential as non-cytotoxic nanomaterials producible by cost effective, scalable procedures, the chemical and mechanical properties of inclusion

* Corresponding authors. Networking Research Centre on Bioengineering, Biomaterials and Nanomedicine, CIBER-BBN, 08193 Barcelona, Spain. Tel.: +34 935801853; fax: +34 935805729.
E-mail addresses: Antoni.Villaverde@uab.cat (A. Villaverde), vecianaj@icmab.es (J. Veciana).

0142-9612/$ – see front matter © 2010 Elsevier Ltd. All rights reserved.
doi:10.1016/j.biomaterials.2010.04.008

bodies remain essentially unexplored. In this regard, only some bibliographic references to their density [10], hydratation level [11] and pH responsiveness [12] are available. For that, we have here approached the physicochemical characterization of *Escherichia coli* inclusion body materials regarding surface chemistry and nanoscale mechanical properties, such as stiffness or hydrophobicity, which might be critical in inclusion body–cell interactions.

2. Materials and methods

2.1. Materials

All materials used are displayed on the Supplementary information.

2.2. Methods

2.2.1. IB's size and Z potential determination by dynamic light scattering (DLS)

The particle sizes and Z potential of IB were determined in a dynamic light scattering (DLS) device (Malvern Nanosizer Z), in suspension on PBS buffer (pH = 7.4, IB final concentration was 20 μg/mL). To facilitate the dispersion on the liquid, 2 mL of the mixture were sonicated for 1 min. DLS measurements were carried out at 37 °C using 1 mL of freshly prepared IBs suspension into a disposable plastic cubette. Each IBs sample was analyzed by triplicate averaging thirty single measurements.

2.2.2. Mixed thiol self assembled monolayer preparation

Different molar ratios of hydrophilic (−OH terminated) and hydrophobic ($-CH_3$ terminated) alkanethiols were used to obtain mixed self assembled monolayers (SAMs) with different degree of hydrophobicity, as shown by static contact angle measurements (Table S1). SAMs with different proportions of 1-undecenethiol ($-CH_3$ terminated) and 11- mercapto-1-undecanol (−OH terminated) were prepared by immersion of the freshly cleaned gold substrates in an ethanolic solution of the organic thiols with the appropriate molar ratio for 24 h. Thus, substrates were rinsed with clean ethanol and sonicated for 5 min in ethanol to remove the physisorbed molecules. Afterwards the substrates were dried under a stream of N_2 and immediately used (see SI).

2.2.3. Contact angle measurements

Wettability of the self assembled monolayer of the mixed thiols before and after being in contact with IBs was determined with an OCA 15+ (Dataphysics, Germany) contact angle goniometer. Data treatment and angle determination were carried out with the software SCA20 (Dataphysics, Germany). Four sets of static contact angles, at different positions on each sample, were measured (see SI).

2.2.4. Coverage of IBs on the mixed SAMs

Freshly prepared mixed monolayers of the thiols were immersed for 2 h into an IB suspension in PBS buffer (IB suspension was sonicated for 5 min prior to the introduction of the substrate). Afterwards, the IBs' covered substrates were gently rinsed with MiliQ water (18.2 MΩ) and dried under a stream of N_2.

Optical fluorescence microscope images of the deposited IBs were performed using an OLYMPUS Bx51 microscope with an OLYMPUS DP20 camera with 3 s shutter time, and an OLYMPUS U-RFL-T mercury lamp accessory. In order to remove background light a GFP pass filter was used. ImageJ (GNU) software was utilized to perform the particle counting.

2.2.5. Atomic force microscopy (AFM)

2.2.5.1. AFM imaging. Atomic force microscopy (AFM) images were taken with a commercial AFM (MFP-3D-SA, Asylum Research, Santa Barbara, USA). Samples were analyzed in dynamic mode working at 8 kHz of frequency and in a liquid environment (PBS buffer media pH = 7.4) in order to mimic the cytoplasmic environment of the cell. Pyramidal NSC35/AlBS silicon tips (Mikromash, USA) having nominal spring constants of 0.28 N/m were used. Sample preparation was done by drop casting of an IBs suspension in the same PBS buffer (20 μg/mL) over freshly cleaved mica.

2.2.5.2. AFM force spectroscopy. AFM indentation measurements were done with a commercial AFM (MFP-3D-SA, Asylum Research, Santa Barbara, USA) equipped with a close loop tracking system and working on liquid environment. Pyramidal NSC35/AlBS silicon tips (Mikromash, USA) having nominal spring constants of 0.28 N/m were used. The spectroscopic calibration of the raw cantilever on liquid media (PBS buffer solution pH = 7.4) was developed by measuring force vs. distance curves, on freshly cleaved mica. Sample preparation was done by drop casting of an IB suspension in the same PBS buffer (20 μg/mL) over freshly cleaved mica. The force curves, consisting of 2048 data points were obtained imposing a maximum applied force of 50 nN at a frequency of 8 kHz. AFM mechanical properties data were calculated from force distance curves according to the procedures described in [13,14] (see SI).

In order to achieve spatial resolution of the spectroscopical measurements, dynamic AFM images of the studied IBs were developed prior and after force vs. distance measurements. Therefore observations allowed us to follow any movement or deformation produced on the sample during the experiment.

2.2.6. Cell proliferation assay

IBs produced and purified from different bacterial strains were sterilized by exposure to a 253 nm UV light germicidal lamp for 4 h. The IBs were resuspended in PBS, and 2.65×10^8 IBs (particles) were added per well to coat untreated Costar 3370 plates, which were left overnight at 4 °C. Wells were washed in PBS and blocked with 3% BSA in PBS for 1 h at 37 °C. Afterwards, 3×10^3 newborn hamster kidney (BHK) cells or 2×10^4 rat pheochromocytoma (PC12) cells were added per well and incubated in Dulbecco's Modified Eagle's Medium (DMEM) supplemented with nonessential amino acids and fetal calf serum (5%), at 37 °C for different times. Blank wells underwent exactly the same treatment as described but without IBs. After incubation, cell proliferation was determined using the EZ4U kit (Biomedica GmbH) following the manufacturer's instructions, and analyzed in the multilabel reader iEMS MF (Labsystems, Helsinki, Finland). The reading absorbances were 450 nm and 620 nm as reference, and the values were standardized with respect to medium-containing wells. A pre-test to select incubation time before saturation was carried out with the kit reagents. All assays were done in triplicate. Data were expressed as the mean ± standard error of the mean (SEM) of the values obtained per condition and evaluated statistically by a *T*-test analysis. Cultured cell pictures under different conditions were taken with a Nikon Eclipse TS100 inverted microscope by using NIS-Elements F 3.00 imaging software.

3. Results

Recent studies on the functionality and applications of IBs have shown their enormous potential, not only from the industrial catalysis point of view, but also in the field of biomaterials [9]. In this regard, IB-decorated or IB-patterned surfaces provide an appropriate topological environment for mammalian cell proliferation [9]. Nevertheless, despite their promising properties as non-cytotoxic and particulate materials, very little is still known about their chemical and physical nanoscale properties [5,15] and how their rational modification at this scale may influence their macroscopic impact on living cells in IB-cell interfaces.

To deeper explore these issues, we have characterized IBs produced in a conventional K-12 wild type (wt) *E. coli* strain, and in derived genetic backgrounds showing deficiencies in the protein quality control network, that is known to regulate, at the systems level, not only protein folding but also aggregation. For that, we have chosen two paradigm mutations affecting different arms of the quality control system, resulting in deficiencies of either DnaK (the main cytosolic chaperone and negative regulator of the heat shock system) or ClpA (foldase and ATPase of the protease ClpP). In these mutants, IBs are distinguishable from those produced in wt cells, in size and biological activity of the embedded proteins [16]. Therefore, we presumed that surface chemistry and mechanical properties of IBs might be eventually affected in these strains.

3.1. Study of the hydrophilic/hydrophobic nature of the IB

Model surfaces with known physicochemical properties have been widely employed for studying not only material surface properties but also complex events such as protein adsorption or cellular responses. Previous studies have already shown how of different surface chemical properties entail variations on the macroscopic behavior of a biomaterial [17], being those related with changes on the chemical charge or material wettability among the most influencing [18,19].

In order to study the wettability properties of IB variants (namely those produced in $DnaK^-$ or $ClpA^-$ mutants vs wt strain), six SAMs on gold substrates were obtained by functionalizing them with different molar ratios (X) of −OH terminated (hydrophilic) and $-CH_3$ terminated (hydrophobic) alkanethiols. As a result, an array of modified gold surfaces bearing controlled contact angles,

ranging from 110 to 20°, were fabricated (see Materials and methods section).

Subsequently, the arrays were immersed in suspensions (20 μg/mL) of IB variants for 2 h and contact angle and IB coverage of the different functionalized gold substrates (X_{OH}) were determined before and after IB deposition. While prior to IB deposition, an increase of 10% in the concentration of the hydroxyl terminated thiol with respect to the $-CH_3$ terminated ones, implied a decrease of 6 ± 1° on the contact angle of the functionalized surface, the measurements performed after the deposition of IBs presented a much smaller reduction (Fig. 1, left). This fact was more intense for $DnaK^-$ and $ClpA^-$ IBs where the decrement was 2.4 ± 0.8 and 1.9 ± 0.5° (Fig. 1b, c left) respectively, than for wt IBs where the diminution was of 4.5 ± 0.8° (Fig. 1a, left). Thus, the presence of IBs on the functional surface, buffers the change of wettability of the substrate at different extent.

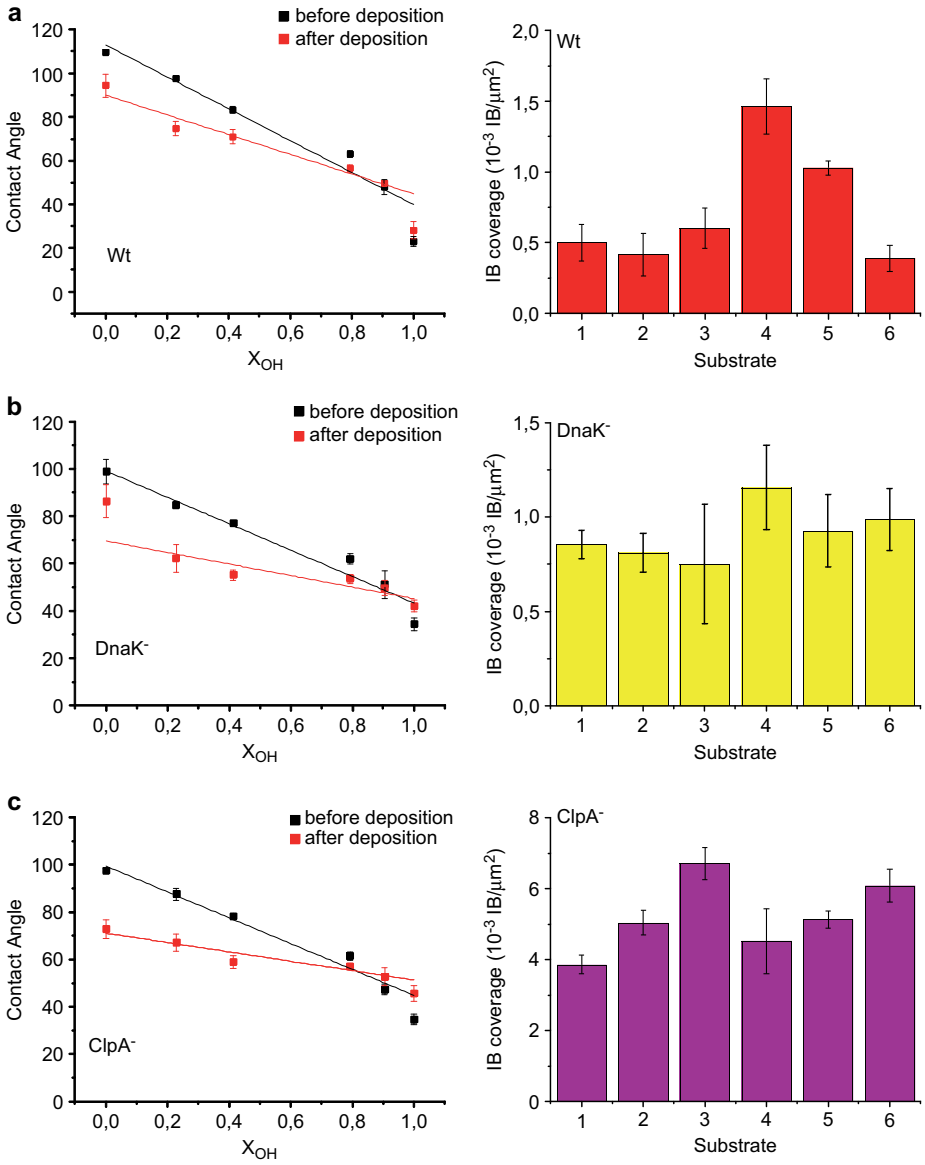

Fig. 1. Left; Contact angles of the 6 different functionalized, containing different molar ratio of −OH terminated (X_{OH}) alkanethiols, gold surfaces before and after deposition of IBs. Right: Dependence of the IB's coverage on the functionalized gold substrate wettability a) Wt, b) $DnaK^-$, c) $ClpA^-$. Substrate wettability ranging from 20 to 30° (1), 40–50° (2), 60–70° (3), 70–80° (4), 80–90° (5) and 100–110° (6).

IB surface coverage dependence with the substrate contact angle was also determined by measuring the density of aggregates per μm^2 using a optical fluorescence microscope. Results obtained for wt IBs (Fig. 1a, right) showed the existence of a maximum of IB coverage reaching absolute values of 0.0015 IB/μm^2, corresponding to a functionalized gold surface contact angle of approximately 80°. Therefore, it is possible to establish a preference of these materials to join slightly hydrophobic surfaces. On the other hand, data obtained from DnaK$^-$ and ClpA$^-$ IBs (Fig. 1b, c right, respectively) exhibited significantly different tendencies. In both cases, the maximum of interaction was slightly shifted to lower contact angles (75 and 60°, respectively) and a gradual increase of the covering of IBs on the modified surfaces at high contact angles (>90°) could also be observed, pointing to the existence of more amphiphilic behaviors of the DnaK$^-$ and ClpA$^-$ IB surfaces. Thus, it is possible to observe how, by changing the IB variant, the substrate contact angle coverage dependence varies from monomodal, with a single maximum at 80° (wt), to bimodal, with two peaks, one at lower angles (75° and 60°) and the other one at higher values (>90°), for DnaK$^-$ and ClpA$^-$ respectively, indicating the existence of two different wettability populations. However, looking at the absolute IBs adsorption values, DnaK$^-$ IBs showed extreme similarity to those obtained with wt IBs, reaching a maximum coverage of 0.0012 IB/μm^2, while ClpA$^-$ IBs depict coverage levels up to 5 times higher (0.007 IB/μm^2). This fact is of extreme importance, as an increase on the IBs density entails the subsequent increase of roughness of the treated surface, usually related to cell proliferation properties modification [20]. Therefore, it was possible to establish that the wettability of the IB surfaces is dependent of the genetic background where they were produced, and that the modification of this parameter has important effects on the interaction of IBs with the media.

3.2. Size determination of IBs

Even though the chemical nature of the surface of a material is extremely important, physical features, such as size or mechanical behavior, might also influence their macroscopic properties. Particle size distribution and Z potential of freshly prepared IBs in aqueous suspension were determined by dynamic light scattering, revealing no significant differences between IBs variants in agreement with previous screenings. Observed particle size ranged from 502 nm for DnaK$^-$ IBs to 580 nm for ClpA$^-$ IBs, while the low Z potential values obtained (see Fig. S1) depict the tendency of all the measured IBs to aggregate with time (Z potential values obtained are lower of |30| mV).

In order to study the influence of a solid interface on the particle size, IBs were imaged by AFM in liquid (PBS buffer solution), once deposited over freshly cleaved mica. Average dimensions obtained from these images show no significant deviation from DLS data previously obtained in PBS. This allowed discarding any strong deformation of the protein aggregates during the adsorption process, which might eventually alter the material properties.

3.3. Nanomechanical properties of IBs determined by AFM

It is known that the mechanical properties of a substrate biomaterial are critically affecting relevant features of mammalian cells growing on it, such as cell morphology [21,22], proliferation [21,22], motility [23] and differentiation [22,24]. During the last decade, AFM has proved its value not only for imaging biological samples [25,26], but also for probing inherent properties of biological structures, like local interaction forces, mechanical properties or dynamics in natural (physiological) environments [27].

To determine how the different genetics of IB bioproduction affects their elasticity, force spectroscopic AFM was employed. This technique consists of an AFM tip which is pressed into the elastic object with a defined force (F), producing the subsequent indentation (δ) at the nanoscale. Spectroscopical measurements were performed in liquid media (PBS buffer pH 7.4) in order to preserve the natural state of the protein aggregates and to mimic the natural cell environment. From the obtained F vs. δ data plot, and using the Hertz model [28–33] (see SI), it was possible to fit the experimental data with the behavior expected for conical (equation (1)) and spherical (equation (2)) indenters, obtaining the Young modulus of the sample. In Fig. 2, an example of the experimental data, together with the subsequent fittings for conical and spherical indenters, is shown. In our case, from the two plausible geometries the one associated with a spherical tip presented the higher agreement, and this compatibility of the experimental data with the model was

$$F = \left[\frac{2E^{*}\tan\alpha}{\pi(1-\nu^2)}\right]\delta^2 \quad (1) \qquad F = \left[\frac{2E^{*}R^{1/2}}{3(1-\nu^2)}\right]\delta^{2/3} \quad (2)$$

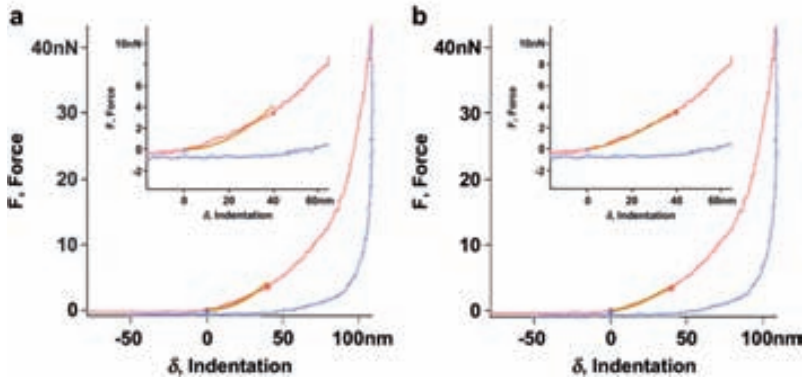

Fig. 2. Conical (a) and spherical (b) fitting of a selected approaching curve measurement over a selected IB. In red is represented the curve resulting from the approaching and indentation of the tip on the IB. In blue is represented the releasing curve generated while moving the AFM tip to its initial position.

verified for the most part of the experimental curves. In order to avoid substrate influence only the first 40 nm of indentation was taken to further analysis.

Statistical studies, presented in Fig. 3, have been obtained after analyzing more than 200 force curves for each aggregate on 7 different IBs obtained in each one of the three different bacterial strains, resulting on different Young modulus distributions according to the IB origin. Stiffness data obtained for wt IBs, represented on Fig. 3a, depicted a monomodal elasticity distribution with a main peak value of 3.73 ± 0.05 MPa and an fwhm (full width at half maximum) of 2.9 ± 0.05 MPa. On the other hand, for DnaK$^-$ and ClpA$^-$ IBs results indicated the presence of two elasticity populations. In the case of DnaK$^-$ IBs (Fig. 3b), the peak at lower strength values was situated at 3.56 ± 0.56 MPa with an fwhm of 3.6 ± 0.48 MPa matching the one obtained for wt particles. However the second population, shifted to harder areas, was placed at 7.75 ± 0.99 MPa with a broader shape of 5.8 ± 0.37 MPa at its fwhm. For ClpA$^-$ IBs (Fig. 3c), the peak distribution was shifted, for both populations, to harder areas with mean peak values of 5.01 ± 0.25 and 10.99 ± 0.30 MPa and fwhm of 3.2 ± 0.28 and 6.6 ± 0.25 MPa, respectively.

These data are in agreement with the results obtained by contact angle measurements, indicating the appearance of two differentiated populations with different wettability and stiffness, in the case of IBs produced in specific phenotypes (DnaK$^-$ and ClpA$^-$), while only one was observed for wt IBs.

3.4. Nanomechanical mapping of the IBs by AFM

AFM spectroscopy might be a destructive technique depending on the sample hardness and the applied force. AFM images of selected IBs, before and after the spectroscopical measurements produced no serious deformation on the IB, which kept its initial shape and structure (see Fig. S2). Therefore, and by the use of an AFM equipped with a closed loop tracking system (see Materials and method), it was possible to obtain the spatial distribution of the elasticity regimes over the different IBs and to develop stiffness maps (Fig. 4), where each force (F) vs. indentation (δ) measurement was spatially localised over the target IB. Fig. 4a shows how the Young modulus was homogeneously spread over the wt IBs, with mean values of 3.6 ± 0.56 MPa. In DnaK$^-$ and ClpA$^-$ IBs two elasticity populations were observed, as entailed in Fig. 4, with the harder areas segregated and localised on the centre of the DnaK$^-$ IBs and on the right side of ClpA$^-$ particles. The above data indicated that, the genetics of IB fabrication, determines the coexistence of more rigid structures and softer ones, and that they seem to be localised on determined areas of individual IB. This fact confirmed the existence of structural diversity inside the protein aggregates. Therefore, it is possible to affirm that the use of modified bacteria for IB production might imply a significant change on their mechanical properties.

3.5. 2D cell proliferation assays

To determine if the alterations in the nanoscale properties observed among variant IBs could be sensed by biological systems, we comparatively explored the abilities of these particulate materials to promote proliferation of mammalian cells, upon decoration of 2D surfaces. In a previous study [14], we have demonstrated that IBs (produced in a DnaK$^-$ strain), when deposited on polystyrene plates, modify the nanoscale topology in a way that stimulated cell proliferation. Therefore, IBs produced in either wt bacteria or in DnaK$^-$ and ClpA$^-$ backgrounds were comparatively tested in a cell culture assay. Interestingly, the proliferation of baby hamster kidney (BHK) cells was favored by all IB variants although at different extents (Fig. 5a). In particular, at 72h after the initiation of the culture the cell density in plates decorated with wt and DnaK$^-$ IBs was about twice than in plates without IBs. While both types of IBs rendered cell density values statistically indistinguishable ($p = 0.538$), ClpA$^-$ IBs dramatically enhanced cell density over the values achieved by other IB variants, although at levels still out the significance level ($p = 0.162$ when comparing with DnaK$^-$ IBs; $p = 0.203$ when comparing with wt IBs). To confirm the differential properties of ClpA$^-$ IBs in stimulating cell proliferation we

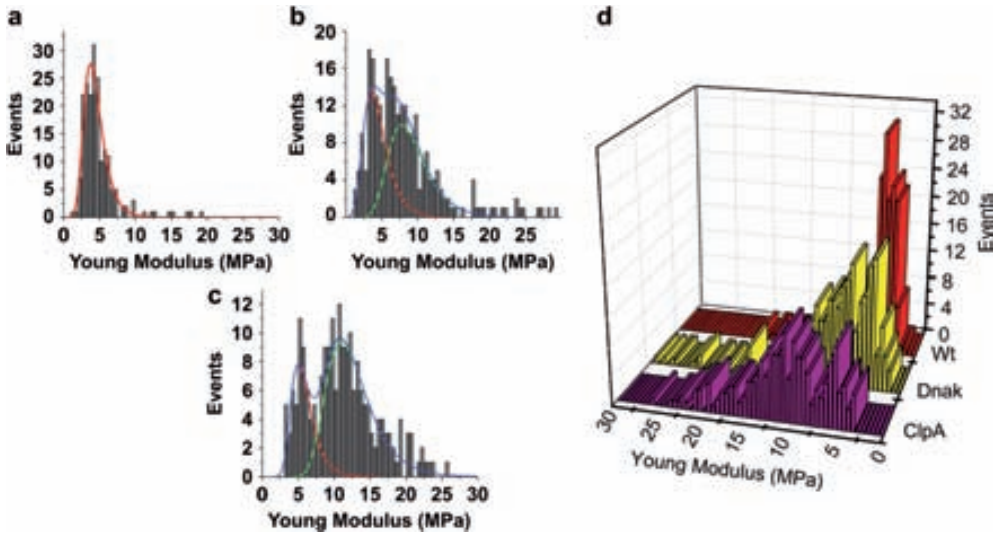

Fig. 3. Histogram representation of the number of events vs. Young modulus for IBs produced in bacterial mutants. a) Wt IBs showing only one peak at 3.73 MPa; b) DnaK$^-$ IBs show two overlapped Young modulus distributions which centered at 3.56 and 7.75 MPa; c) ClpA$^-$ IB show the presence of two different young modulus distributions, at 5.01 and 10.99 MPa; d) 3D representation of the later histograms.

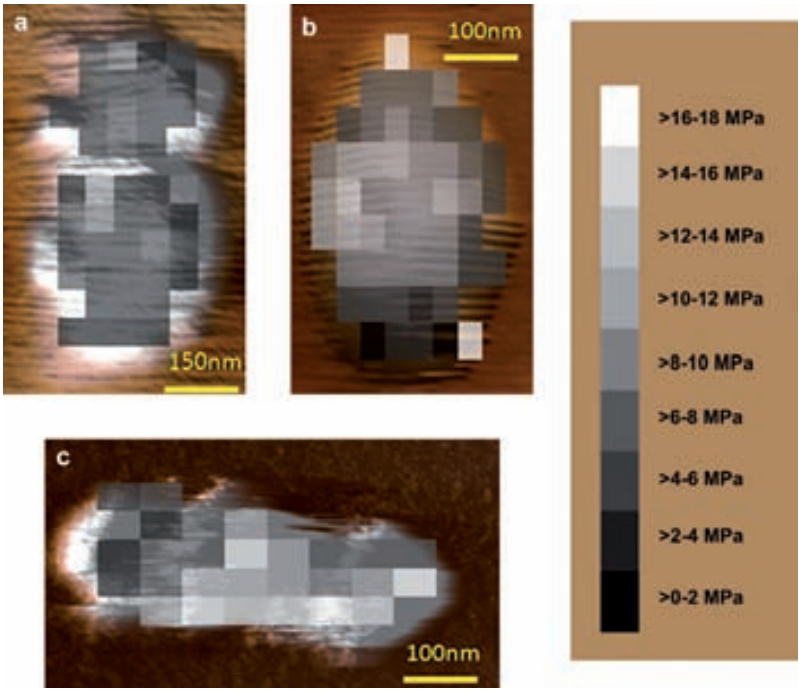

Fig. 4. 2D software developed reconstruction of the elasticity maps of selected IBs from the three genetic backgrounds. a) wt IBs, b) DnaK$^-$ IBs, c) ClpA$^-$ IBs. Observations infer the existence of a homogeneously spread distribution of Young modulus values over the wt IBs. On the other hand, maps obtained for DnaK$^-$ and ClpA$^-$ IBs indicate the existence of two elasticity populations, with the harder areas segregated and localised on the centre of the DnaK$^-$ IBs and on the right side of ClpA$^-$ particles.

extended the study to rat pheochromocytoma (PC12) cells, that tend to grow as floating clusters rather than as firmly attached monolayers. In this model, ClpA$^-$ IBs enhanced cell proliferation over DnaK$^-$ IBs in a still more evident way (Fig. 5b; $p = 0.004$). This confirms that these particles display improved nanoscale properties regarding tissue engineering-oriented topographical modification and that cell proliferation responds to the stiffness increase of the surface decorating material. The progressive temporal increase in the differences in MTT assays promoted by the IB variants indicates that they act stimulating cell proliferation rather than cell adhesion. Interestingly, the similarity between the macroscopic eco of DnaK$^-$ IBs and wt IBs in IB-cell interfaces and the divergent behavior of ClpA$^-$ IBs is highly coincident with the profile of the nanomechanical properties (including wettability and

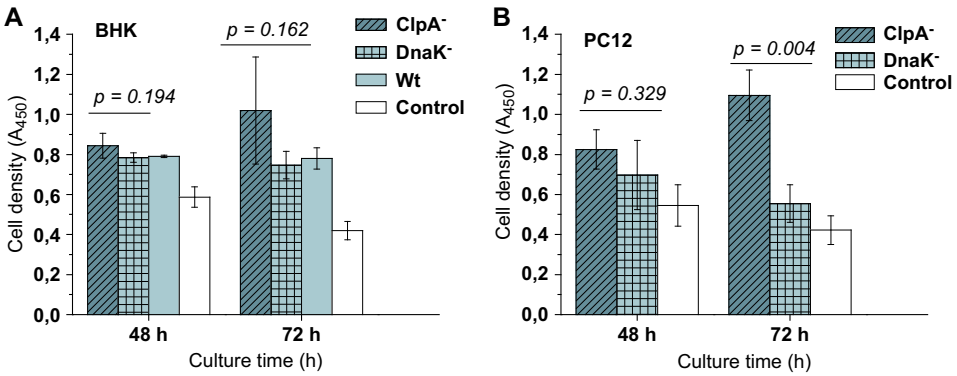

Fig. 5. Cell proliferation determined by a conventional MTT assay monitored in polystyrene plates. Plates were untreated (control) or decorated with 2.65×10^8 IBs per well of different IB variants. The analysis was done in triplicate using BHK (A) and PC12 (B) cell lines. Differences of cell density between IB-decorated wells and IB-free wells (control) were always significant ($p < 0.006$, not shown) in all the experiments. As an exception, growth of PC12 cells on DnaK$^-$ IBs was stimulated over the control in the limits of statistic significance ($p = 0.132$ at 48 h and $p^{\circ} < ^{\circ} 0.047$ at 72 h). The significance as p values of the differences between growth on ClpA$^-$ and DnaK$^-$ IBs are depicted over the corresponding bars.

stiffness) exhibited by the IB variants, again very proximal when comparing IBs produced by wt and DnaK$^-$ cells.

4. Discussion

IBs are formed in recombinant bacteria submitted to conformation stress [9], and are now seen as extremely dynamic protein clusters [34] that contain an important extent of polypeptides with native-like secondary structure and are biologically active [5]. At least a significant fraction of polypeptides embedded in IBs are functional [5]. How functional species can coexist with the amyloid-like pattern (governed by cross molecular beta-sheet interactions) is still unsolved. However, the influence of environmental conditions on the folding state of IB proteins [3,35] indicates an important degree of molecular flexibility. In addition, being the IB protein quality tightly surveyed by the quality control system [4] is not unexpected that functional modifications in the bacterial folding machinery would result in IBs with altered physical properties, as protein folding and degradation, but also protein deposition as IBs and removal from these particles would be mechanistically affected. However, the mechanical properties of IBs at the nanoscale have never been explored as these protein clusters have not attracted any interest as biomaterials, although in a different context, they have been recently observed as intriguing catalizers when formed by enzymes [4,6]. Recent experiments strongly supporting the biocompatibility of IBs as nanoparticulate materials [6] has pushed for a fine characterization and eventual tuning of the biophysical properties that might be relevant to biomedical applications, such as the bottom-up topographic surface modification in tissue engineering [9]. In this context, GFP-containing IBs have been fabricated in bacteria deficient in either DnaK or ClpA, in the hope to identify significant modifications in their properties as particulate nanomaterials. DnaK is the main cytosolic chaperone of *E. coli*, that being a negative regulator of the heat shock system [9] and a potent proteolytic stimulator [36] also show folding, holding and disaggregase activities [16]. ClpA is the ATPase subunit of ClpP and possesses intriguing foldase-like properties [37]. GFP IBs produced in these specific backgrounds are more fluorescent than wt IBs [16], indicating at least conformational variations in the aggregated protein regarding to IBs formed by a fully functional quality control. While IBs produced in wild type *E. coli* depict a maximum coverage at slightly hydrophobic surfaces and a monomodal stiffness profile, those developed either in the DnaK$^-$ or ClpA$^-$ derived background show a disrupted wettability pattern (Fig. 1 right) where the coverage maximum is splitted in two and shifted to higher and lower wettability regions. Furthermore, although its coverage and subsequently the substrate roughness of DnaK$^-$ IBs is similar to those of wt derivates, they manifest an enhanced (but not statistically significant) tendency to favour mammalian cell growth (Fig. 5) in cell proliferation assays if compared to wt ones. This could be related to the enhanced values of the IB stiffness map suggesting a dual protein population, that might increase the cell responsiveness to the altered topography. The absence of the chaperone DnaK, that in IB-forming cells mainly transfers polypeptides to the ClpP and Lon proteases for digestion [16] on the surface of IBs [16], results in IBs, which contain a more heterogenous protein population regarding functionality and conformation status than wt IBs [38]. Interestingly, the absence of the ATPase ClpA, that mediates protein translocation to its cognate protease ClpP [39,40], results not only in a higher coverage and therefore, a rougher system but also in an even more stiff IBs in which the dual stiffness mapping is even more evident than in DnaK$^-$ cells (Fig. 4). In this case, the impact on biological systems is dramatic, proving that the extent of the genetically determined mechanical variations of IBs is within the range of the functional capacity of the cells sensory elements that respond more actively to harder IBs.

Those results are in agreement with previous Fourier transformed infrared spectroscopy analyses (FTIR) of DnaK$^-$ and ClpA$^-$ IBs, in which a downshift in the β-sheet peaks (at 1627 and 1693 cm^{-1}) was observed [41], indicating a more compact and therefore stiffer cross-β-sheet architecture than in wt IBs. In addition, recombinant proteins are stabilized in these backgrounds as a result of a global inhibition of the proteolytic activity of the quality control machinery [16], leading to the incorporation of otherwise degraded protein species into IBs. This dual deposition could be linked to the heterogeneous stiffness maps obtained for DnaK$^-$ and ClpA$^-$ IBs, and indicates that the conformational status of the aggregated polypeptides determines the consistence of the protein clusters at the nanoscale level.

As well as other biomaterials used for cell proliferation, such as polymers or hydrogels, IBs have probed their efficiency as grow vector. However, while regularly used non-biologic materials require the use of complicated or expensive production techniques of even some chemical compounds that may affect the target cells, IBs are naturally produced, highly flexible and non-toxic biomaterials which can be easily produced by bacteria on multigram scale. Furthermore, whereas traditional materials properties are, usually, hard to be modified, IBs properties can be easily tuned just by changing its genetic background. IBs can, therefore, be considered as multifunctional tunable biomaterials able to selectively modify cell proliferation when used to decorate a solid substrate.

5. Conclusions

The conformation status of recombinant proteins in *E. coli*, as regulated by the proteins quality control, defines the nanoscale physicochemical properties of inclusion bodies. Such proteinaceous particulate biomaterial exhibit a range of wettability and stiffness when obtained in wild type, DnaK$^-$ and ClpA$^-$ strains, associated to the style of protein packaging occurring in absence of each of these elements of the heat shock machinery. The inhibition of proteolysis allowing the deposition of otherwise degraded protein species and the associated condensation of the inclusion body cross-β-sheet architecture in DnaK$^-$ and ClpA$^-$ backgrounds can account from the up shift of particle stiffness from around 2 up to 16 MPa. Interestingly, when using inclusion bodies for bottom-up surface decoration in tissue engineering, such range of mechanical properties is sensed by cultured mammalian cells, resulting in a dramatic stimulation of cell proliferation, which increases with the stiffness of the substrate material. Since bacterial inclusion bodies are fully compatible nanomaterials that can be obtained at large scale by cost-effective procedures, their physiological modification during biofabrication in selected genetic backgrounds can be observed as an intriguing possibility to generate improved versions tailored for specific biological interfaces. The tuning opportunities offered through adjusting the quality control, so much explored for recombinant protein solubility issues, definitively expands the spectrum of biomedical applications of this novel bacterial nanomaterial.

Acknowledgments

The authors appreciate the financial support through MEC (BIO2007-61194, BFU2010-17450, and CTQ2006-06333) and AGAUR (2009SGR-108 and 2009SGR-00516) grants and from the CIBER de Bioingeniería, Biomateriales y Nanomedicina (CIBER-BBN, promoted by ISCIII), Spain. AV was distinguished by ICREA (Generalitat de Catalunya) with an ICREA ACADEMIA award. Supporting Information is available online from Wiley InterScience or from the

authors. We recognize the technical support from Dr. G. Oncins (Nanometric Techniques unit, Scientific-Technical Services of the University of Barcelona).

Appendix. Supporting information

Supporting information associated with this article can be found, in the online version, at doi:10.1016/j.biomaterials.2010.04.008.

Appendix

Figures with essential colour discrimination. Certain figures in this article, in particular Fig. 4, are difficult to interpret in black and white. The full colour images can be found in the on-line version, at doi:10.1016/j.biomaterials.2010.04.008.

References

[1] Marston FA. The purification of eukaryotic polypeptides synthesized in *Escherichia coli*. Biochem J 1986;240(1):1–12.
[2] Baneyx F, Mujacic M. Recombinant protein folding and misfolding in *Escherichia coli*. Nat Biotechnol 2004;22(11):1399–408.
[3] Garcia-Fruitos E, Gonzalez-Montalban N, Morell M, Vera A, Ferraz R, Aris A, et al. Aggregation as bacterial inclusion bodies does not imply inactivation of enzymes and fluorescent proteins. Microb Cell Fact 2005;4(1):27.
[4] Gonzalez-Montalban N, Garcia-Fruitos E, Villaverde A. Recombinant protein solubility-does more mean better? Nat Biotechnol 2007;25(7):718–20.
[5] Ventura S, Villaverde A. Protein quality in bacterial inclusion bodies. Trends Biotechnol 2006;24(4):179–85.
[6] Martinez-Alonso M, Gonzalez-Montalban N, Garcia-Fruitos E, Villaverde A. Learning about protein solubility from bacterial inclusion bodies. Microb Cell Fact 2009;8(1):4.
[7] deGroot NS, Sabate R, Ventura S. Amyloids in bacterial inclusion bodies. Trends Biochem Sci 2009;34(8):408–16.
[8] Margreiter G, Messner P, Caldwell KD, Bayer K. Size characterization of inclusion bodies by sedimentation field-flow fractionation. J Biotechnol 2008;138(3–4):67–73.
[9] García-Fruitós E, Rodríguez-Carmona E, Díez-Gil C, Ferraz RM, Vázquez E, Corchero JL, et al. Surface cell growth engineering assisted by a novel bacterial nanomaterial. Adv Mater 2009;21(42):4249–53.
[10] Bowden GA, Paredes AM, Georgiou G. Structure and morphology of protein inclusion bodies in *Escherichia coli*. *Biotechnology* (N.Y.). 1991:725–30.
[11] Foguel D, Silva JL. New insights into the mechanisms of protein misfolding and aggregation in amyloidogenic diseases derived from pressure studies. Biochemistry 2004;43(36):11361–70.
[12] Peternel Š, JevŠevar S, Bele M, Gaberc-Porekar V, Menart V. New properties of inclusion bodies with implications for biotechnology. Biotechnol Appl Biochem 2008;49(4):239–46.
[13] Domke J, Radmacher M. Measuring the elastic properties of thin polymer films with the atomic force microscope. Langmuir 1998;14(12):3320–5.
[14] Parra A, Casero E, Lorenzo E, Pariente F, Vazquez L. Nanomechanical properties of globular proteins: lactate oxidase. Langmuir 2007;23(5):2747–54.
[15] Wang L. Towards revealing the structure of bacterial inclusion bodies. Prion 2009;3:6.
[16] García-Fruitós E, Martínez-Alonso M, Gonzàlez-Montalbán N, Valli M, Mattanovich D, Villaverde A. Divergent genetic control of protein solubility and conformational quality in *Escherichia coli*. J Mol Biol 2007;374(1):195–205.
[17] Faucheux N, Schweiss R, Lützow K, Werner C, Groth T. Self-assembled monolayers with different terminating groups as model substrates for cell adhesion studies. Biomaterials 2004;25(14):2721–30.
[18] Webb K, Hlady V, Tresco PA. Relative importance of surface wettability and charged functional groups on NIH 3T3 fibroblast attachment, spreading, and cytoskeletal organization. J Biomed Mater Res 1998;41(3):422–30.
[19] Andrade J, Hlady V. Protein adsorption and materials biocompatibility: a tutorial review and suggested hypotheses. In: Biopolymers/Non-Exclusion HPLC. Berlin: Springer; 1986. p. 1–63.
[20] Washburn NR, Yamada KM, Simon CG, Kennedy SB, Amis EJ. High-throughput investigation ofosteoblast response to polymer crystallinity: influence of nanometer-scale roughness on proliferation. Biomaterials 2004;25(7–8):1215–24.
[21] Yeung T, Georges P, Flanagan L, Marg B, Ortiz M, Funaki M, et al. Effects of substrate stiffness on cell morphology, cytoskeletal structure, and adhesion. Cell Motil Cytoskeleton 2005;60(1):24–34.
[22] Chen C-C, Hsieh PC-H, Wang G-M, Chen W-C, Yeh M-L. The influence of surface morphology and rigidity of the substrata on cell motility. Mater Lett 2009;63(21):1872–5.
[23] Hadjipanayi E, Mudera V, Brown RA. Close dependence of fibroblast proliferation on collagen scaffold matrix stiffness. J Tissue Eng Regen Med 2009;3(2):77–84.
[24] Cheung Yuk K, Azeloglu Evren U, Shiovitz David A, Costa Kevin D, Seliktar D, Sia Samuel K. Microscale control of stiffness in a cell-adhesive substrate using microfluidics-based lithography. Angew Chem Int Ed Engl 2009;48(39):7188–92.
[25] Teixeira AI, Ilkhanizadeh S, Wigenius JA, Duckworth JK, Inganäs O, Hermanson O. The promotion of neuronal maturation on soft substrates. Biomaterials 2009;30(27):4567–72.
[26] Saha K, Keung AJ, Irwin EF, Li Y, Little L, Schaffer DV, et al. Substrate modulus directs neural stem cell behavior. Biophys J 2008;95(9):4426–38.
[27] Engel A, Muller DJ. Observing single biomolecules at work with the atomic force microscope. Nat Struct Mol Biol 2000;7(9):715–8.
[28] Jaeger MS, Uhlig K, Clausen-Schaumann H, Duschl C. The structure and functionality of contractile forisome protein aggregates. Biomaterials 2008;29(2):247–56.
[29] Koenders MMJF, Yang L, Wismans RG, van der Werf KO, Reinhardt DP, Daamen W, et al. Microscale mechanical properties of single elastic fibers: the role of fibrillin–microfibrils. Biomaterials 2009;30(13):2425–32.
[30] Vinckier A, Semenza G. Measuring elasticity of biological materials by atomic force microscopy. FEBS Lett 1998;430(1–2):12–6.
[31] Heuberger M, Dietler G, Schlapbach L. Mapping the local Young's modulus by analysis of the elastic deformations occurring in atomic force microscopy. Nanotechnology 1995;6(1):12–23.
[32] del Mercato LL, Maruccio G, Pompa PP, Bochicchio B, Tamburro AM, Cingolani R, et al. Amyloid-like fibrils in elastin-related polypeptides: structural characterization and elastic properties. Biomacromolecules 2008;9(3):796–803.
[33] Radmacher M, Fritz M, Cleveland JP, Walters DA, Hansma PK. Imaging adhesion forces and elasticity of lysozyme adsorbed on mica with the atomic force microscope. Langmuir 2002;10(10):3809–14.
[34] Gasser B, Saloheimo M, Rinas U, Dragosits M, Rodriguez-Carmona E, Baumann K, et al. Protein folding and conformational stress in microbial cells producing recombinant proteins: a host comparative overview. Microb Cell Fact 2008;7(1):11.
[35] Garcia-Fruitos E, Aris A, Villaverde A. Localization of functional polypeptides in bacterial inclusion bodies. Appl Environ Microbiol 2007;73(1):289–94.
[36] Rodriguez F, Arsène-Ploetze F, Rist W, Rüdiger S, Schneider-Mergener J, Mayer MP, Bukau B. Molecular basis for regulation of the heat shock transcription factor alpha 32 by the DnaK and DnaJ chaperones. Mol Cell 2008;32(3):347–58.
[37] Mogk A, Deuerling E, Vorderwülbecke S, Vierling E, Bukau B. Small heat shock proteins, ClpB and the DnaK system form a functional triade in reversing protein aggregation. Mol Microbiol 2003;50(2):585–95.
[38] Carrio MM, Villaverde A. Localization of chaperones DnaK and GroEL in bacterial inclusion bodies. J Bacteriol 2005;187(10):3599–601.
[39] Martínez-Alonso M, Vera A, Villaverde A. Role of the chaperone DnaK in protein solubility and conformational quality in inclusion body-forming *Escherichia coli* cells. FEMS Microbiol Lett 2007;273(2):187–95.
[40] Gonzalez-Montalban N, Garcia-Fruitos E, Ventura S, Aris A, Villaverde A. The chaperone DnaK controls the fractioning of functional protein between soluble and insoluble cell fractions in inclusion body-forming cells. Microb Cell Fact 2006;5(1):26.
[41] Piszczek G, Rozycki J, Singh SK, Ginsburg A, Maurizi MR. The molecular chaperone, ClpA, has a single high affinity peptide binding site per hexamer. J Biol Chem 2005;280(13):12221–30.

Supplementary Data

The nanoscale properties of bacterial inclusion bodies and their effect on mammalian cell proliferation

SI 1Materials

All Chemicals were obtained from commercial suppliers and used without any further purification. HPLC grade organic solvents (TEKNOKROMA, SPAIN) were used. Gold substrates were purchased to SSens (Hengelo, Netherland).

1 Bacterial cells, plasmids and IB production:

The *Escherichia coli* strains used in this study were streptomycin resistant MC4100 strain (*araD139 Δ(argF-lac) U169 rpsL150 relA1 flbB5301 deoC1 ptsF25 rbsR*) [1], as a wild-type, and its derivative streptomycin resistant strain JGT4 strain (*clpA::kan*) and tetracycline and streptomycin resistant JGT20 strain (*dnak756 thr::Tn10*), lacking ClpA ATPase and DnaK chaperone, respectively [2]. All strains were transformed with an IPTG-inducible pTVP1GFP plasmid, encoding a green fluorescent protein (GFP) fused to the VP1 capsid protein of foot-and-mouth disease virus [3]. Bacterial cultures were performed with shake flask cultures growing at 37°C and 250 rpm in LB rich medium [1] plus the required antibiotic. Gene expression was induced with 1mM IPTG at OD_{550nm}=0.5. 20 mL culture samples were taken 3 h post-induction and were processed for further analysis. All experiments were done by triplicate.

2 Inclusion body purification

Samples of bacterial cultures (20 mL) were centrifuged at 4^{o}C at 5000 g for 5 min, resuspended in lysis buffer (20 mL, 50 mM TrisHCl (pH 8.1), 100 mM NaCl, and 1mM EDTA) and frozen at -80^{o}C. After that, samples were defrozen and phenylmethanesulphonylfluoride (PMSF) (100 µL, 100mM) and lysozime (400 µL, 1 mg/mL) were added and incubated for 2h at 37^{o}C. Then, 100 µL of Triton X-100 weres added (0.5% Triton X-100). After 1h incubation at room temperature, the sample was ice-jacketed, and sonicated 5 cycles of 10 min each at 40% amplitude under 0.5 s cycles.. Next, the mixture was incubated with DNase (12 µL, 1mg/mL) and $MgSO_4$ (12 µL, 1M) for 45 min at 37^{o}C. Finally, samples were centrifuged at 4^{o}C at 15000g for 15 min, the pellet was washed once with 1 mL of lysis buffer containing Triton X-100 (0.5%) and the sample was centrifuged again at 15000g for 15 min at 4^{o}C. Pellets containing pure inclusion bodies were stored at -80^{o}C until analysis. All incubations were done under gently agitation.

SI 2Methods

1.Gold substrates cleaning protocol:

Prior to monolayer formation, the gold substrates were thoroughly cleaned. After sonication for 5 minutes on clean ethanol, the substrates were air dried and placed in piranha solution (concentrated H_2SO_4 (Panreac) and 35% aqueous H_2O_2 (Aldrich) in a 7:3 ratio) for 30 seconds (CAREFUL, Piranha solutions are extremely energetic and may result in explosion or skin burns if

not handled with extreme caution). Then the substrates were copiously rinsed with ultrapure water (MiliQ with 18.2 MV cm) and dried under a stream of N_2.

2. Contact angle determination of the mixed thiols functionalized SAMs:

Wettability of the self assembled monolayer of the mixed thiols before and after being in contact with IBs was determined with an OCA 15+ (Dataphysics, Germany) contact angle goniometer.

Table S1. Concentration of thiols, ranging from 0 to 1 in molar fraction of 11- mercapto-1-undecanol (X_{OH}), used for the mixed SAM's preparation and wettability (CA) of the resulting monolayers.

Substrate	***Tot. mM***	X_{OH}	X_{CH3}	***C.A(°)***	***St. Dev.(°)***
1	1.99	0.00	1.00	109.8	1.0
2	2.06	0.23	0.77	97.7	0.7
3	2.03	0.41	0.59	83.5	1.6
4	1.93	0.79	0.21	63.2	1.5
5	2.00	0.91	0.09	48.0	3.6
6	2.00	1.00	0.00	23.0	2.2

2. Size and Z potential determination of IBs

The particle sizes and Z potential of IB were determined by dynamic light scattering (DLS). Figure 1a and 1 b depict result obtained, showing no significant difference between IBs. If compared, liquid AFM results obtained for all the different IBs are comparable with those achieved with DLS. Thus, it is possible to conclude that the existence of interactions with the mica substrate does not modify IBs size or shape (figure 1 c and d).

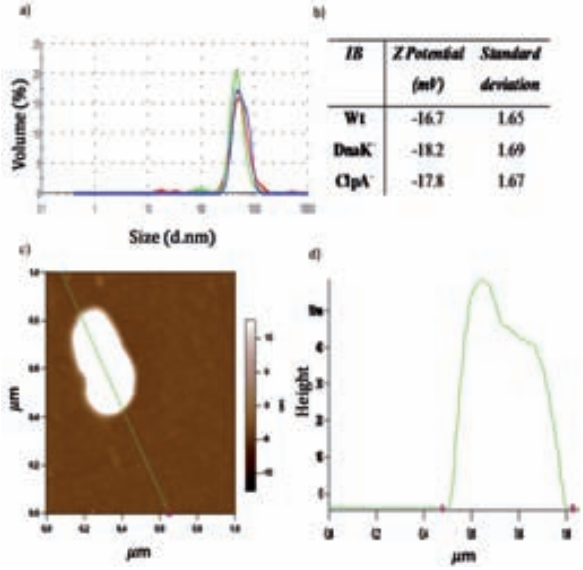

Figure S1. a) Particle size measurements by DLS of the freshly prepared IB suspensions. Green DnaK$^-$; IBs; Red wt IBs; Blue ClpA$^-$ IBs; b) Z potential values of the freshly prepared IB suspensions determined by DLS; c) A selected dynamic mode AFM image performed in liquid of an Wt IB and d) its cross section

SI 3 Data analysis of force curves:

The relationship between the piezo movement *z,* and the cantilever deflection *d*, of a force curve performed on a soft sample, is determined by the equation $d = z - \delta$; where δ represents the indentation suffered by the sample during the measurement [4].

Therefore, and according to Hooke's law, the applied force can be represented by $F = kd = k(z - d)$ being *k* the spring constant of the cantilever.

Among the different theories describing the elastic deformation of a soft sample by a rigid indenter [5] , the Hertzian model [6] has been one of the more used in similar systems [4, 7, 8]. Thus, the analysis of our experimental data was developed following this theoretical approximation.

$$F = A\left[\frac{E^*}{\left(1-\nu^2\right)}\right]\delta^m \quad (1)$$

The applied force and the indentation of a soft sample by a hard tip, can, then, be related through the equation 1; where *E** is the reduced Young's modulus of the sample, ν is the Poisson ratio of the sample, and *A* and *m* are a constants that depend on the indenter radius and shape[9] .

$$F = \left[\frac{4E^* R^{1/2}}{\left(3\left(1-\nu_s^2\right)\right)}\right]\delta^{3/2} \;\; ; \;\; \delta = \left[\frac{\left(3\left(1-\nu_s^2\right)\right)}{4E^* R^{1/2}}\right]^{2/3} F^{2/3} \quad (2)$$

Assuming a spherical geometry for our indenter the relationship between the applied force (F) and the indentation (δ) is reduced to equation 2; where *R* is the tip radius. While in the case of a conical indenter the expression is shown on equation 3; where α is the half opening angle of the conical tip.

$$F = \left[\frac{2E^* \tan\tan\alpha}{\left(\pi\left(1-\nu_s^2\right)\right)}\right]\delta^2 ; \delta = \left[\frac{\left(\pi\left(1-\nu_s^2\right)\right)}{2E^* \tan\tan\alpha}\right]^{\frac{1}{2}} F^{\frac{1}{2}} \quad (3)$$

Indentation (δ) values for each sample were calculated by computing the lateral deviation (along the X axis of the graph) of the piezo movement (*z*) vs. deflexion (*d*) graph respect to the one obtained for the reference mica surface.[10] Assuming a typical Poisson ratio value of 1/3 [7, 10], it is possible to obtain the reduced young modulus (E*) for each experiment by the fitting of the *F* versus δ plots, to the conical or spherical approximations. Real Young modulus of our

sample can be easily obtained from the reduced one following the relationship shown on equation 4, where ν_s, E_s and ν_t, E_t correspond to the Poisson ratio (ν) and the young modulus (E) of the sample and the tip respectively.

$$E^* = \left(\frac{\left(1-\nu_s^2\right)}{E_s} + \frac{\left(1-\nu_t^2\right)}{E_t} \right) \qquad (4)$$

All the F vs. δ fittings were handled using the IGOR PRO 6 software (Wavemetrics, USA). Histogram plotting of the obtained young modulus for each IB family was fitted following a nonsymetrical Gaussian function, due to the slightly bigger weight of the higher young modulus values.

S.I. 4 IBs deformation upon AFM spectroscopical measurement

Two AFM IBs images of selected IBs, before and after the indentation process, are shown in figure 2. As no damage can be observed in the IBs after measuring, it is possible to establish that AFM spectroscopy measurements does not affect the IBs structure.

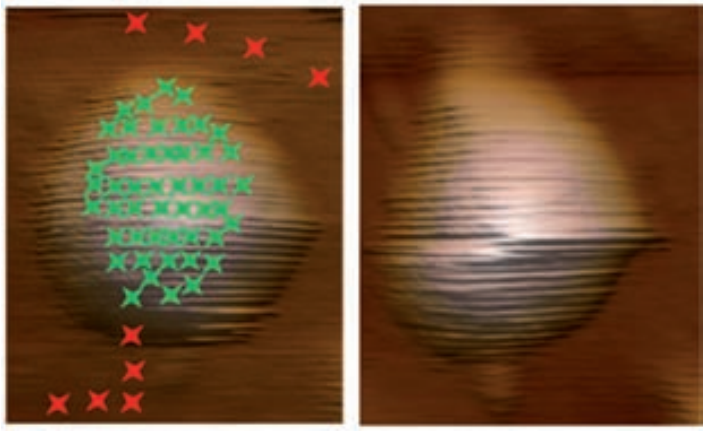

Figure S2. IB's AFM image before (left) and after (right) indenting. Green crosses represent the spectroscopical measurements performed on the IB while red ones are the ones performed over the clean mica surface. It is possible to observe how no damage was performed to the IB integrity while spectroscopical measurements were performed.

1. Sambrook JF, E; Maniatis,T. Molecular Cloning, A Laboratory Manual. New York: Cold Spring Harbor, 1989.
2. Thomas JG, Baneyx F. Roles of the Escherichia coli Small Heat Shock Proteins IbpA and IbpB in Thermal Stress Management: Comparison with ClpA, ClpB, and HtpG In Vivo. The Journal of Bacteriology 1998;180(19):5165-5172.
3. Garcia-Fruitos E, Gonzalez-Montalban N, Morell M, Vera A, Ferraz R, Aris A, et al. Aggregation as bacterial inclusion bodies does not imply inactivation of enzymes and fluorescent proteins. Microbial Cell Factories 2005;4(1):27.
4. Parra A, Casero E, Lorenzo E, Pariente F, Vazquez L. Nanomechanical Properties of Globular Proteins: Lactate Oxidase. Langmuir 2007;23(5):2747-2754.
5. Piétrement O, Troyon M. General Equations Describing Elastic Indentation Depth and Normal Contact Stiffness versus Load. Journal of Colloid and Interface Science 2000;226(1):166-171.
6. Hertz H. On the contact of elastic solids. J reine angew Math 92 1896;92:15.
7. Radmacher M, Fritz M, Cleveland JP, Walters DA, Hansma PK. Imaging adhesion forces and elasticity of lysozyme adsorbed on mica with the atomic force microscope. Langmuir 1994;10(10):3809-3814.
8. Afrin R, Alam MT, Ikai A. Pretransition and progressive softening of bovine carbonic anhydrase II as probed by single molecule atomic force microscopy. Protein Science 2005;14(6):1447-1457.
9. Weisenhorn AL, Khorsandi M, Kasas S, Gotzos V, Butt HJ. Deformation and height anomaly of soft surfaces studied with an AFM. Nanotechnology 1993;4(2):106-113.
10. Vinckier A, Semenza G. Measuring elasticity of biological materials by atomic force microscopy. FEBS Letters 1998;430(1-2):12-16.

ADVANCED MATERIALS

Surface Cell Growth Engineering Assisted by a Novel Bacterial Nanomaterial

By *Elena García-Fruitós, Escarlata Rodríguez-Carmona, César Díez-Gil, Rosa M. Ferraz, Esther Vázquez, José Luis Corchero, Mary Cano-Sarabia, Imma Ratera, Nora Ventosa, Jaume Veciana,** and *Antonio Villaverde**

Bacterial inclusion bodies (IBs) are highly pure protein deposits in the size range of a few hundred nanometers produced by recombinant bacteria.[1] The polypeptide chains that form IBs usually retain a certain amount of native structure, keeping their biological activity (e.g., fluorescence or enzymatic activity), and as a result being suitable for use as functional and biocompatible materials. In this study we characterize the relevant nanometer-scale properties of IBs and explore the extent to which they can be tailored by simple approaches. In addition, as an intriguing proof-of-concept, IB-grafted surfaces have been obtained that dramatically stimulate mammalian cell proliferation, proving the potential of IBs in tissue engineering and regenerative medicine.

Many recombinant polypeptides produced in bacteria aggregate as IBs. These protein deposits appear as highly hydrated, chemically pure particles, as the recombinant protein itself is the main component — up to around 95% of the protein therein.[2,3] Other cell components, such as RNA, DNA, and lipids, are entrapped during IB formation and are present in minor amounts.[4] The formation of IBs is a fast and efficient process, as they are observed a few minutes after the induction of gene expression but can later represent around 50% of the total cell biomass.[3] While in the past IBs were believed to be formed by unfolded or largely misfolded polypeptide chains and therefore biologically inert,[5] recent insights show them to be constituted by folded and biofunctional protein species,[6] whose presence is allowed by a particular amyloid-like organization.[7–9] Therefore, IBs formed by enzymes such as β-galactosidase, D-amino acid oxidase, maltodextrin phosphorylase, sialic acid aldolase, and polyphosphate kinase[8,10–13] can be used as catalysts in different processes. On the other hand, the in vivo formation of IBs is regulated by several cellular genes (mainly encoding proteases and chaperones), which makes the genetic manipulation of their nanometer-scale properties feasible.[14,15] We determine here the most relevant nanometer-scale features of IBs and show that they can be tailored by appropriate genetic and process engineering of the producing bacteria. As they are fully biocompatible and mechanically stable materials, we have furthermore used IBs as nanoparticles to engineer surface roughness for the stimulation of mammalian cell proliferation, as an example of the functional possibilities offered by these novel materials.

IBs formed by green fluorescent protein (GFP) are very convenient models for kinetic and functional analyses of their biological production since they are highly fluorescent.[16] After addition of the lactose analogue isopropyl β-D-1-thiogalactopyranoside (IPTG), IBs were clearly visible by confocal microscopy 1 h after induction of *GFP* gene expression (Fig. 1A) and grew volumetrically until around 3 h during the synthesis of recombinant GFP. Under standard bacterial growth conditions, the yield of IB was higher than 5 mg L^{-1} after 3 h (not shown), data very promising for convenient scaling-up. Also, in this context, previous reports indicate that high-yield production of IBs is feasible through high-cell-density culture, which is extremely appealing from an industrial point of view.[17–19] On the other hand, *Escherichia coli* strains deficient in chaperones or proteases produce different-size IBs (Fig. 1B) owing to different dynamics of in vivo protein deposition.[14,15] While mature IBs purified from wild type (wt) cells showed an average diameter of 340 nm (compatible with independent estimates[20]), this value can be increased progressively up to more than 500 nm in DnaK-deficient cells (Fig. 1C), with a relatively low polydispersity index (PdI) in all analyzed samples. Also, IB particles were observed as moderately (in wt cells) to highly (in $ClpP^-$ cells) fluorescent (Fig. 1D). Therefore, the appropriate combination of time of harvesting (determining IB growth stage) and the producing strain (determining both biological activity and upper size limit) would define particular particle dimensions and fluorescence that could be appropriate for different applications. For instance, IBs obtained in $ClpA^-$ and $ClpP^-$ cells, with a very similar particle size (0.435 and 0.459 nm, respectively), showed different fluorescence emission levels (71 and 184 mean FL1 units

[*] Prof. J. Veciana, Prof. A. Villaverde, Dr. E. García-Fruitós, Dr. E. Rodríguez-Carmona, Dr. C. Diez-Gil, Dr. R. M. Ferraz, Dr. E. Vázquez, Dr. J. L. Corchero, Dr. M. Cano-Sarabia, Dr. I. Ratera, Dr. N. Ventosa
CIBER de Bioingeniería, Biomateriales y Nanomedicina (CIBER-BBN)
Bellaterra, 08193 Barcelona (Spain)
E-mail: vecianaj@icmab.es; antoni.villaverde@uab.es

Dr. J. Veciana, Dr. C. Diez-Gil, Dr. M. Cano-Sarabia, Dr. I. Ratera, Dr. N. Ventosa
Department of Molecular Nanoscience and Organic Materials
Institut de Ciencia de Materials de Barcelona (CSIC)
Bellaterra, 08193 Barcelona (Spain)

Dr. A. Villaverde, Dr. E. García-Fruitós, Dr. E. Rodríguez-Carmona, Dr. R. M. Ferraz, Dr. E. Vázquez, Dr. J. L. Corchero
Institute for Biotechnology and Biomedicine
Universitat Autònoma de Barcelona
Bellaterra, 08193 Barcelona (Spain)

Dr. A. Villaverde, Dr. E. Rodríguez-Carmona, Dr. R. M. Ferraz, Dr. E. Vázquez
Department of Genetics and Microbiology
Universitat Autònoma de Barcelona
Bellaterra, 08193 Barcelona (Spain)

DOI: 10.1002/adma.200900283

ADVANCED MATERIALS www.advmat.de

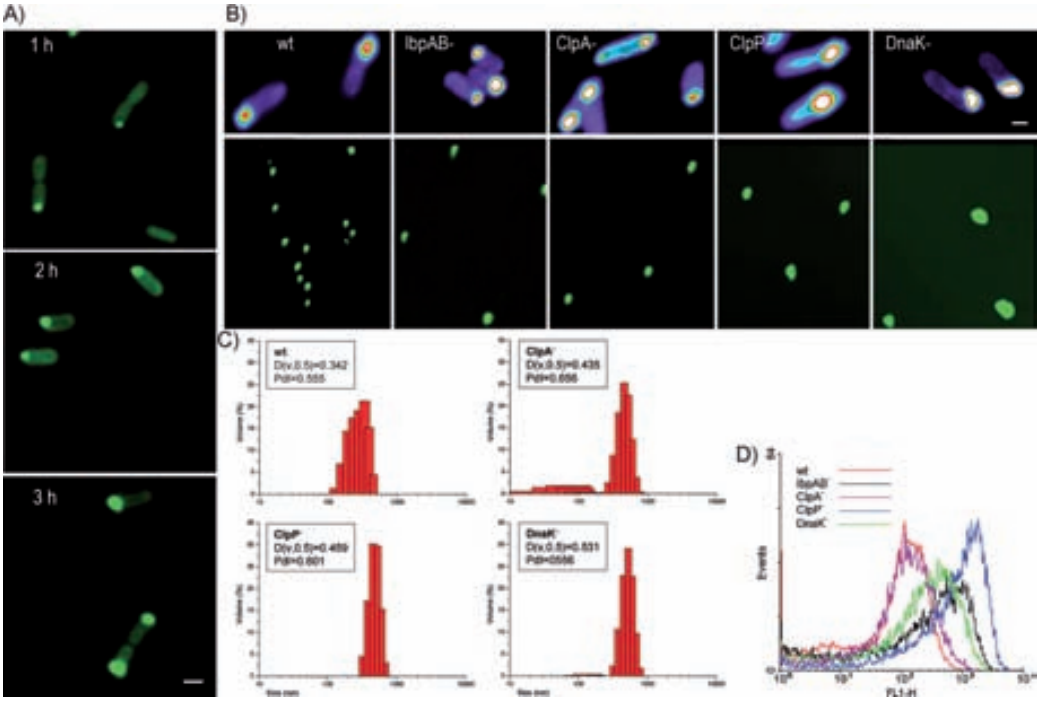

Figure 1. Morphological and functional characterization of IBs. A) Confocal microscopy images of wt cells overproducing GFP IBs. From top to bottom, cell samples at 1 h, 2 h, and 3 h after induction of IB production. Scale bar: 1 μm. B) Confocal microscopy images using metamorph lookup table of wt, IbpAB$^-$, ClpA$^-$, ClpP$^-$, and DnaK$^-$ cells producing 2 h old GFP IBs (top). Confocal microscopy images IBs aged for 3 h and purified from these strains (bottom). Scale bar: 1 μm. C) IB-size distribution of IBs aged for 3 h and isolated from different bacterial strains. IBs from IbpAB-deficient cells were excluded from this study because of their particular tendency to aggregate (not shown). D(v,0.5) is the volume median particle diameter [nm] and the PdI is defined as $[D(v,0.1)/D(v,0.9)] \times 100$. D) Fluorescence, analyzed by flow cytometry, for IB particles from different strains. For details on the AFM and DLS experiments see the Supporting Information.

per particle, respectively). The fluorescence mapping of GFP IBs was, however, comparable in all strains, showing a common homogeneously fluorescent core pattern (Fig. 1B).

To characterize the morphology of IBs at the nanometer scale we explored them by atomic force microscopy (AFM) and scanning electron microscopy (SEM). As can be seen (Fig. 2A–C), AFM of wt GFP IBs shows the presence of spherical or cylindrical entities with average sizes of 300 nm length and 170 nm diameter. The performed cross-sectional measurements confirmed the statistical data obtained from the dynamic light scattering (DLS) measurements (Fig. 1C). SEM observations were in the same line, revealing rough IB surfaces and stressing the size difference between IBs obtained in wt and DnaK$^-$ cells (Fig. 2D). Freshly prepared IB suspensions showed a Z potential of −9.8 mV, which is indicative of slightly negatively charged surfaces and in agreement with the aggregation-prone nature of IB proteins.

On the other hand, IBs are fully stable for long periods of time with respect to both fluorescence emission and architecture at −80 °C, 4 °C, 25 °C, and also 37 °C (Fig. 2E,F), allowing both conservation and convenient manipulation of IBs under physiological assay conditions. Interestingly, IBs were also mechanically and functionally stable during lyophilization (Fig. 2F) and sonication (not shown), extending their potential uses under diverse experimental conditions.

As bacterial IBs are also fully biocompatible materials, we explored their applicability for biomedical purposes by a straightforward exercise. In regenerative medicine, cell binding and proliferation can be stimulated through the topographical modification of the material surfaces by etching, lithography, and similar procedures, depending on the nature of the material itself. Recently, approaches based on surface functionalization with biomaterials[21–24] or decoration with nanoparticles have also permitted a fine tuning of the surface and roughness irrespective of the support material.[25,26] For instance, silica and ceramic nanoparticles between 24 and 1500 nm in diameter can positively modulate cell proliferation.[25,27] Since we wondered if bacterial IBs could also be useful for surface nanoengineering, we deposited GFP IBs on tissue-culture-treated polystyrene plates (Fig. 3A) and tested the growth of BHK21 cells (Figs. 3B,C). At a density of 0.05 particles μm^{-2}, IBs showed a root mean squared (rms) roughness of 55.9 nm. On these modified surfaces, BHK21 cells grew intimately attached to GFP IBs, as observed by the merging of the cell membrane staining (red label) and IB

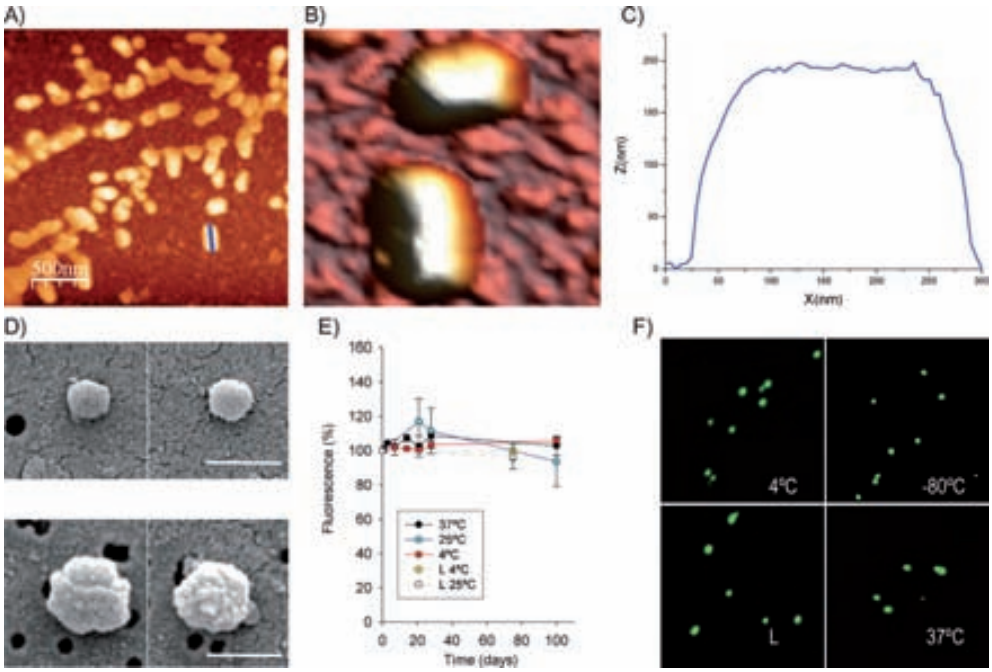

Figure 2. Fine architecture and stability of GFP IBs. A–C) AFM characterization of GFP IBs aged for 3 h. A) 2.5 μm × 2.5 μm topography image of randomly deposited wt IBs on a mica surface. B) 600 nm × 600 nm 3D zoom image from the image in A). C) Topography cross-section of an isolated IB particle (indicated as a blue line in A)), indicating a certain intrinsic rms surface roughness of 1.89 nm. D) SEM images of IBs aged for 3 h and produced in wt (top) and DnaK$^-$ (bottom) cells. Scale bars: 500 nm. E) IBs stabilities in aqueous buffer at 37 °C, 25 °C, and 4 °C, or lyophilized (L) and further stored at 25 °C or 4 °C. F) Confocal microscopy of purified IBs kept for one month at 25 °C, 4 °C, and −80 °C, and after lyophilization/reconstitution (L). For details on the AFM and DLS experiments see the Supporting Information.

fluorescence (green label) (yellowish signals, Fig. 3B). Intriguingly, in the polystyrene surface, which is largely optimized for cell adhesion and growth, the conventional cell-binding agent vitronectin did not have a detectable effect (Fig. 3D,E), while IBs dramatically stimulated cell proliferation (Fig. 3D) in a dose-dependent manner (Fig. 3E). This effect was much more significant than the poorer effects observed with other nanoparticles, which at defined sizes and for some cell lines seem to exhibit inhibitory rather than stimulatory influences.[25,27,28] Interestingly, no cytopathic effects were observed in cells cultured on IB-treated surfaces. A 3D analysis of confocal images (Fig. 3F) showed polystyrene-attached IBs as fully embedded in the cell membranes, indicating an intimate interaction between cell surfaces and IB nanoparticles.

To further prove the validity of IBs as stimulators of cell proliferation, microstructuration of the IBs onto an amino-terminated silicon substrate[29] was performed using the microcontact printing (μCP) technique.[30] Figure 3G shows the silicon surface patterned with IBs at a density of 0.04 IB μm^{-2} and a rms roughness of 32.4 nm, as well as the resulting line-shaped stimulation of cell proliferation in the regions decorated with IBs. This stresses again the ability of IBs to stimulate cell proliferation on surfaces initially not suitable for cell growth.

In summary, IBs are intriguing nanoparticulate materials produced by biological systems in inexpensive processes whose nanometer-scale features can be finely tailored during biological production. As IBs are biofunctional by nature, engineering of IBs might have wide applications in different nanomedical scenarios, and as a first proof-of-concept it is shown that IBs efficiently functionalize surfaces to favor mammalian cell proliferation in regenerative medicine approaches.

Experimental

Bacterial Cells, Plasmids and IB Production: IBs were produced in *E. coli* MC4100 (araD139 Δ(*argF-lac*) *U169 rpsL150 relA1 flbB5301 deoC1 ptsF25 rbsR*)[31] and its derivatives JGT4 (*clpA::kan*), JGT17 (*Δibp::kan*), JGT19 (*clpP::cat*), and JGT20 (*dnak756 thr::Tn10*).[32]

These strains were transformed with the expression vector pTVP1GFP (Ap^R), which encodes GFP fused at the amino terminus to VP1, an hydrophobic capsid protein from foot-and-mouth disease virus,[16] which promotes deposition as IBs.[7] The recombinant gene was expressed under the control of an IPTG inducible-*trc* promoter, in cells growing in Lucia Bertani (LB)-rich medium[31] under standard conditions.[15] IBs were detectable 1 h after IPTG addition (Fig. 1A).

IB Purification: Samples of bacterial cultures (200 mL) were centrifuged at 4 °C at 5000*g* for 5 min and resuspended in lysis buffer (50 mL, 50 mM

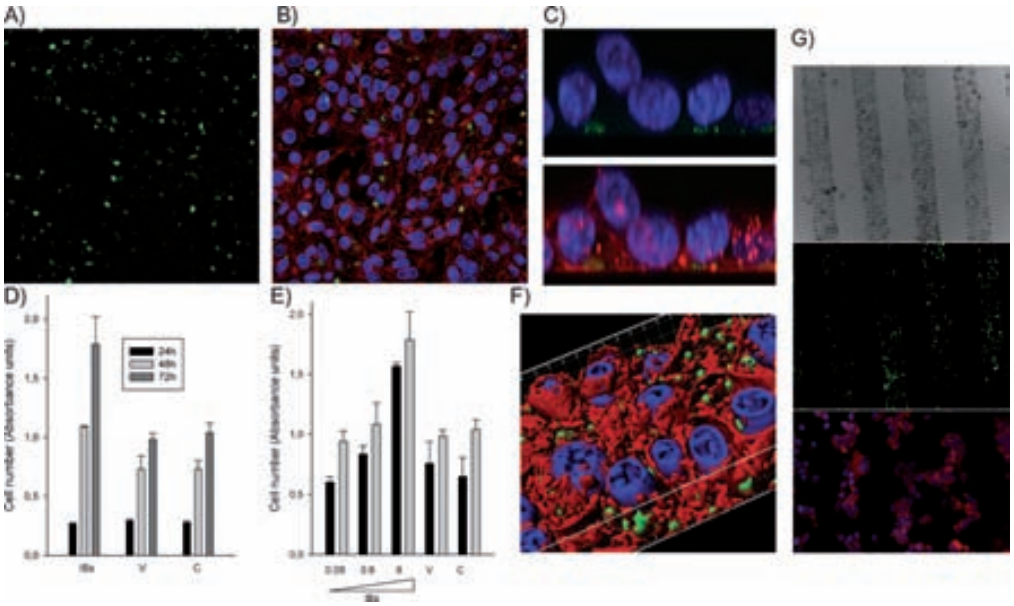

Figure 3. IB-stimulated mammalian-cell proliferation. A) Confocal image of a 35 mm polystyrene plate coated with 240 μg GFP IBs produced in wt cells. B) For the same field, the BHK cell overlay of the 0.6 μm section 75 h after cell deposition, and an *xzy* projection of GFP IBs (top) and cell overlay (bottom) (C). D) BHK cell growth on IB-coated plates (IB), vitronectin-coated plates (V), and control plates (C). E) BHK cell growth on plates coated with different concentrations of IBs compared to vitronectin-coated plates (V) and control plates (C). The experiments were carried out on treated (black bars) and nontreated (gray bars) polystyrene plates. F) Confocal *xyz* stack of 22 sections processed with Imaris 3D software by applying the Isosurface module. G) Images of the 50 μm lined IB-patterned amino-terminated silicon surfaces taken by conventional (top) and confocal microscopy (middle), and BHK cell distribution after 48 h of growth on them (bottom).

TrisHCl (pH 8.1), 100 mM NaCl, and 1 mM EDTA), ice-jacketed, and sonicated between 25 and 40 min at 40% amplitude under 0.5 s cycles. Then, phenylmethanesulphonylfluoride (PMSF) (28 μL, 100 mM) and lysozime (23 μL, 50 mg ml^{-1}) were added, and samples incubated at 37 °C for 45 min. After that, Nonidet P40 (NP-40, 40 μL) was added and the mixture kept at 4 °C for 1 h. DNA was removed with DNase (120 μL, 1 mg mL^{-1}) and Mg_2SO_4 (120 μL, 1 M) for 45 min at 37 °C. Finally, samples were centrifuged at 4 °C at 15000*g* for 15 min, and the pellet containing pure IBs was washed with lysis buffer containing Triton X-100 (0.5%) and stored at −20 °C until analysis. All incubations were done under agitation.

Microscopy Analyses of Bacteria and IBs: Samples were analyzed using a Leica TSC SP2 AOBS confocal fluorescence microscope (Leica Microsystems Heidelberg GmbH, Mannheim, Germany) after excitation at 488 nm, and images were recorded at emission wavelengths between 500 and 600 nm (63×, NA 1.4, oil) using a Plan-Apochromat objective (zoom 8; 1024 × 1024 pixels). Bacterial cells were fixed with formaldehyde (0.2%) in phosphate buffered saline (PBS) and isolated IBs were also resuspended in PBS. SEM was performed by conventional procedures using a Quanta FEI 200 FEG (field-emission gun) ESEM (environmental scanning electron microscope).

Flow Cytometry: IBs resuspended in PBS were sonicated for 4 min under 0.5 s cycles and analyzed by flow cytometry on a FACS Calibur system (Becton Dickinson), using a 15 mW air-cooled argon-ion laser at 488 nm excitation. IB fluorescence emission was measured in the FL1 channel (530/30 nm band pass filter) using a logarithmic mode.

Amino-Terminated Monolayer Preparation: Prior to monolayer formation, the silicon (100) substrates were treated with oxidizing solution ($NH_4OH/H_2O_2/H_2O$ in 1:1:5 ratio) for 30 min at 80 °C and gently rinsed with ultrapure water (MilliQ with 18.2 MΩ cm). Subsequently, the substrates were placed in piranha solution for 15 min (concentrated H_2SO_4 (Panreac) and 33% aqueous H_2O_2 (Aldrich) in a 3:1 ratio), copiously rinsed with ultrapure water, and dried under a stream of nitrogen. Then the substrates were exposed under controlled atmosphere to a solution of *N*-[3-(trimethoxysilyl)propyl]ethylenediamine (5 mM, 97%, Aldrich) in dry toluene for 3 h. Subsequently, substrates were rinsed with toluene and ethanol to remove excess silane. The contact angles of the amino-terminated substrate were measured on a OCA15+ (Data Physics Instruments GmbH, Germany), X-ray photoelectron spectroscopy (XPS) spectra were obtained on a PHI ESCA-5500 instrument (PerkinElmer).

Microcontact Printing: The μCP of IBs onto the amino-terminated silicon substrate was performed using polydimethylsiloxane (PDMS, Sylgard 184, Dow Corning, USA) stamps. Stamps were fabricated by casting a 10:1 (v/v) mixture of PDMS and curing agent (Sylgard 184, Dow Corning) against a photolithographically patterned silicon master, curing for 1 h at 60 °C, and releasing. PDMS stamps were left in the oven at 60 °C for at least 18 h to ensure complete curing. For the μCP-patterned IBs, the stamps were inked with a IB PBS buffer (pH 7.5) suspension for 40 min, dried under nitrogen flow, and placed on the clean amine-terminated silicon substrate. After 1 min contact time the stamp was carefully removed.

Stability Analyses: IBs aged for 5 h and obtained in $DnaK^-$ cells, in PBS with 10 g L^{-1} bovine serum albumin (BSA), sucrose (60 g L^{-1}), gentamicin (40 mg L^{-1}), penicillin (100 U mL^{-1}), and streptomycin (10 μg mL), were incubated at different temperatures for different times. Samples were frozen at −80 °C until fluorescence determination at 510 nm in a Cary Eclipse fluorescence spectrophotometer (Variant, Inc., Palo Alto, C.A) using an excitation wavelength of 450 nm. Results are given as the percentage of remaining activity or fluorescence with respect to fully stable samples at −80 °C. Another set of samples was lyophilized in a Cryodos-80 Telstar lyophilizer and stored at either 4 °C or 25 °C until analysis.

Cell Proliferation Assay: IBs aged for 3 h were sterilized by exposure to a 253 nm UV light germicidal lamp for 4 h. The IBs were resuspended in PBS, and different IB protein amounts were added per well to coat 96-well Falcon 3072 tissue-culture treated polystyrene plates (Becton Dickinson), or nontreated Costar 3370 plates, which were left overnight at 4 °C. Vitronectin (Calbiochem) was used as a reference (at 50 ng cm^{-2}). Wells were washed in PBS and blocked with 3% BSA in PBS for 1 h at 37 °C. Afterwards, 1.5×10^2 newborn hamster kidney (BHK) cells were added per well and incubated in Dulbecco's Modified Eagle's Medium (DMEM) supplemented with nonessential amino acids, fetal calf serum (5%), gentamicine, and antimycotics at 37 °C for different times. Blank wells underwent exactly the same treatment as described but without IBs.

After incubation, cell proliferation was determined using the EZ4U kit (Biomedica GmbH) following the manufacturer's instructions, and analyzed in the multilabel reader VICTOR^{3}V 1420 (PerkinElmer). The reading absorbances were 450 nm and 620 nm as reference, and the values were standardized with respect to medium-containing wells. A pre-test to select incubation time before saturation was carried out with the kit reagents. All assays were done in triplicate. Data were expressed as the mean ± (standard error of the mean) of the values obtained per condition and evaluated statistically by the one-way ANOVA test, followed by Bonferroni's post hoc analysis. For cell growth on silicon, IB-grafted surfaces were cut to appropriate sizes, UV-irradiated, and deposited on 24-well Falcon tissue-culture-treated polystyrene plates where cells were inoculated and cultured using conventional procedures.

Confocal Microscopy Analysis of Cell Cultures: Cell cultures were examined using a spectral confocal Leica TCS SP5 AOBS (Leica Microsystems, Mannheim, Germany) using a Plan-Apochromat 63 × 1.4 NA lens. All images were obtained from living cells grown in Glass Bottom Dishes (MatTek Corporation, Ashland, MA, USA). Cells were seeded at a density of 4×10^4 per well on IBs 72 h before the acquisition and cultured in DMEM + Glutamax 1 (Gibco) supplemented with fetal bovine serum (10%). For nuclear and plasma membrane labeling, cells were incubated with Hoechst 33342 (5 μg mL^{-1}) and CellMask (5 μg mL^{-1}) (both from Molecular Probes, Inc., Eugene, OR, USA), respectively, for 5 min at room temperature, and washed twice prior to confocal detection. Nuclei were excited with 405 nm diode laser beam, and detected at 414–461 nm; plasma membrane was detected by exciting with the light of a 633 nm helium neon laser and fluorescence was detected at 656–789 nm. Finally, the argon laser 488 nm line was used for imaging IBs (emission at 500–537 nm). *Z*-series of 22 optical sections were collected at 0.6 μm intervals. *Z*-stacks were acquired with LAS AF software (Leica Microsystems) and 3D models were generated using Imaris software (Bitplane, Zürich, Switzerland).

Acknowledgements

The authors appreciate the financial support through MEC (BIO2007-61194 and CTQ2006-06333) and AGAUR (2005SGR-00956 and 2005SGR-00591) grants and from the CIBER de Bioingeniería, Biomateriales y Nanomedicina (CIBER-BBN, promoted by ISCIII), Spain. We are also indebted to Prof. E. Domingo for his kind gift of BHK cells, to A. Sanchez for his technical assistance with scanning electron microscopy, and to M. Roldán for her advice and enthusiastic assistance with confocal microscopy. AV was supported by ICREA (Generalitat de Catalunya) through an ICREA ACADEMIA award. Supporting Information is available online from Wiley InterScience or from the authors.

Received: January 26, 2009
Revised: March 14, 2009
Published online:

[1] A. Villaverde, M. M. Carrio, *Biotechnol. Lett.* **2003**, *25*, 1385.
[2] G. A. Bowden, A. M. Paredes, *Biotechnology (NY)* **1991**, *9*, 725.
[3] M. M. Carrio, J. L. Corchero, A. Villaverde, *FEMS Microbiol. Lett.* **1998**, *169*, 9.
[4] P. Neubauer, B. Fahnert, H. Lilie, A. Villaverde, in *Inclusions in Prokaryotes*, (Ed: J. M. Shively), Microbiology Monographs, Vol. *1*, Springer, Berlin **2006**, pp. 237–292.
[5] F. Baneyx, M. R. Mujacic, *Nat. Biotechnol.* **2004**, *22*, 1399.
[6] S. Ventura, A. Villaverde, *Trends Biotechnol.* **2006**, *24*, 179.
[7] M. Carrio, N. Gonzalez-Montalban, A. Vera, A. Villaverde, S. Ventura, *J. Mol. Biol.* **2005**, *347*, 1025.
[8] E. Garcia-Fruitós, A. Aris, A. Villaverde, *Appl. Environ. Microbiol.* **2007**, *73*, 289.
[9] L. Wang, S. K. Maji, M. R. Sawaya, D. Eisenberg, R. Riek, *PLoS Biol.* **2008**, *6*, 195.
[10] J. Nahalka, I. Dib, B. E. Nidetzky, *Biotechnol. Bioeng.* **2008**, *99*, 251.
[11] J. Nahalka, P. Gemeiner, M. Bucko, P. G. Wang, *Artif. Cells Blood Substit. Immobil. Biotechnol.* **2006**, *34*, 515.
[12] J. Nahálka, A. Vikartovska, E. A. Hrabarova, *J. Biotechnol.* **2008**, *134*, 146.
[13] J. Nahálka, *J. Ind. Microbiol. Biotechnol.* **2008**, *35*, 219.
[14] M. M. Carrió, A. Villaverde, *FEBS Lett.* **2003**, *537*, 215.
[15] E. Garcia-Fruitós, M. Martinez-Alonso, N. Gonzalez-Montalban, M. Valli, D. Mattanovich, A. Villaverde, *J. Mol. Biol.* **2007**, *374*, 195.
[16] E. Garcia-Fruitós, N. Gonzalez-Montalban, M. Morell, A. Vera, R. M. Ferraz, A. Aris, S. Ventura, A. Villaverde, *Microbial Cell Factories* **2005**, *4*, 27.
[17] L. F. Vallejo, M. Brokelmann, S. Marten, S. Trappe, J. Cabrera-Crespo, A. Hoffmann, G. Gross, H. A. Weich, U. Rinas, *J. Biotechnol.* **2002**, *94*, 185.
[18] K. R. Babu, S. Swaminathan, S. Marten, N. Khanna, U. Rinas, *Appl. Microbiol. Biotechnol.* **2000**, *53*, 655.
[19] F. Hoffmann, U. Rinas, *Biotechnol. Prog.* **2000**, *16*, 1000.
[20] G. Margreiter, P. Messner, K. D. Caldwell, K. Bayer, *J. Biotechnol.* **2008**, *138*, 67.
[21] P. A. Suci, M. T. Klem, F. T. Arce, T. Douglas, M. Young, *Langmuir* **2006**, *22*, 8891.
[22] M. Uchida, M. T. Klem, M. Allen, P. Suci, M. Flenniken, E. Gillitzer, Z. Varpness, L. O. Liepold, M. Young, T. Douglas, *Adv. Mater* **2007**, *19*, 1025.
[23] D. M. Yanker, J. A. Mauer, *Mol. BioSyst.* **2008**, *4*, 502.
[24] M. J. Ludden, A. Mulder, R. Tampe, D. N. Reinhoudt, J. Huskens, *Angew. Chem. Int. Ed.* **2007**, *46*, 4104.
[25] A. M. Lipski, C. J. Pino, F. R. Haselton, I. W. Chen, V. P. Shastri, *Biomaterials* **2008**, *29*, 3836.
[26] A. R. El-Ghannam, P. Ducheyne, M. Risbud, C. S. Adams, I. M. Shapiro, D. Castner, S. Golledge, R. J. Composto, *J. Biomed. Mater. Res. A* **2004**, *68*, 615.
[27] A. J. Dulgar-Tulloch, R. Bizios, R. W. Siegel, *J. Biomed. Mater. Res. A* **2008**, DOI:10.1002/jbm.a.32116
[28] H. D. Samaroo, J. Lu, T. J. Webster, *Int. J. Nanomedicine* **2008**, *3*, 75.
[29] S.-H. Hsu, D. N. Reinhoudt, J. Huskens, A. H. Velders, *J. Mater. Chem.* **2008**, *18*, 4959.
[30] R. S. Kane, S. Takayama, E. Ostuni, D. E. Ingber, G. M. Whitesides, *Biomaterials* **1999**, *20*, 2363.
[31] J. Sambrook, E. Fritsch, T. Maniatis, *Molecular Cloning: A Laboratory Manual*, Cold Spring Harbor Laboratory Press, Cold Spring Harbor, NY **1989**.
[32] J. G. Thomas, F. Baneyx, *J. Bacteriol.* **1998**, *180*, 5165.

ADVANCED MATERIALS

SURFACE CELL GROWTH ENGINNERING ASSISTED BY A NOVEL BACTERIAL NANOMATERIAL

By Elena García-Fruitós [1,2], Escarlata Rodríguez-Carmona [1,2,3], César Diez-Gil [1,4], Rosa Mª Ferraz [1,2,3], Esther Vázquez [1,2,3], José Luis Corchero [1,2], Mary Cano-Sarabia [1,4], Imma Ratera [1,4], Nora Ventosa [1,4], and Jaume Veciana [1,4] * and Antonio Villaverde [1,2,3] *

[*] J. Veciana. Institut de Ciencia de Materials de Barcelona (CSIC), Bellaterra, 08193 Barcelona, Spain.
Phone: +34 935801853; fax: +34 935805729; E-mail: vecianaj@icmab.es
[*] A. Villaverde. Institute for Biotechnology and Biomedicine, Universitat Autònoma de Barcelona, Bellaterra, 08193 Barcelona, Spain.
Phone: +34 935813086; fax: +34 935812011; E-mail: antoni.villaverde@uab.es

[1] *CIBER de Bioingeniería, Biomateriales y Nanomedicina (CIBER-BBN), Bellaterra, 08193 Barcelona, Spain*
[2] *Institute for Biotechnology and Biomedicine, Universitat Autònoma de Barcelona, Bellaterra, 08193 Barcelona, Spain*
[3] *Department of Genetics and Microbiology, Universitat Autònoma de Barcelona, Bellaterra, 08193 Barcelona, Spain*
[4] *Department of Molecular Nanoscience and Organic Materials, Institut de Ciencia de Materials de Barcelona (CSIC), Bellaterra, 08193 Barcelona, Spain*

SUPPORTING INFORMATION

Atomic force microscopy characterization

Atomic force microscopy (AFM) was performed in air with a commercial atomic force microscope (PicoScan/PicoSPM from Agilent Technologies, Inc., USA) operating in acoustic mode using monolithic silicon tip (PPP-NHC:;42 N/m and 330 kHz; Nanosensors, Inc.). IBs in phosphate buffer at pH=7.4 (0.1 M) were dropcasted onto a mica surface and air dried before measuring.

Dynamic light scattering measurements

Volume IB size distributions and Z-potential were measured in a dynamic light scattering (DLS) analyzer at the wavelength of 633 nm, combined with non-invasive backscatter technology (NIBS) (Zetasizer Nano ZS, Malvern Instruments Limited, Malvern, U.K.). Dispersions of 3 hours-aged IBs (500 ng/µl) in phosphate buffer at pH=7.4 (0.1 M) were prepared by a brief sonication (1 min at room temperature). Aliquots of 3 ml of the resulting dispersion were measured at 20ºC without filtering, and the intensity data were normalized using phosphate buffer at pH=7.4 (0.1 M) as a reference. The mean value of three different measurements was taken as the hydrodynamic IB diameter.